Hybrid Position/Force Control and State Estimation for Position-and-Force-Sensorless Robots

August 2023

Keita SHIMAMOTO

A Thesis for the Degree of Ph.D. in Engineering

Hybrid Position/Force Control
and State Estimation
for Position-and-Force-Sensorless Robots

August 2023

Graduate School of Science and Technology
Keio University

Keita SHIMAMOTO

Acknowledgements

Contents

List of Figures

List of Tables

Chapter 1

Introduction

1.1 Motors and Robots

Motors that convert electrical energy into kinetic energy have been used since the 19th century. Kinetic energy is generated by the interaction between the magnetic field produced by the stator's current and the rotor's magnetic field. Motors are incorporated into various products and devices and are necessary for society. Furthermore, it is expected that products and devices using motors will be utilized in a broader range of fields in the future, as shown in Fig. 1-1[1][2][3].

Motors can be classified as shown in Table 1.1. Since alternate current (AC) motors have the advantage of not requiring maintenance from the commutator and have high torque response by control, they have been widely used in industrial applications. The overview of the structural difference is shown in Table 1.2. Induction motors (IMs) have long been used for a long time because they can rotate by applying a three-phase AC voltage without inverters. In addition, since IMs are suitable for applications requiring high power because they do not consist of magnets, However, IMs have energy conversion efficiency problems due to power losses from secondary winding currents. On the other hand, permanent magnet synchronous motors (PMSMs) consist of permanent magnets in the rotor and can have higher energy conversion efficiency than IMs. PMSMs require inverters, rotor position detection, and control processors to generate the magnetic field in the stator in synchronization with the rotor for an efficient drive. The efficiency and control performance have also advanced with the development of power semiconductors for inverters, position sensors, and processors. Furthermore, the torque density of PMSMs has increased with advances in magnet materials. Therefore, high-torque-density motors can rotate at
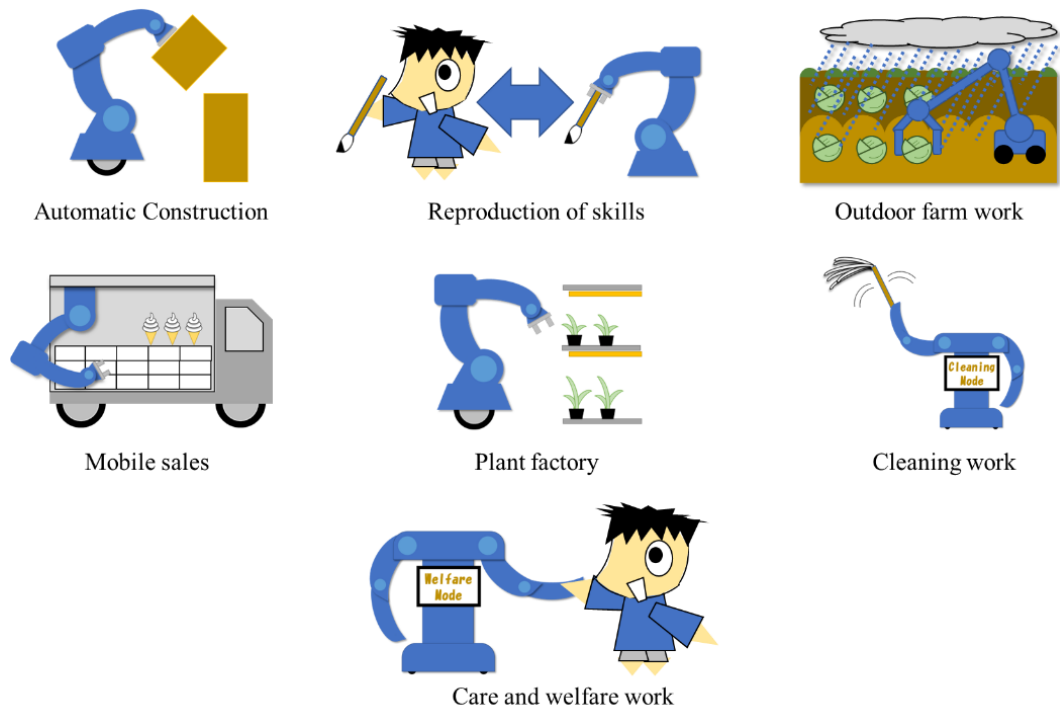
Fig. 1-1: Images of future applications.

high speeds with high precision and realize positioning. Although reluctance motors (RMs), especially synchronous reluctance motors (SynRMs), have higher torque density, and higher efficiency than those of IMs, they are unsuitable for low-speed operation, including positioning. As a result, PMSMs have been utilized in various machines, such as plastic and rubber modeling machines, cranes, compressors, metal processing machines, fans, electric vehicles, and industrial robots. In particular, industrial robots have multi-degree-of-freedom (MDOF), and their demand is expected to increase further to replace manual work and realize more sophisticated tasks than workers.

MDOF industrial robots that enable positioning in arbitrary positions and postures contribute to work automation [4]. Starting with the replacement of welding and painting operations, which are hazardous for workers, in the automotive industry, industrial robots have automated many manual tasks. Recently, robots with a structure that can be used in biomedical and food manufacturing fields, where hygiene control is essential, have been developed. Furthermore, robots collaborating with humans without safety fences are also becoming popular. Robots are expected to drive automation in various fields, such as agriculture, construction, and welfare [5][6][7][8].

Table 1.1: Motor classification.

		Maintenance	Power Range	Power Efficiency	Torque Density	Torque Control	Position Control	Position Detection
DC motor	DC motor with commutator	:(	:)	:(	:)	:)	:)	:)
	Brushless DC motor	:)	:)	:)	:)	:|	:)	:|
AC motor	Induction Motor (IM)	:)	:)	:(	:|	:)	:)	:)
	Interior Permanent Magnet Synchronous Motor (IPMSM)	:)	:)	:)	:)	:)	:)	:|
	Surface Permanent Magnet Synchronous Motor (SPMSM)	:)	:)	:)	:)	:)	:)	:|
	Reluctance Motor	:)	:)	:|	:|	:)	:|	:|
Stepping Motor		:)	:|	:|	:)	:|	:)	:)
Ultrasonic Motor		:(	:(	:|	:)	:(	:)	:)

Table 1.2: Structure overview of AC motors.

	IM	SPMSM	IPMSM	SynRM
Structure				
Torque	Induction	Magnet torque	Magnet torque Reluctance torque	Reluctance torque
Application Examples	Pump Compressor	Industrial robots Semiconductors	Electric vehicles Industrial robots	Train Vacuum cleaner
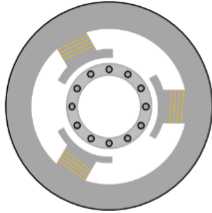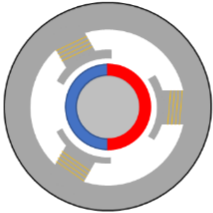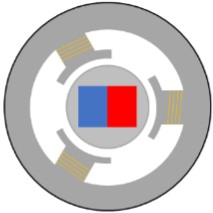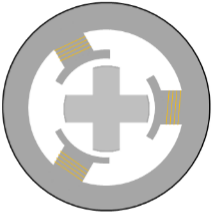
1.2   Transient of Motor Drive

Motor applications have expanded with advances in motor drive technology. The transition of the motor drive technology since the 1980s can be shown in Fig. 1-2. Fig. 1-2 is expressed based on the reference [9]. In the 1980s, as the performance of control processors improved, software realized a variable-frequency drive control method called field-oriented control (FOC), and high-performance IM drive systems were put into practical use [10]. In the 1990s, all-digital control systems using application-specific integrated circuits (ASIC) or field-programmable gate arrays (FPGA) became mainstream. The control performance of IMs can be higher than that of direct current (DC) motors. Motors for variable-frequency drive applications have been IMs due to demand for high response, energy saving, and maintenance-free. Since the 2000s, further high-efficiency utilization of motors and expansion of application fields have been expected to correspond to energy and environmental issues. PMSMs with neodymium magnets with high coercive and magnetic force attracted attention because of their higher efficiency than IMs. PMSMs and the drive technologies to realize higher efficiency, power, and torque density are still being developed.

For the efficient drive of PMSMs, rotor position information is essential to synchronous the magnetic field generated by the stator and that of the rotor. Generally, position sensors such as resolvers and encoders are attached to motors to detect the rotor position. However, using sensors causes problems such as wiring work, malfunction due to detection noise, high cost, and increased volume. In particular, control methods without position sensors are desired because of the failure risk in environments where temperature and humidity are not well regulated or situations in which vibration or shock is significant. Therefore, position-sensorless control of PMSMs is essential for the practical use of PMSMs. Since the late 1990s, various position estimation methods have been proposed [11][12][13][14]. Furthermore, initial magnetic pole position detection techniques were also studied [15]. Position estimation methods continue to improve [16] [17] [18]. Motor design methods for position-sensorless control have been proposed to detect the mechanical angle [19] [20]. Position estimation methods can be classified into two categories: those that use back electromotive force (EMF) and those that use magnetic saliency. Position estimation methods using back EMF are suitable for high-speed operation and applicable to general PMSMs. However, back EMF is small and hard to detect in low-speed operation. Open-loop control can be used at low speeds to increase rotational speed until the estimated position and speed converge [21]. On the other hand, position estimation methods based on magnetic saliency are suitable for low-

speed operation and applicable only PMSMs with magnetic saliency. Since those methods amplify and detect current variation at frequencies sufficiently higher than the motor's rotational frequency, they are unsuitable for high-speed operation. Switching between position estimation methods for low-speed and high-speed allows the system to operate in a wide speed range [22]. Typical PMSMs with magnetic saliency are interior permanent magnet synchronous motors (IPMSMs).

General-purpose drive systems with functions for position-sensorless IPMSMs are commercialized. As position estimation performance improves, drive systems for position-sensorless IPMSMs have been widely used for outdoor applications and contributed to the expansion of the motor market [23][24][25].

Motor drive systems whose primary purpose is positioning operation are called servo drive systems. Synchronized operation of multiple servo amplifiers by higher-layer controllers realize processes with electrical systems. PMSMs with high-resolution position sensors are the target motors. The transition of the motor drive technology since the 1980s can be shown in Fig. 1-3. Fig. 1-3 is expressed based on the reference [26]. Since the 1980s, the resolution of the position sensors has increased, and the size of motors has decreased. Digital control allows for complex calculations, and many methods were studied to achieve robust positioning. Although the basic control is proportional-integral-differential (PID) control, various functions, such as vibration suppression, automatic parameter adjustment, and machine analysis functions, are implemented, and those functions are being improved.

Terms	1990	2000	2010	2020
Demands	Energy saving		High efficiency	
			Compliance with standards for environments	
			Compliance with standards for safety	
	Noise and harmonics reduction	Built-in noise filter		Higher speed
				Higher power
	High start-up torque / Smooth operation at low speeds		Tuning-less	PM sensorless
		Easy maintenance	Robustness to environments	
		Longevity / Life span diagnostics	Life span diagnostics of machines	
Devices	Bipolar transistor	IGBT		Sic GaN
	Higher switching frequency		Soft switching / Lead-free	
	Higher power	Lower loss	Lower noise	
	Intelligent power module			
	16bit processor	ASIC / DSP / 32bit processor	Low voltage drive	
Control	High-frequency PWM inverters	Harmonics reduction	Matrix converters	
	Sensorless FOC	Auto-tuning	Energy-saving	Online tuning	PM motor auto-tuning
	FOC for general motors	Control for PM motors	Sensorless positioning	
Products	Digital		All digital	Communication	Open network
		PMSM drive	3-level	Programmable	Security
		Low noise	Built-in noise filter inverters	Downsizing
		Harmonics reduction / Sine wave input inverters	Sine wave input/output inverters	
		CE Mark	Safety standards	Efficiency standards
			Remote maintenance / Ethernet	

Fig. 1-2: Transient of motor drive [9].

Terms	1990	2000	2010	2020
Demands	Maintenance-free	Downsizing	Energy saving	Fast / High precision (Linear motors)	Safety	Integration of motor and amplifier
	High precision	High function		Life span diagnostics	
	Fast response	Smaller noise	High efficiency	Synchronous motion	Fan-less
	Digital	Easy-to-use	International standard compliance	Environmentally friendly	Sensorless
	Reducing wiring				
	Open-network	Fast communication	Lead-free	Wireless communication	
Motor	Neodymium magnet	Higher density of winding	Larger power	Smaller power	Larger power	Smaller vibration
	Ferrite / Samarium cobalt magnet	Linear motors	IPMSM	Higher power density	Built-in motor	Rare-earth-less
			DD motor		
Sensor	Resolver	Absolute encoder	Downsizing (<φ40)	Downsizing (<φ30)	
	Incremental encoder	Encoder with microcontroller	High resolution	High resolution (>20bit)	Battery-less
		Serial communication			
Amplifier (Power device, Microcontroller, Controller, Implementation)	Bipolar transistor	Intelligent power module	Microprocessor		
	MOSFET	IGBT	Soft switching	Active filter	Downsizing / Lower loss of power devices	SiC / GaN
	All digital	Communication	Open network		
	Microprocessor (8 or 16bit)	RISC (32bit)	RISC (64bit, FPU)	Multi core processor
	DSP	Low voltage drive	Multiprocessor	
	ASIC	Observer / Robust control	Vibration suppression	IoT
	High density	Mechanical analysis	Advanced control (Tuning-less)	Safety standards
	Auto-tuning	Self-diagnosis	Ethernet	

Fig. 1-3: Transient of servo drive [26].

1.3   Transient of Industrial Robots

Robot applications have expanded with the development of hardware components and motion control technology [4] [27] [28]. In the 1960s, industrial robots with 5-degree-of-freedom (5DOF) were commercialized and were hydraulically driven. Industrial robots have been used by teaching playback methods. Their motion has been based on position control using information from position sensors. Scheinman invented the Stanford Arm with 6DOF, which enables the operation of all degrees of freedom of position and posture in 3-dimensional space. From the 1970s, fully electric industrial robots with motors attached to each joint were commercialized. Since electrically-driven robots can operate faster and more accurately than hydraulically-driven robots, electrically-driven robots have been widely used. In the 1980s, as the performance of servo drive systems improved, DC motors for robots were replaced with AC motors. Although these robots were vertically articulated, parallel link mechanisms were utilized to support the links. In the 1990s, serial-link-type mechanisms for robots were realized, and the movable range was expanded. The movable range expansion allowed robots to achieve a variety of postures and work for applications for assembling and material handling. In the 2000s, 7DOF robots and dual-armed robots were released. These robots can avoid obstacles and perform more complex assembly and welding. However, since the robot's motion is based on position control, they were not suited for a flexible motion to avoid damaging the contact object. Complex assembly requires precise force control of the end-effector to contact the object without breaking. Force/Torque (F/T) sensors have been attached to the end-effector of robots [29] [30]. However, the damage to sensors due to impact was a problem. In the late 2000s, a force sensor that is not easily broken even by the impact was commercialized [31]. Robots with F/T sensors, such as a robot shown in Fig. 1-4, have been famous, and assembly and material handling applications have been expanded [32]. In the 2010s, collaborative robots with built-in F/T sensors were put to practical use. They enable robots and workers to work in the same place without fences [33]. Control methods for assembly using the sensors built into collaborative robots have been proposed [34]. In addition, artificial intelligence (AI) technologies for image processing have reached a practical level. The technologies can derive robot commands to move to the target position without teaching playback [35] [36]. As a result, applications of robots have further expanded, as shown in Fig. 1-1.

Examples of tasks requiring force control are rubbing motion for polishing and fitting works [37] [38]. The end-effectors of MDOF robots with force control functions are expected to move based on force control in the contact direction and based on position control in the movement direction. The motion
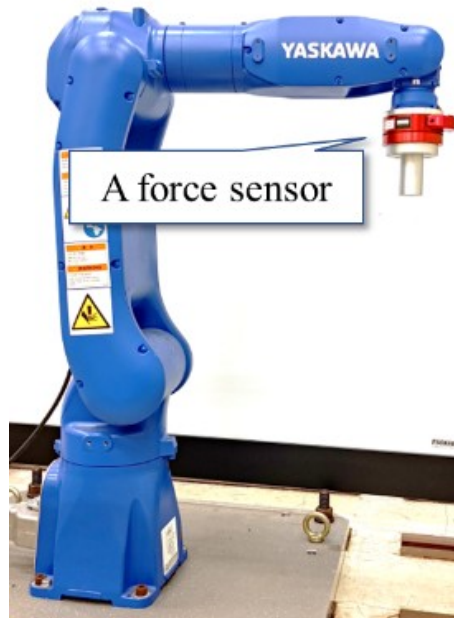
Fig. 1-4: A robot with a F/T sensor.

can be realized by hybrid position/force control. Furthermore, some applications in Fig. 1-1 require a remote operation, which can transmit force information. Those remote operations can be realized by 4ch-bilateral control [39]. The 4ch-bilateral control can be considered as one of the hybrid position/force control systems. Therefore, for future applications, hybrid position/force control is essential.

1.4   Prospects of Motors and Robots

Industrial robots are expected to be used in various applications, such as agriculture, construction, service, and welfare. Fields of these applications are unmaintained environments outside factories. Force control for flexible contact is essential for tasks such as harvesting, assembly work, plastering, and human support. In addition, low cost, ease to use, portability, robustness, and safety are essential keywords for devices in these applications [8]. On the other hand, positioning accuracy is not required as much as with conventional industrial robots.

One of the methods to respond to the demands is position-sensorless robots. Conventional industrial robots use position sensors to obtain the position and posture information of the end-effector. However, position sensors are precision instruments and are not suitable to use with applying vibration and shock. If position sensors can be removed, the mechanical robustness can increase, and the cost and wiring for position sensors can be reduced. In particular, high-resolution position sensors are expensive due to the complexity of the manufacturing process as well as the components. The cost-reduction effect of eliminating position sensors is significant for small-capacity and high-torque-density servo motors. The wiring reduction also reduces the weight of robots.

Furthermore, F/T sensors are also expected to be removed for the same reasons. Since reaction force/torque information is required for safe operation and force control, force/torque estimation is utilized. The other advantage of force-sensorless robots is the reduction of the collocation problem in force control. Generally, sensors are attached to the tip of robots or the end-effector. The driving points by motors and the force detection points are apart. The output force at the end-effectors is a combination of the torque by motors and the effect of the dynamics between motors and the end-effector. The configuration causes a collocation problem and unintentional force response by the uncertain dynamics of mechanical systems, such as reduction gears in the closed loop. However, force estimation methods utilize the information at the control points of motors. As a result, force-sensorless force estimation methods can be more stable from the viewpoint of the collocation problem. Therefore, force-sensorless robots with force control functions have also been expected.

Integrating the above sensorless robots would be position-and-force-sensorless (PFSL) robots. PFSL robots with force-control functions are required for future applications. The position and force information should be estimated without position and F/T sensors to control position and force. The system configuration changes as shown in Fig. 1-5. Table 1.3 shows the essential target bandwidth and current
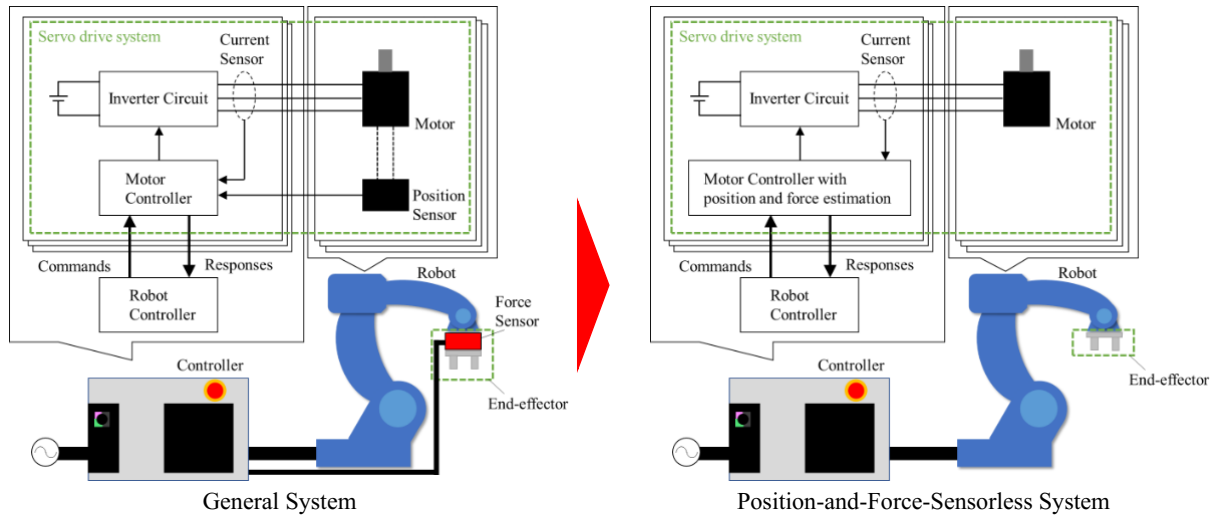
Fig. 1-5: Differences of general systems and position-and-force-sensorless systems.

Table 1.3: Comparing the target bandwidth and current bandwidth that could be achieved with conventional methods by experimental systems in this dissertation.

Description	Force Control	Force Estimation	Position Control	Position Estimation
Goal	10 Hz	20 Hz	10 Hz	200 Hz
Current	-	-	2 Hz (1 axis)	20 Hz (1 axis)

bandwidth that could be achieved with conventional technology for the 1-axis motor with a test motor. The target bandwidth of the control is set considering the bandwidth of human arm movement. The estimated bandwidth is set to be at least twice the control bandwidth. Since the estimated position is required for the force estimation, the target bandwidth of the position is set sufficiently higher than that of the force estimation. Since the current bandwidth depends on the target motors and system configurations, the values are noted based on the experimental results in this dissertation. The estimated force had large vibration, and force control was not realized in the PFSL control system with conventional methods. Therefore, the improvement of position estimation and the realization of force control without position and F/T sensors is expected.

1.5   Challenges of Position Estimation

Position estimation requires high estimation bandwidth and low estimation errors and vibrations. Position estimation methods using back EMF continue to improve [40] [41] [42] [43] [44] [45]. The effects by current measurement errors and uncertainty in inverters have been discussed and compensated [46] [47] [48]. However, their performance over a wide torque output range at low speeds is not as good as those using magnetic saliency. Magnetic saliency-based methods are suitable position estimation methods for low-speed operation, including zero-speed. Since force control functions are generally used at low speeds, magnetic saliency-based methods are attracted in this dissertation. Magnetic saliency-based methods utilize high-frequency voltage and current to detect the rotor position. Since voltage-type inverters are generally used for servo drive systems, detected high-frequency current is used for the estimation. The typical estimation methods are indirect flux detection on-line reactance measurement (INFORM) methods, characteristic pulse width modulation (PWM) methods, and high-frequency voltage injection methods. Estimation methods that perform position estimation processing in a carrier period or half of a carrier period can have a wider estimation bandwidth.

INFORM methods utilize the voltage output pattern based on Space Vector PWM (SVPWM) [49] [50] [51]. The methods insert test voltage output periods for position estimation between the voltage output periods for driving motors. During the zero-voltage vector output period, a pair of voltage vectors pointing in opposite directions instead of zero-voltage vectors are inserted. The current variation by the inserted test voltage is utilized for the position estimation. The advantage of the methods is separating the timing of driving voltage and test signal voltage. The detected current can be easily separated into that for driving and that for position estimation by adjusting the sampling timing of the current. However, a complex ASIC or FPGA, which can adjust the sampling timing at each carrier cycle, is essential. In addition, the number of switching timing within one carrier cycle increases, resulting in increased switching losses.

Characteristic PWM methods utilize extended voltage vectors or special carrier waveform [52] [53] [54] [55] [56] [57] [58]. Some methods lengthen the output time of the voltage vectors for driving and output voltage vectors in opposite directions within the same carrier cycle to cancel each other out. Other methods use three types of triangular waves with different shapes or start timing as carrier waves. Both methods extend the current variation within the carrier period, and position estimation can be performed by detecting the variation. The number of switching timing within one carrier cycle increases, resulting

in increased switching losses, and a complex ASIC of FPGA is essential, as with INFORM methods.

High-frequency voltage injection methods utilize a voltage with a frequency sufficiently higher than the motor's rotational frequency. The waveform of the injected voltage is a sinusoidal wave type or a square wave type [59] [60] [61] [62]. These methods can estimate the rotor position from the current variation by the current sampling in the peaks and valleys of a typical carrier wave and do not increase switching losses. Furthermore, the position estimation bandwidth can be equivalent to the other two methods using a high-frequency voltage synchronized to the carrier wave. In particular, square-wave-type voltage synchronized carrier frequency realizes wide-bandwidth position estimation. The summary of the three estimation methods is shown in Table 1.4. Therefore, the high-frequency voltage injection methods are suitable for implementation.

However, these methods have position estimation errors, although the error values depend on motors and the system configurations. The position estimation errors are caused by the phase delay by the filter in position estimation algorithms, the nonlinearity of inverters and motors, the injected voltage amplitude, the structure of motors, and the magnetic cross-coupling factors in the dq-axes.

The purpose of filters in position estimation algorithms is to reduce the noise from the detected current. Since the high-frequency current response is utilized, noise reduction is essential. Generally, proportional-integral (PI) type phase-locked loop (PLL) filters are used to reduce the noise [60]. The low cut-off frequency of the filter makes the bandwidth of the position-sensorless controller low. Since the bandwidth is important at high speed operation, the improved methods have been applied to position estimation methods based on back EMF [63] [64] [65] [66] [67] [68]. Although the performance improvement could be confirmed, these methods have not been for magnetic saliency-based position estimation methods. In positioning and force control applications, higher position estimation bandwidth is essential to bring control performance closer to that of control using position sensors.

The nonlinearity of inverters and motors makes modeling errors in estimation algorithms and causes position estimation errors. Examples of nonlinearity are voltage drops of power devices, dead time, parasitic capacitance effects, resistance variation by temperature, and inductance variation by the current. The adverse effects from parameter nonlinearity depend on the systems have often been compensated by gain adjustment or prediction. Although control methods considering non-linear characteristics have improved position-sensorless control performance, further improvement is expected [69] [70] [71] [72]. In addition, since the resistance and inductance variation deteriorates the performance of general current control methods without considering the fluctuation, suitable current control methods are required [73].

Table 1.4: Comparing position-sensorless position estimation methods.

	Current Sensing Timing	Switching Loss	Estimation Bandwidth	Noise Bandwidth
INFORM	☹	☹	☺	☹
Characteristic PWM	☹	☺	☺	☹
High-frequency voltage injection (Sinusoidal Wave)	☺	☺	☹	☺
High-frequency voltage injection (Square Wave)	☺	☺	☺	☺

The effects of the injected voltage amplitude on position estimation errors were revealed [74]. However, the injected voltage amplitude is adjusted according to the operating conditions. The required amplitude voltage is used while considering noise. The full compensation for the effects is not practical.

The cross-coupling factors in the dq-axes are the non-diagonal elements of the dq-axes voltage equation, and they are varied according to the rotor position and current according to finite element analysis (FEA) and experimental results [75] [76] [77] [78] [79]. According to the FEA and experimental results, the cross-coupling factors are non-linear parameters depending on current and position. Position estimation errors based on the cross-coupling factors were analyzed and compensated using reference tables made by the previous FEA to the target motor. These compensation methods improved the position estimation accuracy and the control performance. However, since utilized values are static information, the noise, the error, and the dynamical characteristics of input parameters to the reference tables or functions deteriorate the compensation performance. Online position estimation and error compensation methods without reference tables have also been proposed. By using the neural point voltage of stator windings, the effects of the inductance variation were compensated [82]. Considering the inductance variation in the voltage equation reduced the vibration during rotation [81] [80]. However, these methods did not include and estimate cross-coupling factors in the dq-axes inductance. Cross-coupling factors in the dq-axes inductance affect not only position estimation error but also current control and output torque

in position-sensorless control systems. To compensate for these effects, estimation of cross-coupling factors is essential. Therefore, online estimation and compensation methods of the rotor position and the cross-coupling factors without reference tables have been desired.

1.6 Challenges of Hybrid Position/Force Control and Force Estimation in the Workspace

In hybrid position/force control, force control is in the vertical direction of the contact surface, and position control is in the horizontal direction of the contact surface as shown in Fig. 1-6 [83]. Therefore, workspace control in Cartesian coordinates is suitable for hybrid control. Workspace hybrid control can unite the reference values from position control and force control in the force or acceleration dimension by an equivalent mass matrix [84]. The force reference values can be transformed into the torque reference of each motor. Therefore, although the kinematic transformation between the workspace and the joint coordinate space cannot express the dynamics of the workspace, the dynamics can be considered using the equivalent mass matrix. An equivalent mass matrix design method using an oblique coordinate for hybrid control considering the cross-coupling effects between the position control axes and the force control axes has been proposed [85]. An equivalent mass matrix for 4ch-bilateral control was shown [86][87]. Although they were for bilateral control, the cross-coupling effects were discussed. These approaches have improved the hybrid control performance and response at the impact timing. The suitable equivalent mass matrix for position control with DOB has also been proposed [88] [89]. However, the performance of force control during tasks requires further improvement. For example, when hybrid position/force control using an equivalent mass matrix based on the design values of a robot is applied to rubbing motion, the robot sometimes behaves as if it is repelled from the contact object and cannot keep contact with the object. The behavior occurs even if the force command is constant. The main cause of the behavior is the cross-coupling effects between the position and force control axes. Delay in following acceleration commands and the friction between the end-effector and the contact target work as a disturbance in position control axes. Those disturbances are cycled between the position and force control axes through the equivalent mass matrix. Since disturbances directly affect the reaction force in force control axes without dumping effects, the performance of the force control axes can be deteriorated by the disturbances in position control axes. Therefore, the suitable equivalent mass matrix for hybrid position/force control for contact motion differs from the matrix for position control systems without contact. Suitable equivalent mass matrices that consider hybrid control with contact are required.

Force estimation methods can be divided into those that estimate force from displacement and stiffness at contact and those that estimate force by observers based on dynamics [90] [91] [92] [93]. The former methods are effective when the contact position, the contact object, and the robot's stiffness are known.
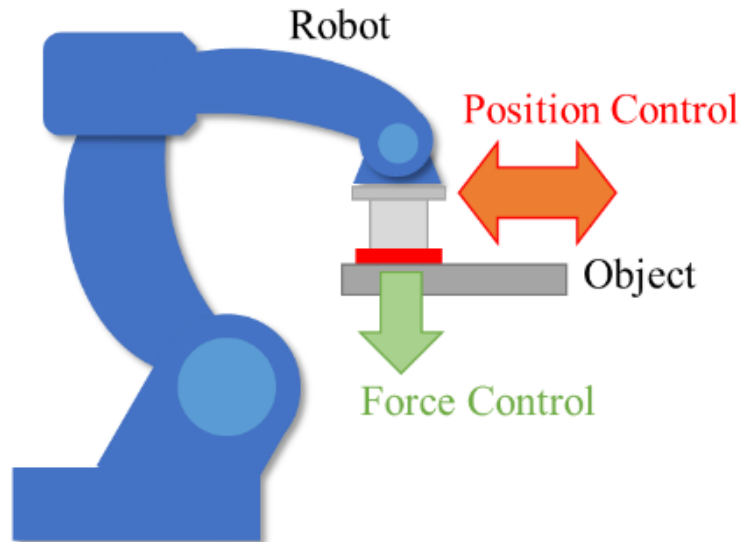
Fig. 1-6: Motion of hybrid control in rubbing motion.

However, feedback information from estimation methods using models without considering non-linear characteristics and uncertainty would worsen the responses when the modeling error is significant. In addition, many adjustable parameters and the algorithm's complexity have made algorithms hard to use. The latter methods are effective when the contact object and the contact point are uncertain. Reaction force observer (RFOB) or reaction torque observer (RTOB) based on disturbance observer (DOB) can realize robust force-sensorless control. These algorithms utilize force/torque command, velocity response, the cut-off frequency of the filter, and inertia or mass information to estimate the external force/torque. The estimated force/torque and disturbances have been utilized for force-sensorless control [86] [94] [95] [96]. It has also been shown that force control using estimated force/torque can provide a wider bandwidth of force control than force sensors [97] [98]. The stability and performance of force-sensorless control with DOB depend on the inertia or mass utilized in the controller. The performance of position control methods of MDOF robots with DOB and force control methods of 1DOF systems with DOB has been researched [99] [100] [101]. However, the discussion on the effect of the equivalent mass matrix during contact motion, including rubbing motion, was insufficient. Therefore, the equivalent mass matrix design method for hybrid control considering contact motion is required.

1.7   Challenges of MDOF Position-and-Force-Sensorless Control

Position-and-force-sensorless (PFSL) control has been researched. Although the observer can simultaneously estimate position and force, the observer was based on the model of the back EMF [102]. The force control performance at low speed was not discussed. Since PFSL robots are required in low-speed operations, position and force should be estimated in low-speed operations, including zero-speed. Some methods, which can be used for low-speed operations, used a special equipment configuration [103] [104]. Therefore, PFSL control systems are required to realize low-speed operation and be with general equipment.

An estimation configuration with position estimation by high-frequency voltage injection and force estimation by RFOB/RTOB can be one of the methods assumed to be practical. The concept can be shown in Fig. 1-7. This estimation configuration allows separate processing of the position estimation and force estimation. Since this configuration is not based on the back EMF, the force can be estimated even at zero speed. However, since PFSL robots do not have position sensors, the velocity response in RFOB/RTOB of PFSL robots is derived from the estimated position. When estimated position values have errors, vibrations, and phase delay, they affect the estimated values by RFOB/RTOB. The cut-off frequency of RFOB/RTOB should be adjusted by considering the position estimation bandwidth. The estimation bandwidth of RFOB/RTOB is lower than the position estimation bandwidth. Therefore, the phase delay of the position estimation method should be reduced.

Furthermore, synchronizing each joint motion is essential to realize accurate workspace control of MDOF PFSL robots. The inaccuracy of the estimated position disturbs the synchronization and the accurate workspace motion. When the joints' motion cannot synchronize, the error is the disturbance of position control axes. Cross-coupling effects from position control axes to force control axes deteriorate the force control axes' performance in hybrid position/force control. The low position estimation accuracy makes PFSL robots difficult to realize smooth motion. A PFSL robot for the experiment could not work by the conventional position estimation method and equivalent mass matrices with design values. The torque reference was diverged when the command was changed. Therefore, reducing the position estimation errors, vibrations, and cross-coupling effects between position and force control axes is required.
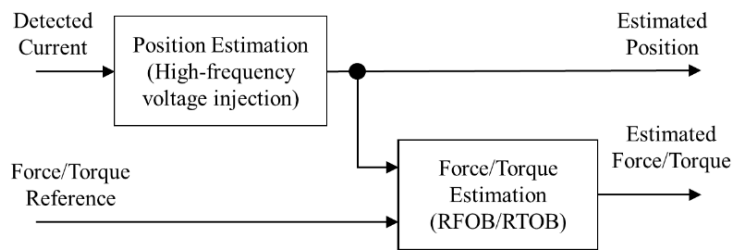
Fig. 1-7: Configuration overview of position and force estimation.

1.8   Motivation and Contribution

The purpose of the study is the realization of position-and-force-sensorless (PFSL) robots for future applications. The estimated position has errors, vibrations, and phase delay as described in Section 1.5. These characteristics are not appropriate for applications requiring precise positioning. Position sensors' resolution is higher than current sensors. The phase delay of the position detection by position sensors is smaller than the position estimation. The differences in positioning performance with and without position sensors are from the hardware and cannot be changed by the compensation with estimation algorithms However, the desired characteristics in applications requiring force control functions differ from those for precise positioning. The reaction force/torque can be more important than the instantaneous position-tracking error during contact motion, including rubbing motion. Therefore, PFSL control systems can be applied to applications requiring contact motion and rubbing motion by force control functions. They are expected to be used not only for simple conventional assembly, polishing, and cleaning work but also for applications that have been foregone due to cost-effectiveness. However, the performance of the position estimation has not achieved the desired level. Furthermore, unintended vibration preventing keeping contact with contact targets has occurred during rubbing motion in MDOF hybrid position/force control systems with equivalent mass matrices as described in Section 1.6. One of the reasons for the vibration is cross-coupling effects from position control axes to force control axes by equivalent mass matrices. In PFSL control systems, the errors and vibrations of the estimated position cause vibrations in position control axes. The reduction of the cross-coupling effects from position control axes to force control axes by equivalent mass matrices is essential.

The performance of position-sensorless control systems is fundamental for PFSL robots, and the cross-coupling effects between position and force control axes should be reduced in PFSL robots. Therefore, the first research step is on position-sensorless control, and the second is MDOF force-sensorless control. Combining these researches achieves the third research step on the PFSL control, as shown in Fig. 1-8.

The proposed position-sensorless control and position estimation improve position-sensorless control systems, which can be implemented on general equipment. The position estimation accuracy improvement reduces the adverse effects. The output of RFOB/RTOB in the proposed position-sensorless control systems can be used for the feedback information of the force control. However, the estimation errors and vibrations remain. The MDOF force-sensorless control with the equivalent mass matrices from the proposed design method decreases the vibration by cross-coupling effects from position control axes to
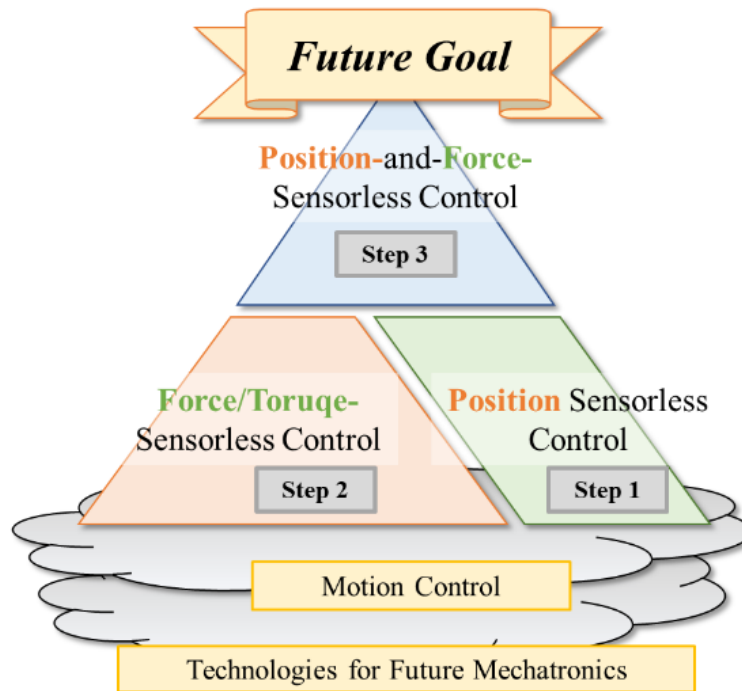
Fig. 1-8: Research steps to realize PFSL robots.

force control axes. The effects of the disturbances in position control axes by the position estimation errors and vibrations can also be reduced in force control axes by the proposed design method in PFSL hybrid position/force control. As a result, PFSL control systems for admittance control, 4ch-bilateral control, and hybrid position/force control for rubbing motion are realized.

The implementation of the processing on general equipment requires a short processing time. In particular, the period of current control and position estimation is short. Therefore, approximations to reduce the processing time are used when the performance or characteristics are similar.

The detail of each proposal is described below.

1.8.1   Position-Sensorless Control and Position Estimation

This dissertation presents the estimation of position and cross-coupling factors and position-sensorless control systems using these estimated values. Furthermore, this dissertation introduces a modeling method of the electrical coordinate system of IPMSMs that considers the dq-axes cross-coupling factors to study their implications as physical phenomena. The proposed algorithm is based on the voltage equation, including dq-axes cross-coupling factors. The cross-coupling factors vary with the motor rotation. The proposed position estimation method utilizes a d-axis high-frequency voltage injection method. In high-frequency voltage injection methods of position estimation, injected voltage is on the estimated d-axis, and the cross-coupling factors and position estimation error vary with the electrical angle at which the voltage is injected. This loop causes the inductance of the control target to vary at a high frequency even if the motor does not rotate. Therefore, the cross-coupling factors can be considered to have low-frequency components and high-frequency components. Estimation for both components improves the accuracy of the estimated position.

Position estimation methods based on magnetic saliency are generally used from the zero-speed to around 10 Hz of the electrical rotational frequency. The analytical results of cross-coupling factors showed a variation in the frequency of 6 times the rotation of the electrical angle. Therefore, the bandwidth for the compensation of low-frequency components is desired to be around 60 Hz. The variations in high-frequency components relate to the estimation period. Therefore, the bandwidth for compensating high-frequency components is desired to be over half or a quarter of the injection frequency.

In addition, the estimated cross-coupling factors are utilized in the model of the current controller to derive voltage command from torque reference. Since the inductance variation is non-linear, sliding-mode control (SMC) and voltage disturbance observer (VDOB) are utilized to derive voltage command from the current command. A conventional model of the relationship between torque and current also does not have cross-coupling factors. The voltage equation considering cross-coupling factors can derive the relationship, including the cross-coupling factors' effect. The current command in the proposed controller is derived from the torque constant and the estimated cross-coupling factors.

Experiments on the proposed position-sensorless control system confirmed the proposed method's validity, the response's vibration, and the torque-velocity characteristics.

1.8.2 Force-Sensorless Hybrid Position/Force Control

This dissertation presents a decoupled rubbing motion by force-sensorless hybrid position/force control with equivalent mass matrices switching. Cross-coupling effects from position control axes to force control axes by equivalent mass matrices in the controller, WOB, and RFOB/RTOB were clarified. A design method of equivalent mass matrices according to the expected velocity of force control axes was devised. When the expected velocity of force control axes is zero, the motion is assumed to be in contact with hard objects. In contact motion, force control performance is more important than position control performance. In order to reduce the cross-coupling effects from position control axes to force control axes, the cross-coupling terms between position control axes and force control axes in equivalent mass matrices are designed to be zero for the controller and workspace observer (WOB). On the other hand, when the velocity of force control axes is not zero, the motion is assumed to be free motion. In non-contact motion, the modeling error should be small to ensure that the response is as designed by the controller gains. According to consideration based on equations, an equivalent mass matrix whose cross-coupling elements between control axes are partially zero elements is applicable in free motion without contact. The derived matrix has a similar position control performance, and the calculation cost can be smaller than that of the equivalent mass matrix whose elements are derived by design values of mechanisms because of the larger number of zeros in the matrix elements. Furthermore, the coordinate transformation is also characteristic. The coordinate transformation in the acceleration dimension is used in the workspace force estimation. The estimated torque by RTOB in each joint is transformed into the workspace force through the acceleration dimension in the workspace. This transformation extracts the cross-coupling effects by the equivalent mass matrix as a proportional relationship. In addition, the coordinate transformation from the workspace acceleration reference to the torque reference in the joint coordinate space uses an equivalent mass matrix and the transposed matrix of the Jacobian matrix. They enable the design of the nominal equivalent mass matrix to realize the desired control characteristics.

Experiments with a 4DOF parallel link manipulator confirmed the validity of the proposed method. The proposed method reduced the vibration of the force control axis during the rubbing motion because of the reduction of cross-coupling effects from position control axes to force control axes by the disturbance applied to the position control axes.

1.8.3 Position-and-Force-Sensorless Control

This dissertation presents the PFSL control methods, including hybrid position/force control for rubbing motion. RFOB/RTOB using estimated position is introduced. The proposed position-sensorless control system reduced the noise in the estimated reaction force/torque. According to the experimental results, the estimated position and force could be used for admittance control and 4ch-bilateral control. Flexible operation depending on the external force and remote operation were realized. In addition, the performance of the rubbing motion with a 4DOF parallel link manipulator was also confirmed. Although position estimation errors became the disturbance of the position control axes. the proposed decoupling method reduced the vibration of force control axes caused by the cross-coupling effects from the position control axes' disturbance. The proposed PFSL control system realized keeping contact with objects.

1.9   Organization of Dissertation

This dissertation is organized into 8 Chapters. The rest of this dissertation is organized into seven chapters, as shown in Fig. 1-9.

In Chapter 2, the fundamental of position-sensorless control used in this dissertation is described In section 2.1, the modeling of an IPMSM is explained. In section 2.2, a general current controller is introduced. In section 2.3, a position estimation method using high-frequency voltage injection on the d-axis is explained.

In Chapter 3, the fundamental of force-sensorless control and robots used in this dissertation is described. In section 3.1, DOB and RFOB/RTOB are explained. In section 3.2, the modeling of the robot utilized in experiments is explained. In section 3.3, the equivalent mass matrix for the utilized robot is explained.

Chapter 4, discusses challenges to be solved in the position-and-force-sensorless (PFSL) control.

In Chapter 5, a development method of position-sensorless control is discussed. In Section 5.1, the cross-coupling factors of IPMSMs are introduced. Section 5.2 explains the proposed estimation method of position and cross-coupling factors based on the voltage equation considering the cross-coupling factors. Section 5.3 describes the proposed current control method with the estimated cross-coupling factors in high-frequency bandwidth. Section 5.4 shows the experimental results of the position-sensorless system with and without considering the cross-coupling factors. Section 5.5 explains the proposed error compensation method for the position estimation and the estimation method of cross-coupling factors in wide-frequency bandwidth. Section 5.6 introduces the proposed current control method with the estimated cross-coupling factors in wide-frequency bandwidth. Section 5.7 shows the experimental results to explain the validity of the proposed position-sensorless control system. This chapter is summarized in Section 5.8.

In Chapter 6, multi-degree-of-freedom (MDOF) force-sensorless hybrid position/force control systems and the design method of equivalent mass matrices in the systems are discussed. In Section 6.1, MDOF force-sensorless workspace hybrid position/force control systems are introduced. In Section 6.2, the effects of the utilized equivalent mass matrix are revealed with equations. In Section 6.3, the proposed equivalent mass matrices for the hybrid control system are introduced. In Section 6.4, the experimental systems and results to confirm the validity of the proposed design method are shown. This chapter is concluded in Section 6.5.

In Chapter 7, the proposed position-and-force-sensorless (PFSL) control is discussed. In Section 7.1, DOB using estimated position is explained. In Section 7.2, the proposed PFSL admittance control system is explained. In Section 7.3, the experimental systems and results to confirm the validity of the proposed PFSL admittance control method are shown. In Section 7.4, the proposed PFSL bilateral control system is explained. In Section 7.5, the experimental systems and results to confirm the validity of the proposed PFSL bilateral control method are shown. In Section 7.6, the proposed PFSL hybrid position/force control system is explained. In Section 7.7, the experimental systems and results to confirm the validity of the proposed hybrid position/force control method are shown. This chapter is summarized in Section 7.8.

This dissertation is concluded in Chapter 8.

This dissertation uses expressions with continuous-time systems and discrete-time systems. The expressions with continuous-time systems show the model and physical meaning. The expressions with discrete-time systems reveal utilized values in processing timing. Especially, position-sensorless control systems estimate position and cross-coupling factors extracted by high-frequency voltage, which varies in each processing timing of the estimation.

Chapter 1
Introduction

Conventional methods

Chapter 2
Position-sensorless control
• Modeling   • Position estimation   • Current control

Chapter 3
Force-sensorless control
• Modeling   • DOB and RTOB   • Equivalent mass matrix

Chapter 4
Position-and-force-sensorless control
• Controller   • Challenges

Proposed methods

Chapter 5
Position-sensorless control
• Modeling considering cross-coupling factors
• Position and cross-coupling factors estimation
• Proposed Current control

Chapter 6
Force-sensorless control
• Workspace hybrid position/force control
• The effects of the equivalent mass matrix
• Design method of the nominal equivalent mass matrix

Chapter 7
Position-and-force-sensorless control
• Controller

Chapter 8
Conclusions

Fig. 1-9: Chapter organization.

Nomenclature

Abbreviations

AC	Alternate current
AI	Artificial intelligence
ASIC	Application-specific integrated circuits
DC	Direct current
DOF	Degree-of-freedom
DOB	Disturbance observer
EMF	Electromotive force
FEA	Finite element analysis
FFT	Fast Fourier transform
FOC	Field-oriented control
FPGA	Field-programmable gate arrays
F/T	Force/torque
HPF	High-pass filter
IM	Induction motor
LPF	Low-pass filter
INFORM	Indirect Flux detection On-line Reactance Measurement
IPMSM	Interior permanent magnet synchronous motor
MDOF	Multi-degree-of-freedom
MTPA	Maximum torque-per-ampere
PI	Proportional-integrated
PID	Proportional-integrated-derivative
PMSM	Permanent magnet synchronous motor
PWM	Pulse width modulation
RFOB	Reaction force observer
RM	Reluctance motor
RTOB	Reaction torque observer
SMC	Sliding-mode control
SPMSM	Surface permanent magnet synchronous motor
SVPWM	Space vector pulse width modulation
SynRM	Synchronous reluctance motor
VDOB	Voltage disturbance observer
WOB	Workspace disturbance observer

Variables

g	Gain

i	Current
k	Timing of sampling
l	Link length
n	Timing of sampling
s	Laplace operator
t	Time
t_{st}	Sampling period
v	Voltage
m	Mass
A	Replacement variable
B	Replacement variable
C	Replacement variable
D	Replacement variable
F	Force
G	Gain
J	Inertia
$\boldsymbol{J}_{aco}$	Jacobian matrix
L	Inductance
M	Mass matrix
P_{olep}	Pole pairs
R	Resistance
$\boldsymbol{S}_{el}$	Selection matrix
$\boldsymbol{S}_{smc}$	Sliding surface of SMC
$\boldsymbol{V}_{smc}$	Lyapunov function for SMC
T	Integral gain
X	Position
γ	Replacement variable
ζ	Attenuation coefficient
θ	Angle
σ	Singular value
τ	Torque
ϕ	Magnetic flux
ω	Angular frequency
Ψ	Flux linkage from the permanent magnets

Superscripts

$\bigcirc^{c}$	Value in motion controller
$\bigcirc^{cmd}$	Value of command
$\bigcirc^{comp}$	Value with compensation

$\bigcirc^{dis}$	Value of disturbance
$\bigcirc^{err}$	Value of error
$\bigcirc^{ext}$	Value of external force/torque
$\bigcirc^{ff}$	Value of decoupling control
$\bigcirc^{fric}$	Value of coulomb friction
$\bigcirc^{g}$	Value of gravity
$\bigcirc^{high}$	Value of compensation in high-frequency bandwidth
$\bigcirc^{inj}$	Value of injected signal
$\bigcirc^{int}$	Value of internal interference
$\bigcirc^{lpf}$	Value of low-pass filter
$\bigcirc^{low}$	Value for compensation in low-frequency bandwidth
$\bigcirc^{ref}$	Value of reference
$\bigcirc^{res}$	Value of response
$\bigcirc^{rfob}$	Value of RFOB
$\bigcirc^{rtob}$	Value of RTOB
$\bigcirc^{sen}$	Value for detected values by sensors
$\bigcirc^{vdob}$	Value of VDOB
$\bigcirc^{vis}$	Value of viscous friction
$\bigcirc^{wide}$	Value for compensation in wide-frequency bandwidth
$\bigcirc^{wob}$	Value of WOB

Subscript

$\bigcirc_{a}$	Value of mean
$\bigcirc_{com}$	Value of common mode
$\bigcirc_{d}$	Value of d-axis
$\bigcirc_{d1}$	Value in the 1st element in a matrix for the d-axis
$\bigcirc_{d2}$	Value in the 2nd element in a matrix for the d-axis
$\bigcirc_{d3}$	Value in the 3rd element in a matrix for the d-axis
$\bigcirc_{d4}$	Value in the 4th element in a matrix for the d-axis
$\bigcirc_{dif}$	Value of differential mode
$\bigcirc_{dq}$	Cross-coupling factors on the dq-axes
$\bigcirc_{e}$	Value for electrical system
$\bigcirc_{enc}$	Derived value with position sensors
$\bigcirc_{f}$	Value of force control
$\bigcirc_{ff}$	Equivalent mass from $\ddot{X}_f$ to F_f
$\bigcirc_{fp}$	Cross-coupling effects from $\ddot{X}_f$ to F_p
$\bigcirc_{g}$	Center of gravity
$\bigcirc_{h}$	High-frequency components
$\bigcirc_{i}$	Value of current control

$\bigcirc_l$	Value of left side
$\bigcirc_m$	Value of ripple amplitude
$\bigcirc_{main}$	Value of "main" system
$\bigcirc_n$	Nominal parameter
$\bigcirc_p$	Value of position control
$\bigcirc_{pp}$	Equivalent mass from $\ddot{X}_p$ to F_p
$\bigcirc_{pf}$	Cross-coupling effects from $\ddot{X}_p$ to F_f
$\bigcirc_q$	Value of q-axis
$\bigcirc_{q1}$	Value in a 1st element in a matrix for the q-axis
$\bigcirc_{q2}$	Value in a 2nd element in a matrix for the q-axis
$\bigcirc_{q3}$	Value in a 3rd element in a matrix for the q-axis
$\bigcirc_{q4}$	Value in a 4th element in a matrix for the q-axis
$\bigcirc_{qd}$	Cross-Coupling Factors on dq-axes
$\bigcirc_r$	Value of Right side
$\bigcirc_{remo}$	Value of "remote" system
$\bigcirc_s$	Value of ripple amplitude
$\bigcirc_{smc}$	Value for sliding mode control
$\bigcirc_u$	Value of U-axis
$\bigcirc_{uv}$	Mutual inductance value between U-axis and V-axis
$\bigcirc_v$	Value of V-axis
$\bigcirc_{vel}$	Value of velocity control
$\bigcirc_{vw}$	Mutual inductance value between V-axis and W-axis
$\bigcirc_w$	Value of W-axis
$\bigcirc_{wu}$	Mutual inductance value between W-axis and U-axis
$\bigcirc_x$	Value of x-axis
$\bigcirc_y$	Value of y-axis
$\bigcirc_\alpha$	Value of α-axis
$\bigcirc_\beta$	Value of β-axis
$\bigcirc_{\alpha\beta}$	Cross-coupling effects in the $\alpha\beta$-axis
$\bigcirc_L$	Value for inductance
$\bigcirc_1$	Link, joint, or element number
$\bigcirc_2$	Link, joint, or element number
$\bigcirc_3$	Link, joint, or element number
$\bigcirc_4$	Link, joint, or element number
$\bigcirc_{1l}$	Value of motor named 1l
$\bigcirc_{1r}$	Value of motor named 1r
$\bigcirc_{2l}$	Value of motor named 2l
$\bigcirc_{2r}$	Value of motor named 2r

Symbols

$\dot{\bigcirc}$	Time derivative
Δ	Time derivative by first-order backward finite difference
δ	Minimal change of the variables

Chapter 2

Fundamental of Position-Sensorless Control

In this chapter, the fundamental of position-sensorless control is described. In section 2.1, the modeling of an IPMSM is explained. In section 2.2, a general current controller is introduced. In section 2.3, a position estimation method using high-frequency voltage injection on the d-axis is explained.

2.1   Modeling of IPMSM

This section describes a basic model of IPMSMs for discussing the fundamental position estimation method and current control. Permanent magnets of IPMSMs are embedded in the iron core of the rotor. As a result, IPMSMs can generate magnet torque and reluctance torque. Magnet torque is generated by the attraction and repulsion between the magnetomotive force by the permanent magnet and the magnetomotive force by the stator's armature reaction. Reluctance torque is generated by the attraction and repulsion between the magnetomotive force from the rotor's magnetic saliency and the stator's armature reaction. As a result, the inductance of IPMSMs varies depending on the rotor position. However, the general voltage equation is derived with the following constraints and assumptions for simplicity.

- The target motor is a three-phase PMSM.

- The magnetomotive force distribution by permanent magnets in the rotor is sinusoidal.

- When a three-phase balanced sinusoidal voltage is applied, a sinusoidal current is generated, and the magnetomotive force distribution by the stator's armature reaction is sinusoidal.

In this dissertation, the electrical model of IPMSMs is discussed as a model with a pair of UVW-phases and NS-poles. The model and coordinate of IPMSMs can be expressed by Fig. 2-1. The center circle expresses the rotor. The red and blue block implemented in the center circle expresses the permanent magnet. The gray part is the iron core. The outer part is the stator. The yellow lines express U-phase, V-phase, and W-phase coils, counterclockwise from right. The rotor position in the electrical model is described as θ_e, called the electrical angle. The reference position at $\theta_e = 0$ corresponds to the U-phase.

Since IPMSMs have embedded permanent magnets in the rotor's iron core, the inductance for the stator varies with the electrical angle. Since the variation is caused by the positional relationship between the stator phase and the rotor magnet, the variation cycle is two revolutions for a revolution of the electrical angle. In addition, each phase interacts with the others magnetically. The voltage equation in the
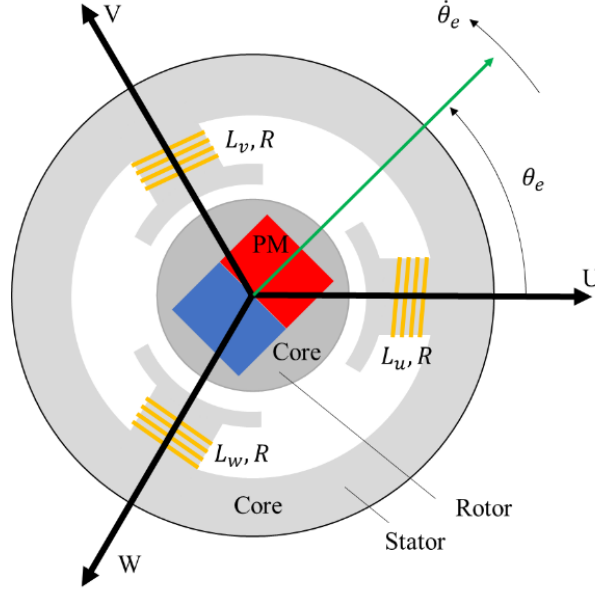
Fig. 2-1: Model and coordinate of IPMSMs.

UVW phases can be expressed by equations from eq. (2.1) to eq. (2.4).

$$
\begin{bmatrix} v_u \\ v_v \\ v_w \end{bmatrix} = R \begin{bmatrix} i_u \\ i_v \\ i_w \end{bmatrix} + \begin{bmatrix} L_u & L_{uv} & L_{wu} \\ L_{uv} & L_v & L_{vw} \\ L_{wu} & L_{vw} & L_w \end{bmatrix} \begin{bmatrix} \dot{i}_u \\ \dot{i}_v \\ \dot{i}_w \end{bmatrix}
$$

$$
+ \begin{bmatrix} \dot{L}_u & \dot{L}_{uv} & \dot{L}_{wu} \\ \dot{L}_{uv} & \dot{L}_v & \dot{L}_{vw} \\ \dot{L}_{wu} & \dot{L}_{vw} & \dot{L}_w \end{bmatrix} \begin{bmatrix} i_u \\ i_v \\ i_w \end{bmatrix} - \dot{\theta}_e \, \Psi' \begin{bmatrix} \sin\left(\theta_e\right) \\ \sin\left(\theta_e - \dfrac{2\pi}{3}\right) \\ \sin\left(\theta_e - \dfrac{4\pi}{3}\right) \end{bmatrix} \tag{2.1}
$$

$$
\begin{bmatrix} L_u \\ L_v \\ L_w \end{bmatrix} = \begin{bmatrix} 1 & \cos\left(2\theta_e\right) \\ 1 & \cos\left(2\theta_{e+}\right) \\ 1 & \cos\left(2\theta_{e-}\right) \end{bmatrix} \begin{bmatrix} L_a \\ L_m \end{bmatrix} \tag{2.2}
$$

$$
\begin{bmatrix} L_{uv} \\ L_{vw} \\ L_{wu} \end{bmatrix} = \frac{1}{2} \begin{bmatrix} -1 & 2\cos\left(2\theta_{e-}\right) \\ -1 & 2\cos\left(2\theta_e\right) \\ -1 & 2\cos\left(2\theta_{e+}\right) \end{bmatrix} \begin{bmatrix} L_a \\ L_m \end{bmatrix} \tag{2.3}
$$

$$
\begin{bmatrix} \theta_{e+} & \theta_{e-} \end{bmatrix} = \begin{bmatrix} \theta_e + \dfrac{\pi}{3} & \theta_e - \dfrac{\pi}{3} \end{bmatrix} \tag{2.4}
$$

The variables $[v_u \ v_v \ v_w]^{\mathrm{T}}$, $[i_u \ i_v \ i_w]^{\mathrm{T}}$, R, t, and Ψ are UVW phase voltage, UVW phase current, winding resistance, time, and flux linkage from the permanent magnets, respectively. The variables L_a and L_m represent the mean value and the ripple amplitude of the effective inductance in each phase.

The voltage and current of each phase in UVW phases can be considered vectors whose phase in polar coordinate is shifted by 120 degrees. They can be defined as UVW-axes. The UVW-axes can be transformed into the $\alpha\beta$-axes, whose α-axis coincides with the U-axis. This transformation allows three-phase AC voltage and current to be considered two-phase AC voltage and current. The voltage and current in the $\alpha\beta$-axes can be described as eq. (2.5) and eq. (2.6) by using transformation matrix $\boldsymbol{T}_{3\to2}$.

$$\begin{bmatrix} v_\alpha \\ v_\beta \end{bmatrix} = \sqrt{\frac{2}{3}} \begin{bmatrix} 1 & -\dfrac{1}{2} & -\dfrac{1}{2} \\ 0 & \dfrac{\sqrt{3}}{2} & -\dfrac{\sqrt{3}}{2} \end{bmatrix} \begin{bmatrix} v_u \\ v_v \\ v_w \end{bmatrix} = \boldsymbol{T}_{3\to2} \begin{bmatrix} v_u \\ v_v \\ v_w \end{bmatrix} \tag{2.5}$$

$$\begin{bmatrix} i_\alpha \\ i_\beta \end{bmatrix} = \sqrt{\frac{2}{3}} \begin{bmatrix} 1 & -\dfrac{1}{2} & -\dfrac{1}{2} \\ 0 & \dfrac{\sqrt{3}}{2} & -\dfrac{\sqrt{3}}{2} \end{bmatrix} \begin{bmatrix} i_u \\ i_v \\ i_w \end{bmatrix} = \boldsymbol{T}_{3\to2} \begin{bmatrix} i_u \\ i_v \\ i_w \end{bmatrix} \tag{2.6}$$

The coefficient $\sqrt{\frac{2}{3}}$ is multiplied so that the transformation does not change the power. The inverse transformation can be expressed by eq. (2.7) and eq. (2.8) by using transformation matrix $\boldsymbol{T}_{2\to3}$.

$$\begin{bmatrix} v_u \\ v_v \\ v_w \end{bmatrix} = \sqrt{\frac{2}{3}} \begin{bmatrix} 1 & 0 \\ -\dfrac{1}{2} & \dfrac{\sqrt{3}}{2} \\ -\dfrac{1}{2} & -\dfrac{\sqrt{3}}{2} \end{bmatrix} \begin{bmatrix} v_\alpha \\ v_\beta \end{bmatrix} = \boldsymbol{T}_{2\to3} \begin{bmatrix} v_\alpha \\ v_\beta \end{bmatrix} \tag{2.7}$$

$$\begin{bmatrix} i_u \\ i_v \\ i_w \end{bmatrix} = \sqrt{\frac{2}{3}} \begin{bmatrix} 1 & 0 \\ -\dfrac{1}{2} & \dfrac{\sqrt{3}}{2} \\ -\dfrac{1}{2} & -\dfrac{\sqrt{3}}{2} \end{bmatrix} \begin{bmatrix} i_\alpha \\ i_\beta \end{bmatrix} = \boldsymbol{T}_{2\to3} \begin{bmatrix} i_\alpha \\ i_\beta \end{bmatrix} \tag{2.8}$$

The voltage equation on the $\alpha\beta$-axes can be derived as eq. (2.9), eq. (2.10) and eq. (2.11).

$$
\begin{bmatrix} v_\alpha \\ v_\beta \end{bmatrix} = \boldsymbol{T}_{3\to2}\left(R\boldsymbol{T}_{2\to3}\begin{bmatrix} i_\alpha \\ i_\beta \end{bmatrix} + \begin{bmatrix} L_u & L_{uv} & L_{wu} \\ L_{uv} & L_v & L_{vw} \\ L_{wu} & L_{vw} & L_w \end{bmatrix}\left(\dot{\boldsymbol{T}}_{2\to3}\begin{bmatrix} i_\alpha \\ i_\beta \end{bmatrix} + \boldsymbol{T}_{2\to3}\begin{bmatrix} \dot{i}_\alpha \\ \dot{i}_\beta \end{bmatrix} \right) \right.
$$

$$
\left. \begin{bmatrix} \dot{L}_u & \dot{L}_{uv} & \dot{L}_{wu} \\ \dot{L}_{uv} & \dot{L}_v & \dot{L}_{vw} \\ \dot{L}_{wu} & \dot{L}_{vw} & \dot{L}_w \end{bmatrix}\boldsymbol{T}_{2\to3}\begin{bmatrix} i_\alpha \\ i_\beta \end{bmatrix} - \dot{\theta}_e \, \Psi \begin{bmatrix} \sin\left(\theta_e\right) \\ \sin\left(\theta_e - \dfrac{2\pi}{3}\right) \\ \sin\left(\theta_e - \dfrac{4\pi}{3}\right) \end{bmatrix} \right)
$$

$$
= \begin{bmatrix} R & 0 \\ 0 & R \end{bmatrix}\begin{bmatrix} i_\alpha \\ i_\beta \end{bmatrix} + \begin{bmatrix} \dot{L}_\alpha & \dot{L}_{\alpha\beta} \\ \dot{L}_{\alpha\beta} & \dot{L}_\beta \end{bmatrix}\begin{bmatrix} i_\alpha \\ i_\beta \end{bmatrix} + \begin{bmatrix} L_\alpha & L_{\alpha\beta} \\ L_{\alpha\beta} & L_\beta \end{bmatrix}\begin{bmatrix} \dot{i}_\alpha \\ \dot{i}_\beta \end{bmatrix} + \dot{\theta}_e \, \Psi \begin{bmatrix} -\sin\theta_e \\ \cos\theta_e \end{bmatrix} \quad (2.9)
$$

$$
\begin{bmatrix} L_\alpha \\ L_\beta \\ L_{\alpha\beta} \end{bmatrix} = \frac{3}{2}\begin{bmatrix} 1 & \cos2\theta_e \\ 1 & -\cos2\theta_e \\ 0 & \sin2\theta_e \end{bmatrix}\begin{bmatrix} L_a \\ L_m \end{bmatrix} \quad (2.10)
$$

$$
\Psi = \sqrt{\frac{3}{2}}\,\Psi' \quad (2.11)
$$

Furthermore, the $\alpha\beta$-axes can be transformed into the dq-axes, whose d-axis coincides with the N-pole of the permanent magnet. The transformation is the rotation by the electrical angle θ_e. This transformation allows the AC system of IPMSMs to be considered the DC system. The voltage and current in the dq-axes can be described as eq. (2.12) and eq. (2.13) by using transformation matrix $\boldsymbol{R}_{\alpha\beta\to dq}$.

$$
\begin{bmatrix} v_d \\ v_q \end{bmatrix} = \begin{bmatrix} \cos\theta_e & \sin\theta_e \\ -\sin\theta_e & \cos\theta_e \end{bmatrix}\begin{bmatrix} v_\alpha \\ v_\beta \end{bmatrix} = \boldsymbol{R}_{\alpha\beta\to dq}\begin{bmatrix} v_\alpha \\ v_\beta \end{bmatrix} \quad (2.12)
$$

$$
\begin{bmatrix} i_d \\ i_q \end{bmatrix} = \begin{bmatrix} \cos\theta_e & \sin\theta_e \\ -\sin\theta_e & \cos\theta_e \end{bmatrix}\begin{bmatrix} i_\alpha \\ i_\beta \end{bmatrix} = \boldsymbol{R}_{\alpha\beta\to dq}\begin{bmatrix} i_\alpha \\ i_\beta \end{bmatrix} \quad (2.13)
$$

The voltage equation on the dq-axes can be derived as eq. (2.14) and eq. (2.15).

$$
\begin{bmatrix} v_d \\ v_q \end{bmatrix} = \boldsymbol{R}_{\alpha\beta\to dq}\left(\begin{bmatrix} R & 0 \\ 0 & R \end{bmatrix}\boldsymbol{R}_{\alpha\beta\to dq}^{-1}\begin{bmatrix} i_d \\ i_q \end{bmatrix} + \begin{bmatrix} L_\alpha & L_{\alpha\beta} \\ L_{\alpha\beta} & L_\beta \end{bmatrix}\left(\dot{\boldsymbol{R}}_{\alpha\beta\to dq}^{-1}\begin{bmatrix} i_d \\ i_q \end{bmatrix} + \boldsymbol{R}_{\alpha\beta\to dq}^{-1}\begin{bmatrix} \dot{i}_d \\ \dot{i}_q \end{bmatrix} \right) \right.
$$

$$
\left. + \begin{bmatrix} \dot{L}_\alpha & \dot{L}_{\alpha\beta} \\ \dot{L}_{\alpha\beta} & \dot{L}_\beta \end{bmatrix}\boldsymbol{R}_{\alpha\beta\to dq}^{-1}\begin{bmatrix} i_d \\ i_q \end{bmatrix} + \dot{\theta}_e \, \Psi \begin{bmatrix} -\sin\theta_e \\ \cos\theta_e \end{bmatrix} \right)
$$

$$
= \begin{bmatrix} R & -\dot{\theta}_e L_q \\ \dot{\theta}_e L_d & R \end{bmatrix}\begin{bmatrix} i_d \\ i_q \end{bmatrix} + \begin{bmatrix} L_d & 0 \\ 0 & L_q \end{bmatrix}\begin{bmatrix} \dot{i}_d \\ \dot{i}_q \end{bmatrix} + \dot{\theta}_e \, \Psi \begin{bmatrix} 0 \\ 1 \end{bmatrix} \quad (2.14)
$$
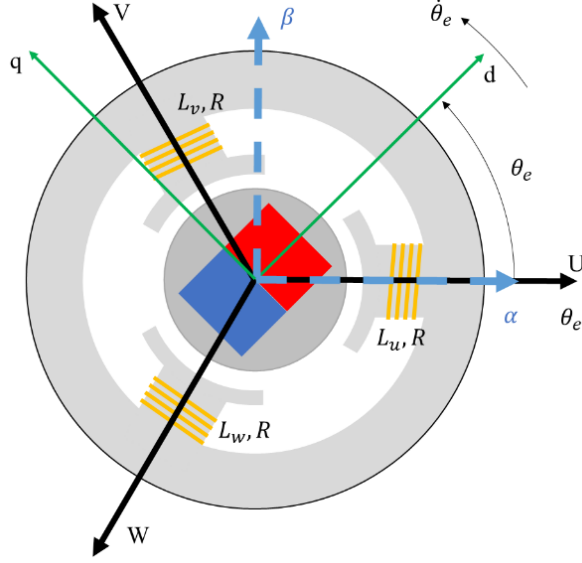
Fig. 2-2: Coordinate transformation of IPMSMs.

$$\begin{bmatrix} L_d \\ L_q \end{bmatrix} = \frac{3}{2} \begin{bmatrix} 1 & 1 \\ 1 & -1 \end{bmatrix} \begin{bmatrix} L_a \\ L_m \end{bmatrix} \tag{2.15}$$

The coordinate transformation of IPMSMs can be expressed by Fig. 2-2.

The power in the dq-axes can be expressed as eq. (2.16).

$$\begin{bmatrix} v_d \\ v_q \end{bmatrix} \cdot \begin{bmatrix} i_d \\ i_q \end{bmatrix} = R \left(i_d^2 + i_q^2 \right) + L_d i_d \dot{i}_d + L_q i_q \dot{i}_q + \dot{\theta}_e \left(\Psi i_q + (L_d - L_q) \, i_d i_q \right) \tag{2.16}$$

The electrical power and the mechanical power are expressed by eq. (2.16). The energy input to the motor is consumed by the electrical circuit and the motion. The term of Ψi_q represents the magnet torque. The term of $(L_d - L_q) \, i_d i_q$ represents the reluctance torque. Therefore, when the number of pole pairs is P_{olep}, the output torque τ of IPMSMs can be expressed by eq. (2.17).

$$\tau = P_{olep} \left(\Psi i_q + (L_d - L_q) \, i_d i_q \right) \tag{2.17}$$

The mechanical angle θ of IPMSMs whose number of pole pairs is P_{olep} can be expressed as eq. (2.18).

$$\theta = \frac{1}{P_{olep}} \theta_e \tag{2.18}$$

When the disturbance τ^{dis} is applied to the IPMSM, the equation of motion can be expressed as eq. (2.19).

$$J\ddot{\theta} = \tau - \tau^{dis} \tag{2.19}$$

Therefore, the desired torque can be generated by appropriate current control.

2.2   General Current Control

In recent years, inverters used in servo drive systems have been voltage-type inverters with current sensors. The overview of motor drive systems is shown in Fig. 2-3. In order to apply the desired current to IPMSMs, the appropriate voltage should be applied to IPMSMs. The desired voltage is applied to IPMSMs by switching the six switching devices on and off. The example is shown in Fig. 2-4. The voltage is applied to each phase by pulse width modulation (PWM), which generates a mean voltage by means of high and low signals of rectangular pulses within carrier periods. PWM pulses are derived by triangular wave comparison methods and space vector PWM (SVPWM) methods. Fig. 2-5 shows the triangular wave comparison method, which is used in this dissertation. The switching devices are switched on and off when the relationship between the magnitude of the voltage command and the triangular wave is switched. The triangular wave is the carrier wave.

The desired voltage can be derived by current control. Generally, the dq-axes current response follows the current command by a proportional-integral (PI) controller. The voltage equation shown in eq. (2.14) can be rewritten as eq. (2.20) using the Laplace operator s.

$$\begin{bmatrix} v_d \\ v_q \end{bmatrix} = \begin{bmatrix} R + sL_d & 0 \\ 0 & R + sL_q \end{bmatrix} \begin{bmatrix} i_d \\ i_q \end{bmatrix} + s\theta_e \begin{bmatrix} -i_q L_q \\ i_d L_d + \Psi \end{bmatrix} \tag{2.20}$$

The voltage equation eq. (2.20) expresses a model in which the electric circuit is orthogonal in the dq-axes and has cross-coupling effects depending on the velocity. Since the circuit model is first-order, the current response can follow the response by a PI controller with the compensation of the cross-coupling effects. The compensation method called decoupling control is often used. The whole structure of the current control is shown in Fig. 2-6. The angular velocity $\dot{\theta}_e^{res}$ of the rotors can be derived by position information detected by position sensors attached to IPMSMs. In the block diagram of Fig. 2-6, the disturbance v_d^{dis} and v_q^{dis} are applied to voltage. Examples of the disturbance are modeling errors and voltage output errors. However, the disturbance component is assumed to be sufficiently small for the discussion in this section. When the decoupling control can work ideally, the current control and the motor model can be expressed by Fig. 2-7. The d-axis current control system and the q-axis current control system are decoupled. Therefore, the control gains of each axis can be set independently to achieve an arbitrary control bandwidth. The open loop transfer function of the block diagram of the
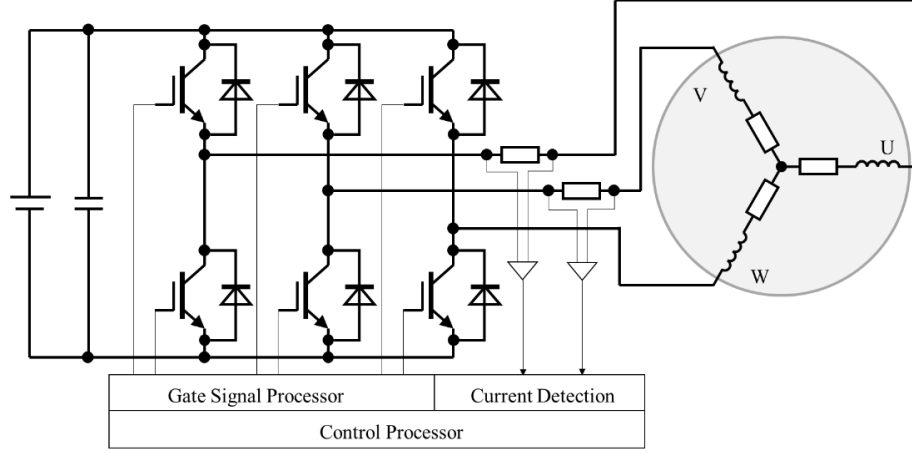
Fig. 2-3: Connection of a voltage-type inverter and an IPMSM.

d-axis current control system can be written as eq. (2.21).

$$\frac{i_d^{res}}{i_d^{cmd}} = \frac{G_{i,d}\left(1 + \dfrac{1}{T_{i,d}s}\right)\left(\dfrac{1}{L_ds + R}\right)}{1 + G_{i,d}\left(1 + \dfrac{1}{T_{i,d}s}\right)\left(\dfrac{1}{L_ds + R}\right)} \tag{2.21}$$

The transfer function can be simplified by using pole-zero cancellation by using gains expressed in eq. (2.23) and eq. (2.23). The gain g_i corresponds to the cut-off frequency of the current controller.

$$G_{i,d} = g_i L_d \tag{2.22}$$

$$T_{i,d} = \frac{L_d}{R} \tag{2.23}$$

The simplified transfer function can be expressed as eq. (2.24).

$$\frac{i_d^{res}}{i_d^{cmd}} = \frac{g_i}{s + g_i} \tag{2.24}$$

Therefore, the frequency characteristic of the current controller can be similar to the first-order LPF. When gains $G_{i,q}$ and $T_{i,q}$ are set as eq. (2.25) and eq. (2.26), respectively, the transfer function of the q-axis current control system can also be expressed as eq. (2.27).

$$G_{i,q} = g_i L_q \tag{2.25}$$

$$T_{i,q} = \frac{L_q}{R} \tag{2.26}$$

(a) Applied voltage

(b) Pairs of switching
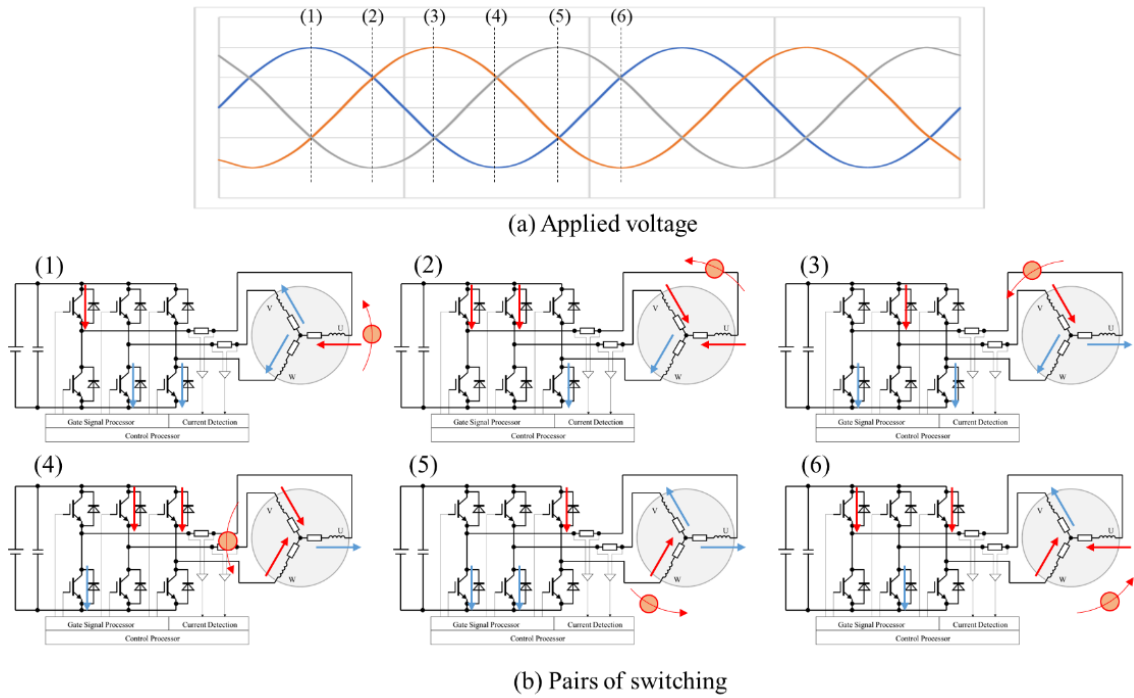
Fig. 2-4: Pairs of switching and applied voltage.

$$\frac{i_q^{res}}{i_q^{cmd}} = \frac{g_i}{s + g_i} \tag{2.27}$$

The current control bandwidth can be adjusted by tuning g_i. The values of resistance and inductance can be obtained by catalogs or measurements as nominal values. The block diagram of IPMSMs from dq-axes current commands to velocity response can be shown in Fig. 2-8. As described above, existing systems cannot be ideal because of the variations and errors in motor parameters and delays caused by digital control systems. However, when the control bandwidth can be high enough, the approximation of the modeling is sufficient to drive motors as desired.
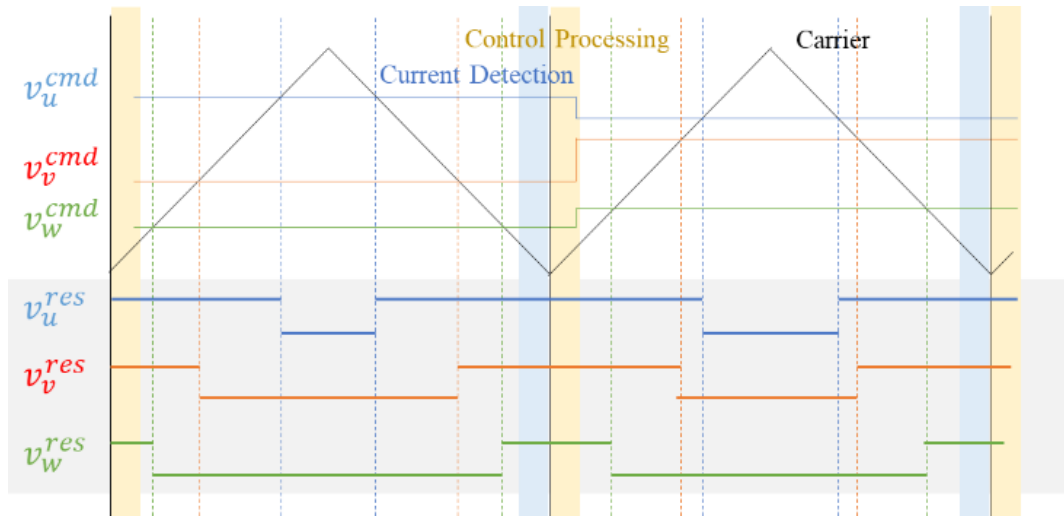
Fig. 2-5: PWM by the triangular wave comparison method.
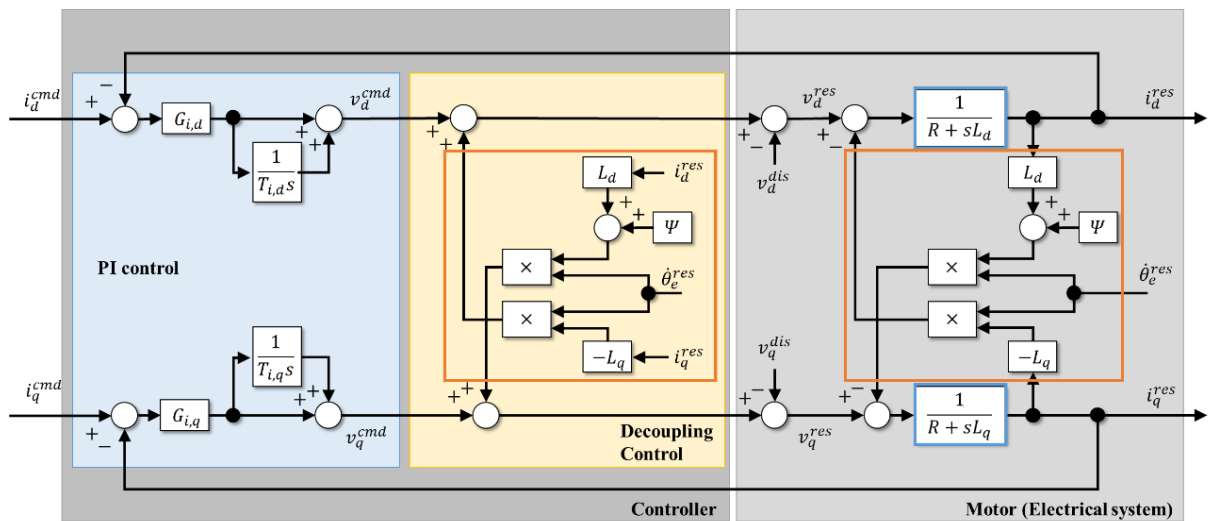
Fig. 2-6: PI controller and decoupling controller for dq-axes current control.
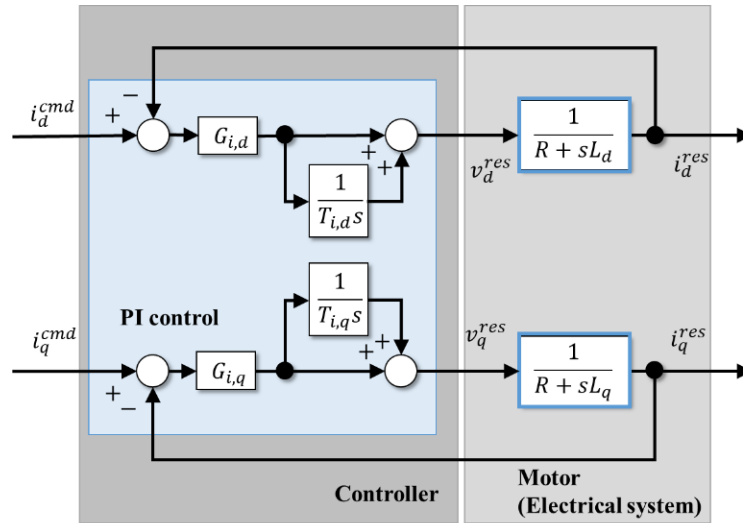
Fig. 2-7: Current control system with ideal decoupling control.
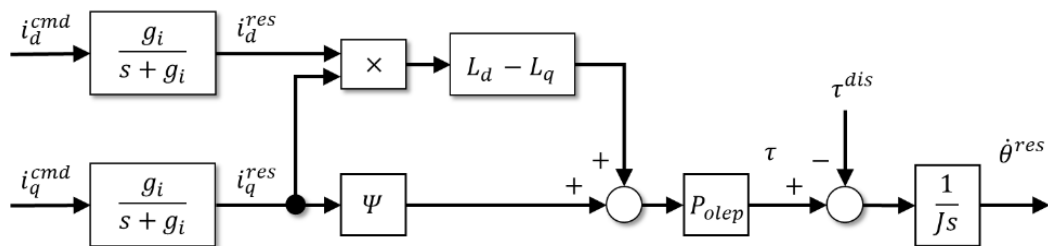
Fig. 2-8: Block diagram from current commands to velocity response.

2.3   Position Estimation with the d-axis High-Frequency Voltage Injection

This section describes a basic position estimation method using high-frequency voltage injection on the d-axis for low-speed operation. In order to realize current control in the dq-axes, the rotor position information is essential for the coordinate transformation. When an IPMSM is equipped with an absolute-type position sensor, the rotor position during rotation can be obtained from the sensor. However, the rotor position has to be estimated in position-sensorless control systems. The position estimation methods in this dissertation utilize a position estimation method using a high-frequency voltage injection on the d-axis. The frequency of the injected voltage is synchronized with a carrier wave, and it is sufficiently higher than the rotational frequency of the electrical angle in the low-speed operation. When the electric angle rotates one revolution with the high-frequency voltage injection on the d-axis, the amplitude of the currents on the α-axis and the β-axis change sinusoidally. The phase difference of the variation in the amplitude of the currents is 90 degrees. Therefore, the rotor position can be estimated by the operation of the inverse tangent using the extracted envelope of the high-frequency currents on the α-axis and β-axis. The overview of the voltage injection and current variation is shown in Fig. 2-9. The variable k represents the estimation processing timing. The following equations can express this phenomenon.

The high-frequency components in the voltage equation of eq. (2.14) can be expressed as eq. (2.28) since the components relating to inductance are dominant in the high-frequency components extracted by the high-frequency voltage.

$$\begin{bmatrix} v_{d,h} \\ v_{q,h} \end{bmatrix} \begin{bmatrix} L_{d,h} & 0 \\ 0 & L_{q,h} \end{bmatrix} \begin{bmatrix} \dot{i}_{d,h} \\ \dot{i}_{q,h} \end{bmatrix} \tag{2.28}$$

The coordinate transformation between dq-axes and $\alpha\beta$-axes can be written as eq. (2.29) from eq. (2.13) and (2.28) in the low-speed operation.

$$\begin{aligned} \begin{bmatrix} \dot{i}_{\alpha,h} \\ \dot{i}_{\beta,h} \end{bmatrix} &= \begin{bmatrix} \cos\theta_e & -\sin\theta_e \\ \sin\theta_e & \cos\theta_e \end{bmatrix} \begin{bmatrix} \dot{i}_{d,h} \\ \dot{i}_{q,h} \end{bmatrix} + \dot{\theta}_e \begin{bmatrix} -\sin\theta_e & -\cos\theta_e \\ \cos\theta_e & -\sin\theta_e \end{bmatrix} \begin{bmatrix} i_{d,h} \\ i_{q,h} \end{bmatrix} \\ &\approx \begin{bmatrix} \cos\theta_e & -\sin\theta_e \\ \sin\theta_e & \cos\theta_e \end{bmatrix} \begin{bmatrix} \dot{i}_{d,h} \\ \dot{i}_{q,h} \end{bmatrix} \\ &= \frac{1}{L_{d,h}L_{q,h}} \begin{bmatrix} \cos\theta_e & -\sin\theta_e \\ \sin\theta_e & \cos\theta_e \end{bmatrix} \begin{bmatrix} L_{q,h} & 0 \\ 0 & L_{d,h} \end{bmatrix} \begin{bmatrix} v_{d,h} \\ v_{q,h} \end{bmatrix} \end{aligned} \tag{2.29}$$

The injected square-wave-type voltage whose amplitude is v^{inj} can be expressed as eq. (2.30). The
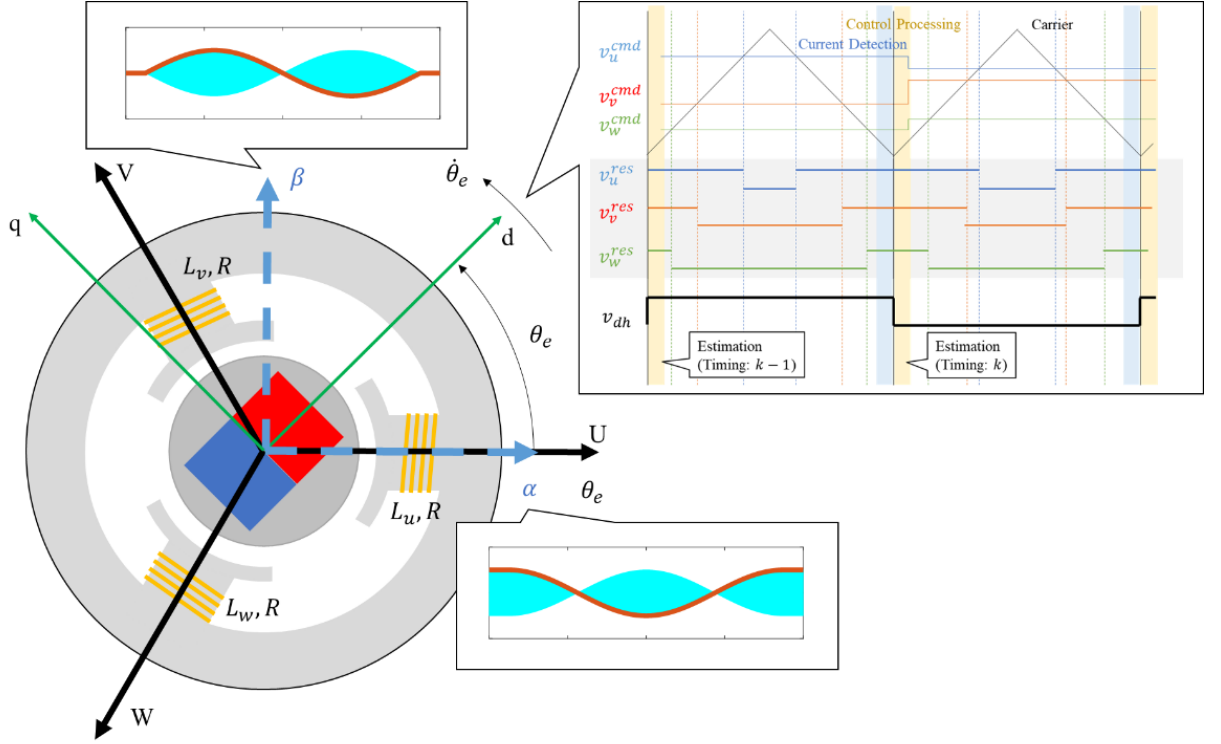
Fig. 2-9: Overview of the voltage injection and the current variation.

variable n is a natural number representing the estimation processing timing.

$$\begin{bmatrix} v_{d,h}[k] \\ v_{q,h}[k] \end{bmatrix} = \begin{bmatrix} v_h[k] \\ 0 \end{bmatrix} \tag{2.30}$$

$$v_h[k] = \begin{cases} v^{inj} & (k = 2n) \\ -v^{inj} & (k = 2n+1) \end{cases}$$

The frequency of the injected voltage is the same or half of the carrier frequency. The amplitude of the injected voltage is adjusted by trial and error to extract enough current variation. As a guide, the standard amplitude of the superimposed voltage is 20 to 40 % of the supply voltage. If the supply voltage is considered to be ± 141 V, the amplitude may be approximately ± 28 V to 56 V. The $\alpha\beta$-axes current can be written as eq. (2.31) by using eq. (2.30).

$$\begin{bmatrix} \dot{i}_{\alpha,h} \\ \dot{i}_{\beta,h} \end{bmatrix} \approx \frac{1}{L_{d,h}L_{q,h}} \begin{bmatrix} \cos\theta_e & -\sin\theta_e \\ \sin\theta_e & \cos\theta_e \end{bmatrix} \begin{bmatrix} L_{q,h} & 0 \\ 0 & L_{d,h} \end{bmatrix} \begin{bmatrix} \pm v^{inj} \\ 0 \end{bmatrix}$$

$$= \frac{\pm v^{inj}}{L_{d,h}} \begin{bmatrix} \cos\theta_e \\ \sin\theta_e \end{bmatrix} \tag{2.31}$$

Therefore, position θ_e by the conventional method can be extracted by eq. (2.32).

$$\theta_e \approx \tan^{-1}\left(\frac{\dot{i}_{\beta,h}}{\dot{i}_{\alpha,h}}\right) \tag{2.32}$$

The algorithm described above is implemented as a discrete-time system. The time derivative terms of current can be approximately expressed by eq. (2.33). Δ denotes first-order backward finite difference, and t_{st} is the current sampling period for the estimation.

$$\begin{bmatrix} \dot{i}_{\alpha,h} \\ \dot{i}_{\beta,h} \end{bmatrix} \approx \begin{bmatrix} \Delta i_{\alpha,h}[k] \\ \Delta i_{\beta,h}[k] \end{bmatrix} = \frac{1}{t_{st}}\begin{bmatrix} i_\alpha[k] - i_\alpha[k-1] \\ i_\beta[k] - i_\beta[k-1] \end{bmatrix} \tag{2.33}$$

Since the high-frequency voltage switches between positive and negative at each half period of the injection, the sign of the time derivative values in eq. (2.33) for the estimation also switches between positive and negative at each half period of the injection to extract the envelope of the high-frequency current. The estimation process with the positive sign is described. The estimated position at estimation timing k is obtained as eq. (2.34).

$$\hat{\theta}_e^{conv}[k] = \tan^{-1}\left(\frac{\Delta i_{\beta,h}[k]}{\Delta i_{\alpha,h}[k]}\right) \tag{2.34}$$

Since the frequency of the injected voltage is generally higher than the cut-off frequency of the electrical characteristics of IPMSMs, the resistance variation does not deteriorate the estimation performance significantly. For example, a simple electrical system expressed by eq. (2.35) was defined to compare the high-frequency current responses by different resistance values in simulation.

$$\frac{i}{v} = \frac{1}{Ls + R} \tag{2.35}$$

The nominal inductance and resistance values were 3.7 mH and 2.87 Ω, respectively. The electrical time constant was 1.29 ms, and the cut-off frequency was 123 Hz. The current responses to a 5.3 kHz voltage pulse, whose amplitude was 40 V, is shown in Fig. 2-10 when the resistance was varied by a factor of 5 or 0.2. The transient responses of the current variation immediately after the start of the voltage injection were different. However, the difference in the amplitude of the current variation is small. There was little difference in the current responses after 30ms depending on the resistance values. Therefore, the resistance variation does not deteriorate the estimation performance significantly. Applications of position-sensorless control systems are often required to be robust to temperature variation. Although temperature variation causes resistance and magnetic characteristics variation, considering magnetic characteristics variation is much more significant to improve the accuracy of position estimation.

Since the current variation has noises from the current detection, the estimated position also have noises. The high-frequency noise deteriorates the current control performance because the coordinate transformation between the UVW-axes and dq-axes becomes inappropriate. Therefore, phase-lock-loop (PLL) is often applied to the estimated position $\hat{\theta}_e^{conv}[k]$. The LPF effect by the PLL causes a phase delay of the estimated position. The cut-off frequency of the LPF function of the PLL is generally under 100Hz. In addition, the estimation method ignores the nonlinearity of the magnetic flux variation, which causes estimation errors and vibrations. The position estimation errors, vibrations, and phase delay deteriorate the performance of the position-sensorless control.

The resolution of the estimated position depends on the current sensors' resolution, the amplitude of the current variation from the injected voltage, and the cut-off frequency of PLL. The resolution of the current sensor corresponding to the high-frequency current variation is the resolution of the estimated position $\hat{\theta}_e^{conv}[k]$. Since the output value of the LPF is internalized of the input values, the resolution improves with the lower cut-off frequency of the LPF. However, the lower cut-off frequency of the LPF causes the phase delay, the adjustment by experiments or simulation is essential. As described in Section 1.5, position estimation errors are caused by the characteristics of motors and inverters. Therefore, the resolution and the accuracy of the estimated position depend on motors, inverters, and estimation methods. Confirmation of these characteristics are required in practical use.

The conventional position-sensorless control system can be expressed as Fig. 2-11. The LPF with the cut-off frequency g^{sen} applied to the detected current removes the current variation by the voltage injection. The motion controller often has an LPF for the torque reference to remove the noise and vibration. The cut-off frequency is g_{tf} in this dissertation.
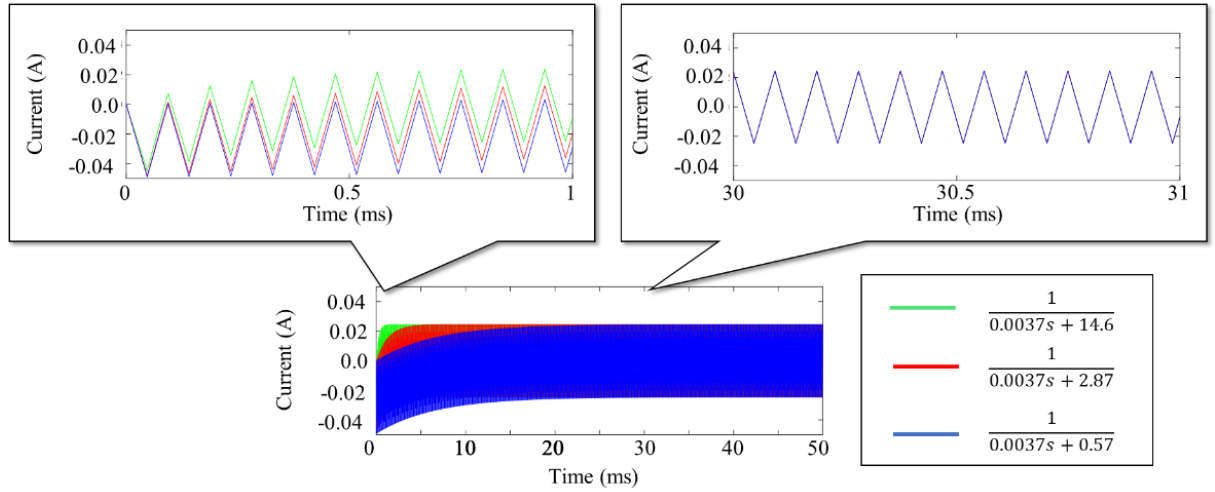
Fig. 2-10: Comparison of high-frequency current responses by different resistance values.
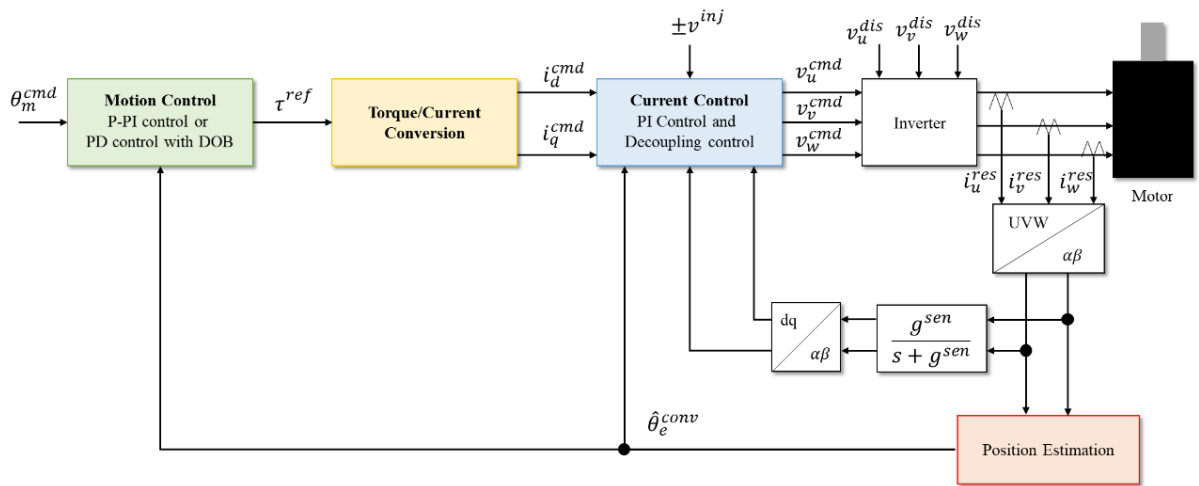
Fig. 2-11: Conventional position-sensorless control.

Chapter 3

Fundamental of Force-Sensorless Control

In this chapter, the fundamental of force-sensorless control and the 4DOF robot used in this dissertation is described. In section 3.1, DOB and RFOB/RTOB are explained. In section 3.2, the modeling of the robot utilized in experiments is explained. In section 3.3, the equivalent mass matrix for the utilized robot is explained.

3.1   Disturbance Observer and Reaction Force/Torque Observer

This section describes disturbance observer (DOB) for disturbance compensation and reaction force/torque observer (RFOB/RTOB) to estimate reaction force/torque. In this dissertation, the difference between the force control and the torque control is only the motion direction. The assumed robots have rotational motors and linear motion in the workspace. Therefore, RTOB is utilized for 1DOF rotational motion and joint coordinate motion, and RFOB is used for the workspace motion.

DOB estimates disturbances applied to systems and adds the estimated values to the control inputs to achieve a robust control system in the bandwidth under the cut-off frequency g_{dob} in the algorithm. Although "disturbances" is a generic term for components out of the modeling in control, external force/torque is excluded. The external force/torque is the control target in the force/torque control based on the law of action and reaction in this dissertation. In a motion controller, the estimated value is the force/torque value. Mechanical disturbances include mechanical parameter errors, response delays, frictional force, a backlash of the reducers, internal interference force, gravity force, and external force. The estimated mechanical disturbances $\hat{\tau}^{dob}$ by DOB in 1DOF systems can be expressed as eq. (3.1). $\bigcirc_n$ denotes the nominal values.

$$\hat{\tau}^{dob} = \frac{g^{dob}}{s + g^{dob}} \left(\tau + J_n g^{dob} \dot{\theta} \right) - J_n g^{dob} \dot{\theta} \tag{3.1}$$

The estimated torque $\hat{\tau}^{dob}$ includes disturbances and external torque. In linear motion systems, the inertia J_n and the angular velocity $\dot{\theta_m}$ are replaced by the mass M_n and the velocity $\dot{X}$. In a current controller, the estimated value is the voltage value. Examples of electrical disturbances are electrical parameter errors, response delays, and voltage output errors due to dead time and internal resistance of semiconductors. DOB for electrical systems is called voltage disturbance observer (VDOB) to distinguish it from DOB for mechanical systems. The estimated electrical disturbances $\hat{v}_d^{vdob}$ and $\hat{v}_q^{vdob}$ can be expressed by eq. (3.2) and eq. (3.3).

$$\hat{v}_d^{vdob} = \frac{g^{vdob}}{s + g^{vdob}} \left(v_d^{cmd} + L_{d,n} g^{vdob} i_d - R_n i_d \right) - L_{d,n} g^{vdob} i_d \tag{3.2}$$

$$\hat{v}_q^{vdob} = \frac{g^{vdob}}{s + g^{dvob}} \left(v_q^{cmd} + L_{q,n} g^{vdob} i_q - R_n i_q \right) - L_{q,n} g^{vdob} i_q \tag{3.3}$$

Block diagrams of DOB for a motion controller and VDOB for a current controller are shown in Fig. 3-1 and Fig. 3-2, respectively. The block diagram for motion control assumes that the control bandwidth of
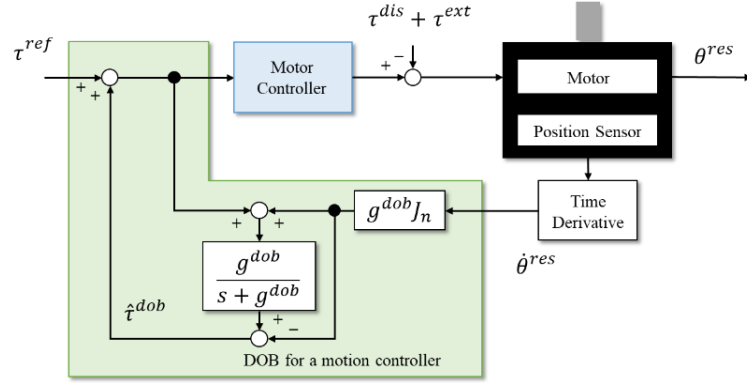
Fig. 3-1: DOB for a motion controller.
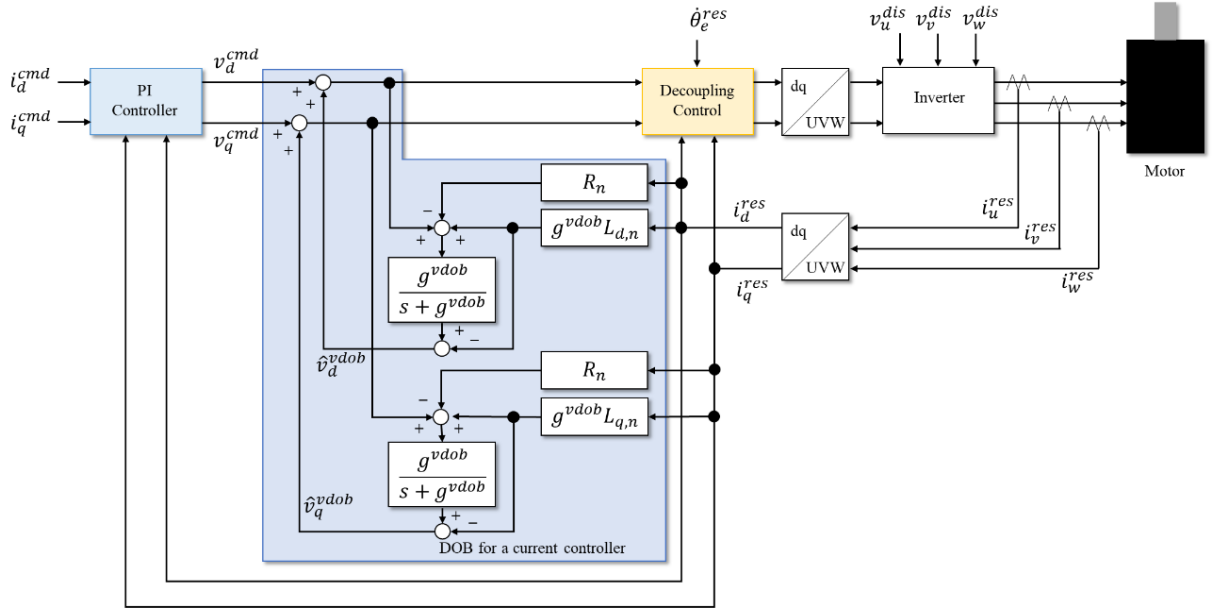
Fig. 3-2: VDOB for a current controller.

the current control system is sufficiently high, and the current control system is omitted from the block diagram.

RFOB/RTOB is a method to estimate external force/torque from mechanical force/torque applied to control systems. In this dissertation, since the external force/torque is the control target of force/torque control, the external force/torque is distinguished from the other mechanical disturbances. The components of mechanical disturbances τ^{dis} can be expressed by eq. (3.4). Variables τ^{int}, τ^{err}, τ^{fric}, τ^{vis}, τ^g are internal interference torque, unintended torque caused by the modeling error, coulomb friction

torque, viscous friction torque, and torque caused by the gravity, respectively.

$$\tau^{dis} = \tau^{int} + \tau^{err} + \tau^{fric} + \tau^{vis} + \tau^{g} \tag{3.4}$$

The purpose of force/torque control is to generate the desired external force/torque. Generating the desired external force/torque is synonymous with controlling the reaction force/torque from the law of action and reaction. RFOB/RTOB estimates only external force/torque by modeling components other than external force/torque and removing them from the estimated torque by DOB. The estimated external torque can be expressed as eq. (3.5).

$$
\begin{aligned}
\hat{\tau}^{rtob} &= \hat{\tau}^{ext} \\
&= \frac{g^{rtob}}{s + g^{rtob}} \left(\tau + J_n g^{rtob}\dot{\theta} - \hat{\tau}^{int} - \hat{\tau}^{err} - \hat{\tau}^{fric} - \hat{\tau}^{vis} - \hat{\tau}^{g} \right) - J_n g^{rtob}\dot{\theta}
\end{aligned} \tag{3.5}
$$

The estimated external torque is inaccurately estimated due to disturbance modeling errors. In particular, accurate modeling of coulomb friction and viscous friction is difficult. Although it is possible to obtain the friction force/torque by preliminary tests using starting torque and constant speed operation, it is difficult to obtain the model of the friction force/torque accurately at all times because it varies with temperature, humidity, and wear. Therefore, the friction in systems with RFOB/RTOB should be smaller. The block diagram of RTOB is shown in Fig. 3-3. Force-sensorless force control can be realized using the estimated external force/torque as feedback information.

$$\tau^{dis} + \tau^{ext} = \tau^{int} + \tau^{err} + \tau^{fric} + \tau^{vis} + \tau^{g} + \tau^{ext}$$
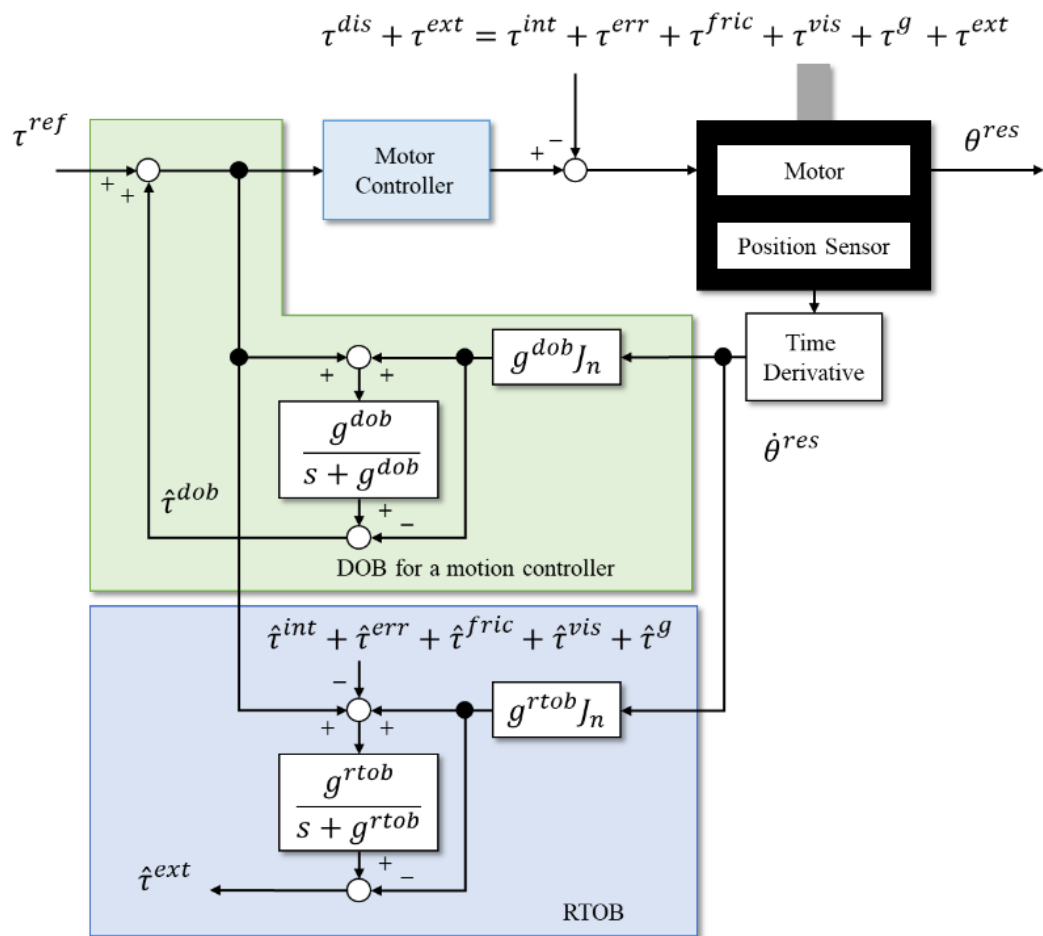
Fig. 3-3: RTOB for a rotational system.

3.2   Modeling of Robots Utilized in Experiments

This section describes the modeling of the robot utilized in experiments.

A direct-drive 4DOF manipulator was utilized in experiments. The robot has a parallel mechanism comprised of two-link parallel manipulators and two additional links connected by free joints. The robot's model and coordinate are shown in Fig. 3-4. The two-link manipulators are in the XY plane. The Z coordinate reference is the tip of the two two-link manipulators. The gravity is applied in the -Z direction. The two-link parallel manipulators are symmetrically placed, and two additional links and free-rotating joints connect the tip of the manipulators with bearings. The free-rotating joints at (X_r, Y_r) and (X_l, Y_l) have two degrees of freedom. Therefore, the motion at (X_r, Y_r) and (X_l, Y_l) can be designed independently. The end-effector is at the connecting point of the additional links. The robot has bearings in the rotating joints. The links of the robot are lightweight. These characteristics reduce the frictional and gravitational disturbances of the robot.

The kinematics and dynamics of the robot are introduced. The coordinates (X_r, Y_r) and (X_l, Y_l) are expressed by eq. (3.6) and eq. (3.7), respectively.

$$\begin{bmatrix} X_r \\ Y_r \end{bmatrix} = \begin{bmatrix} l_1 \cos \theta_{1r} - l_4 \sin \theta_{2r} + l \\ l_1 \sin \theta_{1r} + l_4 \cos \theta_{2r} \end{bmatrix} \tag{3.6}$$

$$\begin{bmatrix} X_l \\ Y_l \end{bmatrix} = \begin{bmatrix} -l_1 \cos \theta_{1l} + l_4 \sin \theta_{2l} - l \\ l_1 \sin \theta_{1l} + l_4 \cos \theta_{2l} \end{bmatrix} \tag{3.7}$$

The end-effector has 4DOF: X, Y, Z, and Φ. The workspace position is defined as eq. (3.8). X-axis motion and Y-axis motion can be expressed by $X_r + X_l$ and $Y_r + Y_l$, respectively. Z-axis motion and Φ-axis motion are substituted by $X_r - X_l$ and $Y_r - Y_l$, respectively.

$$\begin{aligned} \boldsymbol{X} &= \begin{bmatrix} X_{dif} \\ X_{com} \\ Y_{dif} \\ Y_{com} \end{bmatrix} = \frac{1}{2} \begin{bmatrix} X_r - X_l \\ X_r + X_l \\ Y_r - Y_l \\ Y_r + Y_l \end{bmatrix} \\ &= \begin{bmatrix} l_1 (\cos \theta_{1r} + \cos \theta_{1l}) - l_4 (\sin \theta_{2r} + \sin \theta_{2l}) + 2l \\ l_1 (\cos \theta_{1r} - \cos \theta_{1l}) - l_4 (\sin \theta_{2r} - \sin \theta_{2l}) \\ l_1 (\sin \theta_{1r} - \sin \theta_{1l}) + l_4 (\cos \theta_{2r} - \cos \theta_{2l}) \\ l_1 (\sin \theta_{1r} + \sin \theta_{1l}) + l_4 (\cos \theta_{2r} + \cos \theta_{2l}) \end{bmatrix} \end{aligned} \tag{3.8}$$

Joint angles θ_{1r}, θ_{2r}, θ_{1l} and θ_{2l} are expressed by eq. (3.9).

$$\boldsymbol{\theta} = \begin{bmatrix} \theta_{1r} & \theta_{2r} & \theta_{1l} & \theta_{2l} \end{bmatrix}^{\mathrm{T}} \tag{3.9}$$
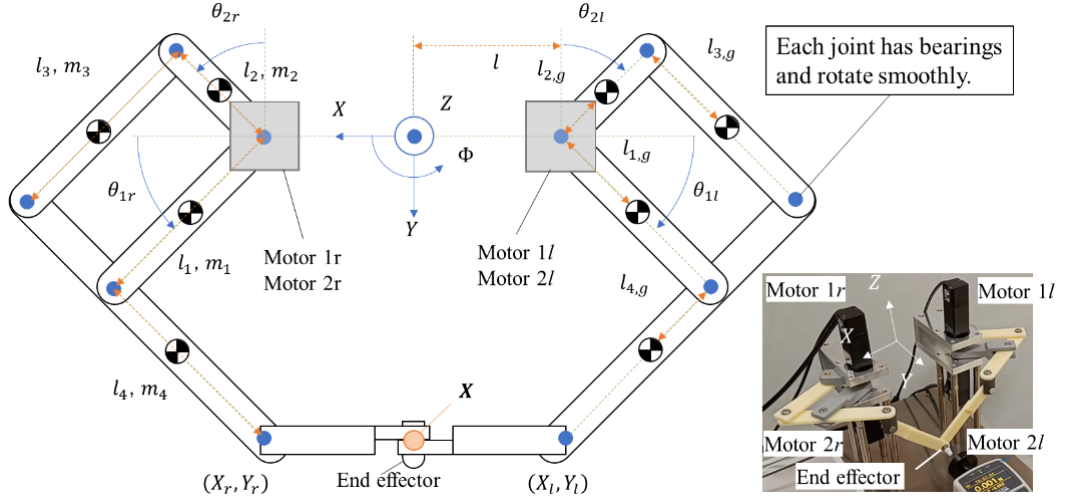
Fig. 3-4: Model of the 4DOF manipulator.

The relation between $\dot{\boldsymbol{X}}$ and $\dot{\boldsymbol{\theta}}$ is described as eq. (3.10). The equation eq. (3.10) is derived by the time derivative of eq. (3.8). The matrix $\boldsymbol{J}_{aco}$ is the Jacobian matrix.

$$
\begin{aligned}
\dot{\boldsymbol{X}} &= \begin{bmatrix} l_1\left(-\dot{\theta}_{1r}\sin\theta_{1r} - \dot{\theta}_{1l}\sin\theta_{1l}\right) - l_4\left(\dot{\theta}_{2r}\cos\theta_{2r} + \dot{\theta}_{2l}\cos\theta_{2l}\right) \\ l_1\left(-\dot{\theta}_{1r}\sin\theta_{1r} + \dot{\theta}_{1l}\sin\theta_{1l}\right) - l_4\left(\dot{\theta}_{2r}\cos\theta_{2r} - \dot{\theta}_{2l}\cos\theta_{2l}\right) \\ l_1\left(\dot{\theta}_{1r}\cos\theta_{1r} - \dot{\theta}_{1l}\cos\theta_{1l}\right) + l_4\left(-\dot{\theta}_{2r}\sin\theta_{2r} + \dot{\theta}_{2l}\sin\theta_{2l}\right) \\ l_1\left(\dot{\theta}_{1r}\cos\theta_{1r} + \dot{\theta}_{1l}\cos\theta_{1l}\right) + l_4\left(-\dot{\theta}_{2r}\sin\theta_{2r} - \dot{\theta}_{2l}\sin\theta_{2l}\right) \end{bmatrix} \\
&= \begin{bmatrix} -l_1\sin\theta_{1r} & -l_1\sin\theta_{1l} & -l_4\cos\theta_{2r} & -l_4\cos\theta_{2l} \\ -l_1\sin\theta_{1r} & l_1\sin\theta_{1l} & -l_4\cos\theta_{2r} & l_4\cos\theta_{2l} \\ l_1\cos\theta_{1r} & -l_1\cos\theta_{1l} & -l_4\sin\theta_{2r} & l_4\sin\theta_{2l} \\ l_1\cos\theta_{1r} & l_1\cos\theta_{1l} & -l_4\sin\theta_{2r} & -l_4\sin\theta_{2l} \end{bmatrix} \begin{bmatrix} \dot{\theta}_{1r} \\ \dot{\theta}_{1l} \\ \dot{\theta}_{2r} \\ \dot{\theta}_{2l} \end{bmatrix} \\
&= \boldsymbol{J}_{aco}\dot{\boldsymbol{\theta}}
\end{aligned}
\tag{3.10}
$$

The relation between joint torque $\boldsymbol{\tau}$ and workspace force $\boldsymbol{F}$ is expressed as eq. (3.11) by virtual work principle.

$$
\boldsymbol{\tau} = \begin{bmatrix} \tau_{1r} \\ \tau_{1l} \\ \tau_{2r} \\ \tau_{2l} \end{bmatrix} = \boldsymbol{J}_{aco}^{\mathrm{T}} \begin{bmatrix} F_{x,dif} \\ F_{x,com} \\ F_{y,dif} \\ F_{y,com} \end{bmatrix} = \boldsymbol{J}_{aco}^{\mathrm{T}}\boldsymbol{F}
\tag{3.11}
$$

The dynamics can be derived by the Lagrange equation of motion. Since the rotation of the additional links is smooth by the bearings and the links are lightweight, the dynamics of the robot can be considered

as consisting of the dynamics of two independent parallel two-link manipulators. In this modeling, the mass point of each link is at the center of the link and that of the additional links is at the tip of the two-link manipulator. The distance between the center of gravity of each link and the joint is indicated by a subscript $\bigcirc_g$. The robot's inertia matrix $\boldsymbol{J}$ is expressed by equations from eq. (3.12) to eq. (3.16). The main moment of inertia of each axis is expressed as $J_{1r,1r}$, $J_{2r,2r}$, $J_{1l,1l}$, and $J_{2l,2l}$. The cross-coupling component of the moment of inertia of each axis is expressed as $J_{1r,2r}$, $J_{2r,1r}$, $J_{1l,2l}$, and $J_{2l,1l}$. The variables $J_{1,g}$, $J_{2,g}$, $J_{3,g}$, and $J_{4,g}$ are the moment of inertia of each link.

$$\boldsymbol{J} = \begin{bmatrix} J_{1r,1r} & J_{1r,2r} & 0 & 0 \\ J_{2r,1r} & J_{2r,2r} & 0 & 0 \\ 0 & 0 & J_{1l,1l} & J_{1l,2l} \\ 0 & 0 & J_{2l,1l} & J_{2l,2l} \end{bmatrix} \tag{3.12}$$

$$J_{1r,1r} = J_{1l,1l} = m_1 l_{1,g}^2 + m_3 l_{3,g}^2 + m_4 l_1^2 + J_{1,g} + J_{3,g} \tag{3.13}$$

$$J_{1r,2r} = J_{2r,1r} = (m_4 l_1 l_{4,g} - m_3 l_2 l_{3,g}) \sin(\theta_{1r} - \theta_{2r}) \tag{3.14}$$

$$J_{1l,2l} = J_{2l,1l} = (m_4 l_1 l_{4,g} - m_3 l_2 l_{3,g}) \sin(\theta_{1l} - \theta_{2l}) \tag{3.15}$$

$$J_{2r,2r} = J_{2l,2l} = m_2 l_{2,g}^2 + m_3 l_2^2 + m_4 l_{4,g}^2 + J_{2,g} + J_{4,g} \tag{3.16}$$

The motion equation is expressed as eq. (3.17).

$$\boldsymbol{J}\ddot{\boldsymbol{\theta}} = \boldsymbol{\tau} - \boldsymbol{\tau}^{dis} - \boldsymbol{\tau}^{ext} \tag{3.17}$$

When the disturbance and external force/torque is zero or the motion is in the steady state, eq. (3.18) can be derived.

$$\boldsymbol{J}\ddot{\boldsymbol{\theta}} = \boldsymbol{\tau} = \boldsymbol{J_{aco}}^{\mathrm{T}} \boldsymbol{F} \tag{3.18}$$

3.3   Equivalent Mass Matrix

This section describes the equivalent mass matrix. The equivalent mass matrix consists of the Jacobian matrix and the inertia matrix. Equivalent mass matrices can unite the reference values from workspace position and force control in the force dimension. The time derivative of eq. (3.10) derives eq. (3.19).

$$\ddot{\boldsymbol{X}} = \boldsymbol{J}_{aco}\ddot{\boldsymbol{\theta}} + \dot{\boldsymbol{J}}_{aco}\dot{\boldsymbol{\theta}} \tag{3.19}$$

The motion of force control during contact with hard objects is low-speed, and the robot's position and posture do not change significantly. Therefore, the fluctuation of the Jacobian matrix can be considered as negligible. When the fluctuation of the Jacobian matrix is small, eq. (3.19) can be rewritten as eq. (3.20).

$$\ddot{\boldsymbol{X}} = \boldsymbol{J}_{aco}\ddot{\boldsymbol{\theta}} \tag{3.20}$$

The relationship between the workspace position $\boldsymbol{X}$ and the workspace force $\boldsymbol{F}$ can be expressed by eq. (3.21) from eq. (3.18) and eq. (3.20).

$$\begin{aligned} \ddot{\boldsymbol{X}} &= \boldsymbol{J}_{aco}\ddot{\boldsymbol{\theta}} \\ &= \boldsymbol{J}_{aco}\boldsymbol{J}^{-1}\boldsymbol{\tau} \\ &= \boldsymbol{J}_{aco}\boldsymbol{J}^{-1}\boldsymbol{J}_{aco}{}^{\mathrm{T}}\boldsymbol{F} \end{aligned} \tag{3.21}$$

Therefore, the equivalent mass matrix $\boldsymbol{M}$ can be defined as eq. (3.22).

$$\boldsymbol{M}^{-1} = \boldsymbol{J}_{aco}\boldsymbol{J}^{-1}\boldsymbol{J}_{aco}{}^{\mathrm{T}} \tag{3.22}$$

The equivalent mass matrix $\boldsymbol{M}$ expresses the mass of the workspace motion. Therefore, DOB and RFOB can be used in the workspace by $\boldsymbol{X}$, $\boldsymbol{F}$, and $\boldsymbol{M}$. The workspace DOB is called WOB.

A workspace hybrid position/force control system using equivalent mass matrices is shown in Fig. 3-5. The gains $\boldsymbol{G}_p\left(s\right)$ and $\boldsymbol{G}_f$ represent position controller gains and force controller gains. The position and force controller derive acceleration reference values. The selection matrix $\boldsymbol{S}_{el}$ extracts the acceleration reference values for the position and force control axes and derives acceleration reference values $s^2\ddot{\boldsymbol{X}}^{ref}$ for the workspace. The acceleration reference values are changed to the force reference values $\boldsymbol{F}^{ref}$ with an equivalent mass matrix. When the equivalent mass matrix has nominal values, the derived values are with the subscript $\bigcirc_n$. The force reference values are transformed into the torque reference values $\boldsymbol{\tau}^{ref}$ for motors by using $\boldsymbol{J}_{aco}{}^{\mathrm{T}}$. The motor output, external force, and disturbance change
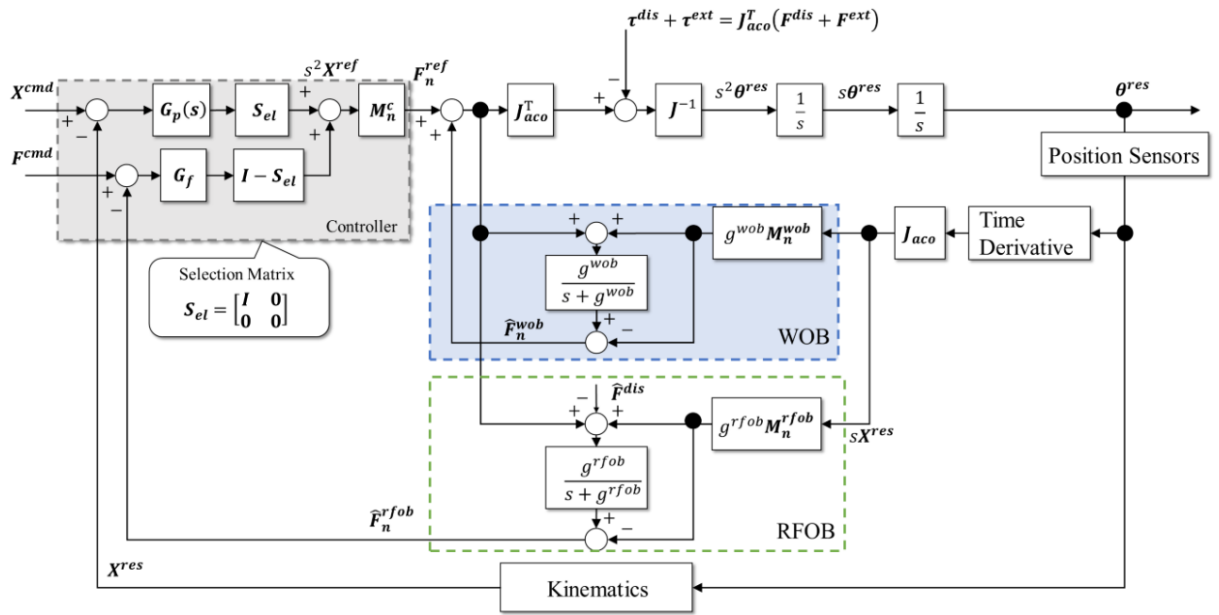
Fig. 3-5: A workspace controller with the equivalent mass matrix.

motors' position responses θ^{res}. Robots' position responses are generally obtained by the position sensors attached to motors. Workspace position responses and workspace velocity responses are obtained by using coordinate transformation. WOB using the force reference values, equivalent mass matrix, and workspace velocity responses, estimates the workspace disturbances and external force and adjusts the output. RFOB estimates the external force in the workspace, and the estimated values are used as the feedback values of force control.

Chapter 4

Challenges of
Position-and-Force-Sensorless Control

This chapter discusses the challenges of realizing position-and-force-sensorless (PFSL) control systems. Problems in general position-sensorless control systems are the position estimation accuracy and robustness. The estimated position has errors, vibrations, and phase delay. These characteristics are not appropriate for applications requiring precise positioning. However, the desired characteristics in applications requiring force control functions are different from them. The reaction force/torque can be more important than the instantaneous position-tracking error during contact motion, including rubbing motion. Therefore, PFSL control systems can be applied to applications with contact motion and rubbing motion.

A PFSL control system with the conventional methods can be expressed as Fig. 4-1. The issues in the PFSL control system are explained. In MDOF PFSL control systems, the workspace position responses and the equivalent mass matrices are derived from the joint coordinate space position responses, which are estimated values. The synchronization of each joint motion is essential to realize accurate workspace control. Therefore, the inaccuracy of the estimated position disturbs the synchronization and the accurate workspace motion. In addition, the estimated position is utilized by RFOB/RTOB in PFSL control systems. Since the estimated force/torque by RFOB/RTOB is the feedback information in force-sensorless control systems, the control performance is deteriorated by the position estimation inaccuracy. Furthermore, the phase delay of the estimated position decreases the control bandwidth of PFSL control systems. Since the bandwidth of the disturbance suppression by integral control or DOB (WOB) is low,
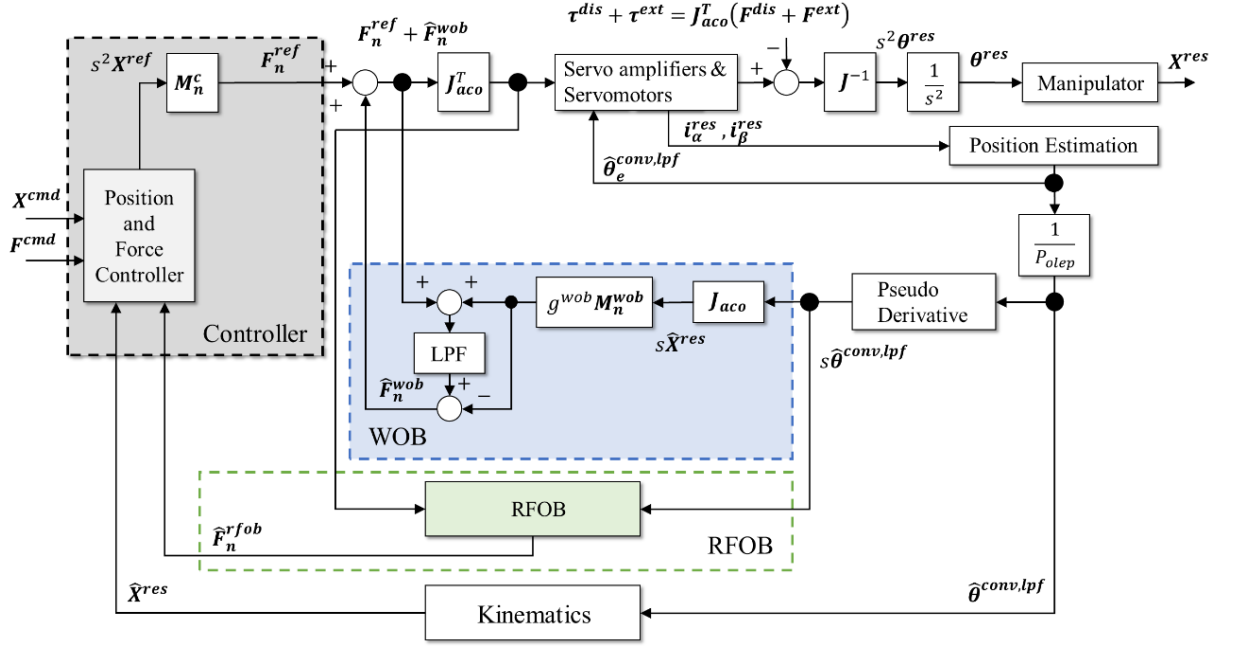
Fig. 4-1: Block diagram of a PFSL hybrid control system with conventional methods.

the control robustness is low.

To confirm the adverse effects described above, the motion by the PFSL hybrid position/force control was confirmed with the 4DOF manipulator in Section 3.2 with IPMSMs. The utilized PFSL hybrid controller used the conventional position estimation method described in Chapter 2 and the force-sensorless control system in Chapter 3. The motion commands were approaching the force gauge near the end-effector and making contact with the force gauge. However, the torque reference diverged, and the manipulator motion went out of control when commands were varied. The system could not achieve the expected motion. Therefore, PFSL control systems with conventional methods have insufficient performance to achieve desired operations. To deal with the problems, this dissertation presents the proposed methods in Chapters 5, 6, and 7.

Chapter 5

Proposed Position-Sensorless Control Considering Cross-Coupling Factors

This chapter discusses development methods for position-sensorless control. In Section 5.1, the cross-coupling factors of IPMSMs are introduced. Section 5.2 explains the proposed estimation method of position and cross-coupling factors based on the voltage equation considering the cross-coupling factors. Section 5.3 describes the proposed current control method with the estimated cross-coupling factors in high-frequency bandwidth. Section 5.4 shows the experimental results of the position-sensorless system with and without considering the cross-coupling factors in high-frequency bandwidth. Section 5.5 explains the proposed error compensation method for the position estimation and the estimation method of cross-coupling factors in wide-frequency bandwidth. Section 5.6 introduces the proposed current control method with the estimated cross-coupling factors in wide-frequency bandwidth. Section 5.7 shows the experimental results to explain the validity of the proposed position-sensorless control system. This chapter is summarized in Section 5.8. The electrical angles' unit is expressed as "elec.."

5.1   Cross-Coupling Factors of IPMSMs

This section explains the modeling of IPMSMs considering cross-coupling factors of inductance. The basic modeling of IPMSMs is described in Section 2.1. In that model, electrical systems in the d-axis and the q-axis are electrically independent other than the influence of velocity. However, according to previous research, there are cross-coupling factors of inductance between the d-axis and q-axis. In this dissertation, JMAG-Designer was used for the FEA, and the 2D analysis was performed at 5 degrees of electrical angle increments. The FEA results of an IPMSM are shown in Fig. 5-1. The values of the injected current were 0 %, 50 %, 100 %, 150 %, and 200 % of the rated current. The inductance values of L_d, L_q, L_{dq}, and L_{qd} were calculated as equations from eq. (5.1) to eq. (5.4). The inductance L_{dq} and L_{qd} are called cross-coupling factors. The variable ϕ_{mag} denotes the flux of the permanent magnet, and the symbol δ denotes the minimal change of the variables.

$$L_d = \frac{\left(\Psi_d \left(i_d + \delta i_d, i_q, \phi_{mag} \right) - \Psi_d \left(i_d, i_q, \phi_{mag} \right) \right)}{\delta i_d} \tag{5.1}$$

$$L_q = \frac{\left(\Psi_q \left(i_d, i_q + \delta i_q, \phi_{mag} \right) - \Psi_q \left(i_d, i_q, \phi_{mag} \right) \right)}{\delta i_q} \tag{5.2}$$

$$L_{dq} = \frac{\left(\Psi_d \left(i_d, i_q + \delta i_q, \phi_{mag} \right) - \Psi_d \left(i_d, i_q, \phi_{mag} \right) \right)}{\delta i_q} \tag{5.3}$$

$$L_{qd} = \frac{\left(\Psi_q \left(i_d + \delta i_d, i_q, \phi_{mag} \right) - \Psi_q \left(i_d, i_q, \phi_{mag} \right) \right)}{\delta i_d} \tag{5.4}$$

The FEA results in Fig. 5-1 show that the inductance values of L_d, L_q, L_{dq}, and L_{qd} vary with the electric angle and current. According to the general modeling of IPMSMs, the terms of cross-coupling factors L_{dq} and L_{qd} are not derived from the transformation between UVW-axes and dq-axes. Therefore, the distribution of the magnetic flux of actual IPMSMs differs from the general model. The distortion of the magnetic flux vector can be assumed. Current controllers and position estimation algorithms, which are calculated based on the orthogonality of the dq-axes, get modeling errors of the cross-coupling factors. The position estimation error can be defined as eq. (5.5).

$$\theta_e^{err} = \hat{\theta}_e^{conv} - \theta_e \tag{5.5}$$
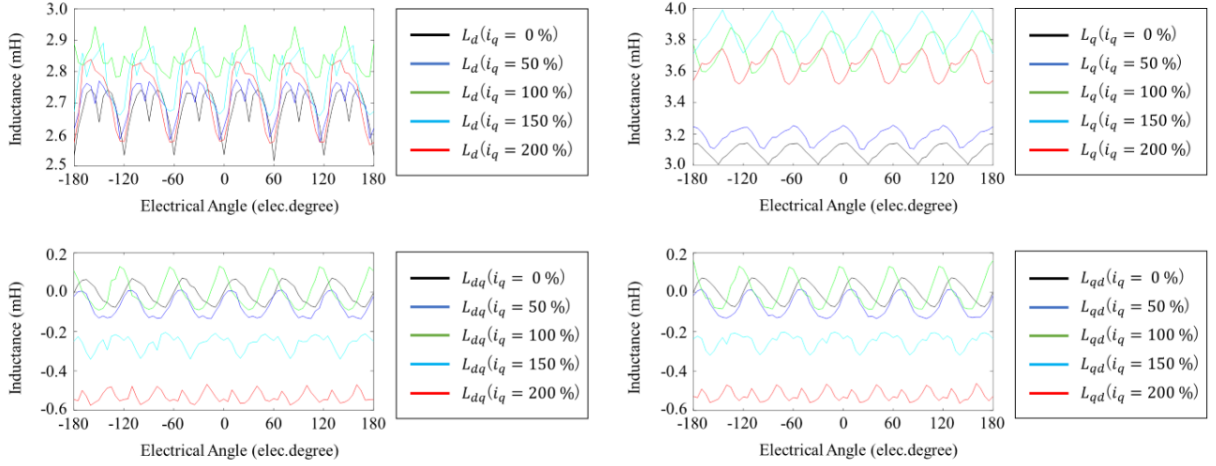
Fig. 5-1: FEA results of the inductance of an IPMSM
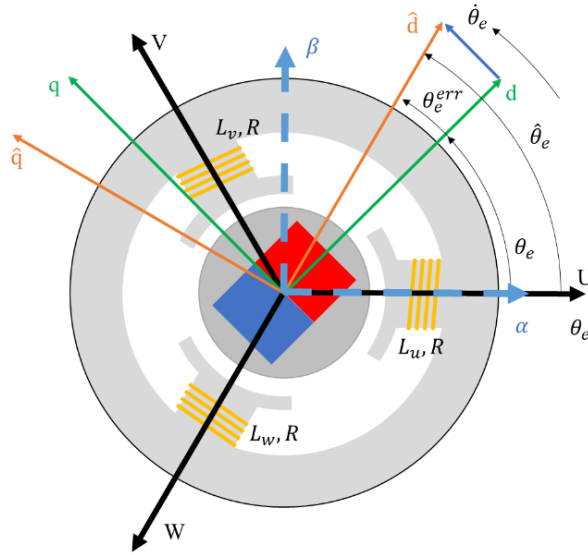
Fig. 5-2: Proposed model of IPMSMs

In this dissertation, an IPMSM model considering the distortion of the magnetic flux vector is introduced. The modeling is shown in Fig. 5-2. Additional points from the general IPMSM model are the orange $\hat{\mathrm{d}}\hat{\mathrm{q}}$-axes and the blue vector. The $\hat{\mathrm{d}}\hat{\mathrm{q}}$-axes, which is the estimated dq-axes in position-sensorless systems, is rotated from $\alpha\beta$-axes by the estimated position $\hat{\theta}_e$. Because of the integrated permanent magnets, the magnetic flux density at the rotor surface varies with position. In addition, high-torque-density motors often use concentrated winding coils. In the case of concentrated winding, the UVW phases are spatially discrete. As a result, the direction of the magnetic flux between the rotor and stator varies with

the rotor position and current. In this dissertation, the magnetic flux vector is called "the magnetic flux vector in the motor" to separate from the magnetic flux vector by integrated permanent magnets called "the magnetic flux vector in the rotor". The direction of the magnetic flux vector in the motor does not match that of the rotor. The blue vector expresses the magnetic vector shift by the distortion. The magnetic vector distortion in the motor causes the position estimation error from the modeling error of IPMSMs.

In section 2.1, the inductance in UVW-axes is expressed by (2.2) with the variables L_a and L_m, representing the mean value and the ripple amplitude of the effective inductance in each phase. In the introduced model, the L_m is considered to be the inductance derived from the magnetic flux vector in the d-axis direction. The inductance L_s is introduced to express the inductance derived from the distortion component of the magnetic flux vector shown by the blue vector. The voltage equation in UVW-axes can be written as equations from eq. (5.6) to eq. (5.8).

$$
\begin{bmatrix} v_u \\ v_v \\ v_w \end{bmatrix} = R \begin{bmatrix} i_u \\ i_v \\ i_w \end{bmatrix} + \begin{bmatrix} L_u\,(i_d,i_q,\theta_e) & L_{uv}\,(i_d,i_q,\theta_e) & L_{wu}\,(i_d,i_q,\theta_e) \\ L_{uv}\,(i_d,i_q,\theta_e) & L_v\,(i_d,i_q,\theta_e) & L_{vw}\,(i_d,i_q,\theta_e) \\ L_{wu}\,(i_d,i_q,\theta_e) & L_{vw}\,(i_d,i_q,\theta_e) & L_w\,(i_d,i_q,\theta_e) \end{bmatrix} \begin{bmatrix} \dot{i}_u \\ \dot{i}_v \\ \dot{i}_w \end{bmatrix}
$$
$$
+ \begin{bmatrix} \dot{L}_u\,(i_d,i_q,\theta_e) & \dot{L}_{uv}\,(i_d,i_q,\theta_e) & \dot{L}_{wu}\,(i_d,i_q,\theta_e) \\ \dot{L}_{uv}\,(i_d,i_q,\theta_e) & \dot{L}_v\,(i_d,i_q,\theta_e) & \dot{L}_{vw}\,(i_d,i_q,\theta_e) \\ \dot{L}_{wu}\,(i_d,i_q,\theta_e) & \dot{L}_{vw}\,(i_d,i_q,\theta_e) & \dot{L}_w\,(i_d,i_q,\theta_e) \end{bmatrix} \begin{bmatrix} i_u \\ i_v \\ i_w \end{bmatrix}
$$
$$
- \dot{\theta}_e\,\Psi' \begin{bmatrix} \sin\left(\theta_e + \theta_e^{err}\right) \\ \sin\left(\theta_e + \theta_e^{err} - \dfrac{2\pi}{3}\right) \\ \sin\left(\theta_e + \theta_e^{err} - \dfrac{4\pi}{3}\right) \end{bmatrix} \tag{5.6}
$$

$$
\begin{bmatrix} L_u\,(i_d,i_q,\theta_e) \\ L_v\,(i_d,i_q,\theta_e) \\ L_w\,(i_d,i_q,\theta_e) \end{bmatrix} = \begin{bmatrix} 1 & \cos\left(2\theta_e\right) & \sin\left(2\theta_e\right) \\ 1 & \cos\left(2\theta_{e+}\right) & \sin\left(2\theta_{e+}\right) \\ 1 & \cos\left(2\theta_{e-}\right) & \sin\left(2\theta_{e-}\right) \end{bmatrix} \begin{bmatrix} L_a\,(i_d,i_q,\theta_e) \\ L_m\,(i_d,i_q,\theta_e) \\ L_s\,(i_d,i_q,\theta_e) \end{bmatrix} \tag{5.7}
$$

$$
\begin{bmatrix} L_{uv}\,(i_d,i_q,\theta_e) \\ L_{vw}\,(i_d,i_q,\theta_e) \\ L_{wu}\,(i_d,i_q,\theta_e) \end{bmatrix} = \frac{1}{2} \begin{bmatrix} -1 & 2\cos\left(2\theta_{e-}\right) & 2\sin\left(2\theta_{e-}\right) \\ -1 & 2\cos\left(2\theta_e\right) & 2\sin\left(2\theta_e\right) \\ -1 & 2\cos\left(2\theta_{e+}\right) & 2\sin\left(2\theta_{e-}\right) \end{bmatrix} \begin{bmatrix} L_a\,(i_d,i_q,\theta_e) \\ L_m\,(i_d,i_q,\theta_e) \\ L_s\,(i_d,i_q,\theta_e) \end{bmatrix} \tag{5.8}
$$

The transformation from the UVW-axes to the dq-axes with θ_e derives the dq-axes voltage equation

shown in eq. (5.9) and (5.10).

$$
\begin{bmatrix} v_d \\ v_q \end{bmatrix} = \begin{bmatrix} R - \dot{\theta}_e L_{qd}\left(i_d, i_q, \theta_e\right) & -\dot{\theta}_e L_q\left(i_d, i_q, \theta_e\right) \\ \dot{\theta}_e L_d\left(i_d, i_q, \theta_e\right) & R + \dot{\theta}_e L_{qd}\left(i_d, i_q, \theta_e\right) \end{bmatrix} \begin{bmatrix} i_d \\ i_q \end{bmatrix}
$$

$$
+ \begin{bmatrix} L_d\left(i_d, i_q, \theta_e\right) & L_{qd}\left(i_d, i_q, \theta_e\right) \\ L_{qd}\left(i_d, i_q, \theta_e\right) & L_q\left(i_d, i_q, \theta_e\right) \end{bmatrix} \begin{bmatrix} \dot{i}_d \\ \dot{i}_q \end{bmatrix} + \dot{\theta}_e\,\Psi \begin{bmatrix} -\sin\left(\theta_e^{err}\right) \\ \cos\left(\theta_e^{err}\right) \end{bmatrix} \tag{5.9}
$$

$$
\begin{bmatrix} L_d\left(i_d, i_q, \theta_e\right) \\ L_q\left(i_d, i_q, \theta_e\right) \\ L_{qd}\left(i_d, i_q, \theta_e\right) \end{bmatrix} = \frac{3}{2} \begin{bmatrix} 1 & 1 & 0 \\ 1 & -1 & 0 \\ 0 & 0 & -1 \end{bmatrix} \begin{bmatrix} L_a\left(i_d, i_q, \theta_e\right) \\ L_m\left(i_d, i_q, \theta_e\right) \\ L_s\left(i_d, i_q, \theta_e\right) \end{bmatrix} \tag{5.10}
$$

The cross-coupling factors are in the non-diagonal elements of the inductance matrix, representing the relationship between voltage and current variation. According to (5.3) and (5.4), the cross-coupling factors are defined as L_{dq} and L_{qd}, which are expressed as the same value in this modeling. The expression is reasonable since the FEA results in Fig. 5-1 show that L_{dq} and L_{qd} were similar.

The motor's power can be expressed as eq. (5.11). The main difference from eq. (2.16) is the term of $-L_{qd}\left(i_d, i_q, \theta_e\right)\left(i_d^2 - i_q^2\right)$.

$$
\begin{bmatrix} v_d \\ v_q \end{bmatrix} \cdot \begin{bmatrix} i_d \\ i_q \end{bmatrix} = R\left(i_d^2 + i_q^2\right) + L_d\left(i_d, i_q, \theta_e\right)\dot{i}_d i_d + L_q\left(i_d, i_q, \theta_e\right)\dot{i}_q i_q
$$

$$
+ L_{qd}\left(i_d, i_q, \theta_e\right)\dot{i}_d i_q + L_{qd}\left(i_d, i_q, \theta_e\right)\dot{i}_q i_d
$$

$$
+ \dot{\theta}_e\left(\Psi i_q \cos\theta_e^{err} - \Psi i_d \sin\theta_e^{err} + \left(L_d\left(i_d, i_q, \theta_e\right) - L_q\left(i_d, i_q, \theta_e\right)\right) i_d i_q\right.
$$

$$
\left. - L_{qd}\left(i_d, i_q, \theta_e\right)\left(i_d^2 - i_q^2\right)\right) \tag{5.11}
$$

Therefore, the motor's output torque can be expressed by eq. (5.12).

$$
\tau = P_{ole}\left(\Psi i_q \cos\theta_e^{err} - \Psi i_d \sin\theta_e^{err} + \left(L_d\left(i_d, i_q, \theta_e\right) - L_q\left(i_d, i_q, \theta_e\right)\right) i_d i_q\right.
$$

$$
\left. - L_{qd}\left(i_d, i_q, \theta_e\right)\left(i_d^2 - i_q^2\right)\right) \tag{5.12}
$$

The effect of the cross-coupling factors in the conventional control method, shown in Fig. 2-11, was confirmed by two kinds of simulation. One used motors with different inductance characteristics as the control target. The other used the two-link parallel manipulator in the 4DOF manipulator described in Section 3.2 as the control target.

In the simulation with motors, the utilized motion control was P-PI control with RTOB. The position command was a ramp signal. It was increased by 1 % of the motor's rated speed. External torque

Table 5.1: Motor and controller parameters for simulation with motors to confirm the effect of the cross–coupling factors.

Motor Parameters	Values	Control Parameters	Values
Resistance R (Ohm)	1.4	d-axis Proportional Gain (H·rad/s)	23.42
d-axis Inductance L_d (mH)	1.9	d-axis Integral Gain (s)	0.0013
q-axis Inductance L_q (mH)	2.3	q-axis Proportional Gain (H·rad/s)	29.02
Torque constant (Nm/A)	0.544	q-axis Integral Gain (s)	0.0016
Ψ (V/(elec. rad/s))	0.109	Velocity Proportional Gain (rad/s)	125.6
Rotor inertia (kgm^2)	0.486×10^{-4}	Velocity Integral Gain (s)	0.0318
Viscosity friction coefficient (Nm/(mech. rad/s) (Mechanical))	6.8×10^{-5}	Position Proportional Gain (1/s)	20.94
		Cut-off frequency of LPF for torque reference (rad/s)	502.7
Rated Power (W)	400		
Rated velocity (mech. rad/s)	314.2	Cut-off frequency of	
Rated torque (Nm)	1.27	PLL for $\hat{\theta}_e^{conv}$ (rad/s)	618.3
Pole pairs	5	Cut-off frequency of DOB (rad/s)	62.8

was applied during the rotation. The control parameters in this simulation are expressed in Table 5.1. Simulation results using two motor models were confirmed. One had fixed inductance parameters of L_d and L_q, and the cross-coupling factors were ignored. The other had the variable inductance, including cross-coupling factors, which were implemented by a parameter reference table. The simulation results are shown in Fig. 5-3 and Fig. 5-4, respectively. Both figures show the position, the velocity, the torque reference, and the external torque from the top. According to these results, responses by the simulation using a motor model considering the cross-coupling factors had larger vibration.

In the simulation with the two-link parallel manipulator, the utilized motion control was P-PI control in the workspace, and the coordinate transformation was based on the equivalent mass matrix with design values. The manipulator model and the motion command in the simulation are shown in Fig. 5-5 and Fig. 5-6, respectively. The characteristics of the two motors in the manipulator were the same in each simulation. External torque was not applied. The control parameters in this simulation are expressed in Table 5.2.   Simulation results using four kinds of motor models were compared. The motors had the cross-coupling factors' values that were 1, 0.5, 0.25, and 0.125 times those obtained by FEA. The simulation results are shown in Fig. 5-7 and Fig. 5-8. The larger the cross-coupling factors, the larger the vibration in the workspace position responses and the larger the differences between responses and estimated values. The position responses by "$1 \times L_{qd}$" and "$0.5 \times L_{qd}$" did not converge at position
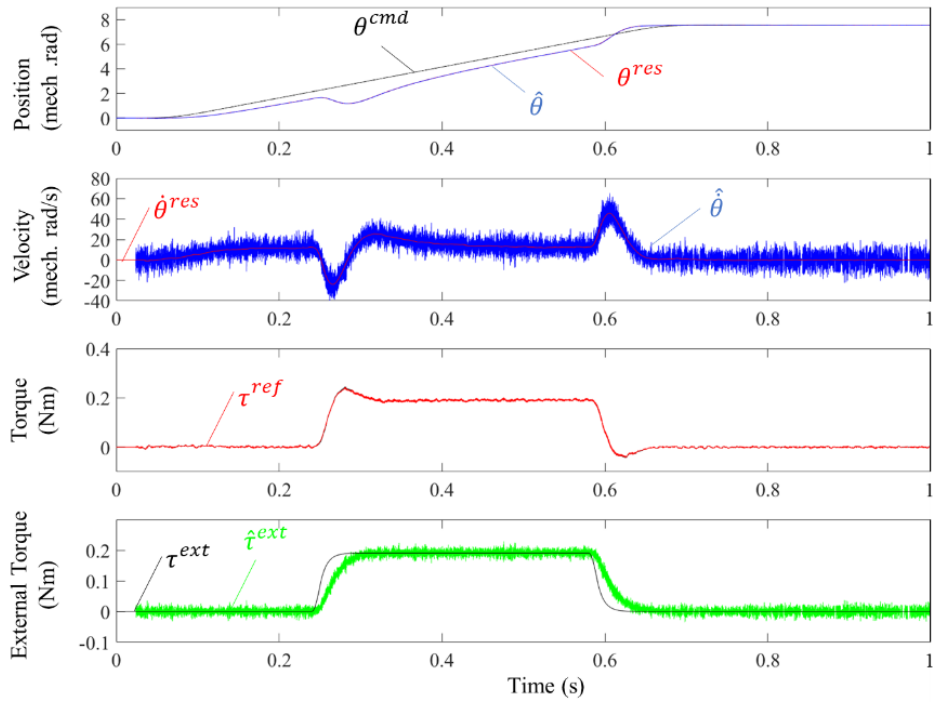
Fig. 5-3: Simulation results with a motor model with fixed inductance.
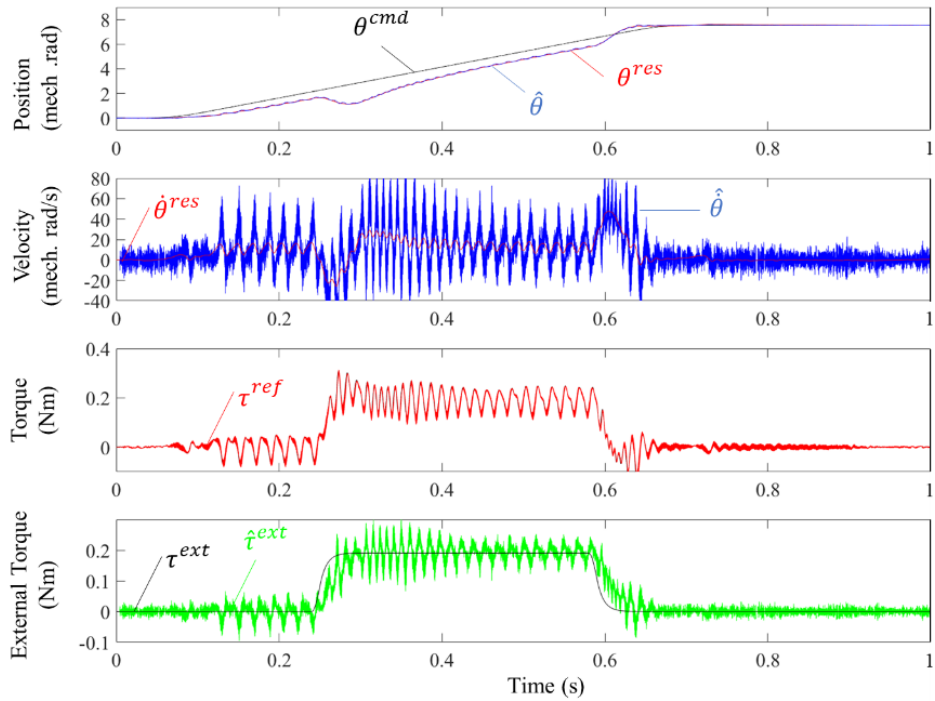
Fig. 5-4: Simulation results with a motor model with variable inductance based on FEA results.

Table 5.2: Motor and controller parameters for simulation with the two-link manipulator to confirm the effect of the cross-coupling factors

Motor Parameters	Values	Control Parameters	Values
Resistance R (Ohm)	1.4	d-axis Proportional Gain (H·rad/s)	23.42
d-axis Inductance L_d (mH)	1.9	d-axis Integral Gain (s)	0.0013
q-axis Inductance L_q (mH)	2.3	q-axis Proportional Gain (H·rad/s)	29.02
Torque constant (Nm/A)	0.544	q-axis Integral Gain (s)	0.0016
Ψ (V/(elec. rad/s))	0.109	Velocity Proportional Gain (rad/s)	31.4
Rotor inertia (kgm^2)	0.486×10^{-4}	Velocity Integral Gain (s)	0.127
Viscosity friction coefficient (Nm/(mech. rad/s) (Mechanical))	6.8×10^{-5}	Position Proportional Gain (1/s)	7.85
Rated Power (W)	400	Cut-off frequency of LPF for torque reference (rad/s)	250.0
Rated velocity (mech. rad/s)	314.2	Cut-off frequency of PLL for $\hat{\theta}_e^{conv}$ (rad/s)	314.1
Rated torque (Nm)	1.27		
Pole pairs	5		
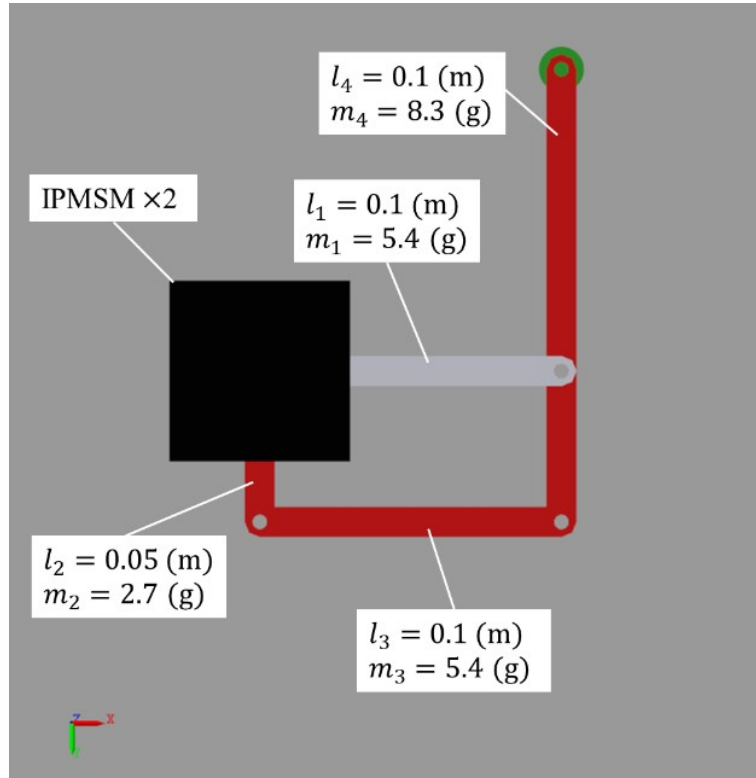
Fig. 5-5: Simulation model of the two-link parallel manipulator.
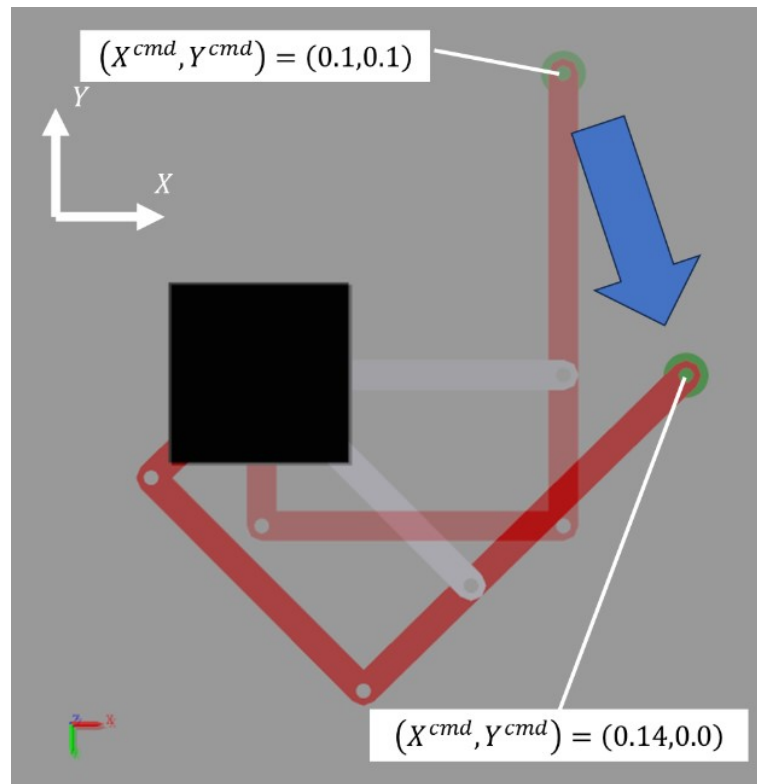
Fig. 5-6: Motion command of the two-link manipulator in the simulation.

command even at 3 s. These undesired responses can be considered the reason for the divergence of the torque reference in the experiment described in Chapter 4. Since actual motors have the cross-coupling factors in the dq-axes inductance, vibration reduction by considering the cross-coupling factors is required. It is desirable to reduce the adverse effects of cross-coupling factors to the level where a response of "$0.25 \times L_{qd}$" can be obtained. The maximum estimation errors of the electrical position in each joint are shown in Table 5.3. According to Table 5.3, the maximum estimation errors were over 0.34 elec. rad without compensation. When the maximum estimation error is lower than 0.06 elec. rad, the workspace position responses converged. The target value for estimation error reduction is 0.06 elec. rad or less.
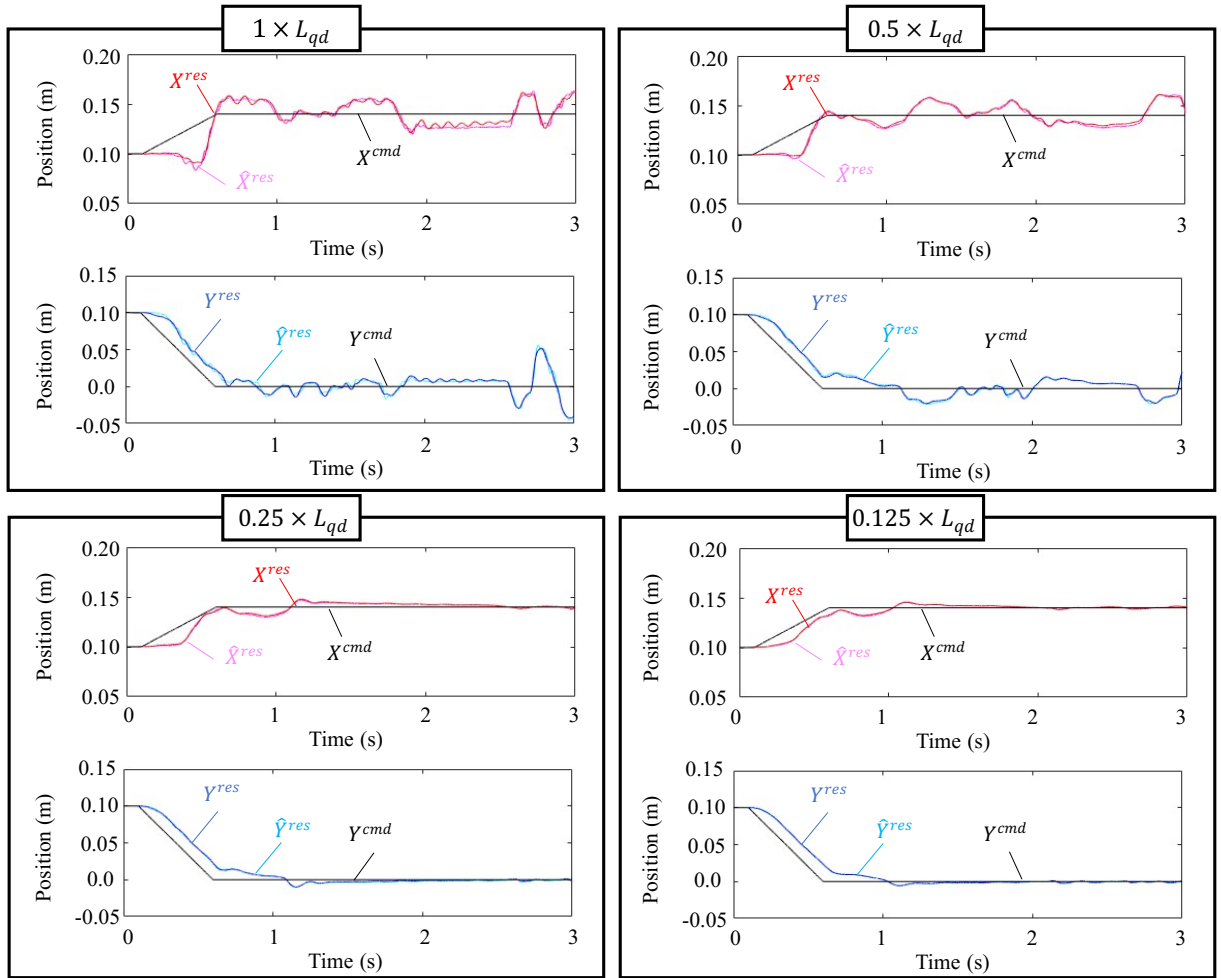
Fig. 5-7: Comparison among workspace position responses depending on the cross-coupling factors in the simulation of the two-link manipulator.
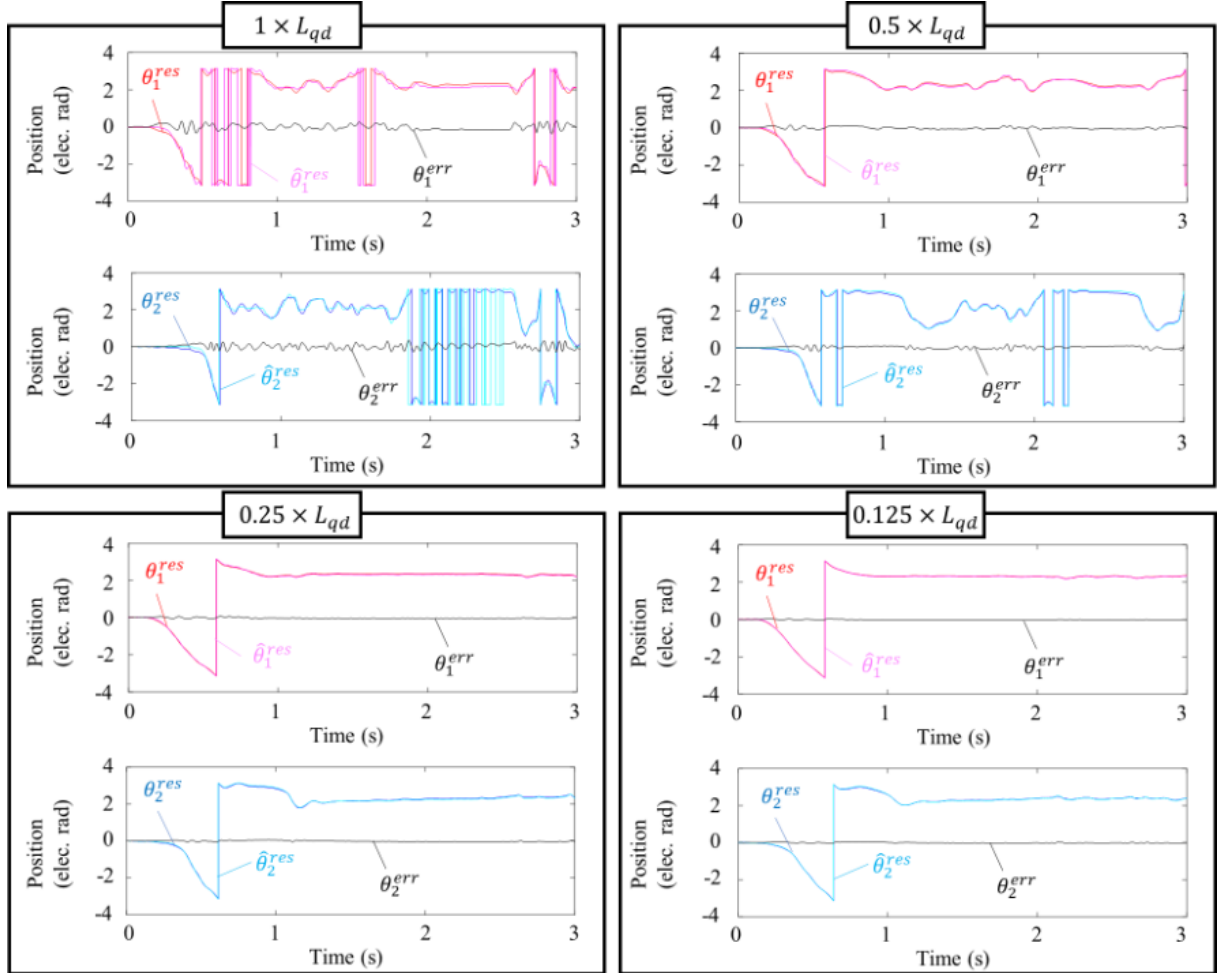
Fig. 5-8: Comparison among electrical position responses depending on the cross-coupling factors in the simulation of the two-link manipulator.

Table 5.3: Comparison among the maximum estimated errors in the simulation of the two-link manipulator.

	"$1 \times L_{qd}$"	"$0.5 \times L_{qd}$"	"$0.25 \times L_{qd}$"	"$0.125 \times L_{qd}$"
Joint 1	0.34 (elec. rad)	0.15 (elec. rad)	0.06 (elec. rad)	0.03 (elec. rad)
Joint 2	0.38 (elec. rad)	0.24 (elec. rad)	0.07 (elec. rad)	0.04 (elec. rad)

5.2 Proposed Estimation Method of Position and High-Frequency Cross-Coupling Factors

This section explains the proposed estimation method of position and cross-coupling factors based on the voltage equation considering the cross-coupling factors. The proposed estimation method is based on the method described in section 2.3.

The frequency of the injected voltage is synchronized with a carrier wave, and it is sufficiently higher than the rotational frequency of the electrical angle in the low-speed operation. Furthermore, the amplitude of the injected voltage is constant. The high-frequency components in the voltage equation of eq. (5.9) can be expressed as eq. (5.13) since the components relating to current variation are dominant in the bandwidth around the frequency of the injected voltage.

$$\begin{bmatrix} v_{d,h} \\ v_{q,h} \end{bmatrix} = \begin{bmatrix} L_{d,h}\left(i_d, i_q, \theta_e\right) & L_{qd,h}\left(i_d, i_q, \theta_e\right) \\ L_{qd,h}\left(i_d, i_q, \theta_e\right) & L_{q,h}\left(i_d, i_q, \theta_e\right) \end{bmatrix} \begin{bmatrix} \dot{i}_{d,h} \\ \dot{i}_{q,h} \end{bmatrix} \tag{5.13}$$

The inductance matrix in eq. (5.13) is defined as eq. (5.14).

$$\boldsymbol{L}_h\left(i_d, i_q, \theta_e\right) = \begin{bmatrix} L_{d,h}\left(i_d, i_q, \theta_e\right) & L_{qd,h}\left(i_d, i_q, \theta_e\right) \\ L_{qd,h}\left(i_d, i_q, \theta_e\right) & L_{q,h}\left(i_d, i_q, \theta_e\right) \end{bmatrix} \tag{5.14}$$

The relationship between the time derivative terms of current on $\alpha\beta$-axis and dq-axes can be written as eq. (5.15) since the velocity is low in the assumed operation.

$$\begin{aligned}
\begin{bmatrix} \dot{i}_{\alpha,h} \\ \dot{i}_{\beta,h} \end{bmatrix} &= \begin{bmatrix} \cos\theta_e & -\sin\theta_e \\ \sin\theta_e & \cos\theta_e \end{bmatrix} \begin{bmatrix} \dot{i}_{d,h} \\ \dot{i}_{q,h} \end{bmatrix} + \dot{\theta}_e \begin{bmatrix} -\sin\theta_e & -\cos\theta_e \\ \cos\theta_e & -\sin\theta_e \end{bmatrix} \begin{bmatrix} i_{d,h} \\ i_{q,h} \end{bmatrix} \\
&\approx \begin{bmatrix} \cos\theta_e & -\sin\theta_e \\ \sin\theta_e & \cos\theta_e \end{bmatrix} \begin{bmatrix} \dot{i}_{d,h} \\ \dot{i}_{q,h} \end{bmatrix} \\
&= \begin{bmatrix} \cos\theta_e & -\sin\theta_e \\ \sin\theta_e & \cos\theta_e \end{bmatrix} \boldsymbol{L}_h^{-1}\left(i_d, i_q, \theta_e\right) \begin{bmatrix} v_{d,h} \\ v_{q,h} \end{bmatrix} \\
&= \frac{1}{\det\left(\boldsymbol{L}_h\left(i_d, i_q, \theta_e\right)\right)} \begin{bmatrix} \cos\theta_e & -\sin\theta_e \\ \sin\theta_e & \cos\theta_e \end{bmatrix} \cdot \\
&\quad \begin{bmatrix} L_{q,h}\left(i_d, i_q, \theta_e\right) & -L_{qd,h}\left(i_d, i_q, \theta_e\right) \\ -L_{qd,h}\left(i_d, i_q, \theta_e\right) & L_{d,h}\left(i_d, i_q, \theta_e\right) \end{bmatrix} \begin{bmatrix} v_{d,h} \\ v_{q,h} \end{bmatrix}
\end{aligned} \tag{5.15}$$

Since the injected high-frequency voltage is on the estimated d-axis, the voltage is expressed as eq. (5.16).

$$\begin{bmatrix} v_{d,h}[k] \\ v_{q,h}[k] \end{bmatrix} = \begin{bmatrix} v_h[k]\cos\theta_e^{err} \\ v_h[k]\sin\theta_e^{err} \end{bmatrix} \tag{5.16}$$

$$v_h[k] = \begin{cases} v_{inj} & (k = 2n) \\ -v_{inj} & (k = 2n+1) \end{cases}$$

The time derivative terms of current on the $\alpha\beta$-axes by the injected voltage are expressed by equations from eq. (5.17) to eq. (5.22).

$$
\begin{bmatrix} \dot{i}_{\alpha,h} \\ \dot{i}_{\beta,h} \end{bmatrix} \approx \frac{1}{\det\left(\boldsymbol{L_h}\left(i_d, i_q, \theta_e\right)\right)} \begin{bmatrix} \cos\theta_e & -\sin\theta_e \\ \sin\theta_e & \cos\theta_e \end{bmatrix} \cdot
$$

$$
\begin{bmatrix} L_{q,h}\left(i_d, i_q, \theta_e\right) & -L_{qd,h}\left(i_d, i_q, \theta_e\right) \\ -L_{qd,h}\left(i_d, i_q, \theta_e\right) & L_{d,h}\left(i_d, i_q, \theta_e\right) \end{bmatrix} \begin{bmatrix} \pm v^{inj}\cos\theta_e^{err} \\ \pm v^{inj}\sin\theta_e^{err} \end{bmatrix}
$$

$$
= A_L\left(i_d, i_q, \theta_e\right) \begin{bmatrix} \cos\theta_e^{err} - c\left(i_d, i_q, \theta_e\right)\sin\theta_e^{err} \\ -c\left(i_d, i_q, \theta_e\right)\cos\theta_e^{err} + \gamma\left(i_d, i_q, \theta_e\right)\sin\theta_e^{err} \end{bmatrix}
$$

$$
\begin{array}{cc} c\left(i_d, i_q, \theta_e\right)\cos\theta_e^{err} - \gamma\left(i_d, i_q, \theta_e\right)\sin\theta_e^{err} \\ \cos\theta_e^{err} - c\left(i_d, i_q, \theta_e\right)\sin\theta^{err} \end{array} \Bigg] \begin{bmatrix} \cos\theta_e \\ \sin\theta_e \end{bmatrix}
$$

$$
= A_L\left(i_d, i_q, \theta_e\right) \begin{bmatrix} 1 \\ -\dfrac{c\left(i_d, i_q, \theta_e\right)\cos\theta_e^{err} - \gamma\left(i_d, i_q, \theta_e\right)\sin\theta_e^{err}}{\cos\theta_e^{err} - c\left(i_d, i_q, \theta_e\right)\sin\theta_e^{err}} \end{bmatrix}
$$

$$
\begin{array}{c} \dfrac{c\left(i_d, i_q, \theta_e\right)\cos\theta_e^{err} - \gamma\left(i_d, i_q, \theta_e\right)\sin\theta_e^{err}}{\cos\theta_e^{err} - c\left(i_d, i_q, \theta_e\right)\sin\theta_e^{err}} \\ 1 \end{array} \Bigg] \begin{bmatrix} \cos\theta_e \\ \sin\theta_e \end{bmatrix}
$$

$$
= B_L\left(i_d, i_q, \theta_e\right) \begin{bmatrix} 1 & C_L\left(i_d, i_q, \theta_e\right) \\ -C_L\left(i_d, i_q, \theta_e\right) & 1 \end{bmatrix} \begin{bmatrix} \cos\theta_e \\ \sin\theta_e \end{bmatrix}
$$

$$
= B_L\left(i_d, i_q, \theta_e\right) \begin{bmatrix} \cos\theta_e & \sin\theta_e \\ \sin\theta_e & -\cos\theta_e \end{bmatrix} \begin{bmatrix} 1 \\ C_L\left(i_d, i_q, \theta_e\right) \end{bmatrix} \tag{5.17}
$$

$$
c\left(i_d, i_q, \theta_e\right) = \frac{L_{qd,h}\left(i_d, i_q, \theta_e\right)}{L_{q,h}\left(i_d, i_q, \theta_e\right)} \tag{5.18}
$$

$$
\gamma\left(i_d, i_q, \theta_e\right) = \frac{L_{d,h}\left(i_d, i_q, \theta_e\right)}{L_{q,h}\left(i_d, i_q, \theta_e\right)} \tag{5.19}
$$

$$
A_L\left(i_d, i_q, \theta_e\right) = \frac{\pm v^{inj}}{L_{q,h}\left(i_d, i_q, \theta_e\right)\det\left(\boldsymbol{L_h}\left(i_d, i_q, \theta_e\right)\right)} \tag{5.20}
$$

$$
\begin{aligned} B_L\left(i_d, i_q, \theta_e\right) &= A_L\left(i_d, i_q, \theta_e\right)\left(\cos\theta_e^{err} - c\sin\theta_e^{err}\right) \\ &= \frac{\pm v^{inj}\left(\cos\theta_e^{err} - c\left(i_d, i_q, \theta_e\right)\sin\theta_e^{err}\right)}{L_{q,h}\left(i_d, i_q, \theta_e\right)\det\left(\boldsymbol{L_h}\left(i_d, i_q, \theta_e\right)\right)} \end{aligned} \tag{5.21}
$$

$$
C_L\left(i_d, i_q, \theta_e\right) = \frac{c\left(i_d, i_q, \theta_e\right)\cos\theta_e^{err} - \gamma\left(i_d, i_q, \theta_e\right)\sin\theta_e^{err}}{\cos\theta_e^{err} - c\left(i_d, i_q, \theta_e\right)\sin\theta_e^{err}} \tag{5.22}
$$

The variable γ corresponds to the inverse of the saliency ratio, with values ranging from 0.5 to 1 for most IPMSMs. The relationship between the time differential terms of current on $\alpha\beta$-axes and the electrical angle can be rewritten as eq. (5.23).

$$\begin{bmatrix} \cos\theta_e \\ \sin\theta_e \end{bmatrix} \approx \frac{1}{B_L(i_d,i_q,\theta_e)\left(C_L^2(i_d,i_q,\theta_e)+1\right)} \begin{bmatrix} 1 & -C_L(i_d,i_q,\theta_e) \\ C_L(i_d,i_q,\theta_e) & 1 \end{bmatrix} \begin{bmatrix} \dot{i}_{\alpha,h} \\ \dot{i}_{\beta,h} \end{bmatrix} \quad (5.23)$$

The position θ_e can be derived as eq. (5.24) by the additive theorem for the inverse tangent.

$$\begin{aligned} \theta_e &= \tan^{-1}\frac{\sin\theta_e}{\cos\theta_e} \\ &\approx \tan^{-1}\left(\frac{C_L(i_d,i_q,\theta_e)\dot{i}_{\alpha,h}+\dot{i}_{\beta,h}}{\dot{i}_{\alpha,h}-C_L(i_d,i_q,\theta_e)\dot{i}_{\beta,h}}\right) \\ &= \tan^{-1}\left(\frac{C_L(i_d,i_q,\theta_e)+\dfrac{\dot{i}_{\beta,h}}{\dot{i}_{\alpha,h}}}{1-C_L(i_d,i_q,\theta_e)\dfrac{\dot{i}_{\beta,h}}{\dot{i}_{\alpha,h}}}\right) \\ &= \tan^{-1}\left(\frac{\dot{i}_{\beta,h}}{\dot{i}_{\alpha,h}}\right)+\tan^{-1}\left(C_L(i_d,i_q,\theta_e)\right) \end{aligned} \quad (5.24)$$

The first term on the right side is the value derived by conventional position estimation. The second term shows the estimation error in the conventional position estimation method. Since estimation error is defined as eq. (5.5), eq. (5.25) can be obtained.

$$\tan^{-1}(C_L) = -\theta_e^{err} \quad (5.25)$$

The equations eq. (5.22) and eq. (5.25) can derive eq. (5.26).

$$-\tan\theta_e^{err} = \frac{c(i_d,i_q,\theta_e)\cos\theta_e^{err}-\gamma(i_d,i_q,\theta_e)\sin\theta_e^{err}}{\cos\theta_e^{err}-c(i_d,i_q,\theta_e)\sin\theta_e^{err}} \quad (5.26)$$

The position estimation error can be derived as eq. (5.27).

$$\theta_e^{err} = \frac{1}{2}\tan^{-1}\left(\frac{2L_{qd,h}(i_d,i_q,\theta_e)}{L_{d,h}(i_d,i_q,\theta_e)-L_{q,h}(i_d,i_q,\theta_e)}\right) \quad (5.27)$$

Therefore, the conventional estimated position has the estimation error shown in eq. (5.27).

The instantaneous variation of the inductance is ignored in the estimation algorithm. However, the high-frequency voltage injection methods cause the high-frequency variation of the estimated position and the cross-coupling factors. When the estimated position varies, the estimated d-axis, on which the high-frequency voltage is injected, also varies. Since the cross-coupling factors relate to the magnetic

flux vector distortion, the variation of the voltage injection angle causes the cross-coupling factors variation. As shown in eq. (5.27), the variation of the cross-coupling factors and the position estimation error are related. Therefore, the position estimation error variation and cross-coupling factors are circulated. As a result, the cross-coupling factors can be varied in each voltage injection timing, and the variation is in high-frequency bandwidth. Even if the rotor position is fixed, the circulation occurs, and the estimated position gets vibration. In addition, cross-coupling factors are not zero in the steady state. Therefore, the cross-coupling factors variation are in wide-frequency bandwidth.

The algorithm described above is implemented as discrete-time systems. The relationship shown in eq. (5.17) can be rewritten as equations from eq. (5.28) to eq. (5.30) in discrete-time systems.

$$
\begin{aligned}
\begin{bmatrix} \Delta i_{\alpha,h}[k] \\ \Delta i_{\beta,h}[k] \end{bmatrix} &\approx B_L[k] \begin{bmatrix} 1 & C_L[k] \\ -C_L[k] & 1 \end{bmatrix} \begin{bmatrix} \cos \theta_e[k] \\ \sin \theta_e[k] \end{bmatrix} \\
&= B_L[k] \begin{bmatrix} \cos \theta_e[k] & \sin \theta_e[k] \\ \sin \theta_e[k] & -\cos \theta_e[k] \end{bmatrix} \begin{bmatrix} 1 \\ C_L[k] \end{bmatrix}
\end{aligned} \tag{5.28}
$$

$$
\begin{bmatrix} \cos \theta_e[k] \\ \sin \theta_e[k] \end{bmatrix} \approx \frac{1}{B_L[k]\left(C_L^2[k]+1\right)} \begin{bmatrix} 1 & -C_L[k] \\ C_L[k] & 1 \end{bmatrix} \begin{bmatrix} \Delta i_{\alpha,h}[k] \\ \Delta i_{\beta,h}[k] \end{bmatrix} \tag{5.29}
$$

$$
\begin{bmatrix} 1 \\ C_L[k] \end{bmatrix} \approx \frac{1}{B_L[k]} \begin{bmatrix} \cos \theta_e[k] & \sin \theta_e[k] \\ \sin \theta_e[k] & -\cos \theta_e[k] \end{bmatrix} \begin{bmatrix} \Delta i_{\alpha,h}[k] \\ \Delta i_{\beta,h}[k] \end{bmatrix} \tag{5.30}
$$

The estimated position $\theta_e[k]$ and $C_L[k]$ can be obtained by eq. (5.31) and eq. (5.32), respectively.

$$
\theta_e[k] \approx \tan^{-1}\left(\frac{\Delta i_{\beta,h}[k]}{\Delta i_{\alpha,h}[k]}\right) + \tan^{-1}\left(C_L[k]\right) \tag{5.31}
$$

$$
C_L[k] \approx \frac{\Delta i_{\alpha,h} \sin \theta_e[k] - \Delta i_{\beta,h} \cos \theta_e[k]}{\Delta i_{\alpha,h} \cos \theta_e[k] + \Delta i_{\beta,h} \sin \theta_e[k]} \tag{5.32}
$$

However, since $\theta_e[k]$, which is required to derive $C_L[k]$, still has not been estimated in this processing timing in discrete-time systems, the latest estimated position $\hat{\theta}_e[k-1]$ at this processing timing is substituted into $\theta_e[k]$ in eq. (5.32), as shown in eq. (5.33).

$$
\hat{C}_L[k] = \frac{\Delta i_{\alpha,h}[k] \sin \hat{\theta}_e[k-1] - \Delta i_{\beta,h}[k] \cos \hat{\theta}_e[k-1]}{\Delta i_{\alpha,h}[k] \cos \hat{\theta}_e[k-1] + \Delta i_{\beta,h}[k] \sin \hat{\theta}_e[k-1]} \tag{5.33}
$$

By substituting eq. (5.33) to eq. (5.31) and using an additional gain g_h, the estimated position can be obtained as eq. (5.34). The gain g_h adjusts the effect of using the previous value $\hat{\theta}_e[k-1]$ in eq. (5.33).

$$
\hat{\theta}_e[k] = \tan^{-1}\left(\frac{\Delta i_{\beta,h}[k]}{\Delta i_{\alpha,h}[k]}\right) + g_h \tan^{-1}\left(\hat{C}_L[k]\right) \tag{5.34}
$$

The variable $\hat{C}_L[k]$ can be expressed as eq. (5.35) from eq. (5.33) by the additive theorem for the inverse tangent.

$$\tan^{-1}\hat{C}_L[k] = \hat{\theta}_e[k-1] - \tan^{-1}\left(\frac{\Delta i_{\beta,h}[k]}{\Delta i_{\alpha,h}[k]}\right) \tag{5.35}$$

The estimated position $\hat{\theta}_e[k]$ can be rewritten as eq. (5.36).

$$\hat{\theta}_e[k] = (1 - g_h)\tan^{-1}\left(\frac{\Delta i_{\beta,h}[k]}{\Delta i_{\alpha,h}[k]}\right) + g_h\hat{\theta}_e[k-1] \tag{5.36}$$

Therefore, the gain g_h works as the cut-off frequency of a 1st-order LPF in the position estimation. In addition, eq. (5.35) can be also rewritten as eq. (5.37).

$$\begin{aligned}
\tan^{-1}\left(\hat{C}_L[k]\right) &= g_h\tan^{-1}\left(\hat{C}_L[k-1]\right) + \tan^{-1}\left(-\frac{\Delta i_{\beta,h}[k]}{\Delta i_{\alpha,h}[k]}\right) \\
&\quad - \tan^{-1}\left(-\frac{\Delta i_{\beta,h}[k-1]}{\Delta i_{\alpha,h}[k-1]}\right)
\end{aligned} \tag{5.37}$$

The gain g_h works as the cut-off frequency of a 1st-order HPF in the C_L estimation. Therefore, the estimation method can compensate for the high-frequency variation of the estimated position. However, the position estimation error in the low-frequency bandwidth caused by the cross-coupling factors cannot be compensated only by the algorithm.

Since cross-coupling factors $L_{qd,h}$ is in the variable c, as shown in eq. (5.18), $L_{qd,h}$ can be derived by using eq. (5.18), eq. (5.22), and eq. (5.25). The variable c in discrete-time systems can be expressed as $c[k]$ shown in eq. (5.38).

$$c[k] = \frac{1 - \gamma[k]}{1 - C_L[k]^2}C_L[k] \tag{5.38}$$

By using nominal or actual values of $L_{q,n}$ obtained from catalogs or measurements, the cross-coupling factors $L_{qd,h}$ in the high-frequency bandwidth can be estimated as eq. (5.39).

$$\hat{L}_{qd,h}^{high}[k] = \frac{1 - \gamma[k]}{1 - \hat{C}_L[k]^2}\hat{C}_L[k]L_{q,n}[k] \tag{5.39}$$

When reference tables or functions for variable values of $L_{q,n}$ and $L_{d,n}$ from FEA results or experimental results, the variable values can be applied to $L_{q,n}$ and $L_{d,n}$. If the input values have few errors and vibrations, the estimation accuracy can increase.

When the high-frequency voltage is approximated as being injected on the actual d-axis, an assumption $\theta_e^{err} \approx 0$ can be assumed in equations. Similar calculation derives the estimated position and

cross-coupling factors, expressed as equations from eq. (5.40) to eq. (5.42).

$$\hat{\theta}_e[k] = \tan^{-1}\left(\frac{\Delta i_{\beta,h}[k]}{\Delta i_{\alpha,h}[k]}\right) + \tan^{-1}(\hat{c}[k]) \tag{5.40}$$

$$\hat{c}[k] = \hat{C}_L[k] = \frac{\Delta i_{\alpha,h}[k]\sin\hat{\theta}_e[k-1] - \Delta i_{\beta,h}[k]\cos\hat{\theta}_e[k-1]}{\Delta i_{\alpha,h}[k]\cos\hat{\theta}_e[k-1] + \Delta i_{\beta,h}[k]\sin\hat{\theta}_e[k-1]} \tag{5.41}$$

$$\hat{L}_{qd,h}^{high}[k] = \hat{c}[k]L_{q,n}[k] \tag{5.42}$$

The similarity of eq. (5.34) and eq. (5.40) indicates that the estimated positions are thef same. This algorithm can obtain similar position estimation results with or without consideration of the axis on which the high-frequency voltage is injected. This advantage is linked to the disadvantage of not being able to compensate for the position estimation error in the low-frequency bandwidth. The estimated cross-coupling factors of eq. (5.39) and eq. (5.42) are different. IPMSMs where the magnetic saliency is $L_q < L_d$ are generally used, and $\gamma < 1$ can be assumed. The cross-coupling factors of general IPMSMs are smaller than L_d and L_q. The values of $\hat{C}_L[k]$ by eq. (5.33) and $\hat{c}[k]$ by eq. (5.41) are sufficiently smaller than 1. Therefore, the estimated cross-coupling factors of eq. (5.42) are larger than that of eq. (5.39). However, since the values have only high-frequency values and are smaller than L_q and L_d, the difference in the effects on the control systems is small. The estimation processing time to derive eq. (5.42) is shorter than that of eq. (5.39). Since the period of current control and estimation are short, the processing time of them is required to be short. The estimation algorithm shown in equations from eq. (5.40) to eq. (5.42) is adopted in this dissertation. The estimated cross-coupling factors can be used in the current control based on the voltage equation considering cross-coupling factors.

The block diagram of the estimation method can be shown in Fig. 5-9. The difference in the viewpoint of the estimation bandwidth can be shown in Fig. 5-10. The upper part in Fig. 5-10 shows the conventional position estimation method and cross-coupling factors from reference tables. The lower part in Fig. 5-10 shows the proposed position and cross-coupling factors estimation described in this section. In conventional methods, cross-coupling factors are derived from reference tables whose input information is the estimated position. Since the estimated position is through an LPF function, the derived cross-coupling factors are in the low-frequency bandwidth. The cut-off frequency of the LPF is often smaller than the frequencies of current control bandwidth, 6 times the electrical rotation, and the high-frequency vibration caused by the relationship between the position estimation error and the cross-coupling factors.
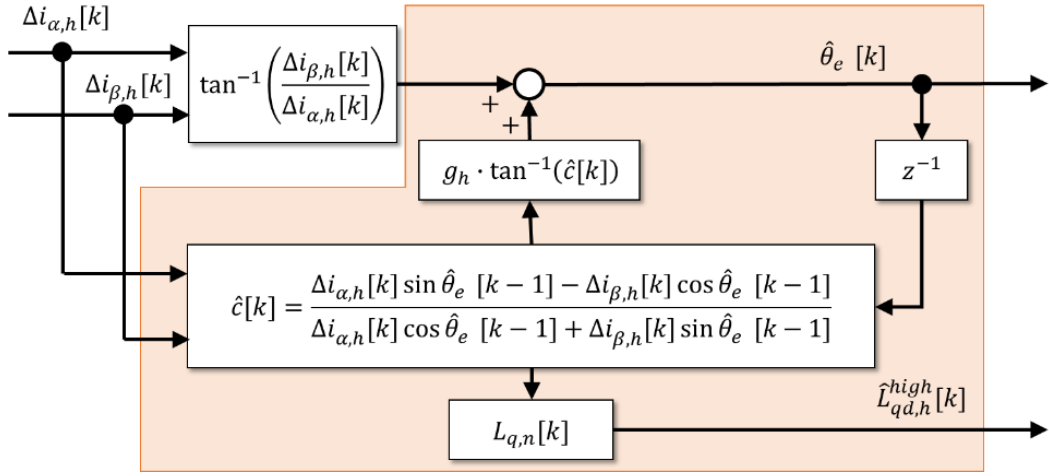
Fig. 5-9: Block diagram of the position and cross-coupling factors estimation
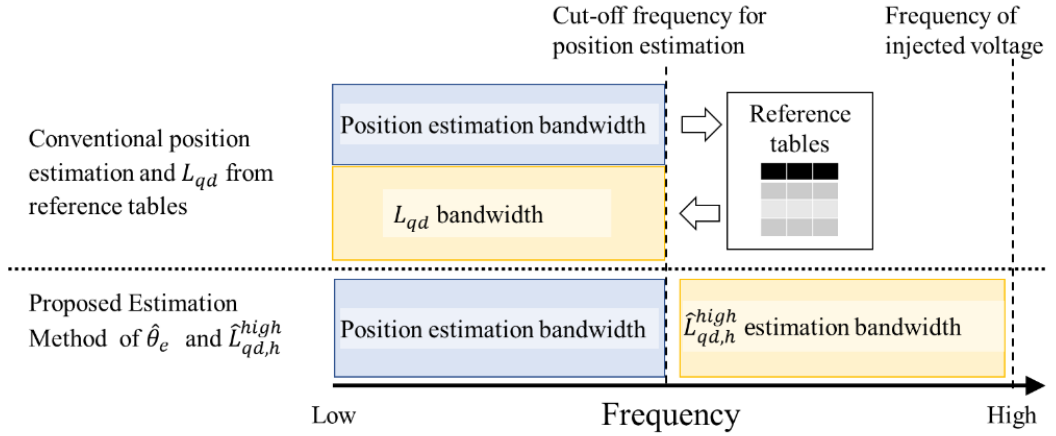
Fig. 5-10: Block diagram of the position and cross-coupling factors estimation

In addition, when the estimated position has errors or vibrations, the obtained cross-coupling factors also get errors. The conventional method with reference tables cannot completely compensate for those problems. On the other hand, the proposed method does not require reference tables and has inductance models in high-frequency bandwidth. Since values in high-frequency bandwidth can be utilized in the current control, the disturbances from the cross-coupling factors in high-frequency bandwidth can be reduced. Although the low-frequency errors cannot be reduced, the errors cannot be reduced to zero, even with the reference tables. Therefore, the proposed method is more practical because it can be used without prior analysis or experiments.

5.3   Proposed Current Control Considering Cross-Coupling Factors

This section explains the proposed current control method using the estimated position and cross-coupling factors.

General current controllers use the PI controller and the decoupling control described in Section 2.2. Although the control theory is based on fixed motor parameters, inductance varies with the rotor position and current, as shown in Fig. 5-1. High integral control gains can compensate for the modeling errors up to high bandwidth. However, position-sensorless control systems cannot have high integral control gains because of position estimation errors and vibrations. Therefore, the responsiveness and robustness of current control by PI control in position-sensorless systems are lower than those of systems with position sensors. The compensation for the cross-coupling factors can be included as shown in Fig. 5-11. The compensation value by the decoupling control can be expressed by eq. (5.43).

$$
\begin{bmatrix} v_d^{ff} \\ v_q^{ff} \end{bmatrix} = s\theta_e \begin{bmatrix} -i_q L_{q,n} \\ i_d L_{d,n} + \varPsi_n \end{bmatrix} + \begin{bmatrix} si_q L_{qd,h}^{high} \\ si_d L_{qd,h}^{high} \end{bmatrix} \tag{5.43}
$$

Although the vibrations from the cross-coupling factors in high-frequency bandwidth can be reduced, the disturbances, such as parameters fluctuation in the bandwidth around the electrical rotation and current control, are not compensated. In order to deal with the nonlinearity of motor parameters and position estimation errors, a nonlinear control structure is proposed. The proposed control method uses a sliding-mode current controller (SMC) and voltage disturbance observer (VDOB) based on the voltage equation considering the cross-coupling factors in the dq-axes inductance.

The state-space representation of the voltage equation can be expressed by equations from eq. (5.44) to eq. (5.49). The speed electromotive force terms are considered disturbances and included in $\boldsymbol{D_e}$.

$$
\dot{\boldsymbol{i}} = \boldsymbol{A_e}\left(i_d, i_q, \theta_e\right)\boldsymbol{i} + \boldsymbol{B_e}\left(i_d, i_q, \theta_e\right)\boldsymbol{v} + \boldsymbol{D_e} \tag{5.44}
$$

$$
\boldsymbol{i} = \begin{bmatrix} \int i_d dt & i_d & \int i_q dt & i_q \end{bmatrix}^{\mathrm{T}} \tag{5.45}
$$

$$
\boldsymbol{v} = \begin{bmatrix} v_d & v_q \end{bmatrix}^{\mathrm{T}} \tag{5.46}
$$

$$
\boldsymbol{A_e}\left(i_d, i_q, \theta_e\right) = \begin{bmatrix} 0 & 1 & 0 & 0 \\ 0 & -\dfrac{L_q\left(i_d, i_q, \theta_e\right)R}{\det\left(\boldsymbol{L}\left(i_d, i_q, \theta_e\right)\right)} & 0 & \dfrac{L_{qd}\left(i_d, i_q, \theta_e\right)R}{\det\left(\boldsymbol{L}\left(i_d, i_q, \theta_e\right)\right)} \\ 0 & 0 & 0 & 1 \\ 0 & \dfrac{L_{qd}\left(i_d, i_q, \theta_e\right)R}{\det\left(\boldsymbol{L}\left(i_d, i_q, \theta_e\right)\right)} & 0 & -\dfrac{L_d\left(i_d, i_q, \theta_e\right)R}{\det\left(\boldsymbol{L}\left(i_d, i_q, \theta_e\right)\right)} \end{bmatrix} \tag{5.47}
$$
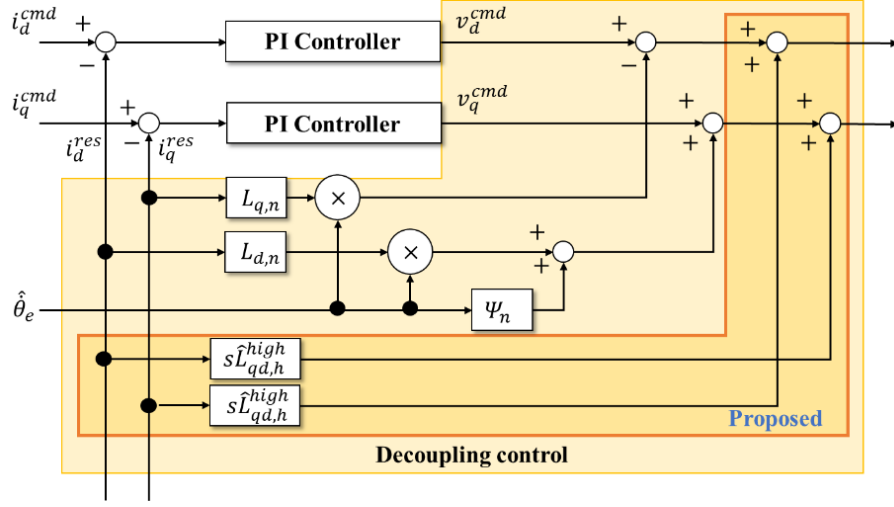
Fig. 5-11: Block diagram of the decoupling control with compensation for cross-coupling factors.

$$\boldsymbol{B_e}\left(i_d, i_q, \theta_e\right) = \begin{bmatrix} 0 & \dfrac{L_q\left(i_d, i_q, \theta_e\right)}{\det\left(\boldsymbol{L}\left(i_d, i_q, \theta_e\right)\right)} & 0 & -\dfrac{L_{qd}\left(i_d, i_q, \theta_e\right)}{\det\left(\boldsymbol{L}\left(i_d, i_q, \theta_e\right)\right)} \\ 0 & -\dfrac{L_{qd}\left(i_d, i_q, \theta_e\right)}{\det\left(\boldsymbol{L}\left(i_d, i_q, \theta_e\right)\right)} & 0 & \dfrac{L_d\left(i_d, i_q, \theta_e\right)}{\det\left(\boldsymbol{L}\left(i_d, i_q, \theta_e\right)\right)} \end{bmatrix}^{\mathrm{T}}$$

(5.48)

$$\boldsymbol{L}\left(i_d, i_q, \theta_e\right) = \begin{bmatrix} L_d\left(i_d, i_q, \theta_e\right) & L_{qd}\left(i_d, i_q, \theta_e\right) \\ L_{qd}\left(i_d, i_q, \theta_e\right) & L_q\left(i_d, i_q, \theta_e\right) \end{bmatrix}$$

(5.49)

As shown in Fig. 5-1, L_d and L_q are larger than the cross-coupling factors, $\det\left(\boldsymbol{L}\right)$ cannot be zero. The error between the current command and response is defined as eq. (5.50).

$$\boldsymbol{e} = \boldsymbol{i}^{res} - \boldsymbol{i}^{cmd}$$

(5.50)

The proposed SMC is expressed by equations from eq. (5.51) to eq. (5.58). Since the parameters fluctuation of R, L_d, and L_q are considered disturbances and included in $\boldsymbol{D_e}$, nominal parameters are used in $\boldsymbol{A}_{smc}^{high}$ and $\boldsymbol{B}_{smc}^{high}$. The matrices $\boldsymbol{A}_{smc}^{high}$ and $\boldsymbol{B}_{smc}^{high}$ have the estimated cross-coupling factors $\hat{L}_{qd,h}^{high}$. Gains for SMC are $\boldsymbol{p}$ and $\boldsymbol{K}$. The subscripts from $\bigcirc_{d1}$ to $\bigcirc_{q4}$ in $\boldsymbol{p}$ indicate the matrix element number to distinguish each other. The f is a saturation function to avoid the chattering from the signature function in the basic sliding mode control.

$$\boldsymbol{v}^{cmd}[k] = -\left(\boldsymbol{p}^{\mathrm{T}}\boldsymbol{B}_{smc}^{high}[k]\right)^{-1}\boldsymbol{p}^{\mathrm{T}}\boldsymbol{A}_{smc}^{high}[k]\boldsymbol{e}[k] - \left(\boldsymbol{p}^{\mathrm{T}}\boldsymbol{B}_{smc}^{high}[k]\right)^{-1}\boldsymbol{K}f\left(\boldsymbol{p}^{\mathrm{T}}\boldsymbol{e}[k]\right)$$

(5.51)

$$A_{smc}^{high}[k] = \begin{bmatrix} 0 & 1 & 0 & 0 \\ 0 & -\dfrac{L_{q,n}[k]R_n}{\det\left(\boldsymbol{L_n}[k]\right)} & 0 & \dfrac{\hat{L}_{qd,h}^{high}[k]R_n}{\det\left(\boldsymbol{L_n}[k]\right)} \\ 0 & 0 & 0 & 1 \\ 0 & \dfrac{\hat{L}_{qd,h}^{high}[k]R_n}{\det\left(\boldsymbol{L_n}[k]\right)} & 0 & -\dfrac{L_{d,n}[k]R_n}{\det\left(\boldsymbol{L_n}[k]\right)} \end{bmatrix} \tag{5.52}$$

$$B_{smc}^{high}[k] = \begin{bmatrix} 0 & \dfrac{L_{q,n}[k]}{\det\left(\boldsymbol{L_n}[k]\right)} & 0 & -\dfrac{\hat{L}_{qd,h}^{high}[k]}{\det\left(\boldsymbol{L_n}[k]\right)} \\ 0 & -\dfrac{\hat{L}_{qd,h}^{high}[k]}{\det\left(\boldsymbol{L_n}[k]\right)} & 0 & \dfrac{L_{d,n}[k]}{\det\left(\boldsymbol{L_n}[k]\right)} \end{bmatrix}^T \tag{5.53}$$

$$\boldsymbol{L_n^{high}}[k] = \begin{bmatrix} L_{d,n}[k] & \hat{L}_{qd,h}^{high}[k] \\ \hat{L}_{qd,h}^{high}[k] & L_{q,n}[k] \end{bmatrix} \tag{5.54}$$

$$\boldsymbol{p} = \begin{bmatrix} \boldsymbol{p_d} & \boldsymbol{p_q} \end{bmatrix} = \begin{bmatrix} p_{d1} & p_{d2} & p_{d3} & p_{d4} \\ p_{q1} & p_{q2} & p_{q3} & p_{q4} \end{bmatrix}^{\mathrm{T}} \tag{5.55}$$

$$\boldsymbol{K} = \begin{bmatrix} K_d & 0 \\ 0 & K_q \end{bmatrix} \tag{5.56}$$

$$f\left(\boldsymbol{p}^{\mathrm{T}}\boldsymbol{e}[k]\right) = \begin{bmatrix} \mathrm{sat}\left(\boldsymbol{p_d}^{\mathrm{T}}\boldsymbol{e}[k]\right) & \mathrm{sat}\left(\boldsymbol{p_q}^{\mathrm{T}}\boldsymbol{e}[k]\right) \end{bmatrix}^{\mathrm{T}} \tag{5.57}$$

$$\mathrm{sat}\left(x\right) = \begin{cases} 1 & (x > 1) \\ x & (-1 \le x \le 1) \\ -1 & (x < -1) \end{cases} \tag{5.58}$$

The voltage equation on the SMC can be expressed by eq. (5.59) from eq. (5.44) and eq. (5.51).

$$\begin{aligned} \dot{\boldsymbol{e}} &= \boldsymbol{A}_{smc}^{high}\boldsymbol{e} + \boldsymbol{B}_{smc}^{high}\boldsymbol{v}^{cmd} + \boldsymbol{D}_{smc}^{high} \\ &= \boldsymbol{D}_{smc}^{high} + \boldsymbol{p}^{-\mathrm{T}}\left(\boldsymbol{p}^{\mathrm{T}}\boldsymbol{A}_{smc}^{high}\boldsymbol{e} + \boldsymbol{p}^{\mathrm{T}}\boldsymbol{B}_{smc}^{high}\boldsymbol{v}^{cmd}\right) \\ &= \boldsymbol{D}_{smc}^{high} - \boldsymbol{p}^{-\mathrm{T}}\boldsymbol{K}f\left(\boldsymbol{p}^{\mathrm{T}}\boldsymbol{e}\right) \end{aligned} \tag{5.59}$$

In the sliding surface $\boldsymbol{S_{smc}}$, eq. (5.60) can be expressed. The integral terms are transformed to Laplace operator s.

$$\begin{aligned} \boldsymbol{S_{smc}}\left(\boldsymbol{e}\right) &= \boldsymbol{p}^{\mathbf{T}}\boldsymbol{e} \\ &= \begin{bmatrix} \frac{1}{s}p_{d1}e_d + p_{d2}e_d + \frac{1}{s}p_{d3}e_q + p_{d4}e_q \\ \frac{1}{s}p_{q1}e_d + p_{q2}e_d + \frac{1}{s}p_{q3}e_q + p_{q4}e_q \end{bmatrix} \\ &= 0 \end{aligned} \tag{5.60}$$

From eq. (5.60), eq. (5.61) can be derived.

$$
\left(\left((p_{d3}p_{q1} - p_{d1}p_{q3}) + (p_{d4}p_{q2} - p_{d2}p_{q4})\,s^2 \right.\right. \\
\left.\left. + (p_{d3}p_{q2} + p_{d4}p_{q1} - p_{d2}p_{q3} - p_{d1}p_{q4})\,s\right)\right)
\begin{bmatrix} e_d \\ e_q \end{bmatrix} = \mathbf{0}
\tag{5.61}
$$

The natural frequency ω_{smc} and the attenuation coefficient ζ_{smc} can be written as eq. (5.62) and eq. (5.63).

$$
\omega_{smc} = \sqrt{\frac{p_{d3}p_{q1} - p_{d1}p_{q3}}{p_{d4}p_{q2} - p_{d2}p_{q4}}}
\tag{5.62}
$$

$$
\zeta_{smc} = \frac{p_{d3}p_{q2} + p_{d4}p_{q1} - p_{d2}p_{q3} - p_{d1}p_{q4}}{2\omega_{smc}\,(p_{d4}p_{q2} - p_{d2}p_{q4})}
\tag{5.63}
$$

Gains in $\boldsymbol{p}$ can be designed to set desired ω_{smc} and ζ_{smc}.

When Lyapunov function $\boldsymbol{V_{smc}}$ is defined as eq. (5.64), the time derivative term of $\boldsymbol{V_{smc}}$ can be expressed by eq. (5.65).

$$
\boldsymbol{V_{smc}}\left(\boldsymbol{e}\right) = \frac{1}{2}\boldsymbol{S_{smc}}^{\mathrm{T}}\left(\boldsymbol{e}\right)\boldsymbol{S_{smc}}\left(\boldsymbol{e}\right)
\tag{5.64}
$$

$$
\begin{aligned}
\boldsymbol{\dot{V}_{smc}} &= \left(\frac{1}{2}\boldsymbol{\dot{S}}_{smc}^{T}\boldsymbol{S_{smc}} + \frac{1}{2}\boldsymbol{S}_{smc}^{T}\boldsymbol{\dot{S}_{smc}}\right) \\
&= \boldsymbol{S}_{smc}^{T}\frac{\partial \boldsymbol{S_{smc}}}{\partial \boldsymbol{e}}\boldsymbol{\dot{e}} \\
&= \boldsymbol{S}_{smc}^{T}\boldsymbol{p}^{\mathrm{T}}\left(\boldsymbol{A}_{smc}^{high}\boldsymbol{e} + \boldsymbol{B}_{smc}^{high}\boldsymbol{v}^{cmd} + \boldsymbol{D}_{smc}^{high}\right) \\
&= \boldsymbol{S}_{smc}^{T}\left(\boldsymbol{p}^{T}\boldsymbol{D}_{smc}^{high} - \boldsymbol{K}f\left(\boldsymbol{S_{smc}}\right)\right)
\end{aligned}
\tag{5.65}
$$

When K_d and K_q are enough larger than disturbances, $\boldsymbol{\dot{V}_{smc}}$ can be negative definite function. The system can be stable with large K_d and K_q by suppressing disturbances. However, too large gains cannot make the control systems stable in actual systems. Therefore, VDOB is also applied to the proposed current control. The electrical models of SMC and VDOB are the same.

VDOB modifies the voltage command calculated by SMC. VDOB compensates for the disturbances, including parameter variations. under the bandwidth of the cut-off frequency. The block diagram of the proposed VDOB is shown in Fig. 5-12. The differences from the disturbance observer shown in Fig. 3-2 are the estimated cross-coupling factors. When the model-based resistance compensation is applied to each voltage in the UVW-axes after the compensation by VDOB, VDOB can remove the resistance terms.
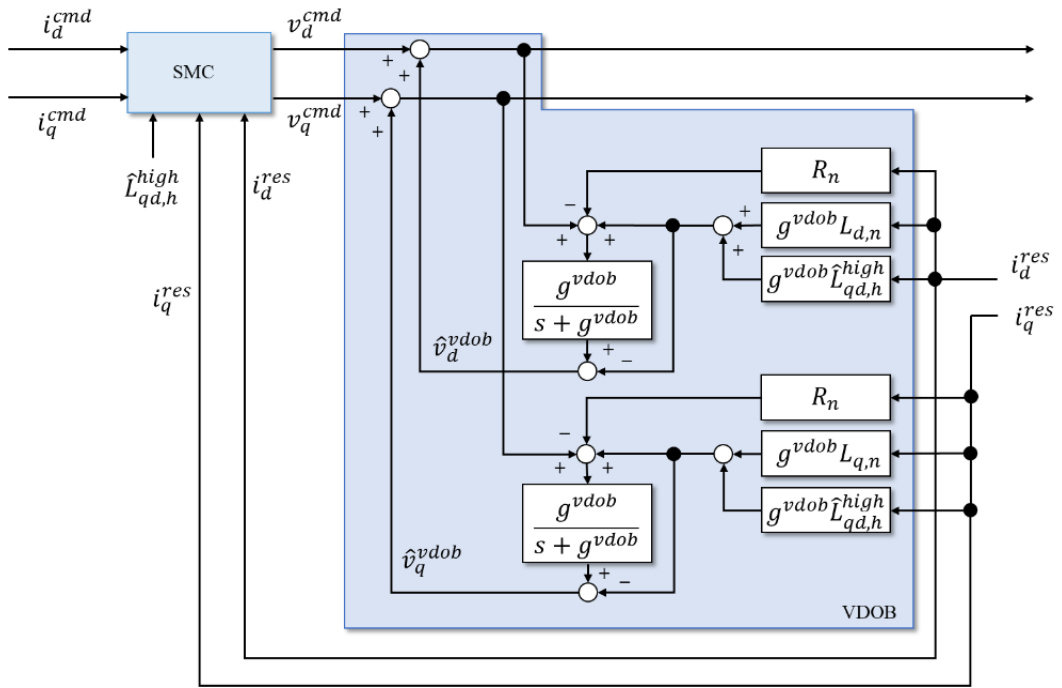
Fig. 5-12: Block diagram of proposed voltage disturbance observer with cross-coupling factors in the high-frequency bandwidth.

5.4   Experiments to Confirm the Validity of Considering Cross-Coupling Factors

This section shows the experimental results to confirm the methods in Section 5.2 and Section 5.3.

5.4.1   Setup and Parameters for Experiments to Confirm the Validity of the Cross-Coupling Factors

The responses from four control systems in Table 5.4 were compared. The decoupling control includes the compensation terms of cross-coupling factors, as shown in Fig. 5-11.

The block diagrams for the experiments are shown in Fig. 5-13 and Fig. 5-14. Fig. 5-13 was for "PI I" and "PI II." Fig. 5-14 was for "SMC I" and "SMC II." The LPF with the cut-off frequency g^{sen} removed the current variation and noises caused by the voltage injection. The bandwidth of the LPF with g^{sen} is enough higher than the current control bandwidth.

The experiments focused on estimation error, vibration during position control, and torque-velocity characteristics. The electric and mechanical angles units are expressed differently as "elec." and "mech.".

The experimental systems are shown in Fig. 5-15. These motors and controllers were made by YASKAWA Electric Corporation. The motors were SGM7J-04A7A61 and SGM7A-04AFA61. SGM7J-04A7A61 was the test motor, and SGM7A-04AFA61 was the load motor. Their shafts were connected by a coupling. Although each motor had position sensors, the information was for the actual response confirmation and the control of the load motor. The feedback position information in the test motor control was the estimated position. The current control systems, including position and cross-coupling factors estimation shown in the yellow parts in Fig. 5-13 and Fig. 5-14, were implemented on the functional test board. The motion controller MP3300 had the motion control function shown in the blue parts in Fig. 5-13 and Fig. 5-14. The motion controller MP3300 also collected the command and responses of the motors. The motion control was P-PI-type position control or PI-type velocity control. An LPF was applied to the torque reference, which is the output of the position or velocity controller. The oscilloscope collects the U-phase current data. The load motor was driven by the normal function of the servo amplifier and the motion controller MP3300. The test motor was driven by the control methods for the evaluation.

The Laplace operator "s" were implemented on the controller as a first-order backward difference to save memory and reduce processing time. The time derivative methods for the velocity depend on

Table 5.4: Main different points of confirmed four control methods.

Methods Name	Current Control	g_h(Cut-off frequency)	i_d^{cmd}
PI I	PI control and Decoupling Control	0.8 (424 Hz)	1 %
PI II	PI control and Decoupling Control	0.8 (424 Hz)	5 %
SMC I	SMC and VDOB	0	1%
SMC II (Proposed)	SMC and VDOB	0.5 (1698 Hz)	1 %
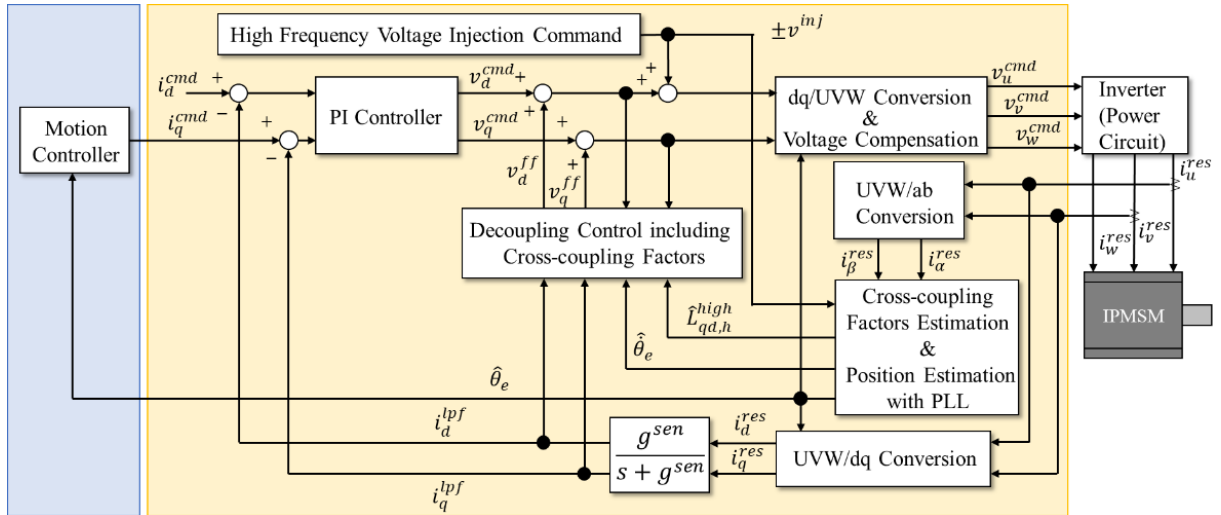
Fig. 5-13: Block diagram of the control system with PI current controller for experiments to confirm the validity of considering cross-coupling factors.

the controller. The velocity response of Fig. 5-13 was derived by a first-order backward difference of the estimated position in the motion controller since a PI-type phase-lock-loop (PLL) for the position estimation reduced the high-frequency noise. On the other hand, The velocity response of Fig. 5-14 was derived by a pseudo derivative of the estimated position in the motion controller. The pseudo derivative was implemented on the motion controller. Since the position estimation bandwidth setting of Fig. 5-14 was higher than that of Fig. 5-13, noise reduction was required.

The nominal parameters of the test motor are shown in Table 5.5. Control parameters, including sampling periods, are shown in Table 5.6 and Table 5.7
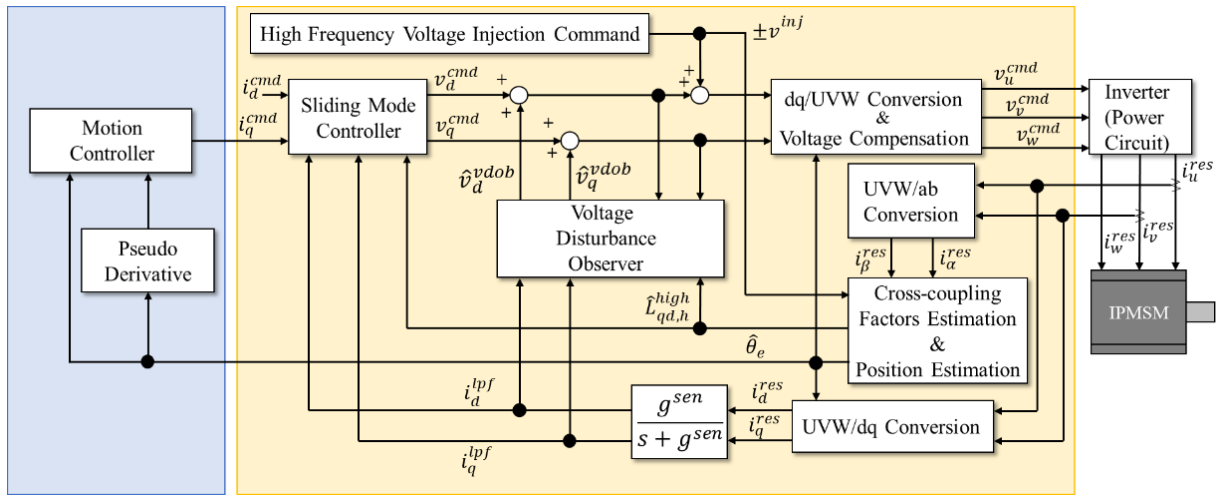
Fig. 5-14: Block diagram of the control system with SMC for experiments to confirm the validity of considering cross-coupling factors.
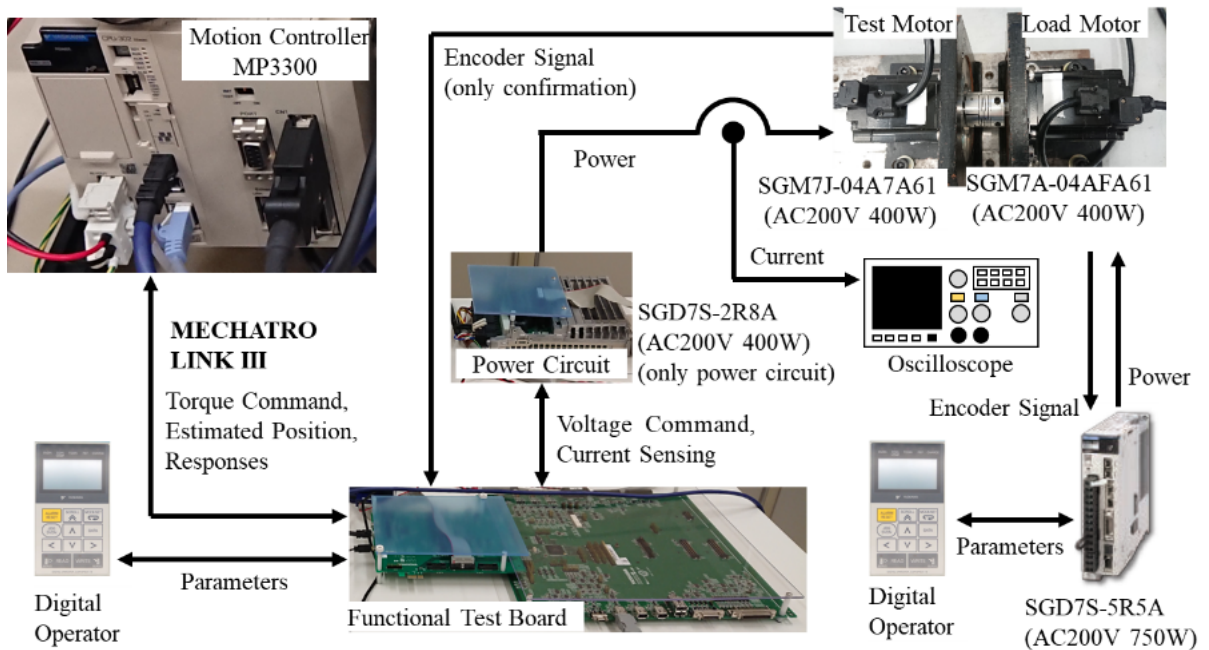
Fig. 5-15: System configuration for experiments to confirm the validity of considering cross-coupling factors.

The control parameters were adjusted by trial and error to prevent significant vibration in a steady state. The sampling periods of the motion control were adjusted to reduce vibration while checking the response. SMC Gains p were adjusted to make ω_{smc} and ζ_{smc} 133 Hz and 1, respectively. SMC Gains

Table 5.5: Nominal parameters of the test motor in experiments to confirm the validity of considering cross-coupling factors.

Parameter	Value
R (Ohm)	1.4
L_d (mH)	1.9
L_q (mH)	2.3
Torque constant (Nm/A)	0.544
Ψ (V/(elec. rad/s))	0.109
Rotor inertia (kgm^2)	0.486×10^{-4}
Viscosity friction coefficient (Nm/(rad/s) (Mechanical))	6.8×10^{-5}
Rated Power (W)	400
Rated velocity (mech. rad/s)	314.2
Rated torque (Nm)	1.27
Pole pairs	5

K_d and K_q were decided by trial and error from the small values. The bandwidth of the PI controller and the cut-off frequency of VDOB were adjusted to be similar, and values were larger than the electrical velocity in the low-speed operation, under 20 % rated speed (50 Hz). Although the motion control gains and a sampling period of "PI I" and "PI II" were lower than those of "SMC I" and "SMC II," the adjustment was based on the same policy to prevent significant vibration.

Table 5.6: Control parameters for "PI I" and "PI II".

Parameter	"PI I","PI II"
Sampling Period (Motion) (μs)	2000
Sampling Period (Current) (μs)	94
Position Proportional Gain (1/s)	2
Velocity Proportional Gain (rad/s)	32
Velocity Integral Gain (s)	0.02
Cut-off frequency of Torque Filter (rad/s)	250
Cut-off frequency of Pseudo differentiation (rad/s)	-
Gain in Position Estimation	0.8 (2666 rad/s)
d-axis Proportional Gain (H·rad/s)	1.91
d-axis Integral Gain (ms)	1.3
q-axis Proportional Gain (H·rad/s)	2.31
q-axis Integral Gain (ms)	1.6
Cut-off frequency g_{sen}(rad/s)	10667
PLL Cut-off frequency (rad/s)	144

Table 5.7: Control parameters for "SMC I" and "SMC II".

Parameter	"SMC I"	"SMC II"
Sampling Period (Motion) (μs)	125	125
Sampling Period (Current) (μs)	94	94
Position Proportional Gain (1/s)	32	32
Velocity Proportional Gain (rad/s)	94	94
Velocity Integral Gain (s)	0.003	0.003
Cut-off frequency of Torque Filter (rad/s)	250	250
Cut-off frequency of Pseudo differentiation (rad/s)	1600	1600
Gain in Position Estimation	0.0	0.5 (10667 rad/s)
SMC Gains $\boldsymbol{p^T}$	$\begin{bmatrix} 1333 & 1.4 & 27 & 0.0025 \\ 27 & 0.0025 & 1333 & 1.8 \end{bmatrix}$	
SMC Gains K_d,K_q	21	21
VDOB gain g^{vob} (rad/s)	1099	1099
Cut-off frequency g_{sen}(rad/s)	10667	10667

5.4.2   Results of Position Estimation Error

The error between the estimated and detected positions by the position sensors attached to the motors was compared. The data of the estimated and detected position were acquired at 4 elec. degrees each and 30 elec. degrees each. Position control was performed for 0.6 s at each angle. The sampling period of the data logging was 1 ms. The compared methods were "SMC I" and "SMC II" to reveal the difference from considering the cross-coupling factors. The mean values of estimation errors at each electrical angle are shown in Fig. 5-16. The variance of the estimation errors at each electrical angle is shown in Fig. 5-17. The red points are "SMC I" results, and the blue are "SMC II" results. As shown in Fig. 5-16 and Fig. 5-17, the maximum mean value of "SMC II" was larger than that of "SMC I," However, since the relationship between the magnitude of the error depends on the electric angle, it cannot be concluded that one was more valid than the other. On the other hand, the maximum variance value of "SMC II" was smaller than that of "SMC I." When the estimation error variance was large, the estimated position vibrated at the electrical angle. The fast Fourier transform (FFT) results of the estimated position at 60 elec. degree and 108 elec. degree are shown in Fig. 5-18 and Fig. 5-19, respectively. As shown in Fig. 5-18 and Fig. 5-19, the peak level of "SMC II" was smaller than that of "SMC I." The experimental results show that the position estimation considering cross-coupling factors into account reduced the vibration, although it cannot reduce the steady state estimation error, as shown in eq. (5.36).
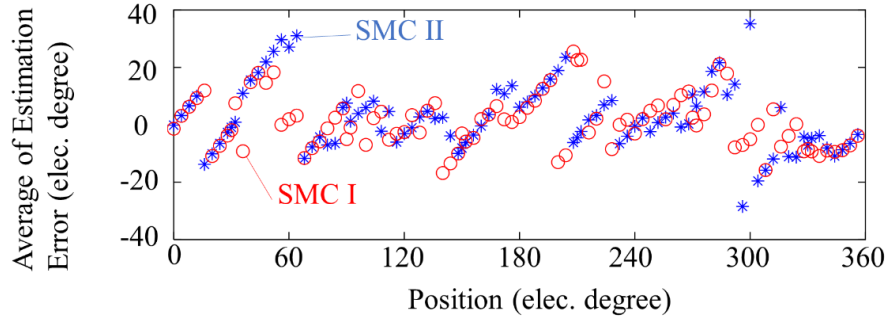
Fig. 5-16: The mean values of position estimation errors in experiments to confirm the validity of considering cross-coupling factors.
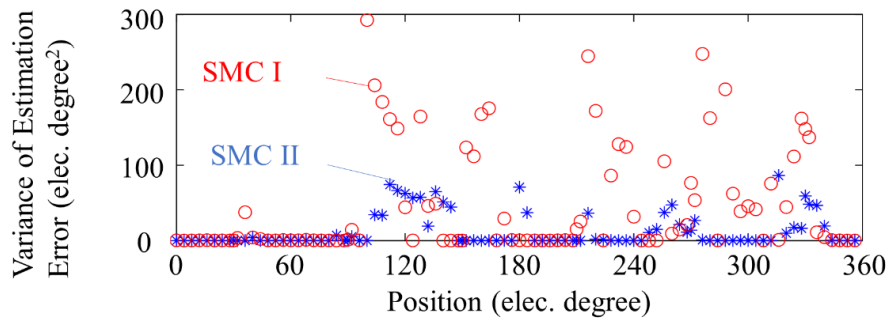
Fig. 5-17: The variance of position estimation errors in experiments to confirm the validity of considering cross-coupling factors.
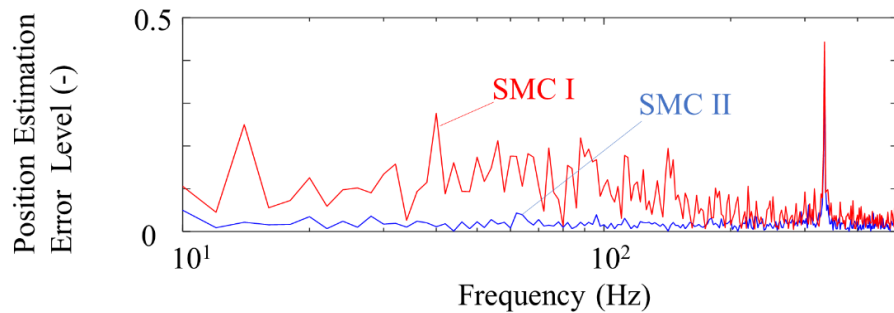
Fig. 5-18: FFT results of position estimation errors at 60 elec. degrees in experiments to confirm the validity of considering cross-coupling factors.
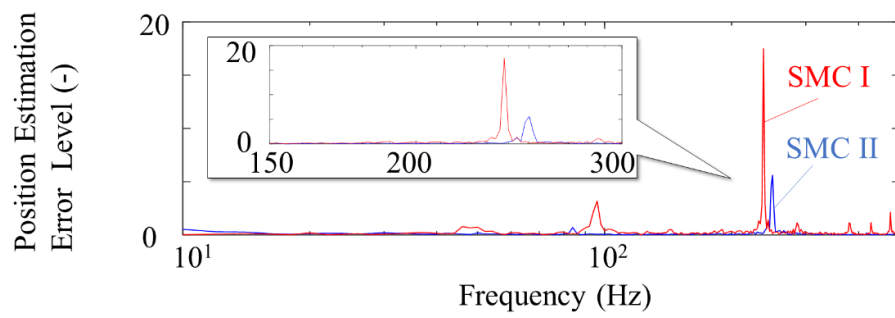
Fig. 5-19: FFT results of position estimation errors at 108 elec. degrees in experiments to confirm the validity of considering cross-coupling factors.

5.4.3   Results of Vibration during Position Control

The command tracking performance and the vibration during rotation were verified. The position command was increased in constant until the target position 25.1 mech. rad. The increased value was equivalent to 3.14 mech.rad/s, which is 1 % of the rated speed, and 2.5 Hz for the electrical rotation. The compared methods were "PI I," "SMC I," and "SMC II" to reveal the differences depending on the control methods and the proposed methods considering the cross-coupling factors. The experimental results are shown in figures from Fig. 5-20 to Fig. 5-23

Fig. 5-20 shows the position command and position responses. All position responses followed the command and achieved the target position.

Fig. 5-21 shows the velocity responses with a 2.5 Hz LPF applied. According to Fig. 5-21, the velocity responses of "SMC I" and "SMC II" quickly rose. The responses of "SMC I" and "SMC II"' were almost similar. However, the rising time of "PI I" was longer than those of "SMC I" and "SMC II" as "PI I" had lower motion control gains. The peaks of the vibration in the steady state velocity between 2.5 s and 8 s were similar for the three methods,

The differences in the vibration can be confirmed in Fig. 5-22 and Fig. 5-23. These figures show that the FFT results of the velocity response and the current response from 0.5 s to 2.5 s (2000 sampling points). In Fig. 5-22, the peak level of "PI I" were higher than those of "SMC I" and "SMC II" over 10Hz, which was over the control bandwidth of "PI I." The FFT results of "SMC I" and "SMC II" were similar under the velocity control bandwidth. In addition, the peak level of "SMC I" and "SMC II" were smaller than that of "PI I." Therefore, velocity control performance can be improved by SMC and VDOB. The peak level of "SMC I" was larger than that of "SMC II" around 220Hz, over the current control bandwidth. A similar difference over the current control bandwidth can be shown in Fig. 5-23. "SMC II" had the estimated cross-coupling factors in the controller. Therefore, current control performance can be improved by using the estimated cross-coupling factors.
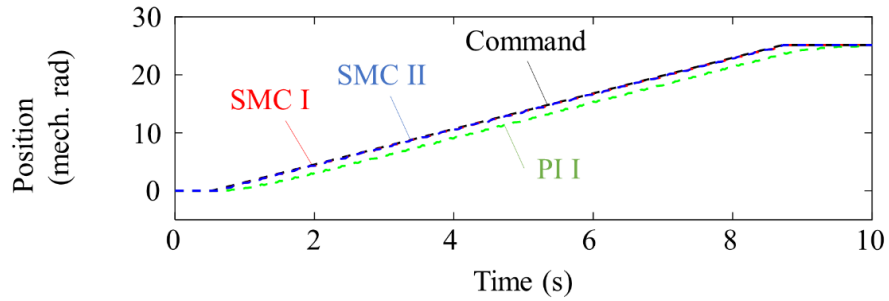
Fig. 5-20: Position command and response in experiments to confirm the validity of considering cross–coupling factors.
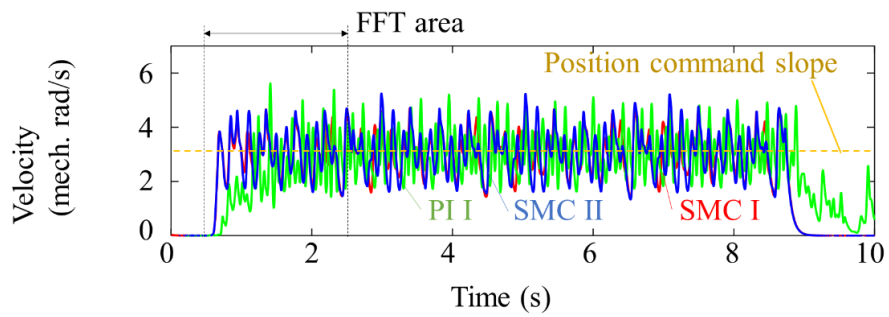
Fig. 5-21: Velocity response in experiments to confirm the validity of considering cross-coupling factors.
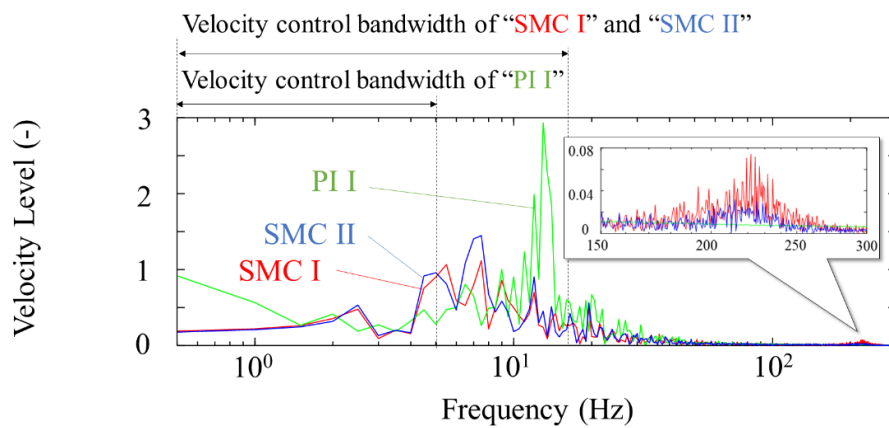
Fig. 5-22: FFT results of the velocity response in experiments to confirm the validity of considering cross-coupling factors.
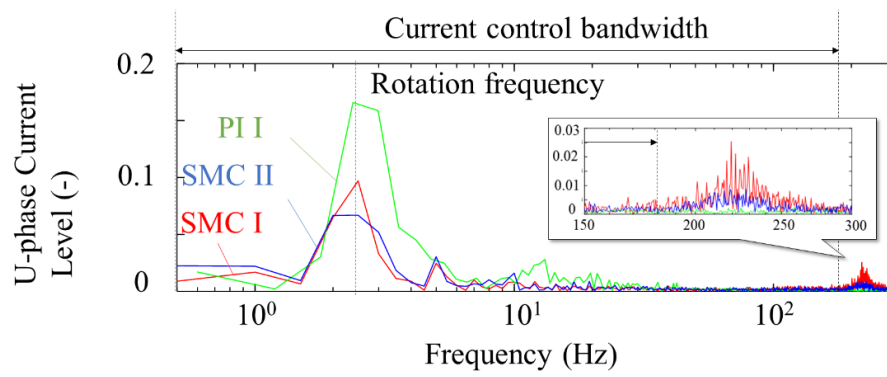
Fig. 5-23: FFT results of the U-axis current response in experiments to confirm the validity of considering cross-coupling factors.

5.4.4 Results of Torque-Velocity Characteristics

It was confirmed how much load torque the position-sensorless control system could operate without stalling for each velocity command. The velocity commands were shifted by 6.28 mech. rad/s up to 62.8 mech rad/s, which was 20 % of the rated speed. The load torque applied by the load motor was gradually increased for each velocity command. The maximum load torque was 1.27 Nm, which was 100 % of the rated torque. The operation in each velocity command was stopped when the load motor rotated the test motor or the error between the estimated and detected position was larger than 1 mech. rad. The load torque values, which were at the stop timing, were measured. When the test motor could rotate without stalling with the maximum load torque, the maximum load torque was recorded. The measured or recorded values are shown in Fig. 5-24. According to Fig. 5-24, "SMC II" could rotate at low-speed without stalling under the load torque of nearly 100 % of the rated torque.

In "PI I," the test motor did not start properly with the load motor. In "PI II," the test motor was out of control at low-speed under 31 mech. rad/s (10 % of the rated speed) with 0.2 Nm (15 % of the rated torque), and it was out of control at 63 mech. rad/s(20 % of the rated torque). However, it was possible to operate under a load torque of more than 1 Nm (90 % of the rated torque). Since the difference between the "PI I" and "PI II" were the d-axis current, one of the reasons for the "PI I" results was the disturbance caused by output voltage error at low current.

In "SMC I" and "SMC II," similar characteristics were confirmed. "SMC II" was more robust than "SMC I." "SMC II" was able to operate more than 15 mech. rad/s under the load torque more than 1 Nm.
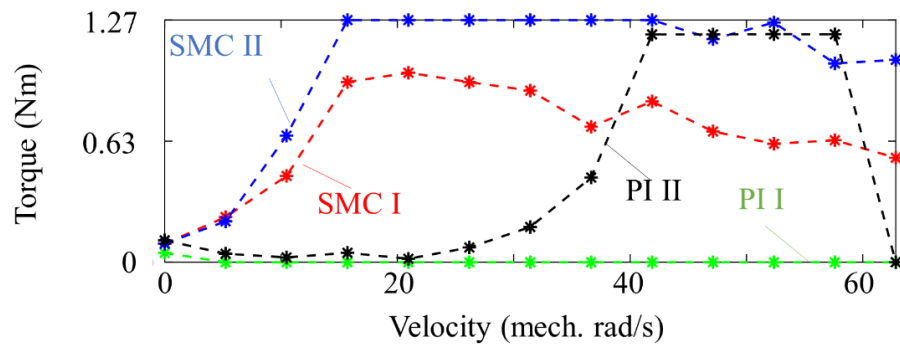
Fig. 5-24: Torque-velocity characteristics in experiments to confirm the validity of considering cross–coupling factors.

5.4.5 Discussion of the Experimental Results of Methods Considering Cross-Coupling Factors

"SMC II" had large mean values of estimated errors around 60 elec. degree and 300 elec. degree but smaller variance over a wide range of electrical angles in Fig. 5-16 and Fig. 5-17. The maximum value of the variance was less than one-third. Since the variance in "SMC I" exceeded 100 elec. degree^2, the instantaneous estimation error can be more than 10 elec. degree higher than the mean values. As shown in Fig. 5-18 and Fig. 5-19, the frequency of position estimation vibration was over 10 Hz, which was higher than the motion control bandwidth. The peak frequency was around 220 Hz, which was higher than the current control bandwidth. The vibration was a disturbance for the controller, and the sensitivity function effect cannot be ignored. Therefore, less variance in the estimated positions over a wide range of electrical angles is desired to allow a more stable operation. The estimated positions in "SMC II" had smaller estimation error variances and vibration by applying the model of the cross-coupling factors in the estimation algorithm. In addition, "SMC II" had the LPF function, as shown in eq. (5.36). As Table 5.7 shows, the cut-off frequency was 1698 Hz, which was much higher than that of generally used PLL. Therefore, the estimated positions in "SMC II" are more reliable than the conventional estimated position because there is small variability and phase delay from the filter.

According to Fig. 5-22 and Fig. 5-23, the levels were large around 220 Hz. Since the cut-off frequency of VDOB was 1099 rad/s (175 Hz), it was related to the sensitivity function of VDOB. When the controller had no model on dq-axes cross-coupling factors, the cross-coupling effects from the other axis were all disturbance for the controller. In "SMC II", SMC and VDOB had the estimated cross-coupling factors, and the cross-coupling effects were compensated in the controller. On the other hand, "SMC I" did not have the cross-coupling factors and the cross-coupling effects were disturbances. As a result, "SMC I" got larger vibration than "SMC II".

The higher robustness of "SMC II" shown in Fig. 5-24 came from the above two advantages. Although the effects of the position estimation errors in the low-frequency bandwidth remained, the robustness to the mechanical external force has been improved because it is not necessary to compensate for the variance of the estimated position and the cross-coupling effects between the current control axes during rotation as disturbances. All experimental results show the control performance of "PI I" and "PI II" were worse than that of "SMC I" and "SMC II." The integral gain cannot be high because of uncertainty in the PI controller. Low-gain PI controllers cannot adequately compensate for the effects of estimation

error and model uncertainty. By using SMC, the uncertainty is compensated by the robustness of the controller. Therefore, the current controller with SMC and VDOB considering cross-coupling factors is suitable for position-sensorless servo drive systems.

These experimental results suggest that the problems to be solved were the steady state position estimation errors and the stalling by the load torque at zero-speed operation. Since the estimation error relates to the cross-coupling factors, the cross-coupling factors estimation in low-frequency bandwidth is required. In addition, an output torque compensation is also required.

5.5 Proposed Estimation Error Compensation and Wide-Bandwidth Cross-Coupling Factors Estimation

This section explains the proposed estimation of the cross-coupling factors in the low-frequency bandwidth, the position estimation error compensation, and the output torque compensation. In addition, the estimation of the cross-coupling factors in the wide-frequency bandwidth is also explained.

The current variation on the dq-axes by the injected voltage can be expressed by eq. (5.66).

$$
\begin{bmatrix} \dot{i}_{d,h} \\ \dot{i}_{q,h} \end{bmatrix} \approx \frac{\pm v^{inj}}{\det\left(\boldsymbol{L_h}\left(i_d, i_q, \theta_e\right)\right)} \begin{bmatrix} L_{q,h}\left(i_d, i_q, \theta_e\right) & -L_{qd,h}\left(i_d, i_q, \theta_e\right) \\ -L_{qd,h}\left(i_d, i_q, \theta_e\right) & L_{d,h}\left(i_d, i_q, \theta_e\right) \end{bmatrix} \begin{bmatrix} \cos\theta_e^{err} \\ \sin\theta_e^{err} \end{bmatrix} \tag{5.66}
$$

The relation among the estimation errors, cross-coupling factors, and current is derived by eq. (5.67).

$$
\tan\theta_e^{err} \approx \frac{L_{qd,h}\left(i_d, i_q, \theta_e\right)\dot{i}_{d,h} + L_{q,h}\left(i_d, i_q, \theta_e\right)\dot{i}_{q,h}}{L_{d,h}\left(i_d, i_q, \theta_e\right)\dot{i}_{d,h} + L_{qd,h}\left(i_d, i_q, \theta_e\right)\dot{i}_{q,h}} \tag{5.67}
$$

The approximation sign is considered an equal sign. From the additive theorem of tangent shown in eq. (5.68), eq. (5.69) can be derived from eq. (5.27) and eq. (5.67).

$$
\tan 2\theta_e^{err} = \frac{2\tan\theta_e^{err}}{1 - \tan^2\theta_e^{err}} \tag{5.68}
$$

$$
\frac{2L_{qd,h}\left(i_d, i_q, \theta_e\right)}{L_{d,h}\left(i_d, i_q, \theta_e\right) - L_{q,h}\left(i_d, i_q, \theta_e\right)} = \frac{2\dfrac{L_{qd,h}\left(i_d, i_q, \theta_e\right)\dot{i}_{d,h} + L_{q,h}\left(i_d, i_q, \theta_e\right)\dot{i}_{q,h}}{L_{d,h}\left(i_d, i_q, \theta_e\right)\dot{i}_{d,h} + L_{qd,h}\left(i_d, i_q, \theta_e\right)\dot{i}_{q,h}}}{1 - \left(\dfrac{L_{qd,h}\left(i_d, i_q, \theta_e\right)\dot{i}_{d,h} + L_{q,h}\left(i_d, i_q, \theta_e\right)\dot{i}_{q,h}}{L_{d,h}\left(i_d, i_q, \theta_e\right)\dot{i}_{d,h} + L_{qd,h}\left(i_d, i_q, \theta_e\right)\dot{i}_{q,h}}\right)^2} \tag{5.69}
$$

Therefore, eq. (5.70) can be obtained by the transformation of eq. (5.69).

$$
\det\left(\boldsymbol{L_h}\left(i_d, i_q, \theta_e\right)\right)\left(L_{qd,h}\left(i_d, i_q, \theta_e\right)\left(\left(\dot{i}_{d,h}\right)^2 - \left(\dot{i}_{q,h}\right)^2\right)\right)
$$
$$
+ \left(L_{q,h}\left(i_d, i_q, \theta_e\right) - L_{d,h}\left(i_d, i_q, \theta_e\right)\right)\left(\dot{i}_{d,h}\right)\left(\dot{i}_{q,h}\right)\right) = 0 \tag{5.70}
$$

Since the determinant of $\boldsymbol{L_h}$ is not zero, the cross-coupling factors can be derived by eq. (5.71).

$$
\begin{aligned}
L_{qd,h}\left(i_d, i_q, \theta_e\right) &= \frac{\left(L_{d,h}\left(i_d, i_q, \theta_e\right) - L_{q,h}\left(i_d, i_q, \theta_e\right)\right)\left(\dot{i}_{d,h}\right)\left(\dot{i}_{q,h}\right)}{\left(\dot{i}_{d,h}\right)^2 - \left(\dot{i}_{q,h}\right)^2} \\
&= \frac{\left(L_{d,h}\left(i_d, i_q, \theta_e\right) - L_{q,h}\left(i_d, i_q, \theta_e\right)\right)}{1 - \left(\dfrac{\left(\dot{i}_{q,h}\right)}{\left(\dot{i}_{d,h}\right)}\right)^2} \cdot \frac{\left(\dot{i}_{q,h}\right)}{\left(\dot{i}_{d,h}\right)}
\end{aligned} \tag{5.71}
$$

In discrete-time systems, the dq-axes current values are obtained after the position and cross-coupling factors estimation processing. The latest dq-axes current responses in the cross-coupling factors estimation at timing k are values at timing $k - 1$. The estimated cross-coupling factors can be expressed by eq. (5.72)

$$\hat{L}_{qd,h}[k] = \frac{(L_{d,n}[k] - L_{q,n}[k])}{1 - \left(\dfrac{\Delta i_q[k-1]}{\Delta i_d[k-1]}\right)^2} \cdot \frac{\Delta i_q[k-1]}{\Delta i_d[k-1]} \tag{5.72}$$

When the high-frequency voltage is approximated as being injected on the actual d-axis, an assumption $\theta_e^{err} \approx 0$ can be assumed, and eq. (5.66) can be rewritten as eq. (5.73).

$$\begin{bmatrix} \dot{i}_{d,h} \\ \dot{i}_{q,h} \end{bmatrix} = \frac{\pm v^{inj}}{\det\left(\boldsymbol{L_h}\left(i_d, i_q, \theta_e\right)\right)} \begin{bmatrix} L_{q,h}\left(i_d, i_q, \theta_e\right) \\ -L_{qd,h}\left(i_d, i_q, \theta_e\right) \end{bmatrix} \tag{5.73}$$

The cross-coupling factors can be approximately derived by eq. (5.74).

$$L_{qd,h}\left(i_d, i_q, \theta_e\right) \approx -L_{q,h}\left(i_d, i_q, \theta_e\right) \frac{\left(\dot{i}_{q,h}\right)}{\left(\dot{i}_{d,h}\right)} \tag{5.74}$$

The estimated cross-coupling factors can be expressed by eq. (5.75).

$$\hat{L}_{qd,h}[k] = -L_{q,n}[k] \frac{\Delta i_{q,h}[k-1]}{\Delta i_{d,h}[k-1]} \tag{5.75}$$

Since the injected voltage is on the estimated d-axis, $\Delta i_{d,h}$ is sufficiently larger than $\Delta i_{q,h}$ and the square of the current ratio in eq. (5.72) can be approximated as 1. The main difference is the coefficient of the current ratio, $L_{dh,n}[k] - L_{qh,n}[k]$ and $-L_{qh,n}[k]$. Although actual L_d and L_q vary during operation, fixed values are often used in control processing. Therefore, the accuracy of the cross-coupling factors estimation depends on the utilized values of inductance. Furthermore, the detected current also has errors. Since these effects can be adjusted by a gain, both eq. (5.72) and eq. (5.75) with a gain can be utilized for the cross-coupling factors estimation in a low-frequency bandwidth. From the viewpoint of the processing time, the processing time for eq. (5.75) is shorter than that of eq. (5.72). Therefore, the estimation of eq. (5.75) is adopted in this dissertation.

Since the detected current has noise, the cross-coupling factors $\hat{L}_{qd,h}^{low}$ in the low-frequency bandwidth are estimated by eq. (5.76) by applying a 1st-order LPF with a cut-off frequency g^{low}. The variable t_{st} denotes the sampling period of the estimation.

$$\hat{L}_{qd,h}^{low}[k] = \frac{1}{1 + g^{low}t_{st}}\left(g^{low}t_{st}\left(-\frac{\Delta i_{q,h}[k-1]}{\Delta i_{d,h}[k-1]}L_{q,n}[k]\right) + \hat{L}_{qd,h}^{low}[k-1]\right) \tag{5.76}$$

The position estimation error in the low-frequency bandwidth is estimated by eq. (5.77). The gain g^{comp} adjusts the effect of the assumption $\theta_e^{err} \approx 0$ to use eq. (5.73).

$$\hat{\theta}_e^{err}[k] = \frac{1}{2} g^{comp} \tan^{-1}\left(\frac{2\hat{L}_{qd,h}^{low}[k]}{L_{d,n}[k] - L_{q,n}[k]} \right) \tag{5.77}$$

The estimated position with the error compensation can be derived by eq. (5.78).

$$\begin{aligned}
\hat{\theta}_e^{comp}[k] &= \hat{\theta}_e[k] - \hat{\theta}_e^{err}[k] \\
&= \hat{\theta}_e[k] - \frac{1}{2} g^{comp} \tan^{-1}\left(\frac{2\hat{L}_{qd,h}^{low}[k]}{L_{d,n}[k] - L_{q,n}[k]} \right)
\end{aligned} \tag{5.78}$$

Furthermore, the wide-bandwidth cross-coupling factors can be estimated by eq. (5.79). The gain g_L adjust the effect of the assumption $\theta_e^{err} \approx 0$ to use eq. (5.73).

$$L_{qd,h}^{wide}[k] = g_L L_{qd,h}^{low}[k] + L_{qd,h}^{high}[k] \tag{5.79}$$

The block diagram of the whole estimation algorithm is shown in Fig. 5-25.

The conversion between the torque reference and the current command is modified. The position estimation method utilizes high-frequency voltage injection on the d-axis. The injected voltage has the same amplitude and alternates between positive and negative values. The mean value of the d-axis current in the low-frequency bandwidth can be considered zero. Therefore, the reluctance torque can be considered zero when the d-axis current command is zero. According to eq. (5.12), the output torque has a term $-L_{qd}\left(i_d^2 - i_q^2\right)$. Since the amplitude of the injected voltage is large to extract the current variation, i_d^2 by the injected voltage cannot be ignored. The relationship between torque and current can be expressed by eq. (5.80).

$$i_q = \frac{\tau}{P_{olep}\,\Psi \cos\theta_e^{err}} - \frac{L_{qd}}{\Psi}\left(i_d^2 - i_q^2\right) \tag{5.80}$$

Although the proposed estimation method can estimate the position estimation error $\hat{\theta}_e^{err}$, the accuracy and the vibrations are not suitable to compensate for the magnet torque components in the torque reference in the viewpoint of the bandwidth. Therefore, the proposed conversion between torque reference and current command is derived as eq. (5.81).

$$i_q^{cmd,comp}[k] = \frac{\tau^{cmd}[k]}{P_{olep}\Psi_n} - \frac{g_L \hat{L}_{qd,h}^{low}[k]}{\Psi_n}\left(i_d^{res^2}[k] - i_q^{res^2}[k]\right) \tag{5.81}$$

The utilized estimated cross-coupling factors are not $\hat{L}_{qd,h}^{wide}[k]$ but $\hat{L}_{qd,h}^{low}[k]$. Since an LPF with cut-off frequency g_{tf} is applied to the torque reference to reduce the noise of the current command, the
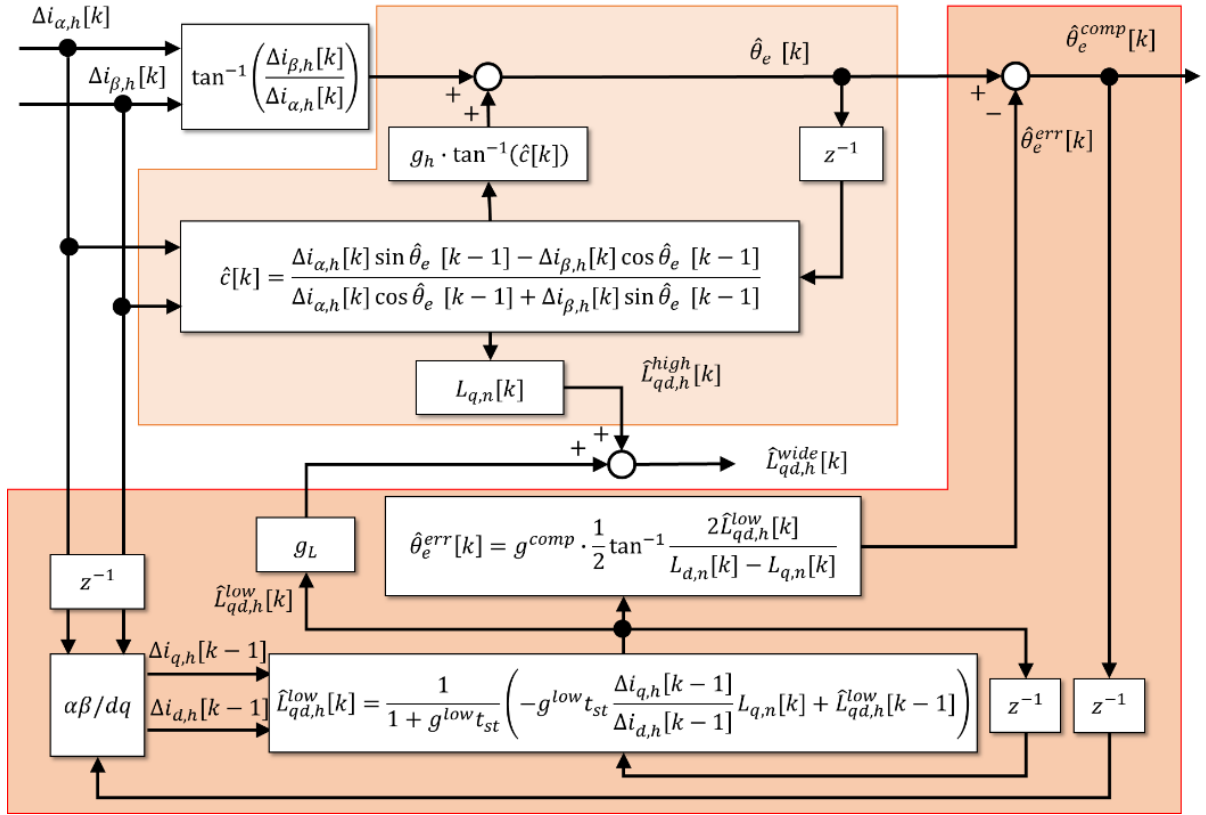
Fig. 5-25: Block diagram of the position and cross-coupling factors estimation with compensation in low-frequency bandwidth.
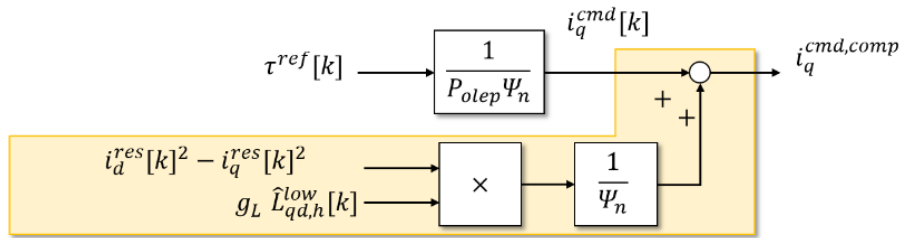
Fig. 5-26: Conversion from the torque command to the current command.

compensation terms without the detected values should have only low-frequency components. The block diagram of the conversion can be expressed as Fig. 5-26. More complex calculations are required when the reluctance torque is utilized for maximum torque-per-ampere (MTPA) control or field-weakening control. However, the main topic of this dissertation is considering the effect of the cross-coupling factors, those calculations are future work.

5.6 Proposed Current Control using Estimated Cross-Coupling Factors in Wide-Frequency Bandwidth

This section explains the proposed current control method using the estimated position and cross-coupling factors in wide-frequency bandwidth.

The base of the proposed current controller is described in Section 5.3. The proposed SMC is expressed by equations from eq. (5.82) to eq. (5.89). The utilized cross-coupling factors are changed from $\hat{L}_{qd,h}^{high}$ to $\hat{L}_{qd,h}^{wide}$. Other terms are the same as equations in Section 5.3.

$$\boldsymbol{v}^{cmd}[k] = -\left(\boldsymbol{p}^{\mathrm{T}}\boldsymbol{B}_{smc}^{wide}[k]\right)^{-1}\boldsymbol{p}^{\mathrm{T}}\boldsymbol{A}_{smc}^{wide}[k]\boldsymbol{e}[k] - \left(\boldsymbol{p}^{\mathrm{T}}\boldsymbol{B}_{smc}^{wide}[k]\right)^{-1}\boldsymbol{K}f\left(\boldsymbol{p}^{\mathrm{T}}\boldsymbol{e}[k]\right) \tag{5.82}$$

$$\boldsymbol{A}_{smc}^{wide}[k] = \begin{bmatrix} 0 & 1 & 0 & 0 \\ 0 & -\dfrac{L_{q,n}[k]R_n}{\det\left(\boldsymbol{L_n}[k]\right)} & 0 & \dfrac{\hat{L}_{qd,h}^{wide}[k]R_n}{\det\left(\boldsymbol{L_n}[k]\right)} \\ 0 & 0 & 0 & 1 \\ 0 & \dfrac{\hat{L}_{qd,h}^{wide}[k]R_n}{\det\left(\boldsymbol{L_n}[k]\right)} & 0 & -\dfrac{L_{d,n}[k]R_n}{\det\left(\boldsymbol{L_n}[k]\right)} \end{bmatrix} \tag{5.83}$$

$$\boldsymbol{B}_{smc}^{wide}[k] = \begin{bmatrix} 0 & \dfrac{L_{q,n}[k]}{\det\left(\boldsymbol{L_n}[k]\right)} & 0 & -\dfrac{\hat{L}_{qd,h}^{wide}[k]}{\det\left(\boldsymbol{L_n}[k]\right)} \\ 0 & -\dfrac{\hat{L}_{qd,h}^{wide}[k]}{\det\left(\boldsymbol{L_n}[k]\right)} & 0 & \dfrac{L_{d,n}[k]}{\det\left(\boldsymbol{L_n}[k]\right)} \end{bmatrix}^{\mathrm{T}} \tag{5.84}$$

$$\boldsymbol{L_n}[k] = \begin{bmatrix} L_{d,n}[k] & \hat{L}_{qd,h}^{wide}[k] \\ \hat{L}_{qd,h}^{wide}[k] & L_{q,n}[k] \end{bmatrix} \tag{5.85}$$

$$\boldsymbol{p} = \begin{bmatrix} \boldsymbol{p_d} & \boldsymbol{p_q} \end{bmatrix} = \begin{bmatrix} p_{d1} & p_{d2} & p_{d3} & p_{d4} \\ p_{q1} & p_{q2} & p_{q3} & p_{q4} \end{bmatrix}^{\mathrm{T}} \tag{5.86}$$

$$\boldsymbol{K} = \begin{bmatrix} K_d & 0 \\ 0 & K_q \end{bmatrix} \tag{5.87}$$

$$f\left(\boldsymbol{p}^{\mathrm{T}}\boldsymbol{e}[k]\right) = \begin{bmatrix} \mathrm{sat}\left(\boldsymbol{p_d^T}\boldsymbol{e}[k]\right) & \mathrm{sat}\left(\boldsymbol{p_q^T}\boldsymbol{e}[k]\right) \end{bmatrix}^{\mathrm{T}} \tag{5.88}$$

$$\text{sat}\,(x) = \left\{ \begin{array}{ll} 1 & (x > 1) \\ x & (-1 \leq x \leq 1) \\ -1 & (x < -1) \end{array} \right. \tag{5.89}$$

The discussion on the sliding surface and the responsiveness are the same as in Section 5.3.

VDOB can also use $\hat{L}_{qd,h}^{wide}$. The block diagram of the proposed current control is shown in Fig. 5-27.

The position-sensorless control system using all proposed methods is expressed as the block diagram shown in Fig. 5-28.

The estimation and compensation bandwidth can be expressed as Fig. 5-29
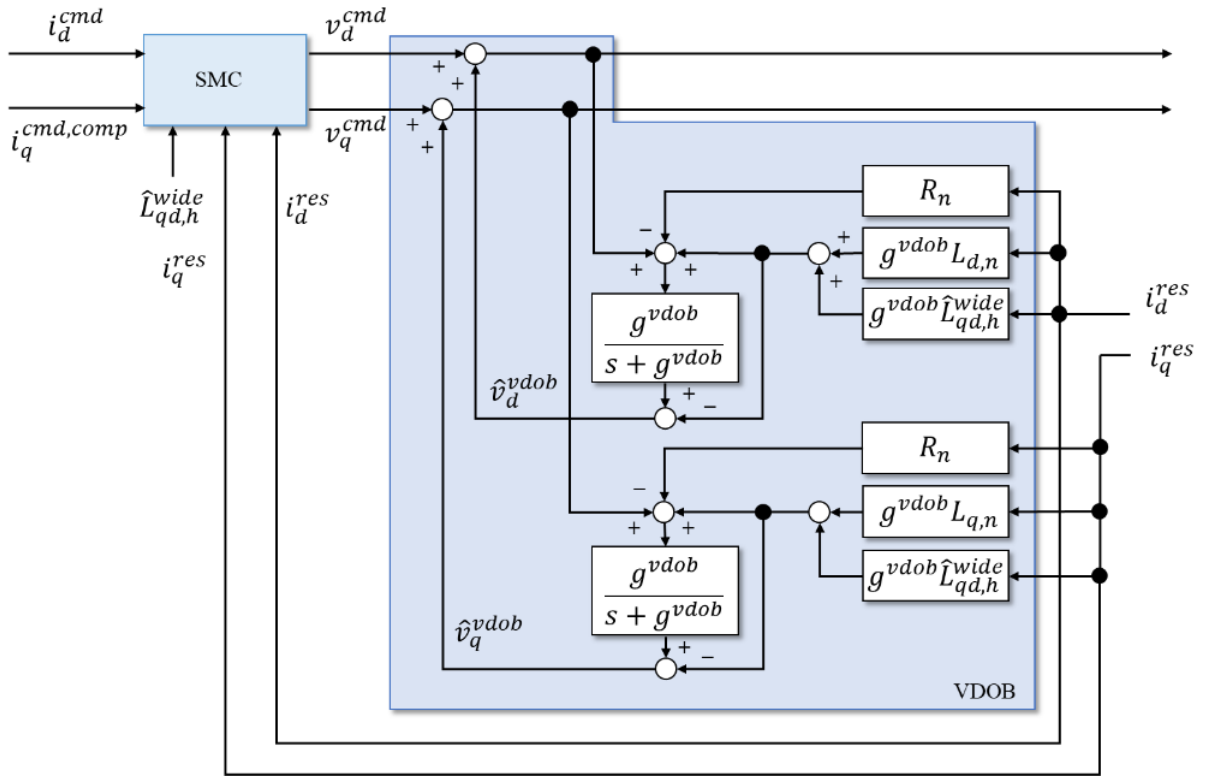
Fig. 5-27: Block diagram of proposed voltage disturbance observer.
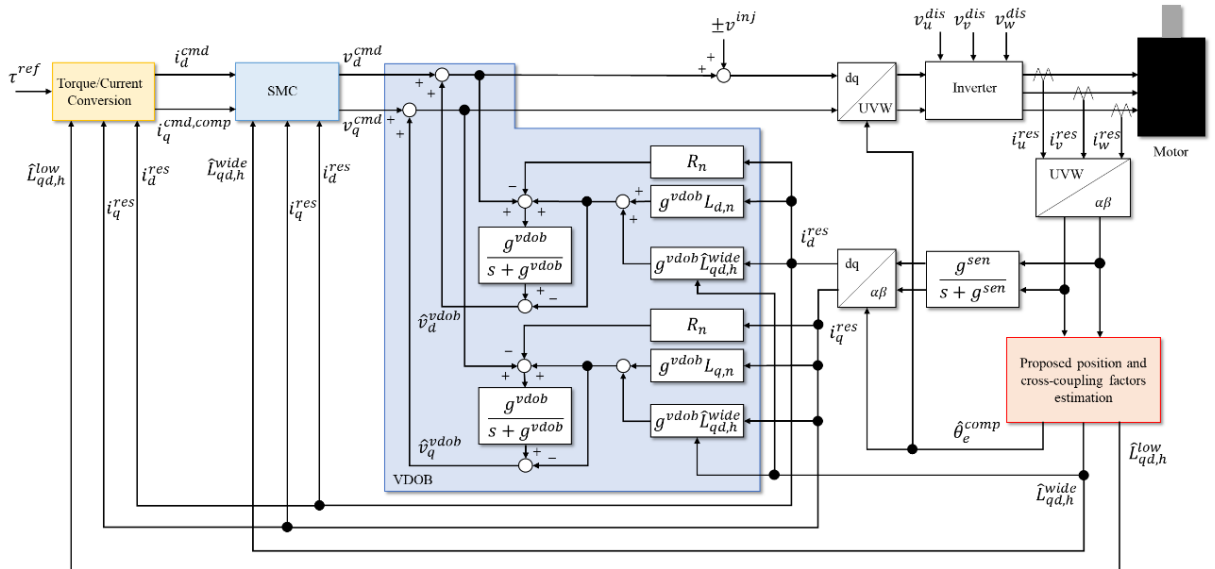
Fig. 5-28: Proposed position-sensorless current control.

Fig. 5-29: The estimation and compensation bandwidth.

5.7 Experiments to Confirm the Validity of using the Estimated Cross-Coupling Factors in Wide-Frequency Bandwidth

This section explains experimental results to confirm the validity of the proposed position-sensorless control system with cross-coupling factors estimation in wide-frequency bandwidth.

5.7.1 Setup and Parameters for Experiments to Confirm the Validity of the Compensation in Low-frequency Bandwidth.

The responses from the three control systems in Table 5.8 were compared to evaluate the position estimation error, the vibration during rotation, and the torque-velocity characteristics. The block diagrams for the experiments are shown in Fig. 5-30 and Fig. 5-31. Fig. 5-30 was for "Base" and "High." Fig. 5-31 was for "Prop."

The experimental systems are shown in Fig. 5-32. The system configuration was almost similar to that described in Section 5.4. The different point is the connection between the motion controller and the servo amplifier for the load motor. The responses of the test motor and the load motor can be obtained synchronously.

The nominal parameters of the test motor are shown in Table 5.9 Control parameters, including sampling periods, are shown in Table 5.10. The compensation bandwidth in low-frequency was under 30 Hz since g_{lqd} was 188 rad/s. Gains for current control were higher than those shown in Table 5.7. The gains are set as high as possible based on the same policy to prevent significant vibration with experiments in Section 5.4. Since the experimental results are not compared with the results of the method using PI control, there is no need to align the bandwidth with PI control. Therefore, the gains were higher than those of experiments in Section 5.4.
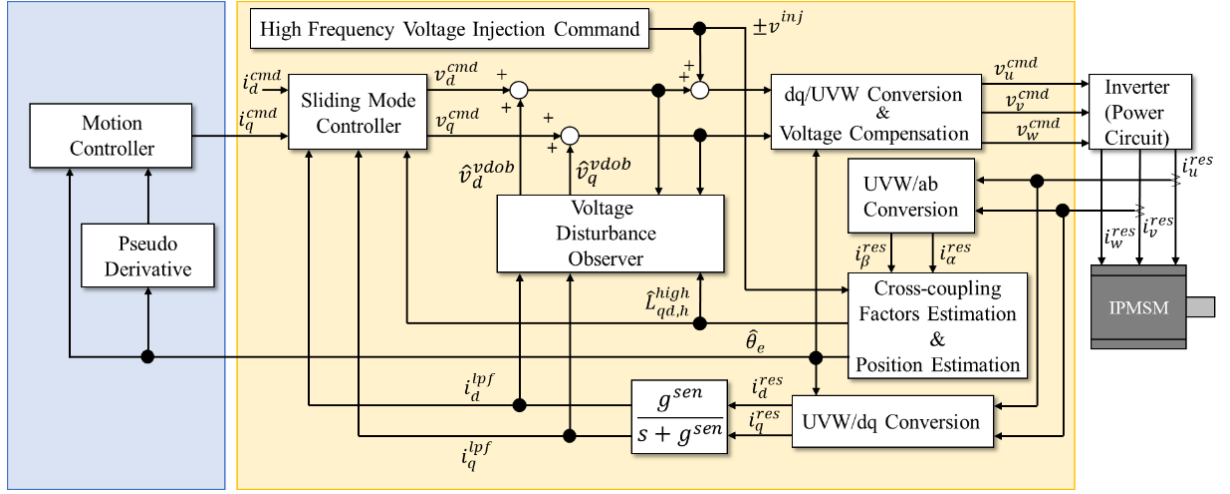
Fig. 5-30: Block diagram of the position-sensorless control system without compensation in low-frequency bandwidth.
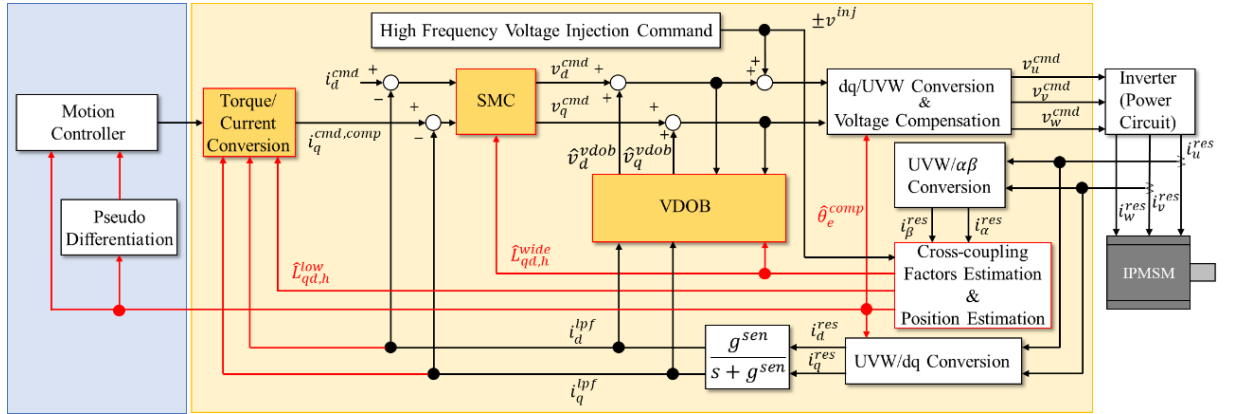
Fig. 5-31: Block diagram of the position-sensorless control system with compensation in low-frequency bandwidth.

Table 5.8: Relationship between indexes and experimental conditions.

Index of Condition	Estimated Position	Estimated Cross-Coupling Factors	Compensation of Current Command
Base	$\hat{\theta}_e \, (g_h = 0)$	-	-
High	$\hat{\theta}_e \, (g_h = 0.5)$	$\hat{L}_{qd,h}^{high}$	-
Prop	$\hat{\theta}_e \, (g_h = 0, 5)$	$\hat{L}_{qd,h}^{wide}, \hat{L}_{qd,h}^{high}, \hat{L}_{qd,h}^{low}$	Utilized
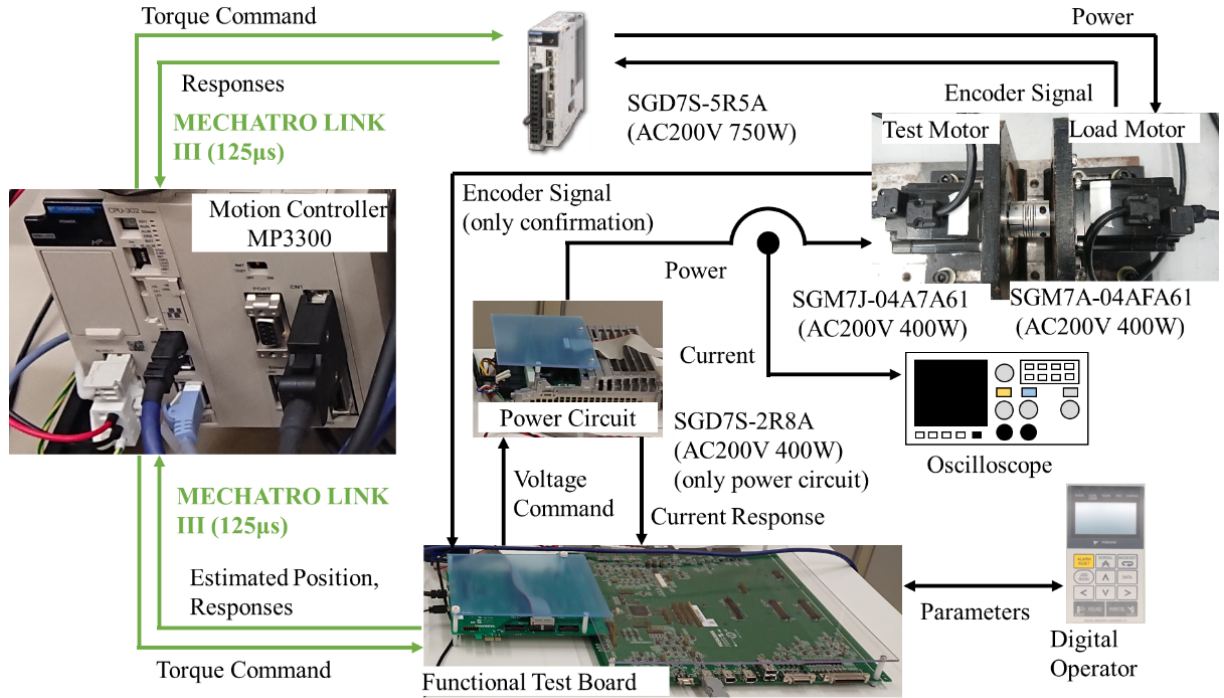
Fig. 5-32: System configuration for experiments to confirm the validity of the compensation in low-frequency bandwidth.

Table 5.9: Nominal parameters of the test motor in experiments to confirm the validity of the compensation in low-frequency bandwidth.

Parameter	Value	Parameter	Value
R (Ohm)	1.4	Rated Power (W)	400
L_d (mH)	2.6	Rated velocity (mech. rad/s)	314.2
L_q (mH)	3.1	Rated torque (Nm)	1.27
Torque constant (Nm/Arms)	0.544	Pole pairs	5
Rotor inertia (gm^2)	0.0486		

Table 5.10: Control parameters for experiments to confirm the validity of the compensation in low-frequency bandwidth.

Parameter	"Base"	"High"	"Prop"
Sampling Period (Motion) (μs)		125	
Sampling Period (Current) (μs)		94	
Position Proportional Gain (1/s)		48	
Velocity Proportional Gain (rad/s)		192	
Velocity Integral Gain (s)		0.0156	
SMC Gains $\boldsymbol{p^T}$ for the hyperplane	$\begin{bmatrix} 91 & 0.07 & 1 & 1.6 \times 10^{-5} \\ 1 & 1.6 \times 10^{-5} & 91 & 0.07 \end{bmatrix}$		
SMC Gains K_d, K_q		50	
VDOB gain g^{vob} (rad/s)		1099	
Cut-off frequency of Torque Filter (rad/s)		250	
Cut-off frequency of Pseudo differentiation (rad/s)		127	
Cut-off frequency g_{sen} of LPF for current (rad/s)		10667	
Gain g_h to derive $\hat{\theta}_e$	0	0.5	0.5
Gain g_L with $\hat{L}_{dq}^{low}$ in $\hat{L}_{dq}^{wide}$	0	0	0.25
Gain g^{comp} in $\hat{\theta}_e^{err}$	0	0	0.025
Cut-off frequency g_{lqd} of LPF for $\hat{L}_{dq}^{low}$ (rad/s)	0	0	188

5.7.2 Results of Position Estimation Accuracy

The detected position by the position sensor and the estimated position were compared to confirm the estimation accuracy. The data of the estimated and detected position were acquired at 4 elec. degrees each and 30 elec. degrees each. The sampling period was 1 ms. Position control was performed for 0.6 s at each angle. The mean values of the estimation errors are shown in Fig. 5-33. The green points are "Base" results, the red points are "High" results, and the blue points are "Prop" results. The root mean square (RMS) and variance of the estimation error in one round of the electric angle are shown in Table 5.11. As shown in Fig. 5-33, the position estimation error was not reduced to zero, even with the proposed compensation method. However, the RMS shows the position estimation error reduction by the proposed method. In addition, the variance also decreased. These results indicate the proposed method can achieve rotation with less vibration. Therefore, the proposed method improved the position estimation accuracy.
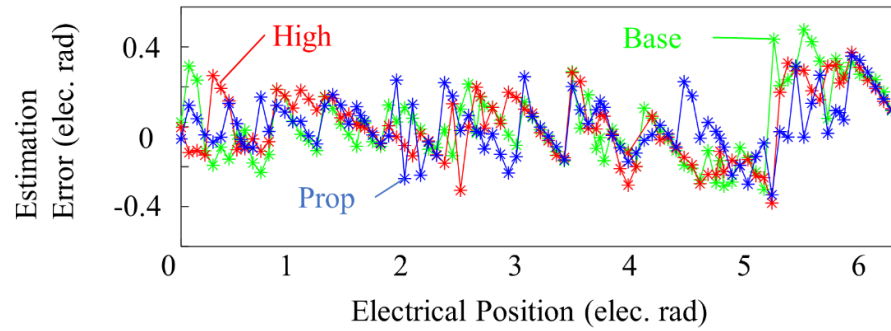
Fig. 5-33: The mean values of position estimation errors in experiments to confirm the validity of the compensation in low-frequency bandwidth.

Table 5.11: RMS and variance of estimation error in a rotation.

Item	Base	High	Prop
RMS (elec. rad)	0.18	0.17	0.14
Variance (elec. rad^2)	0.032	0.030	0.019

5.7.3   Results of Vibration during Position Control

The command tracking performance and the vibration during position control were verified. The position command was increased in constant until the target position was 25.1 mech. rad. The increased value was equivalent to 3.14 mech.rad/s, which was 1 % of the rated speed and 2.5 Hz for the electrical angle rotation. The experimental results are shown in figures from Fig. 5-34 to Fig. 5-40

Fig. 5-34 shows that the responses by the three methods followed the position command, and the steady state errors were in the assumed estimation error range from the results in Table 5.11. No characteristic difference cannot be seen in Fig. 5-34.

Fig. 5-35 shows the velocity responses with a 2.5 Hz LPF applied. According to Fig. 5-35, the transient velocity responses were similar, and the vibration of the "Prop" was smallest between 0.5 s and 8 s. The FFT results of the velocity between 0.5 s and 2.5 s are shown in Fig. 5-36. The FFT results also show the vibration by "Prop" was the smallest in the compared methods. In particular, the peaks at 7.5 Hz, 12.5 Hz, and 15 Hz were reduced.

Fig. 5-37 and Fig. 5-38 show the estimated cross-coupling factors. Fig. 5-37 shows the time-series values, and Fig. 5-38 shows the values per electrical angle. According to Fig. 5-37 and Fig. 5-38, the proposed wide-bandwidth cross-coupling factors estimation could obtain the variance of the cross-coupling factors. The FFT results of the estimated cross-coupling factors between 0.5 s and 2.5 s are shown in Fig. 5-39. The peak values are 7.5 Hz and 15 Hz, which were 3 and 6 times the rotational frequency, respectively.

The FFT results of the U phase current between 0.5 s and 2.5 s are shown in Fig. 5-40. The results of "Prop" had a larger peak at the rotation frequency than the others. In addition, the peaks at 12.5 Hz and 15 Hz were reduced by "Prop". Therefore, the suitable current could be applied to the IPMSMs by "Prop." These results expressed the performance of the position-sensorless control was improved by the proposed methods.
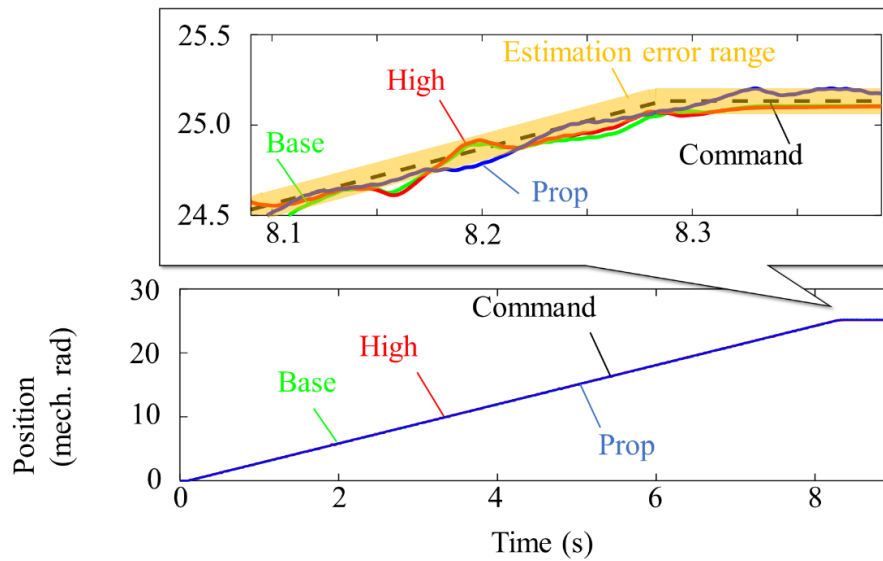
Fig. 5-34: Position command and response in experiments to confirm the validity of the compensation in low-frequency bandwidth.
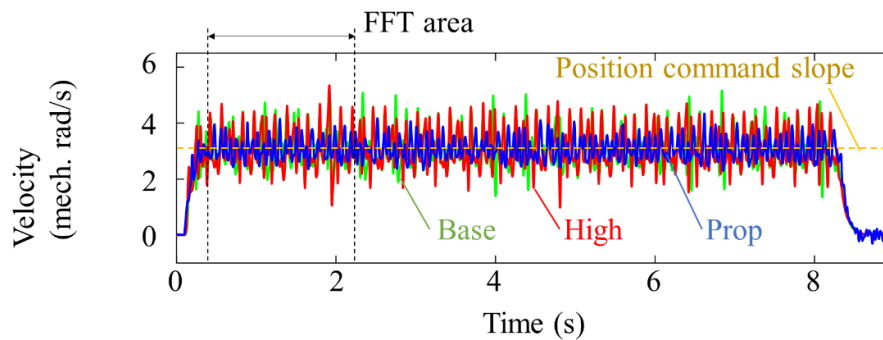
Fig. 5-35: Velocity response in experiments to confirm the validity of the compensation in low-frequency bandwidth.
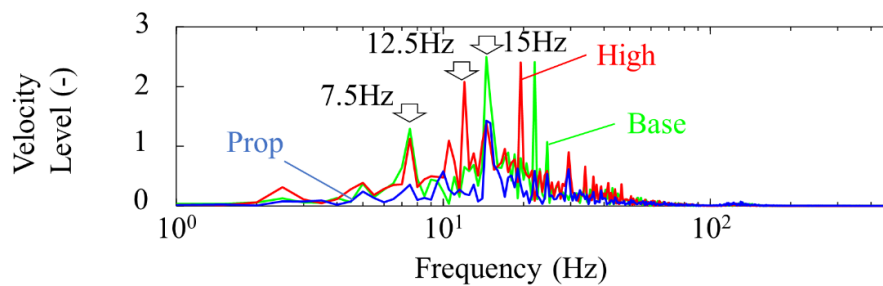
Fig. 5-36: FFT results of the velocity response in experiments to confirm the validity of the compensation in low-frequency bandwidth.
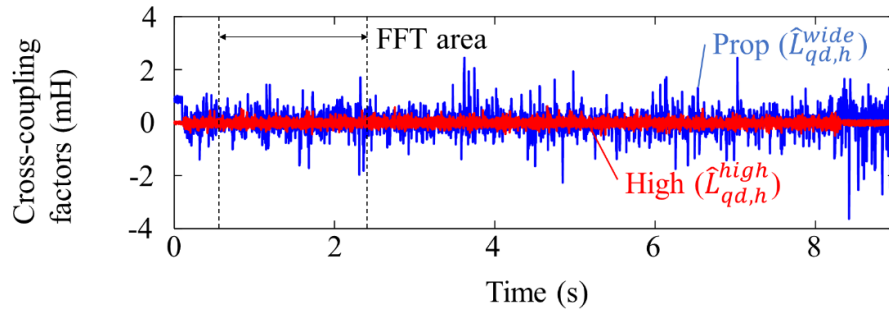
Fig. 5-37: Time series estimated cross-coupling factors in experiments to confirm the validity of the compensation in low-frequency bandwidth.
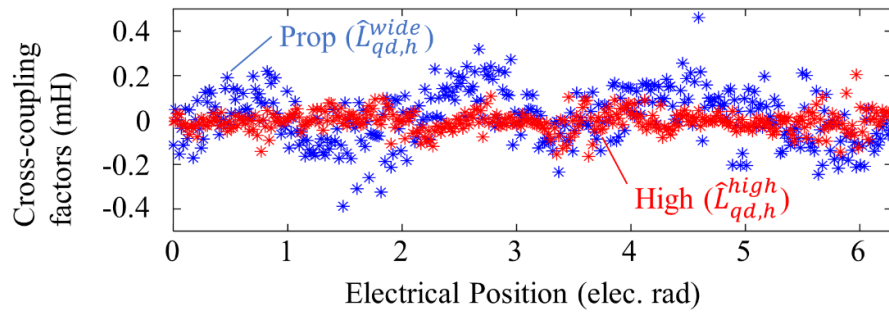
Fig. 5-38: Estimated cross-coupling factors per electrical angle in experiments to confirm the validity of the compensation in low-frequency bandwidth.
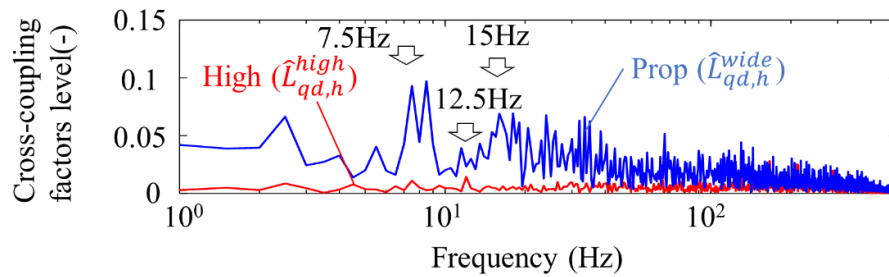
Fig. 5-39: FFT results of the estimated cross-coupling factors in experiments to confirm the validity of the compensation in low-frequency bandwidth.
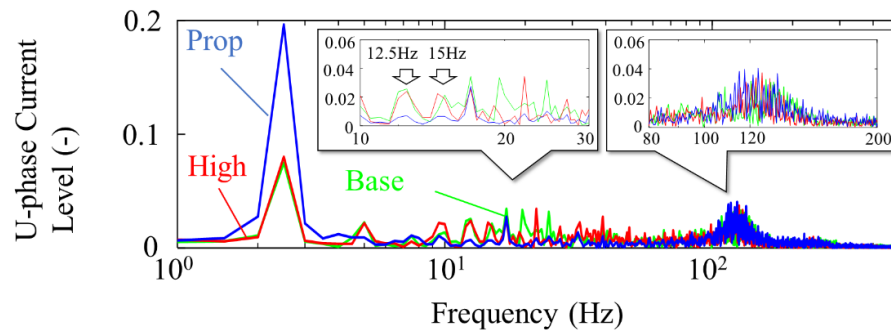
Fig. 5-40: FFT results of the U-axis current response in experiments to confirm the validity of the compensation in low-frequency bandwidth.

5.7.4 Results of Torque-Velocity Characteristics

The torque-velocity characteristics were compared to confirm how much load torque the position-sensorless control system could operate without stalling for each velocity command. The load torque was increased from 0 % to 100 % of the rated torque in 6.25 s for each velocity command of the test motor. The velocity commands were shifted by 6.28 mech. rad/s from 0 to 62.8 mech. rad/s. The maximum load torque was 1.27 Nm, which was 100 % of the rated torque. The operation in each velocity command was stopped when the load motor rotated the test motor or the error between the estimated and detected position was larger than 1 mech. rad. The load torque values, which were at the stop timing, were measured. When the test motor could rotate without stalling with the maximum load torque, the maximum load torque was recorded. The measured or recorded load torque values were shown in Fig. 5-41. All systems could operate without stalling over 20 mech. rad/s with over 75 % rated load torque. The main difference was at zero speed. Only the proposed control system could operate without stalling at zero speed even at 100 % rated load torque. Therefore, the compensation using estimated cross-coupling factors improved the robustness at low-speed operation, including positioning.
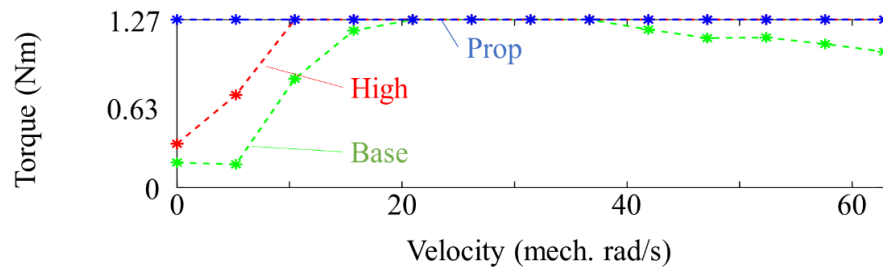
Fig. 5-41: Torque-velocity characteristics in experiments to confirm the validity of the compensation in low-frequency bandwidth.

5.7.5   Discussion of the Experimental Results with Estimated Cross-Coupling Factors in Wide-Frequency Bandwidth

The problems of the method described in Section 5.2 were the steady state position estimation errors and the stalling by the load torque at zero-speed operation according to the experimental results. Since "Prop" did not stall at zero-speed operation, the robustness was improved by the proposed compensation methods. However, the steady-state position estimation errors could not be zero. According to RMS values in Table 5.11, the RMS of the estimation errors by the proposed method was reduced from 0.18 to 0.14 elec. rad. According to Fig. 5-33, the maximum estimation error by the proposed method was over 0.3 elec. rad. The simulation results in Fig. 5-7, Fig. 5-8, and Table 5.3 showed the results of "$0.25 \times L_{qd}$" and "$0.125 \times L_{qd}$" were desired responses. The simulation results showed the maximum estimation error should be smaller than 0.06 elec. rad (3.4 elec. degree) for MDOF position-sensorless control systems. The possible causes of errors are gains g_L and g^{comp}, output voltage error, modeling error of the current, current sensor noise, and current sensor resolution.

Gains g_L and g^{comp} changes the estimated values. However, the variation frequency per electrical rotation frequency cannot be changed by gains. In addition, the analyses show the appropriate values of g_L. Although the range of the assumed values of g^{comp} is wide, the value was adjusted by trial and error in the experimental system. Therefore, there were other reasons the proposed method could not reduce the estimation errors to zero.

The output voltage is affected by dead time in PWM and the characteristics of power semiconductors in the UVW phase. The output voltage error cause the unexpected current in the dq-axes. Since the method uses high-frequency voltage synchronized with the carrier period, it is highly sensitive to disturbances at each carrier period. The disturbances may cause errors in the position and cross-coupling factors estimation. One of the solutions to decrease the errors is that the frequency of the injected voltage is lower than the carrier frequency to equalize the disturbances to the high-frequency current. Since a trade-off exists between injected voltage frequency and estimated bandwidth, the injected voltage frequency cannot be lowered to maintain a high estimation bandwidth. Therefore, using power semiconductors that can switch faster and inverters that can set higher carrier frequencies will improve the estimation performance. However, it can only be applied to specific inverter and motor combinations because there is a suitable carrier period depending on the motor characteristics. Furthermore, the switching loss may be the problem of the systems.

The modeling error of the current is from the coordinate transformation from the UVW-axes to the dq-axes and the nominal parameters. Since the current responses are derived by the transformation using $\hat{\theta}_e^{comp}$, the utilized current responses are not the dq-axes current responses but the $\hat{\mathrm{d}}\hat{\mathrm{q}}$-axes current responses. The current controller in the $\hat{\mathrm{d}}\hat{\mathrm{q}}$-axes or a new control axis considering the oblique coordinate will be required for the estimation performance improvement. In addition, $L_{d,n}$ and $L_{q,n}$ were the fixed parameters in experiments. According to the FEA results shown in Fig. 5-1, L_d and L_q vary with position and current. A position-sensorless system, which can acquire those variations, the estimation performance will be improved Future work focuses on methods to solve this point.

Current sensor noise and current sensor resolution cause errors in the dq-axes responses. However, the equipment used in these experiments was designed and adjusted as a product. Therefore, the effect on the estimation errors was considered small.

The estimated values per electrical angle in Fig. 5-38 differed from the FEA results shown in Fig. 5-1. The analytical results showed a variation in the frequency of 6 times the rotation of the electrical angle, while the estimated results with an actual motor showed a different variation. The reasons for the difference are the simplified motor model for the FEA and the same reasons for the position estimation error.

In Fig. 5-40, the results of "Prop" had a larger peak at the rotation frequency than the others and smaller peaks at other frequencies. While other methods used torque generated by currents with components different from the rotational frequency to rotate, the "Prop" could rotate the motor by currents corresponding to the rotational frequency. Since unintended current harmonics lead to energy loss, the proposed method cannot only improve robustness but also contribute to highly efficient drives.

According to the gains in Table 5.10, the compensation bandwidth was under 30 Hz, and the estimation bandwidth of cross-coupling factors in high-frequency bandwidth was over 1.7 kHz. When the cross-coupling factors vary with the frequency of 6 times the rotation of the electrical angle, as shown in FEA result, the compensation in low-frequency bandwidth worked until 5 Hz of the electrical angle rotation. Since the compensation corresponded to zero-speed motion, the proposed method improved the torque-velocity characteristics at zero speed. However, position estimation methods based on magnetic saliency are generally used from the zero-speed to around 10 Hz of the electrical rotational frequency. Therefore, the expansion of the compensation bandwidth is expected, and it will be achieved by the assumed improvement methods described above. Since the high-frequency cross-coupling factors' variation relates to estimation frequency, the estimation bandwidth of cross-coupling factors in high-frequency

bandwidth was enough.

The robustness of the disturbance was improved by the proposed method. However, the results of the torque-velocity characteristics were on the disturbances in the steady state. The effects of the disturbance variation were not confirmed. Load torque in each joint torque of robots varies with the motion and tasks. Therefore, the confirmation of the robustness of the disturbance variation is also future work. Motor temperatures also change during prolonged operation. As temperature varies, resistance and magnetic characteristics vary. The effect of resistance variation on position estimation is small, as shown in Fig. 2-10. However, the variation in magnetic characteristics affects the accuracy of position estimation. The proposed method corresponds to the dynamic variation of the cross-coupling factors. Therefore, a part of the effects can be compensated by the proposed methods by using nominal inductance values of L_d and L_q in the application environments. However, the validity is not quantitatively confirmed. These issues in actual operation also need to be evaluated in future work.

5.8   Summary

This chapter presented a position-sensorless control system considering cross-coupling factors of dq-axes inductance. The voltage equation considering the cross-coupling factors was introduced. The position and cross-coupling factors estimation based on the high-frequency voltage injection on the d-axis was proposed. The $\alpha\beta$-axes current responses were utilized to estimate position and cross-coupling factors in high-frequency bandwidth. The vibration reduction and the improvement of the robustness by the estimation were confirmed by experiments. However, the steady-state position estimation error and the robustness at zero speed were the subject to be solved. The position estimation error compensation method using the estimated cross-coupling factors in low-frequency bandwidth and the torque compensation considering the cross-coupling factors improved the estimation performance and robustness. In particular, the system could operate without stalling at zero speed with the load torque at the rated torque. Therefore, the performance of position-sensorless control systems was improved by the proposed methods.

Chapter 6

Force-Sensorless Control with Proposed Equivalent Mass Matrices for Rubbing Motion

---

This chapter discusses multi-degree-of-freedom (MDOF) force-sensorless hybrid position/force control systems and the design method of equivalent mass matrices in the systems. In Section 6.1, MDOF force-sensorless workspace hybrid position/force control systems are introduced. In Section 6.2, the effects of the utilized equivalent mass matrices are revealed with equations. In Section 6.3, the proposed equivalent mass matrices for the hybrid control system are introduced. In Section 6.4, the experimental systems and results to confirm the validity of the proposed design method are shown. This chapter is concluded in Section 6.5. In this chapter, position response is not the estimated values but the detected values by position sensors.

6.1   MDOF Workspace Hybrid Position/Force Control

This section describes two MDOF force-sensorless hybrid control systems. They are shown in Fig. 6-1 and Fig. 6-2. The difference between the two control systems is the reaction force estimation methods. One uses the workspace RFOB, and the other utilizes the joint coordinate space RTOB and the coordinate transformation from the joint coordinate space to the workspace. The general method of the coordinate transformation is from the joint coordinate space torque to the workspace force by J_{aco}^{T}. However, the coordinate transformation in the acceleration dimension is utilized. The estimation method using RTOB with the coordinate transformation in the acceleration dimension is called RTOBwCT in this dissertation. The inertia matrix J_n^{rtob} can be the inertia matrix J with design values since they can be derived in any posture. When the equivalent mass matrices M_n^{rfob} and M_n^{rtob} are the same as M with design values, the estimated force $\hat{F}_n^{rfob}$ and $\hat{F}_n^{rtob}$ are the same value.

The detected values are the position responses of motors at joints. The velocity responses at joints and workspace responses are derived by calculation. In hybrid control, position and force control are in the workspace control axes. The components of equivalent mass matrices can be expressed as eq. (6.1). The mass matrices with subscripts $\bigcirc_{pf}$ and $\bigcirc_{fp}$ indicate the cross-coupling effects between position and force control axes.

$$\ddot{X} = \begin{bmatrix} \ddot{X}_p \\ \ddot{X}_f \end{bmatrix} = M^{-1}F = \begin{bmatrix} M_{i,pp} & M_{i,pf} \\ M_{i,fp} & M_{i,ff} \end{bmatrix} \begin{bmatrix} F_p \\ F_f \end{bmatrix} = \begin{bmatrix} M_{pp} & M_{pf} \\ M_{fp} & M_{ff} \end{bmatrix}^{-1} \begin{bmatrix} F_p \\ F_f \end{bmatrix} \tag{6.1}$$

In MDOF control systems, cross-coupling effects between control axes physically exist. Position control based on a physically accurate model can reduce disturbances from the modeling error and make it easy to design arbitrary control responses. However, in hybrid position/force control, the cross-coupling effects disturb the force control response. In particular, arbitrarily designed equivalent mass matrices generate undesired disturbances from the modeling error. Therefore, suitable nominal equivalent mass matrices for hybrid position/force control for contact motion are required.
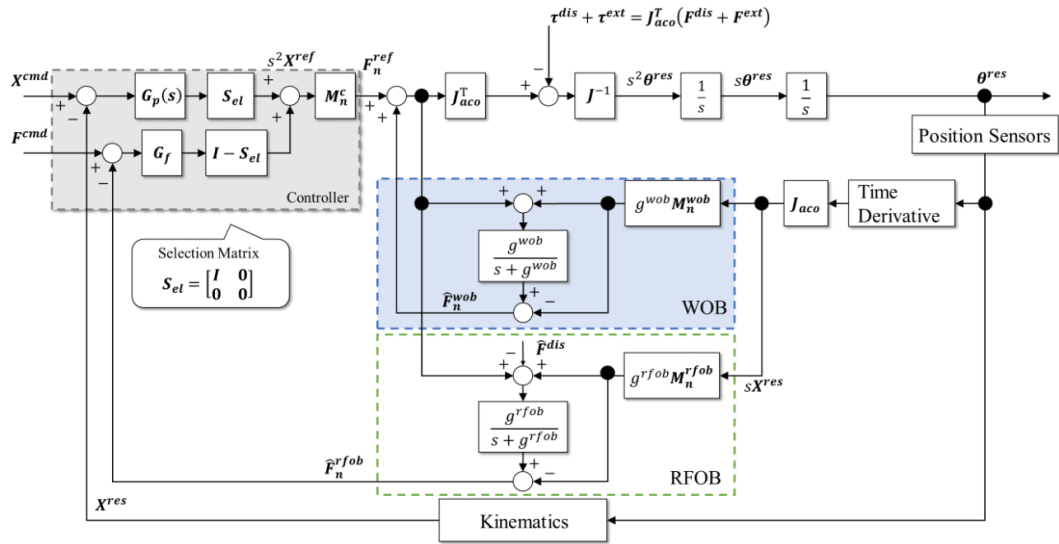
Fig. 6-1: Workspace hybrid controller with RFOB.
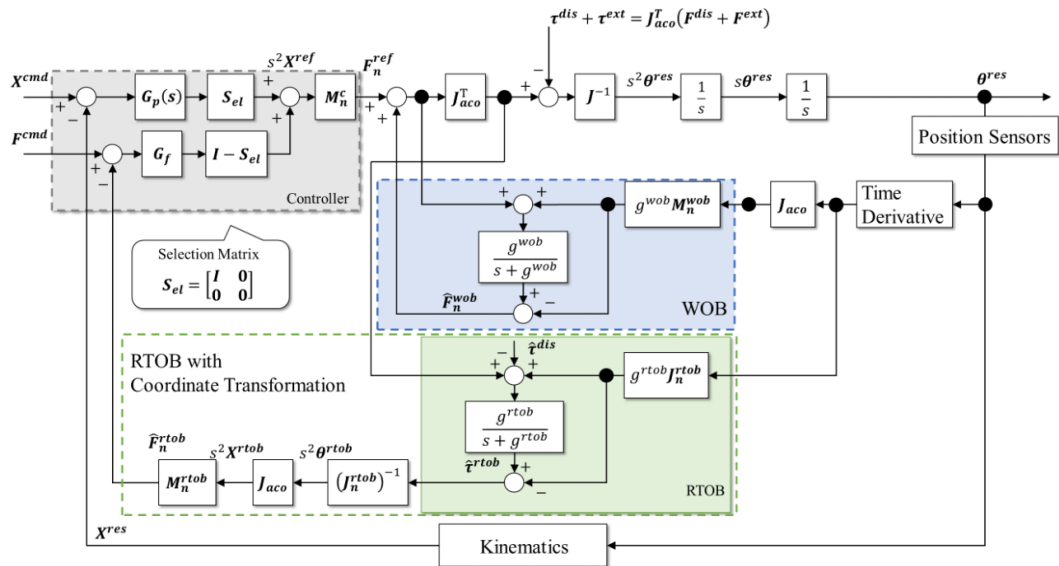
Fig. 6-2: Workpsace hybrid controller with RTOB and the coordinate transformation.

6.2   Effects of the Equivalent Mass Matrices

This section describes the effects of the equivalent mass matrices in the workspace hybrid controller. Force-sensorless workspace hybrid control systems have equivalent mass matrices in the controller, WOB, RFOB, and RTOBwCT. General equivalent mass matrices are with design values. However, the inverse Jacobian matrix diverges to infinity around singular configurations of robots. Designed nominal mass or inertia parameters can change the controllers' response and stability. For these reasons, equivalent mass matrices are often arbitrarily designed. These equivalent mass matrices can be expressed by nominal equivalent mass matrices. The nominal equivalent mass matrices are expressed by M_n^c, M_n^{wob}, M_n^{rfob}, M_n^{rtob} in the controller, WOB, RFOB, and RTOBwCT, respectively.

The relationship between the velocity response and the acceleration reference can be shown in Fig. 6-3. The acceleration reference values are derived by the position controller with gains $G_p(s)$, the force controller with gains G_f, and the selection matrix S_{el}. The output of WOB in Fig. 6-3 is written by eq. (6.2).

$$\hat{F}_n^{wob} = \left(\frac{g^{wob}}{s}\right)\left(M_n^c s^2 X^{ref} - M_n^{wob} s^2 X^{res}\right) \tag{6.2}$$

When M_n^c and M_n^{wob} are the same as M_n, the WOB output can be simplified as eq. (6.3).

$$\begin{aligned}
\hat{F}_n^{wob} &= \left(\frac{g^{wob}}{s}\right) M_n M^{-1}\left(M s^2 X^{ref} - M s^2 X^{res}\right)\\
&= M_n M^{-1}\hat{F}^{wob}
\end{aligned} \tag{6.3}$$

The acceleration response is expressed by eq. (6.4).

$$s^2 X^{res} = M^{-1}\left(M_n^c s^2 X^{ref} + \hat{F}_n^{wob}\right) - M^{-1}\left(F^{dis} + F^{ext}\right) \tag{6.4}$$

Regarding force response, eq. (6.5) can be obtained when M_n^c and M_n^{wob} are the same as M_n.

$$\begin{aligned}
F^{res} &= M s^2 X^{res}\\
&= M_n M^{-1}\left(F^{ref} + \hat{F}^{wob}\right) - F^{dis} - F^{ext}
\end{aligned} \tag{6.5}$$

The estimated workspace force by RFOB is described in eq. (6.6).

$$\begin{aligned}
\hat{F}_n^{rfob} &= \left(\frac{g^{rfob}}{s + g^{rfob}}\right)\left(\left(I - M_n^{rfob} M^{-1}\right)\left(M_n s^2 X^{ref} + \hat{F}^{wob}\right)\right.\\
&\left.\quad + M_n^{rfob} M^{-1}\left(F^{dis} + F^{ext}\right) - \hat{F}^{dis}\right)
\end{aligned} \tag{6.6}$$
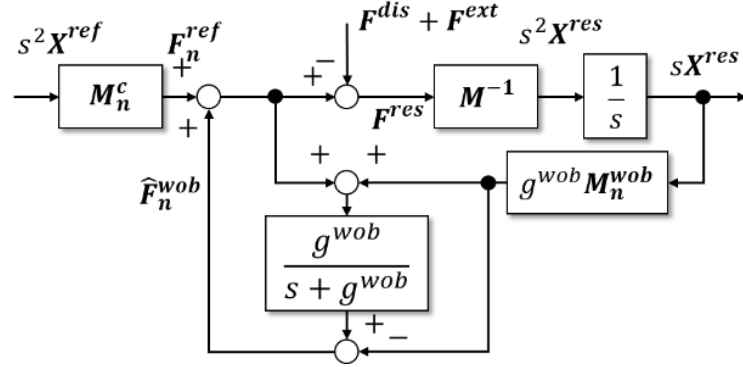
Fig. 6-3: The velocity response from the acceleration reference..

The estimated workspace force by RTOBwCT is expressed by eq. (6.7). The inertia matrix is $\boldsymbol{J}$ with design values.

$$\hat{\boldsymbol{F}}_n^{rtob} = \boldsymbol{M}_n^{rtob} \boldsymbol{M}^{-1} \left(\frac{g^{rtob}}{s + g^{rtob}} \right) \left(\boldsymbol{F}^{dis} - \hat{\boldsymbol{F}}^{dis} + \boldsymbol{F}^{ext} \right) \tag{6.7}$$

When $\boldsymbol{M}_n^{rfob}$ and $\boldsymbol{M}_n^{rtob}$ are the same as $\boldsymbol{M}$, eq. (6.6) and eq. (6.7) are rewritten as eq. (6.8). The cut-off frequencies g^{rtob} and g^{rfob} are also considered the same.

$$\hat{\boldsymbol{F}}^{rfob} = \hat{\boldsymbol{F}}^{rtob} = \left(\frac{g^{rtob}}{s + g^{rtob}} \right) \left(\boldsymbol{F}^{dis} - \hat{\boldsymbol{F}}^{dis} + \boldsymbol{F}^{ext} \right) \tag{6.8}$$

According to eq. (6.6), eq. (6.7), and eq. (6.8), the estimation error comes from the difference between the nominal equivalent mass matrices and the actual matrix, as shown in $\boldsymbol{M}_n \boldsymbol{M}^{-1}$. The main difference between eq. (6.6) and eq. (6.7) is the LPF effect. Since $\boldsymbol{M}_n \boldsymbol{M}^{-1}$ is out of the LPF, the effect of the nominal equivalent mass matrix $\boldsymbol{M}_n^{rtob}$ can be designed. The characteristic is based on deriving the acceleration dimension values of the estimated torque by the inertia matrix derived from design values or identified values in RTOBwCT. When the coordinate transformation is from the joint coordinate space torque to the workspace force by $\boldsymbol{J}_{aco}{}^{\mathrm{T}}$, the effect of the equivalent mass matrix cannot be extracted. Therefore, this dissertation utilizes the hybrid controller with RTOBwCT.

The transfer function from the disturbance and the external force to the force response can be expressed as eq. (6.9) based on Fig. 6-3 when $\boldsymbol{F}_n^{ref}$ is zero.

$$\boldsymbol{F}^{res} = -\left(\boldsymbol{I} + \frac{g^{wob}}{s} \boldsymbol{M}_n^{wob} \boldsymbol{M}^{-1} \right)^{-1} \cdot \left(\boldsymbol{F}^{dis} + \boldsymbol{F}^{ext} \right) \tag{6.9}$$

This equation expresses the sensitivity function. The characteristic is also affected by the product of $\boldsymbol{M}_n$

and M^{-1}. When $M_n M^{-1}$ is not the identity matrix I, the disturbance force in a control axis works as disturbances in other control axes because of the cross-coupling elements in the matrix.

When the velocity of the force control axes is zero, the block diagram of the force controller can be rewritten as Fig. 6-4. The velocity of the force control axes is zero or negligibly small during motion contacting with hard objects. Since the velocity of the force control axes is zero, the output force by motors is the same as the disturbance force and the external force based on the law of action and reaction. The force control axes force are derived as eq. (6.10).

$$
\begin{aligned}
F_f^{dis} + F_f^{ext} &= F_{f,n}^{ref} + \hat{F}_{f,n}^{wob} \\
&= \left(1 + \frac{g^{wob}}{s}\right)\left(M_{ff,n}^{c} s^2 X_f^{ref} + M_{fp,n}^{c} s^2 X_p^{ref}\right) \\
&\quad - \left(\frac{g^{wob}}{s} M_{fp,n}^{wob} s^2 X_p^{res}\right)
\end{aligned}
\tag{6.10}
$$

This equation indicates that the force applied to the contact object gets the cross-coupling effects from the position control axes. When the estimated force matches the force command, the acceleration reference in the force control axes is zero. As eq. (6.10) shows, output force in force control axes has effects from position control axes command and response. Therefore, force response in force control axes is varied by the motion of the position control axes even though the force response follows the force command. The cause of the cross-coupling effects between the position control axes and the force control axes is from M_n, which is different from $M_n M^{-1}$ shown in equations from eq. (6.2) to eq. (6.9). Since eq. (6.5) and eq. (6.10) are different, suitable equivalent mass matrices to reduce the cross-coupling effects depend on the velocity of the force control axes.
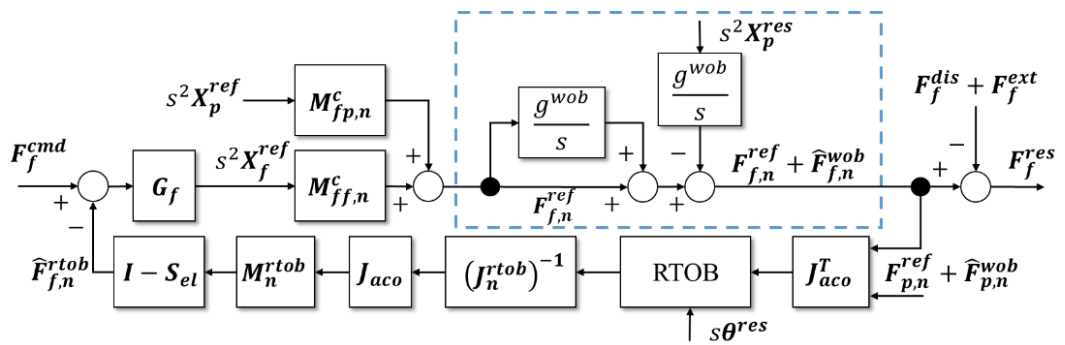
Fig. 6-4: Block diagram of force control when the velocity is zero.

6.3 Proposed Design Method of Equivalent Mass Matrices

This section presents the method to decrease the cross-coupling effects from position control axes to force control axes.

According to equations from eq. (6.1) to eq. (6.10), the cross-coupling effects caused by equivalent mass matrices depend on the velocity of the force control axes. Desired hybrid control performance depends on the motion. Although position control performance is important during non-contact (free motion), force control performance is important during contact. In rubbing motion during contact with hard objects, the velocity of force control axes is zero or negligibly small, and the force response of force control contributes to the operation results. Therefore, equivalent mass matrices according to the expected velocity of the force control axes are designed.

When the velocity is not zero, the relationship between F and F_n is expressed as eq. (6.11).

$$F = M M_n^{-1} F_n \tag{6.11}$$

The relationship is similar in reference values, WOB, RTOBwCT, and the sensitivity function. On the other hand, when the velocity is zero, the external force depends on M_n, as shown in eq. (6.10). Since the transfer function from force to position has s^{-2}, and usual systems have mechanical damping, the cross-coupling effects can be suppressed in position response. On the other hand, the cross-coupling effects in the force dimension directly affect the force control performance. Therefore, reducing the cross-coupling effects from position control axes to the force control axes in force dimension by equivalent mass matrices is effective. The cross-coupling terms in $M M_n^{-1}$ and M_n are desired to be zero with switching operation depending on the expected velocity of the force control axes.

When the velocity of force control axes is not zero, the suitable equivalent mass matrix is M based on the physically accurate modeling. However, suitable equivalent mass matrices other than M are also required to reduce the calculation time. One of the other suitable equivalent mass matrix candidates is expressed as eq. (6.12).

$$M_n^{-1} = M_{n3}^{-1} = \begin{bmatrix} M_{i,pp} & 0 \\ M_{i,fp} & M_{i,ff} \end{bmatrix} \tag{6.12}$$

The relationship between the actual control axis force and calculated control axis force is expressed as eq. (6.13).

$$\begin{bmatrix} F_p \\ F_f \end{bmatrix} = \begin{bmatrix} I & M_{pf} M_{i,ff} \\ 0 & M_{ff} M_{i,ff} \end{bmatrix} \begin{bmatrix} F_{p,n} \\ F_{f,n} \end{bmatrix} \tag{6.13}$$

This equation shows that the cross-coupling terms from position control axes to force control axes are zero. As the terms from force control axes to force control axes are not I, a gain adjustment can be used to compensate with $M_{ff}M_{i,ff}$ for further control performance improvement.

If the equivalent mass matrix M can be derived, the nominal values can be set as eq. (6.14).

$$M_n = M_{n3} = \begin{bmatrix} M_{pp} & 0 \\ M_{fp} & M_{ff} \end{bmatrix} = \begin{bmatrix} A_{pp} & 0 \\ B_{fp} & D_{ff} \end{bmatrix}^{-1} \tag{6.14}$$

The relationship between the actual control axis force and calculated control axis force is expressed as eq. (6.15).

$$\begin{bmatrix} F_p \\ F_f \end{bmatrix} = \begin{bmatrix} M_{pf}B_{fp} + I & M_{pf}D_{ff} \\ 0 & I \end{bmatrix} \begin{bmatrix} F_{p,n} \\ F_{f,n} \end{bmatrix} \tag{6.15}$$

Unlike eq. (6.13), the terms from force control axes to force control axes are I, and there is no need to be compensated. The cross-coupling elements from the calculated force in the position control axes to that in the force control axes are zero in eq. (6.13) and eq. (6.15). Since the force control axes can avoid the undesired disturbance from position control axes, unexpected motion in the force control axes can be prevented. Conventional decoupling methods have used a nominal equivalent mass matrix with zero in all non-diagonal elements. However, an equivalent mass matrix in which all elements vary based on the posture and design values is shown to be suitable for MDOF position control. The proposed design method uses elements in position control axes, which vary based on posture and design values. The decoupling is between the position and force control axes. Therefore, M_{n3} is one of the suitable nominal equivalent mass matrices when the velocity of force control axes is not zero. Since the matrix has zeros as elements, the calculation time can be reduced. Position control axes get cross-coupling effects from force control axes. Position control axes can suppress the disturbance because of the control robustness from the higher control bandwidth than the force control axes' motion bandwidth. The component of the disturbance acting on the force control axes that interfere with the position control axes is suppressed within the range of the disturbance suppression of the position control axes.

When the velocity of force control axes is zero, the suitable equivalent mass matrix candidates for reference values and WOB are expressed as eq. (6.16) and eq. (6.17).

$$M_{n2}^{-1} = \begin{bmatrix} M_{i,pp} & 0 \\ 0 & M_{i,ff} \end{bmatrix} \tag{6.16}$$

$$M_{n2} = \begin{bmatrix} M_{pp} & 0 \\ 0 & M_{ff} \end{bmatrix} \tag{6.17}$$

According to eq. (6.10), $F_f^{dis} + F_f^{ext}$ is independently generated from position control axes and force control axes by the equivalent mass matrices shown in eq. (6.16) and eq. (6.17). The reaction force by the controller with equivalent mass matrices with design value can be expressed by eq. (6.18) by substituting eq. (6.1) for eq. (6.10).

$$
\begin{aligned}
F_f^{dis} + F_f^{ext} \ &= \ F_f^{ref} + \hat{F}_f^{wob} \\
&= \ \left(1 + \frac{g^{wob}}{s}\right)\left(M_{ff}^c s^2 X_f^{ref} + M_{fp}^c s^2 X_p^{ref}\right) \\
&\quad - \left(\frac{g^{wob}}{s} M_{fp}^{wob} s^2 X_p^{res}\right)
\end{aligned}
\tag{6.18}
$$

When M_{pf} and M_{fp} are not zero, the motion of the position control axes interferes with the motion of the force control axes. On the other hand, when eq. (6.17) is utilized, eq. (6.10) is rewritten as eq. (6.19).

$$
\begin{aligned}
F_f^{dis} + F_f^{ext} \ &= \ F_{f,n}^{ref} + \hat{F}_{f,n}^{wob} \\
&= \ \left(1 + \frac{g^{wob}}{s}\right)\left(M_{ff}^c s^2 X_f^{ref}\right)
\end{aligned}
\tag{6.19}
$$

Therefore, M_{n2} is a suitable nominal equivalent mass matrix when the expected velocity of force control axes is zero.

When the bandwidth of WOB is infinity, M_{n2} decouples the axes even in the motion, whose velocity in the force control axes is not zero. However, the cut-off frequency of WOB has an upper limit, and the limit is lower than the disturbance bandwidth in practical use. The proposed method also utilizes the nominal equivalent mass matrix M_{n2} in the controller. The matrix in the controller decouples the position and force control axes in the force reference derived by the commands and responses. As a result, cross-coupling effects between position control axes and force control axes are suppressed. Furthermore, robots need to move as fast as possible in free motion to decrease the operation time. The acceleration is also high. When M_{n2} is utilized in the controller and WOB in the free motion, the modeling error in the non-diagonal elements makes the controller's and WOB's compensation values larger. Since actual systems have torque limitations, which cramp the output force, the compensation cannot work correctly. In addition, the cut-off frequency of WOB with M_{n2} may be smaller than that with M. Therefore, M_{n2} is unsuitable when the velocity of force control axes is not zero. On the other hand, since the speed and acceleration are not high in contact motion, the force control performance is more important than the stability. Therefore, M_{n2} can be used to decouple the position control axes' and force control axes' motions.
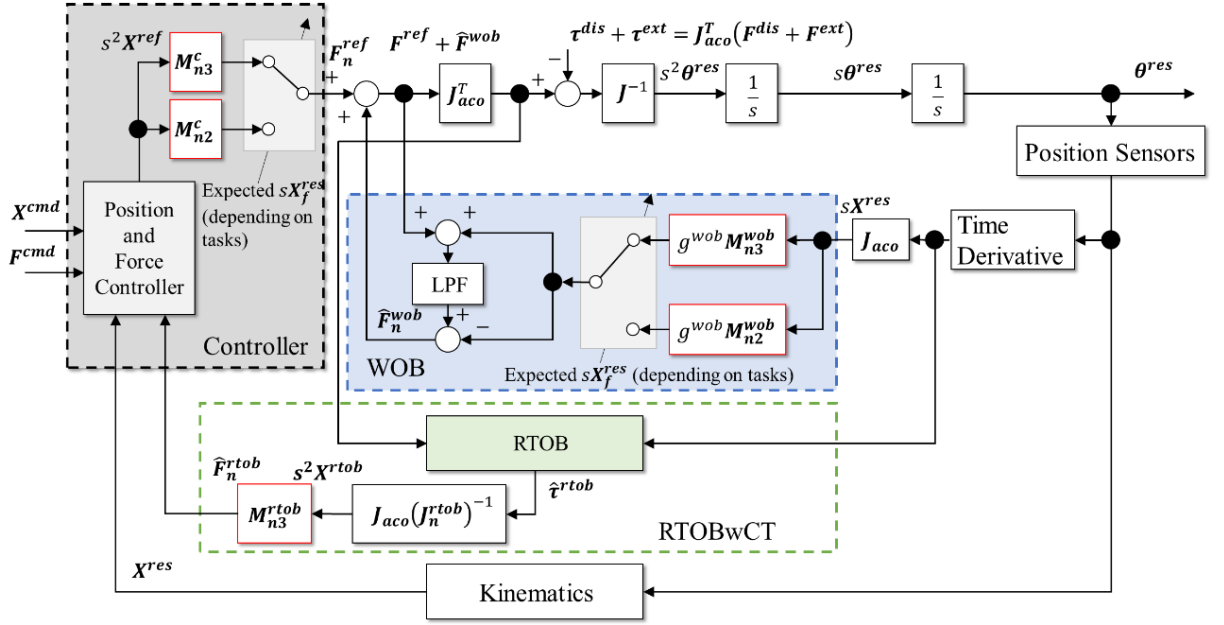
Fig. 6-5: Block diagram of the proposed hybrid position/force control with equivalent mass matrices switching.

Since the suitable equivalent mass matrices depend on the expected velocity of the force control axes in the viewpoint of the force control performance, the parameter switching depending on tasks is introduced. The block diagram of the proposed controller is shown in Fig. 6-5. The controller uses RTOBwCT for the workspace reaction force estimation since the interference effect between control axes can be simply expressed according to eq. (6.7).

Utilized equivalent mass matrices in the controller and WOB are changed between motions, such as approaching and rubbing motions. When motions are changed, the previous motion is steady, and the velocity of position control axes is zero or negligibly small. Therefore, chattering from the switching can be negligible. Moreover, as shown in Fig. 6-3, when sX^{res} is zero, the output of WOB depends on only F_n^{ref}. The switching effect of M_n^c is like a step command for WOB. When the changed elements are large values in the equivalent mass matrices or the interference from the other axes is dominant, the switching may make the system unstable. The unstable situations are considered when the robot's posture is around the singular configuration or has a large disturbance force on the position control axes, even in the steady state. However, the problem can be negligible since general robot applications with rubbing motion are not used in a singular configuration and with a large load in position control axes. Therefore, when both controllers with M_{n2} and M_{n3} can be in a stable state, the proposed controller

can be in a stable state after the switching. Furthermore, the difference in the elements between M_{n2} and M_{n3} is smaller than that between M_{n2} and M in the viewpoint of the number of zero elements. Therefore, the switching effect can be smaller by using M_{n2} and M_{n3} in the control system.

Since the force controller to derive $s^2 X^{ref}$ independents with the equivalent mass matrices switching, an arbitrary force controller can be used with the proposed method. A simple proportional controller was used in this paper for clarity. When stable responses at the impact to contact objects are required, other controllers, such as a controller with velocity feedback, can be used.

6.4   Experiments of Force-Sensorelss Hybrid Control

In this section, force response vibration and estimated external force during rubbing motion were evaluated.

6.4.1   Setup and Parameters for Experiments to Confirm the Validity of the Proposed Equivalent Mass Matrices

A parallel link type 4DOF manipulator was used in experiments. The kinematics and dynamics are described in Section 3.2. The inertia matrix J_n^{rtob} was the inertia matrix J with design values. The length and mass of links and the frequency characteristics of the pushing motion to the force gauge (Y_{com}-axis) are expressed by Fig. 6-6. The connection and the communication of devices are expressed by Fig. 6-7. The material of these links was ABS. Each joint has bearings, and the friction at each joint was small enough to be ignored. The manipulator does not have reduction gears to remove the friction from the gears. Therefore, the disturbance force F^{dis} (torque τ^{dis}) was assumed to be zero, and the main estimated force was the external force at the end-effector. The main external force at the end-effector is the pushing force to the force gauge on the Y_{com}-axis, and the friction force between the end-effector and the force gauge on the X_{dif}-axis and the X_{com}-axis. The force gauge on the Y_{com}-axis detected the pushing force on the Y_{com}-axis. The Y_{com}-axis was the force control axis, and the other axes were the position control axes. The proposed hybrid controller was implemented on the motion controller MP3300 with CPU302 made by YASKAWA. The Laplace operator s was approximated as first-order backward differencing. The force gauge and the motion controller were connected to the PC for data logging. The frequency characteristics of Y_{com}-axis push motion are also shown in Fig. 6-6. The characteristics were obtained by injecting a chirp signal to $F_{y,com}^{ref}$ with the hybrid controller whose equivalent mass matrices were M. The position control axes commands were constant, and the force control axes command were 0.5 N. According to the result, the resonance frequencies were around 20 Hz and 60 Hz.

The validity of the proposed controller was confirmed by four kinds of experimental commands shown in Table 6.1. "Step" showed the force control performance during contact with the force gauge. "Freq" was to confirm the similarity of the motion in a non-contact motion among the equivalent mass matrix conditions. "Chirp" showed the cross-coupling effects and the vibration suppression by the proposed method in rubbing motion by sinusoidal command. In the experiments for "Chirp," the responses by the
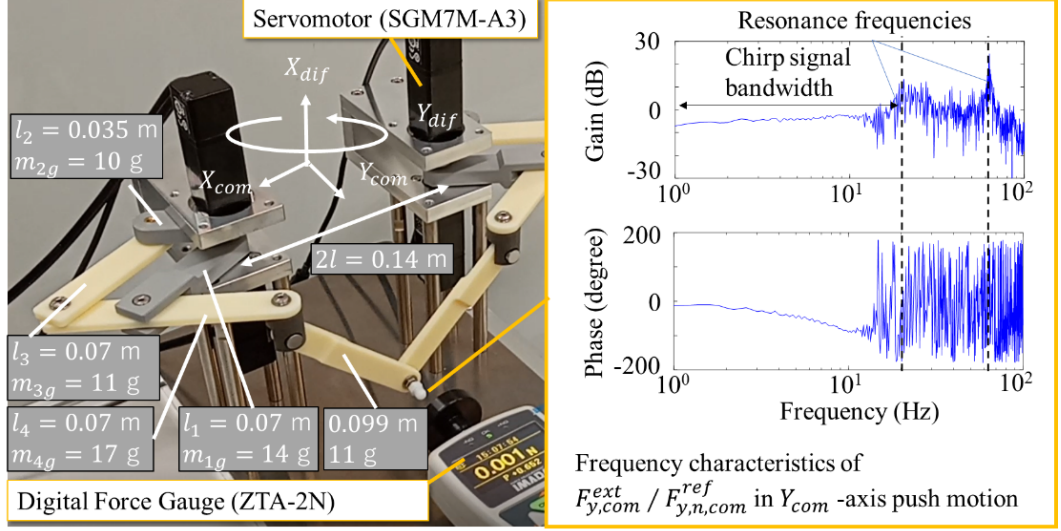
Fig. 6-6: The 4DOF manipulator and the frequency characteristics of the pushing motion.

experimental commands and the switching effect of equivalent mass matrices were confirmed. "Slide" showed results in rubbing motion by repeated step commands. The sequence of the motions imitated the expected rubbing motion. The center of the end effector and the force gauge was at $(X_{dif}, X_{com}, Y_{dif}) = (0.068, 0, 0)$. Since the force gauge can measure the accurate force around the center, the area of the motion was around the center of the force gauge. Force commands were decided according to the rated torque of motors in experiments "Step," "Chirp," and "Slide." The force command in the experiment "Freq" was decided to suppress the Y_{com}-axis motion. The acceleration reference values $s^2 \boldsymbol{X}^{ref}$ are derived as eq. (6.20).

$$
s^2 \boldsymbol{X}^{ref} = \begin{bmatrix}
(G_p + G_{vel}s)\left(X_{dif}^{cmd} - X_{dif}^{res}\right) \\
(G_p + G_{vel}s)\left(X_{com}^{cmd} - X_{com}^{res}\right) \\
(G_p + G_{vel}s)\left(Y_{dif}^{cmd} - Y_{dif}^{res}\right) \\
G_f\left(F_{y,com}^{cmd} - \hat{F}_{y,com}^{rtob}\right)
\end{bmatrix}
\tag{6.20}
$$

The conditions of equivalent mass matrices during the experimental commands are shown in Table 6.2. The condition "M" is an ideal controller for free motion since the equivalent mass matrices in the controller were the same as the mechanical model. The responses from condition "M" was the standard of the comparison. The condition "M3" is the proposed controller for tasks whose expected velocity of the force control axes is not zero. On the other hand, the condition "M2" is the proposed controller for tasks whose expected velocity of the force control axes is zero.
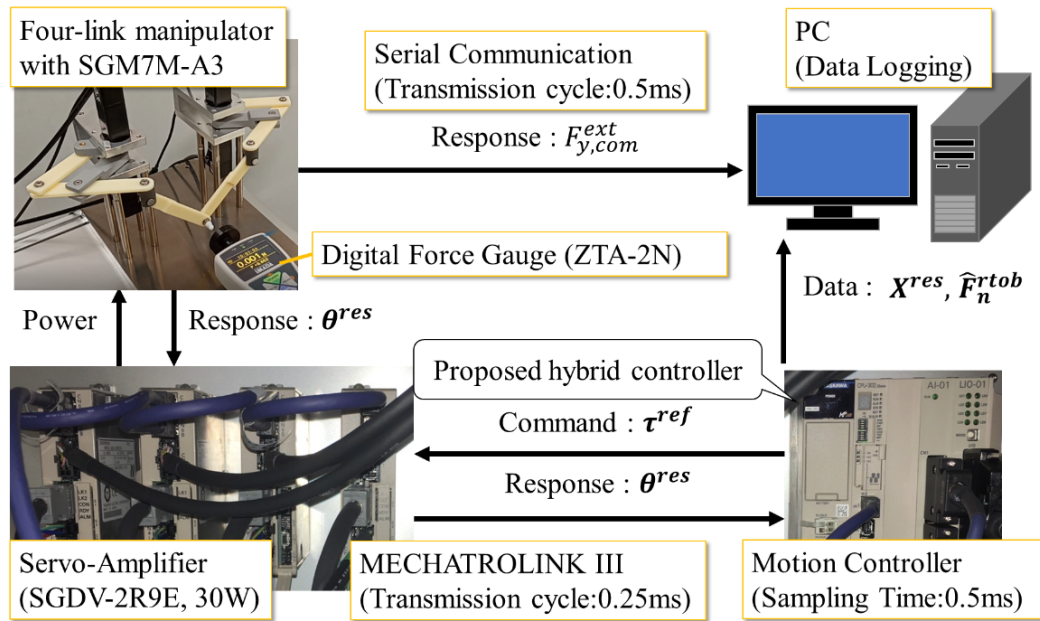
Fig. 6-7: System configuration for experiments of force-sensorless hybrid control.

In the experiment using the condition "M2", equivalent mass matrices were switched between the task of approaching and experimental commands. The switching timing was in a steady state between the motion. The whole sequence for the experiment "Step," "Chirp," and "Slide" using the condition "M2" is shown in Fig. 6-8. Since the peak value of the noise in the velocity response was under 3 mm/s, the threshold to judge the steady state was 3 mm/s after the vibration was converged. In experiments "Step," "Chirp," and "Slide," experimental commands started in a steady state after the manipulator contacted the force gauge.

The experimental parameter is shown in Table 6.3. The parameters were designed by trial and error based on the frequency characteristics shown in Fig. 6-6.

Table 6.1: Relationship between indexes and experimental command.

Index of Experimental Command	$F_{y,com}^{cmd}$ (N)	$X_{dif}^{cmd}, X_{com}^{cmd}, Y_{dif}^{cmd}$ (m)
Step	Step signal: $F_{y,com}^{cmd} = 0.3$ and 0.6	Constant values: $X_{dif}^{cmd} = 0.07$, $X_{com}^{cmd} = 0.0$, $Y_{dif}^{cmd} = 0.0$
Freq	Constant value: $F_{y,com}^{cmd} = 0.02$	Constant frequency signals: $X_{dif}^{cmd} = 0.068 - 0.02\sin 2\pi t$, $X_{com}^{cmd} = 0.02\sin \pi t$, $Y_{dif}^{cmd} = 0.015\sin 6\pi t$
Chirp	Step signal: $F_{y,com}^{cmd} = 0.0$ and 0.3	Chirp frequency signals during: $F_{y,com}^{cmd} = 0.3$ $X_{dif}^{cmd} = 0.068 - 0.002\cos 2\pi t^2$ $X_{com}^{cmd} = 0.002\sin 2\pi t^2$, $Y_{dif}^{cmd} = 0.0$
Slide	Constant value: $F_{y,com}^{cmd} = 0.3$	Repeated step signals: $X_{dif}^{cmd} = 0.0675$ and 0.0655, $X_{com}^{cmd} = 0.0$, $Y_{dif}^{cmd} = 0.0$

Table 6.2: Relationship between indexes and equivalent mass matrices setting.

Index of Condition	Utilized Parameters during Experimental Commands			Confirmation Points of Experimental Responses
	M_n^c	M_n^{wob}	M_n^{rtob}	
M	M	M	M	Standard of comparison
M3	M_{n3}	M_{n3}	M_{n3}	Similarity with "M"
M2	M_{n2}	M_{n2}	M_{n3}	Reducing vibration

Table 6.3: Parameters for the experiments for force-sensorless control methods.

Parameters	Values	Remarks	Parameters	Values	Remarks
Position Gain G_p	987	5 Hz	g^{wob}	5 Hz	
Velocity Gain G_{vel}	63	5 Hz	g^{rtob}	5 Hz	
Force Gain G_f	15		Encoder Resolution	20 bit	
Sampling Time	0.5 ms				
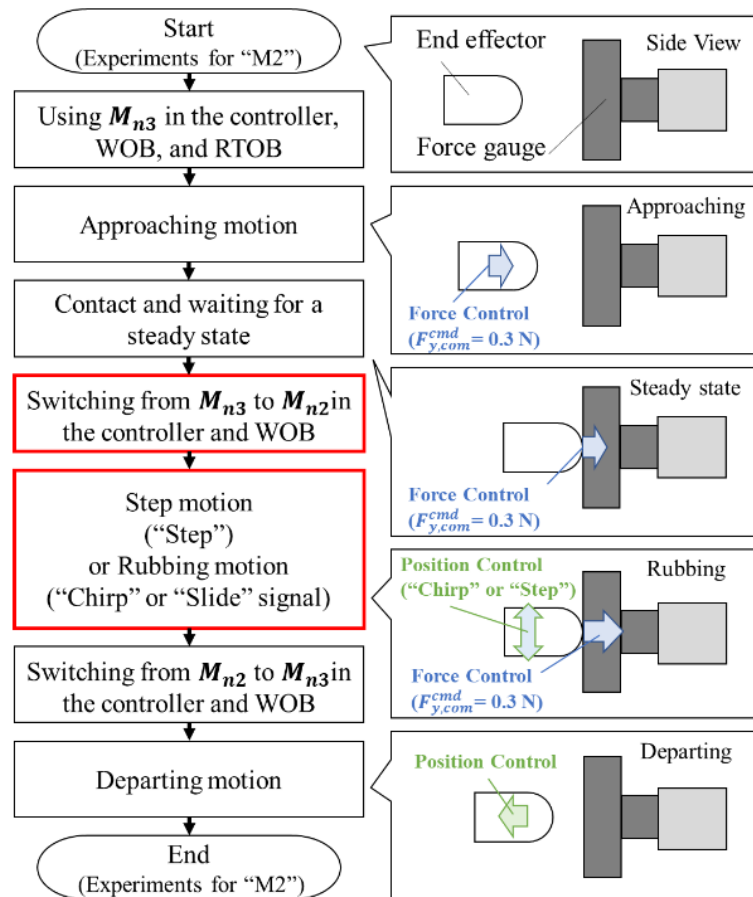
Fig. 6-8: Sequence of the experiment using the condition "M2."

6.4.2   Results of "Step"

Experimental results of the detected force and estimated force in "Step" are shown in Fig. 6-9. The estimated force was similar to each condition and followed the external force. The motion was only on the Y_{com}-axis. These results showed that "M3" and "M2" performed similarly to "M" when there was no interference from other control axes. The detected force had a vibration and an overshoot in the transient response. According to Fig. 6-6, the resonance frequency was around 20 Hz. The frequency of transient response vibration was also around 20 Hz. The main cause of the vibration was the frequency characteristics from the mechanical impedance. The overshoot was generated since this paper used a simple proportional force controller to confirm the difference from the equivalent mass matrices. The overshoot can be suppressed by a force controller with velocity feedback.
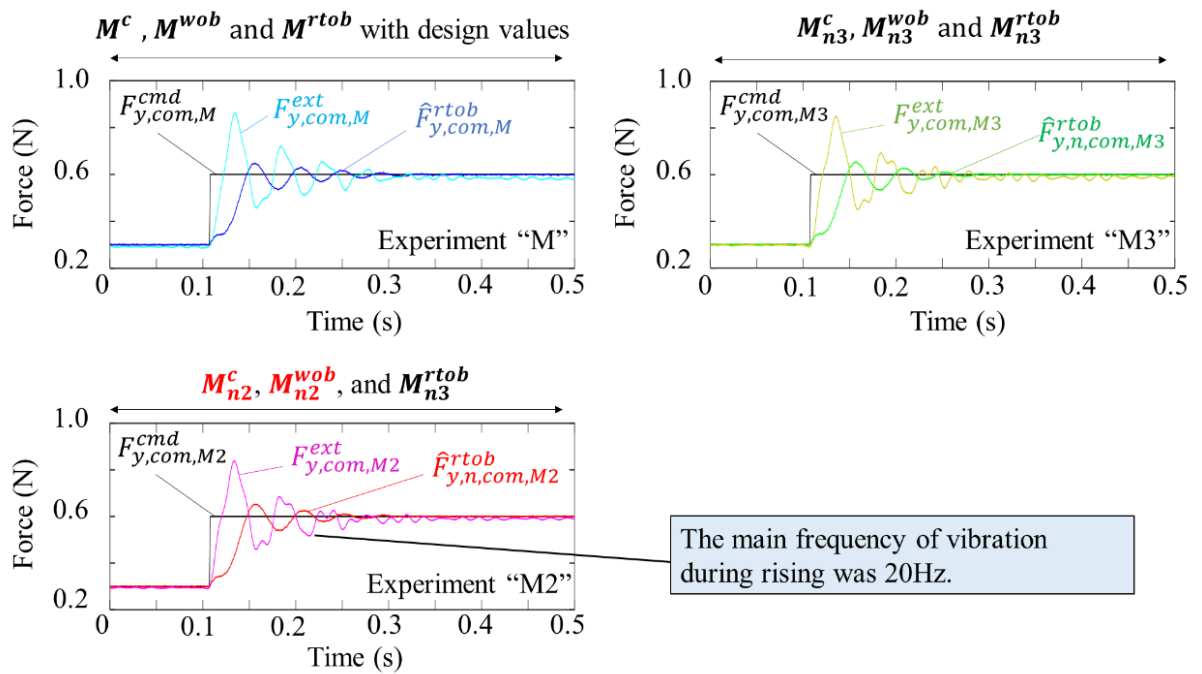
Fig. 6-9: Force responses in experiments "Step."

6.4.3 Results of "Freq"

Experimental results of position response and fast Fourier transform (FFT) results of $\hat{\boldsymbol{F}}^{wob}$ in "Freq" are shown in Fig. 6-10 and Fig. 6-11, respectively. The position responses and estimated disturbance in position control axes were similar in each condition. According to Fig. 6-11, the response of "M3" was similar to that of "M" in the force control axis. However, it was different from that of "M2." In "Freq," the motion of the force control axes was not constrained, and the end effector could move freely according to the command and disturbance. The difference is from the interference between the position and force control axes. Since the non-diagonal elements of $MM_{n2}{}^{-1}$ were not zero, the output force had errors from the calculated force reference values according to eq. (6.11). If the disturbance by the interference is larger, the difference will increase. Since "M" is an ideal controller for free motion, the condition "M3" is better than "M2" for the motion without contact on force control axes.
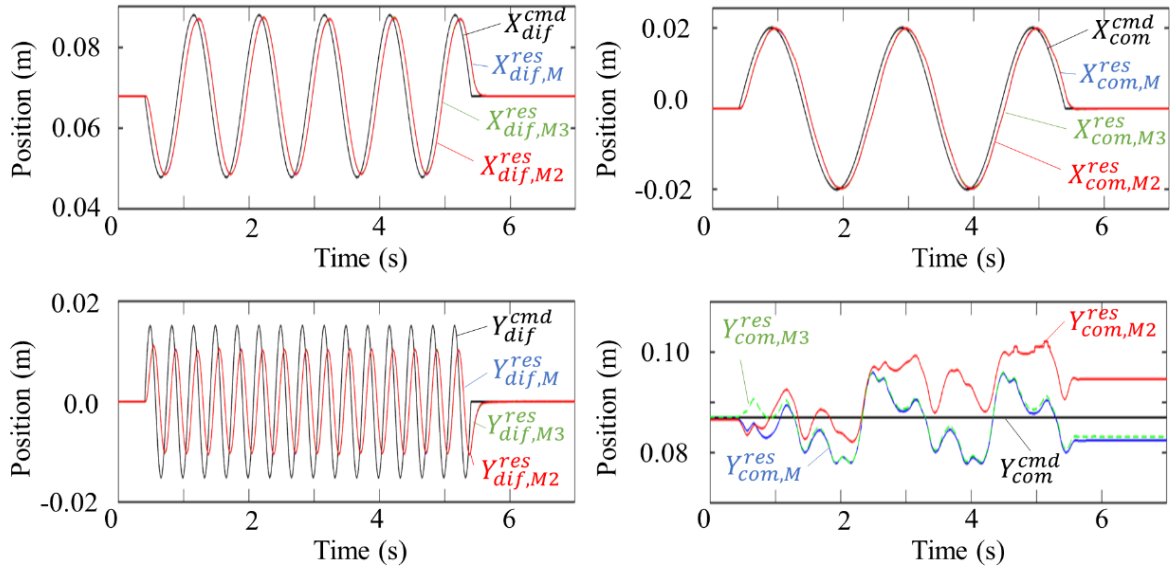
Fig. 6-10: Position responses in experiments "Freq."
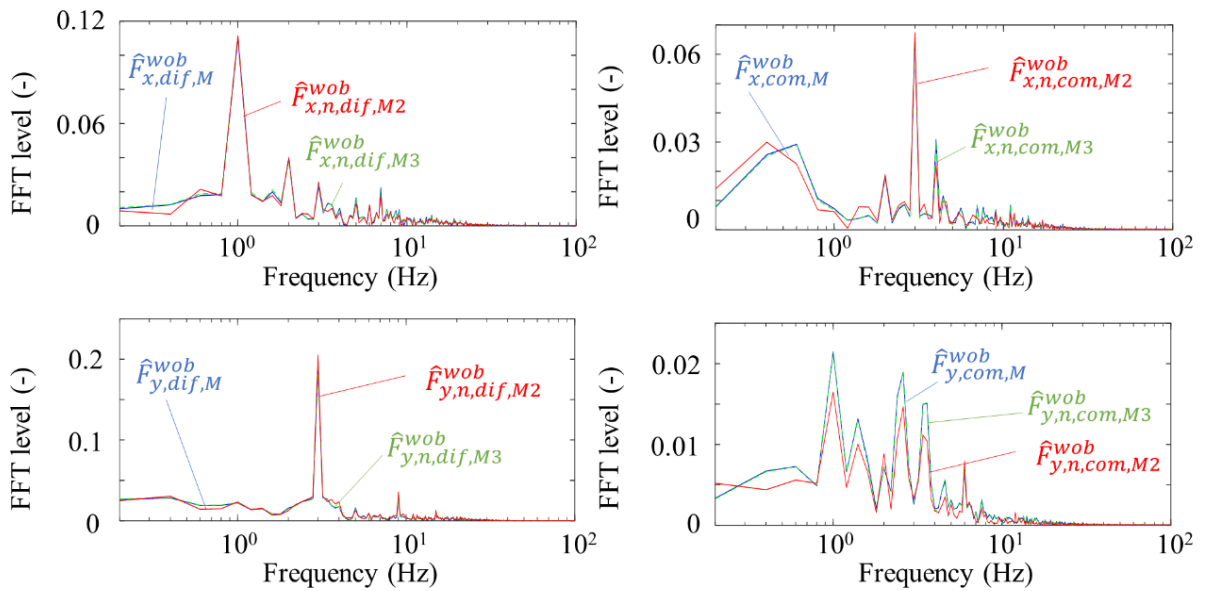
Fig. 6-11: FFT results of $\boldsymbol{F}^{wob}$ in experiments "Freq."

6.4.4   Results of "Chirp"

Experimental results of force response and FFT results of detected force in "Chirp" are shown in figures from Fig. 6-12 to Fig. 6-17. In the experiment using "M2", equivalent mass matrices were switched between the task of approaching and experimental commands. The switching timing is shown by dashed lines (0.9 s and 6.2 s) in Fig. 6-12, Fig. 6-15, Fig. 6-16, and Fig. 6-17. These figures show the response from "Start" to "End" in Fig. 6-8. Fig. 6-12 and Fig. 6-13 show the estimated force and force response detected by the force gauge. Fig. 6-14 shows the FFT results of $F_{y,com}^{ext}$ during the rubbing motion. Fig. 6-13 shows the force responses vibrated in all conditions, although the force command was constant. According to Fig. 6-14, the vibration was mainly up to 10 Hz, which was the chirp signal bandwidth in the position control axes. Since the position control bandwidth was 5 Hz, the response could not follow the chirp signal command, whose bandwidth was up to 10 Hz. That worked as a disturbance in position control axes. In addition, the frictional force between the end effector and the force gauge worked as a disturbance. Therefore, the vibration of force control axes under 10 Hz was caused by interference from the motion of position control axes. The difference in vibration amplitude was large in the bandwidth from 5 Hz to 10 Hz, which was outside of the control bandwidth. Fig. 6-13 and Fig. 6-14 show that the detected force in "M2" had smaller vibration than the others, even though the bandwidth is higher than the control bandwidth.

Fig. 6-15 shows the WOB outputs of all axes. Fig. 6-16 and Fig. 6-17 show singular values σ and elements of M_n^c and M_n^{wob}, respectively. The equivalent mass matrices switching was once and instantaneous. The WOB outputs of "M2" did not become unstable, as shown in Fig. 6-15. According to Fig. 6-16 and Fig. 6-17, the matrices and the switching can be applied. Therefore, "M2" is better than "M" and "M3" for a rubbing motion when the velocity of the force control axes is expected to be zero during contact with hard objects.
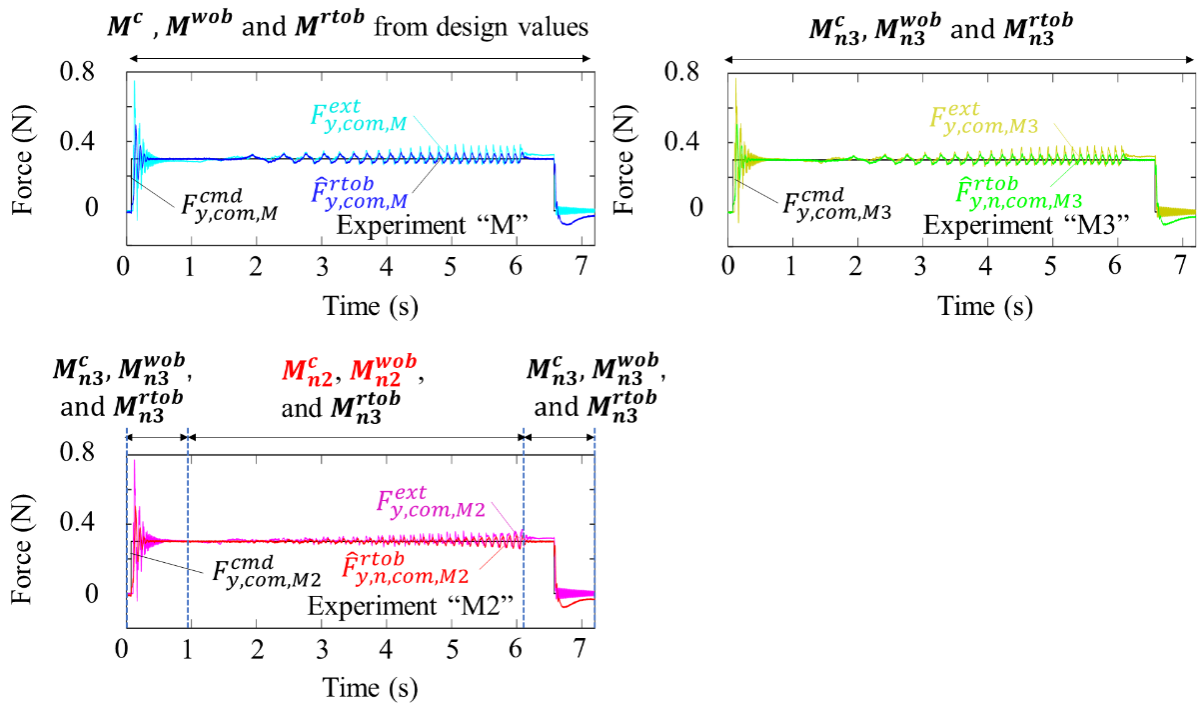
Fig. 6-12: Force responses in experiments "Chirp."
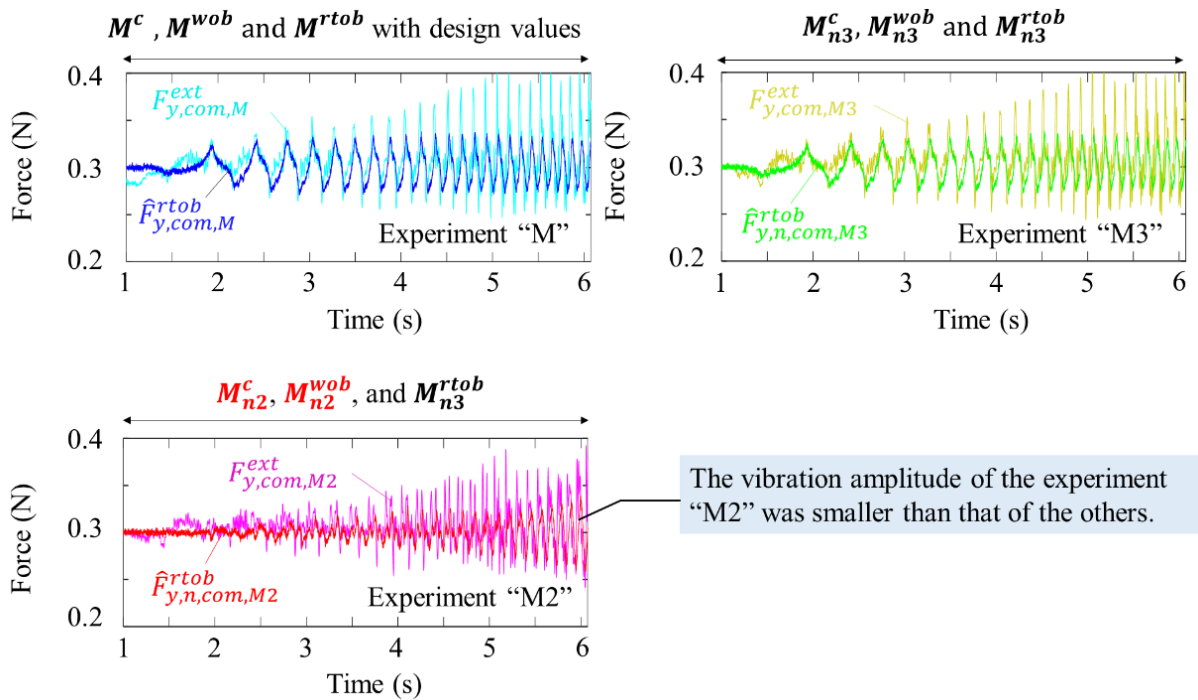
Fig. 6-13: Enlarged view of force responses in experiments "Chirp."
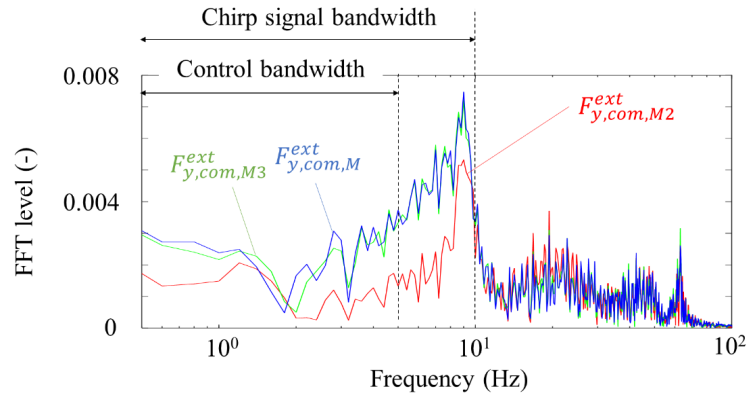
Fig. 6-14: FFT results of $F_{y,com}^{ext}$ in experiments "Chirp."
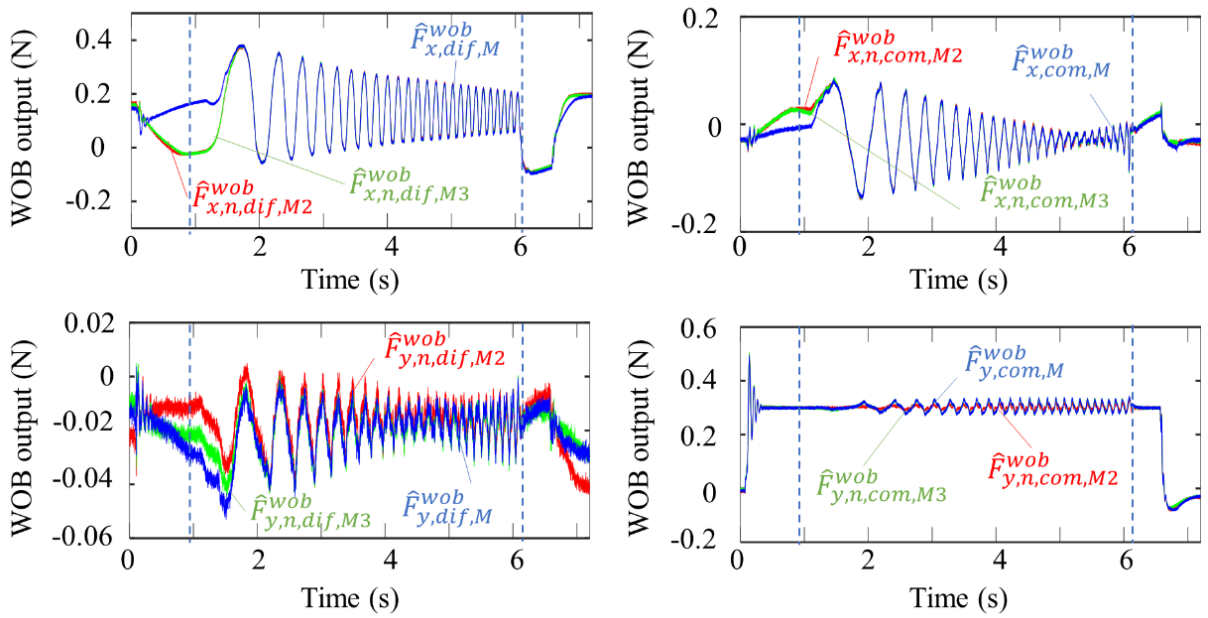
Fig. 6-15: WOB outputs in experiments "Chirp."
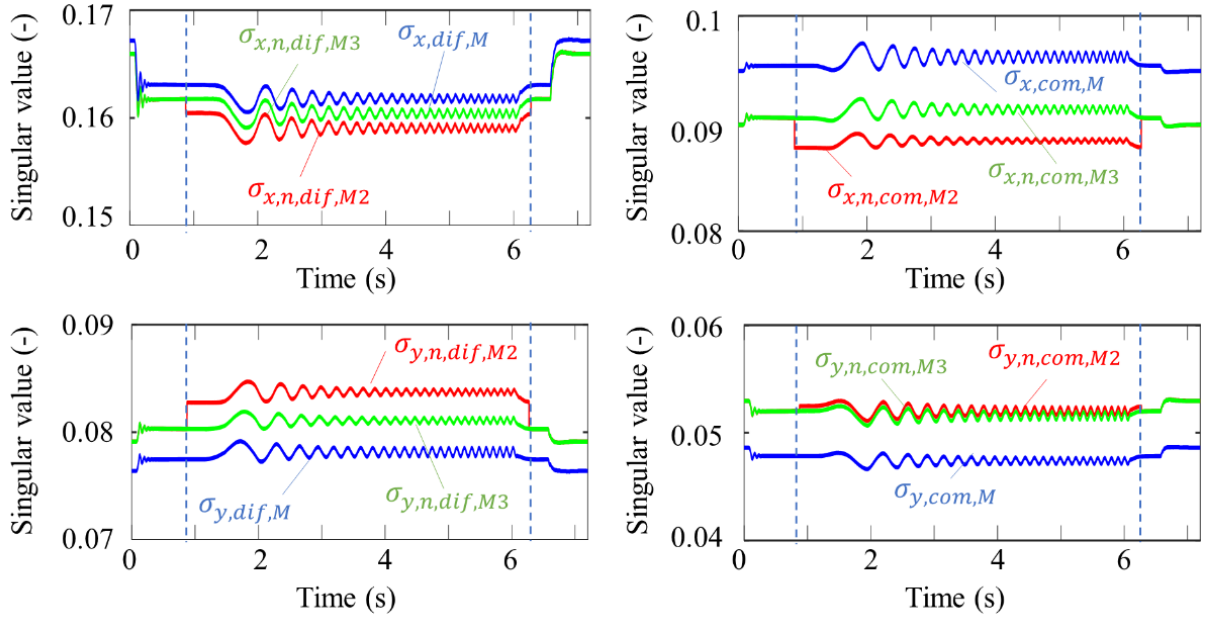
Fig. 6-16: Singular values of M_n^c and M_n^{wob} in experiments "Chirp."
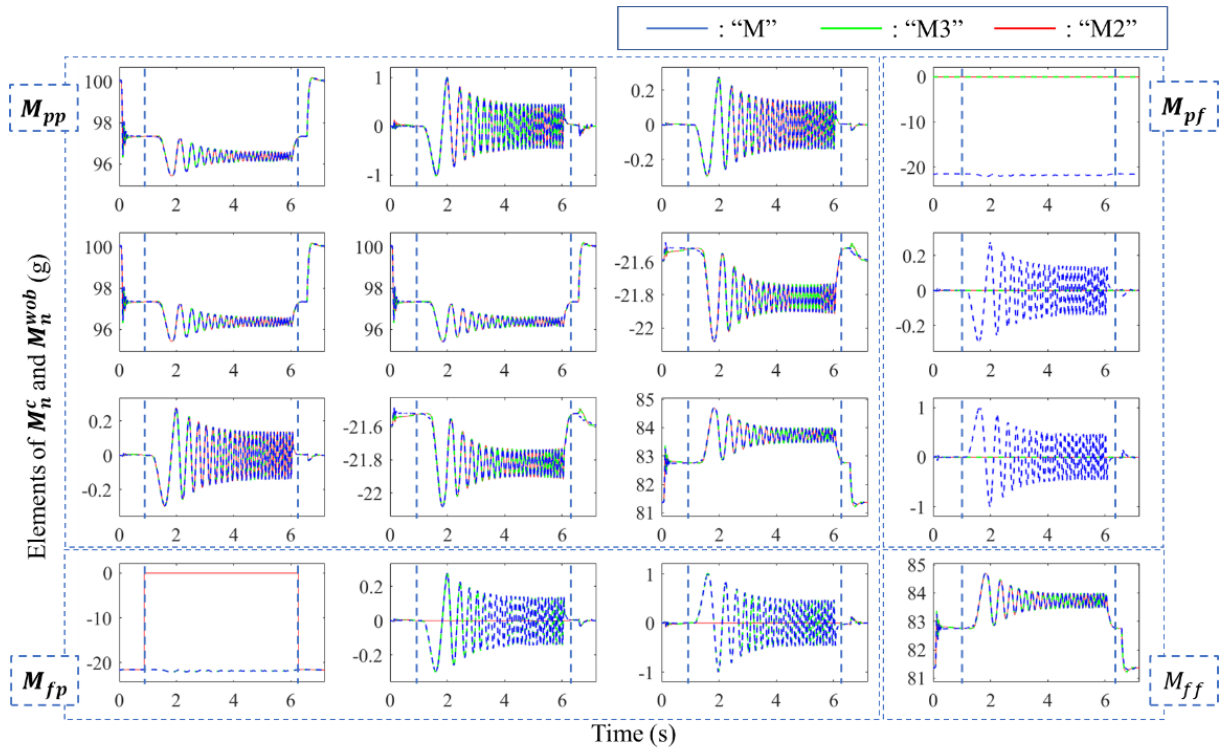
Fig. 6-17: Elements of M_n^c and M_n^{wob} in experiments "Chirp."

6.4.5   Results of "Slide"

In this experiment, the repeated step position command was applied to X_{dif}^{cmd} instead of the chirp signal in experiments "Chirp." The friction between the end effector and the force gauge at the beginning of the motion was the interference disturbance force. The position response X_{dif}^{cmd}, force response $F_{y,com}$, and FFT results of $F_{y,com}$ are shown in Fig. 6-18, Fig. 6-19, and Fig. 6-20, respectively. Fig. 6-18 showed that the position responses were similar to others. Fig. 6-19 showed that the force gauge response had a vibration at the beginning of the step motion, and the peak in the response of "M2" was smaller than that of the others. The smaller vibration can also be confirmed in Fig. 6-20. The cause of the error between the estimated and detected force by the force gauge was the modeling error of friction, backlash, and stiffness. A mechanical improvement and higher gains may be required to decrease the error. However, the validity of the proposed method was confirmed since the mechanical condition and controller gains were the same.
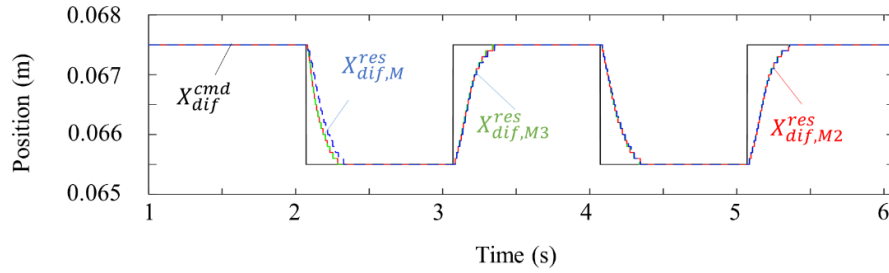
Fig. 6-18: Position responses in experiments "Slide."
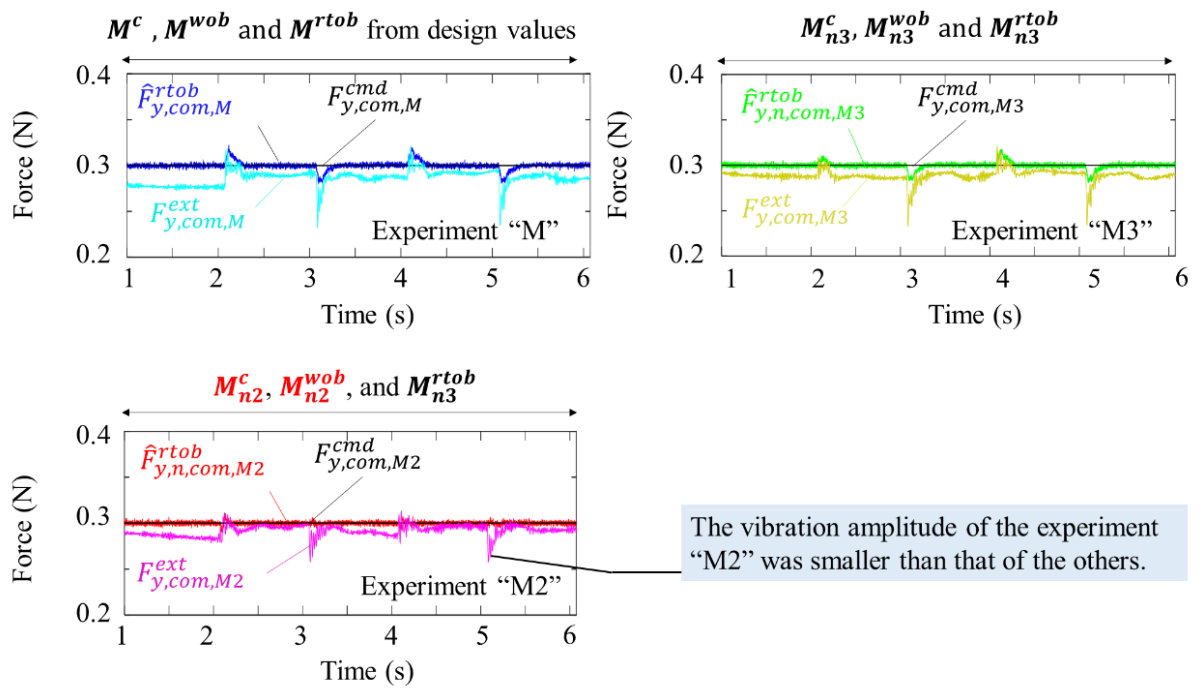
Fig. 6-19: Force responses in experiments "Slide."
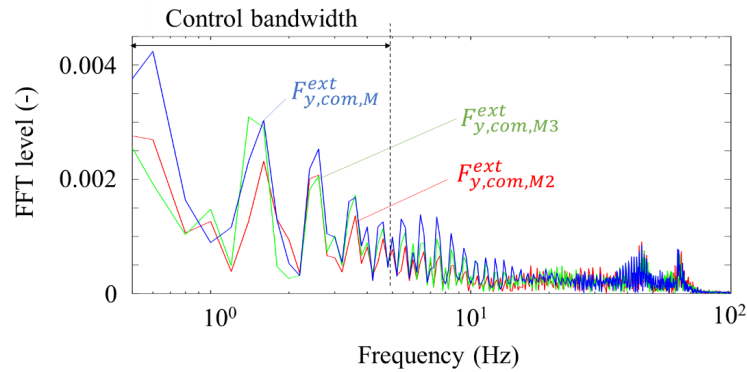
Fig. 6-20: FFT results of $F_{y,com}^{ext}$ in experiments "Slide."

6.5 Summary

This dissertation presented design methods of equivalent mass matrices in the force-sensorless hybrid position/force controller for rubbing motion. In free motion, the equivalent mass matrix M with design values or the nominal equivalent mass matrix expressed by M_{n3} are suitable. Since the controller for position control axes has appropriate dynamics, the undesired disturbance from the modeling error can be small, and the systems are more stable. On the other hand, the nominal equivalent mass matrix expressed by M_{n2} is suitable in the controller and WOB in contact motion, including rubbing motion. Since the motion is at a low speed and force control performance is more important than the position control performance, decoupling the position control axes' motion and the force control axes' motion is required. According to the experimental results, the decoupling of the motion was achieved by the proposed design method.

Chapter 7

Proposed Position-and-Force-Sensorless Control

This chapter discusses the proposed position-and-force-sensorless (PFSL) control. In Section 7.1, DOB using estimated position is explained. In Section 7.2, the proposed PFSL admittance control system is explained. In Section 7.3, the experimental systems and results to confirm the validity of the proposed PFSL admittance control method are shown. In Section 7.4, the proposed PFSL bilateral control system is explained. In Section 7.5, the experimental systems and results to confirm the validity of the proposed PFSL bilateral control method are shown. In Section 7.6, the proposed PFSL hybrid position/force control system is explained. In Section 7.7, the experimental systems and results to confirm the validity of the proposed hybrid position/force control method are shown. This chapter is summarized in Section 7.8.

7.1　DOB and RTOB using estimated position

This section explains the DOB and RTOB using estimated position.

In PFSL control systems, DOB and RTOB for a motor utilize the estimated position. The block diagram is shown in Fig. 7-1. Since the position estimation utilizes the detected current, the resolution of the estimated position depends on the current sensor. The resolution of current detection is generally lower than the resolution of position sensors attached to servomotors. In low-speed operation, the resolution of the velocity derived by the first-order backward differential is low, and the high-frequency component is amplified. Therefore, the estimated velocity is derived by pseudo derivative. A higher cut-off frequency is better regarding phase delay, but a lower cut-off frequency is better for pseudo-increasing the resolution of the estimated velocity. Therefore, g^{pse} is set to a value lower than the cut-off frequency of position estimation determined by the gain g_h and higher than the DOB and RTOB cut-off frequency. Since the cut-off frequency of PLL in conventional position estimation methods is generally set lower than 100 Hz. However, the cut-off frequency of the proposed position estimation was 1.7 kHz, according to the utilized gain g_h. Therefore, the proposed method expands the estimation bandwidth, and the cut-off frequency of DOB and RTOB can be higher.
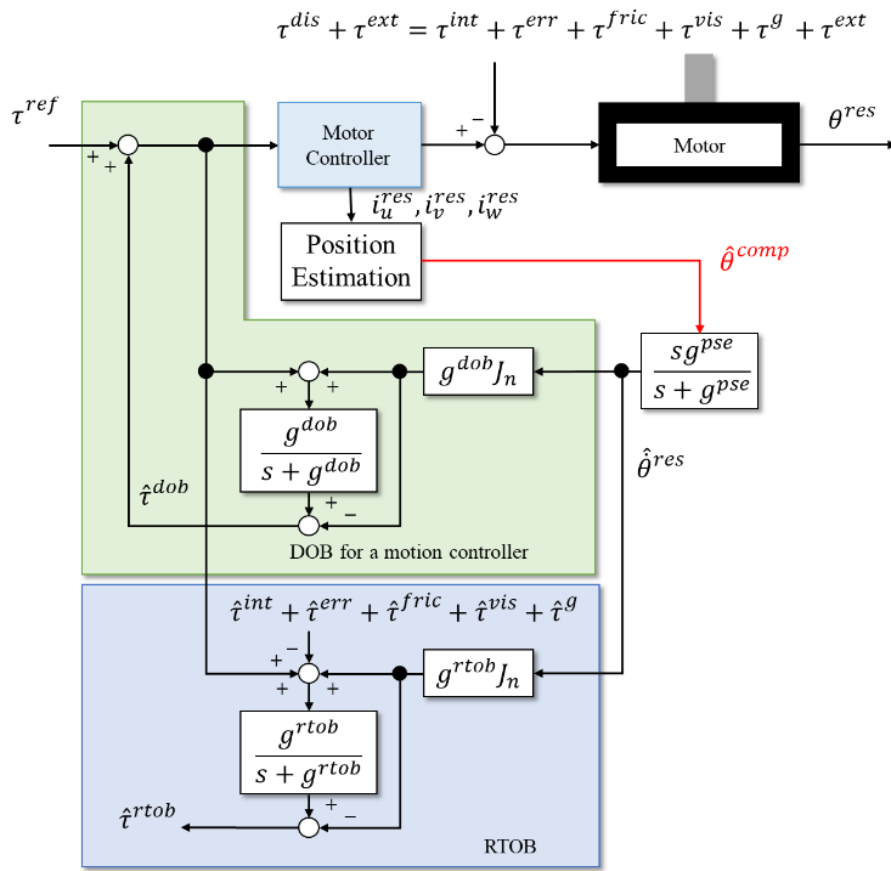
Fig. 7-1: DOB and RTOB using estimated position.

7.2   Proposed PFSL Admittance Control

This section explains the proposed PFSL admittance control systems.

Admittance controllers are outside the position control loop and derive the position and velocity command from the force command and force response to realize the desired admittance or impedance between the control targets and the contact objects. General industrial position control systems have a P-PI controller, which derives velocity command from the position controller. Therefore, the utilized admittance controller derives only position command in this dissertation. Since the integral control is implemented in the velocity control part, DOB is not used for the disturbance compensation. The block diagram of the admittance control with estimated position is expressed in Fig. 7-2.
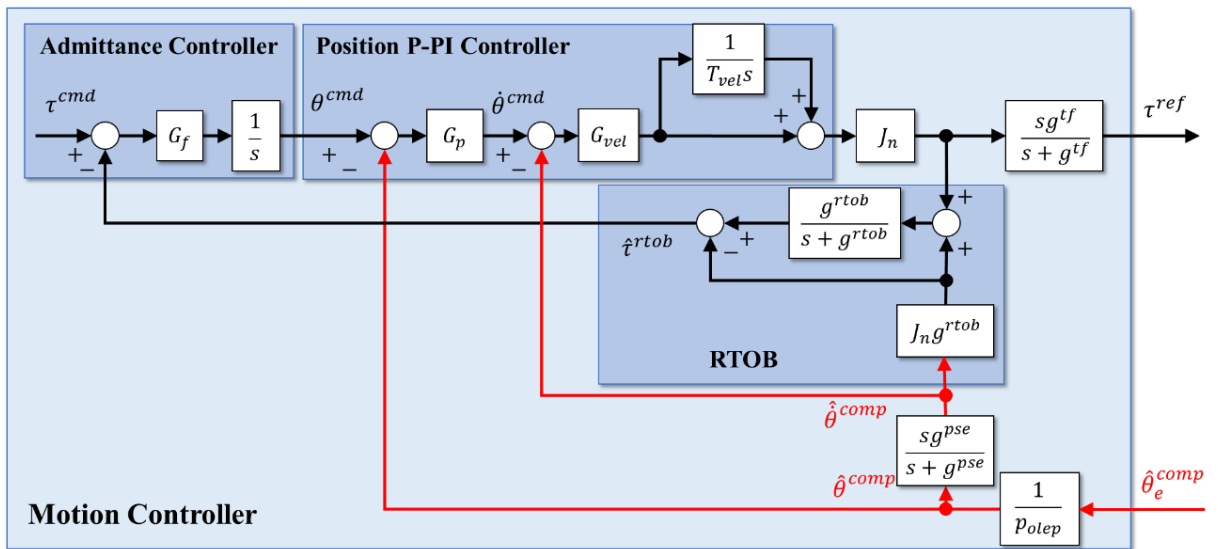
Fig. 7-2: Block diagram of the proposed PFSL admittance control.

7.3   Experiments with the Proposed PFSL Admittance Control

This section shows the experimental setup and results of the proposed PFSL admittance control.

The experimental system shown in Fig. 7-3 was utilized. The control parameters for the proposed PFSL admittance control are described in Table 7.1. The control was compared with the PFSL admittance control without compensation in the low-frequency bandwidth described in Section 5.5. The experimental results are expressed using superscripts $\bigcirc^{high}$ and $\bigcirc^{prop}$. The torque command was 0.13 Nm. The load torque was a sinusoidal chirp signal, whose amplitude was 0.13Nm and frequency was from 0 Hz to 3 Hz. The load imitates contact with flexible objects. Frequency analysis of the estimated torque could confirm the intended RTOB output and unintended vibrations.

The experimental results are shown in Fig. 7-4, Fig. 7-5, and Fig. 7-6. According to Fig. 7-4 and Fig. 7-5, the test motor rotation was varied according to the load torque. Therefore, a flexible motion was achieved. However, the position responses were different though the load torque was the same. The green dashed line in Fig. 7-4 shows the desired position command from the load torque. The effect was removed from the desired position command since the identified dynamic friction value was 0.025 Nm. The position response by the proposed method was much similar to the desired position command. Fig. 7-6 shows the FFT results of RTOB output from 1.1 s to 7.5 s (6400 sampling points). In the FFT results, the peak levels of the proposed method were smaller than those of the conventional method over 5 Hz. The FFT results of the estimated torque by the proposed method were much similar to those of the load torque. When the feedback torque information has an error, the admittance control response cannot achieve the desired performance. In addition, since the undesired vibration in the estimated reaction torque makes it hard to tune the force controller, the proposed method is suitable for PFSL control systems.
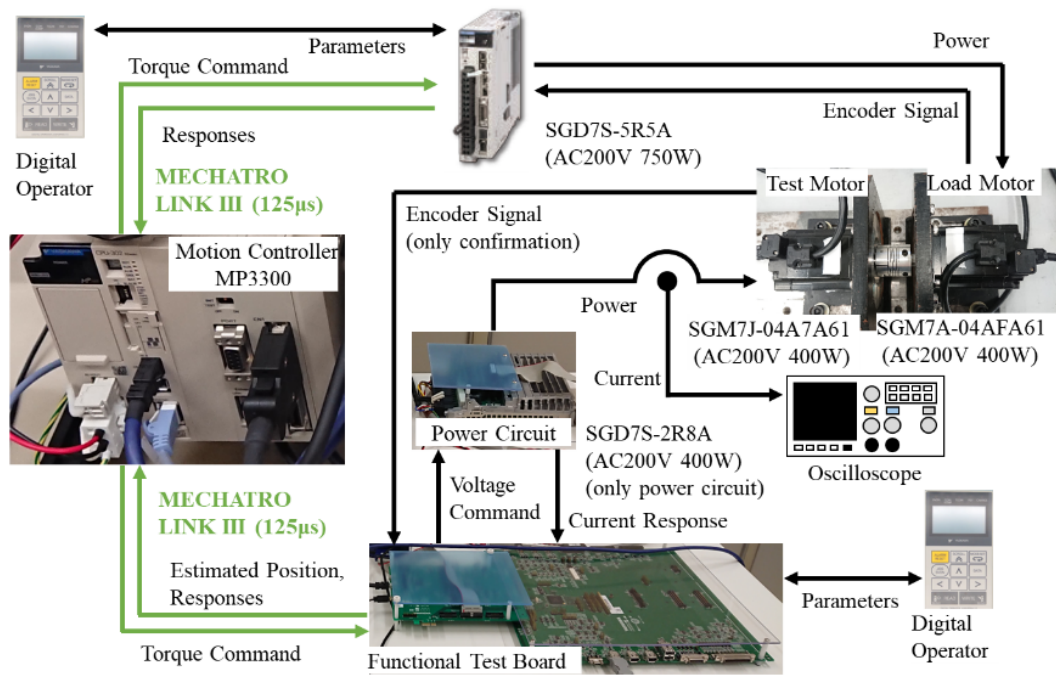
Fig. 7-3: System configuration for experiments to confirm the validity of the proposed PFSL admittance control.

Table 7.1: Control parameters for experiments of the proposed PFSL admittance control.

Parameter	Values
Sampling Period (Motion) (μs)	125
Estimation Period (Position) (μs)	94
Torque Proportional Gain (rad/s/Nm)	185
Position Proportional Gain (1/s)	48
Velocity Proportional Gain (rad/s)	192
Velocity Integral Gain (s)	0.0156
Cut-off frequency for Torque Command (rad/s)	250
Cut-off frequency of Compensation (rad/s) g^{sen}	10667
Cut-off frequency of Compensation (rad/s) g^{low}	760
Cut-off frequency of Pseudo Derivation (rad/s) g^{pse}	127
Cut-off frequency of RTOB (rad/s) g^{rtob}	62.8
Cut-off frequency of DOB (rad/s)	62.8
Gain in Position Estimation g_h	0.5
Gain in Error Estimation g^{comp}	0.025
SMC Gains $\boldsymbol{p}^{\mathrm{T}}$ for the hyperplane	$\begin{bmatrix} 91 & 0.07 & 1 & 1.6 \times 10^{-5} \\ 1 & 1.6 \times 10^{-5} & 91 & 0.07 \end{bmatrix}$
SMC Non-linear Gain	50
Cut-off frequency of VDOB (rad/s)	1280

Fig. 7-4: Position command and responses in experiments to confirm the validity of the proposed PFSL admittance control.
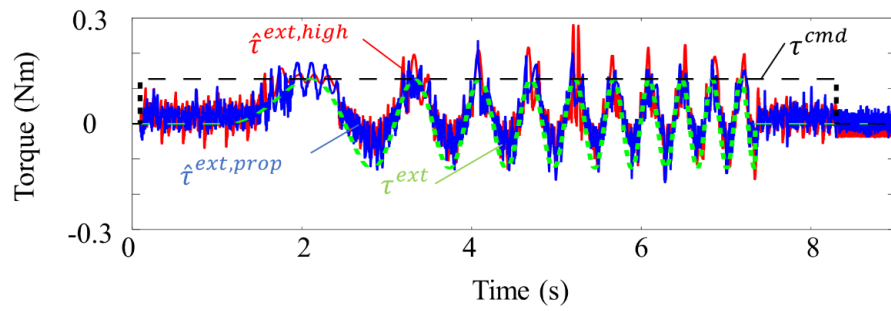
Fig. 7-5: Torque command and estimated torque in experiments to confirm the validity of the proposed PFSL admittance control.
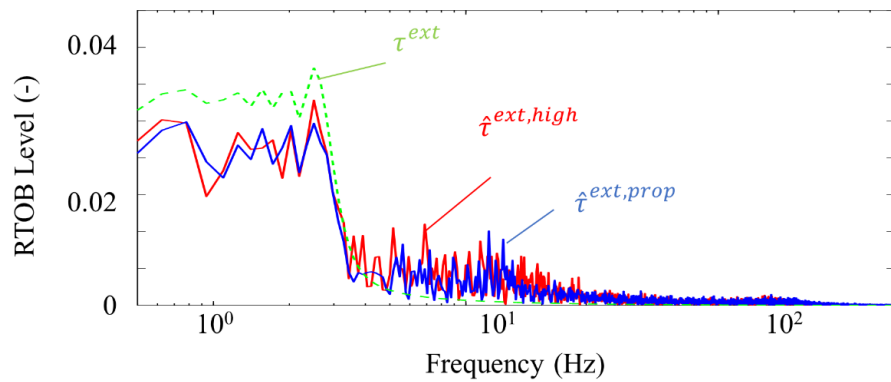
Fig. 7-6: FFT results of the estimated torque in experiments to confirm the validity of the proposed PFSL admittance control.

7.4   Proposed PFSL 4ch-Bilateral Control

This section explains the proposed PFSL 4ch-bilateral control systems.

4ch-bilateral control systems have "main" and "remote" systems. The "main" systems are used by operators, and the "remote" systems work to realize tasks at remote places. The control goals of the 4ch-bilateral control are to achieve the positional following (differential mode) and the action-reaction law (common mode) between the "main" and "remote" systems. In this dissertation, the "main" system is the force-sensorless system, and the "remote" system is the PFSL system to imitate the systems in harsh environments. Since the "main" system can be in the same place as the operator and include the position sensor attached to the motor, the current control system can be used in the standard system in servo-amplifier products. The control goal can be expressed by eq. (7.1) and eq. (7.2).

$$\theta_{dif} = \frac{1}{2} \left(\theta_{main} - \theta_{remo} \right) = 0 \tag{7.1}$$

$$\tau_{com} = \frac{1}{2} \left(\tau_{main} + \tau_{remo} \right) = 0 \tag{7.2}$$

The "remote" system is the PFSL system. The information of θ_{remo} is $\hat{\theta}_{remo}^{comp}$ in the controller. Since RFOB/RTOB with short sampling time and high-resolution position sensors can estimate external force/torque in wider bandwidth than F/T sensors, 4ch-bilateral control systems often have RFOB/RTOB. The information of τ_{main} and τ_{remo} is the estimated value in the controller. In PFSL systems, DOB is applied to each mode, and RTOB is applied to each system. Achieving the control target in each mode is more important than the instantaneous tracking performance of each system in 4ch-bilateral control systems. The block diagram can be expressed in Fig. 7-7. The common mode controller was a proportional controller, and the differential mode controller was a proportional-differential controller.

The "remote" system utilizes the proposed position and cross-coupling factors estimation and the proposed current controller using SMC and VDOB. Even if the same type of motor is used, there will be differences in the characteristics exhibited by the motor between the "main" and "remote" systems. However, this can be compensated for because DOB is applied in each mode.
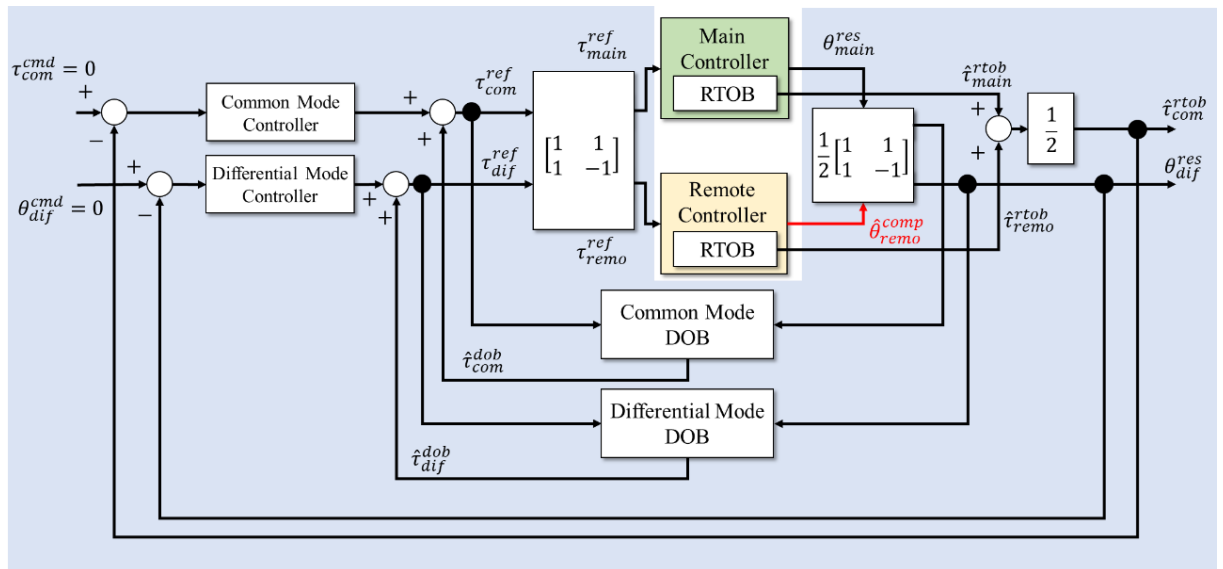
Fig. 7-7: Block diagram of the 4ch-bilateral control with the PFSL system in the "remote" controller.

7.5 Experiments with the Proposed PFSL Bilateral Control

This section shows the experimental setup and results of the proposed 4ch-bilateral control, including the PFSL control system in the "remote" system.

The experimental system shown in Fig. 7-8 was utilized. The control parameters are described in Table 7.2 A handle was attached to each motor. The handle in the "main" system was used by the operator, and the handle in the "remote" system rotated and contacted the aluminum block. The operation consisted of two back-and-forth free motions and two pressing movements against the aluminum block. The pressing movements were finished when the user felt the large reaction force, and the handle was released. The experimental results are shown in Fig. 7-9, Fig. 7-10, Fig. 7-11, and Fig. 7-12.

The position responses and estimated position are shown in Fig. 7-9. The position sensor values in the "remote" system are obtained to confirm the estimation error effect. The estimated torque values are shown in Fig. 7-10. The estimated torque $\hat{\tau}_{m,remo,enc}^{rtob}$ was derived by the torque command and the position response by the position sensor. Although the values were not used in the control, they were obtained to confirm the estimation accuracy of the estimated torque by the estimated position. In free motion, although the differential mode responses had errors and delays, the position response in the "main" system and the estimated position in the "remote" system followed each other. In contact motion, since the "remote" system contacted the aluminum block, the position could not move. On the other hand, the "main" system's position was varied. The action-and-reaction was achieved. Therefore, although the operator could not know the actual stiffness of the aluminum block, could detect the contact and feel the reaction force. The reason for the differential mode error was considered the low controller gain in the differential mode.
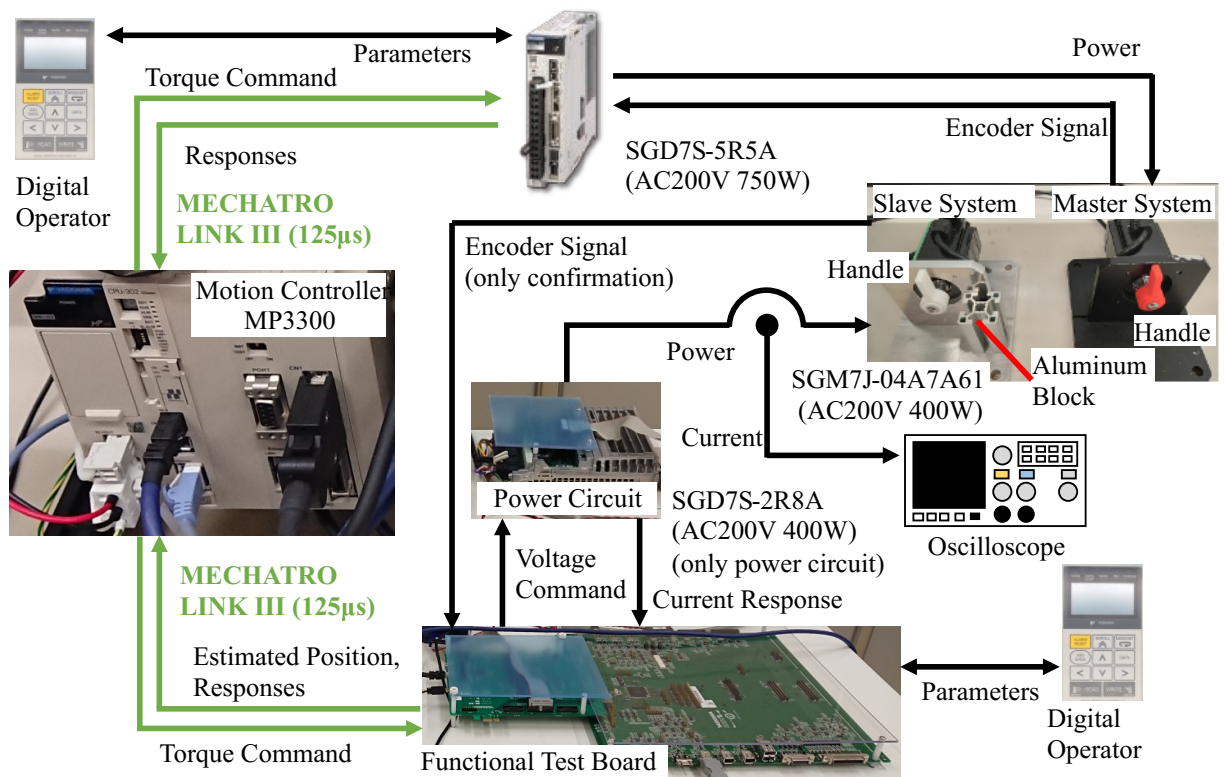
Fig. 7-8: System configuration for experiments for the proposed PFSL bilateral control.

Table 7.2: Control parameters for experiments for the proposed PFSL bilateral control.

Parameter	Values
Sampling Period (Motion) (μs)	125
Estimation Period (Position) (μs)	94
Position Proportional Gain ($1/s^2$)	3948
Velocity Proportional Gain ($1/s$)	125
Cut-off frequency of Compensation (rad/s) g^{sen}	10667
Cut-off frequency of Compensation (rad/s) g^{low}	760
Cut-off frequency of Pseudo Derivation (rad/s) g^{pse}	127
Cut-off frequency of RTOB (rad/s) g^{rtob}	62.8
Cut-off frequency of Common mode DOB (rad/s)	31.4
Cut-off frequency of Differential mode DOB (rad/s)	62.8
Gain in Error Estimation g^{comp}	0.025
SMC Gains $\boldsymbol{p}^{\mathbf{T}}$ for the hyperplane	$\begin{bmatrix} 91 & 0.07 & 1 & 1.6 \times 10^{-5} \\ 1 & 1.6 \times 10^{-5} & 91 & 0.07 \end{bmatrix}$
SMC Non-linear Gain	50
Cut-off frequency of VDOB (rad/s)	1280

Fig. 7-9: Position command and responses in experiments for the proposed PFSL bilateral control.
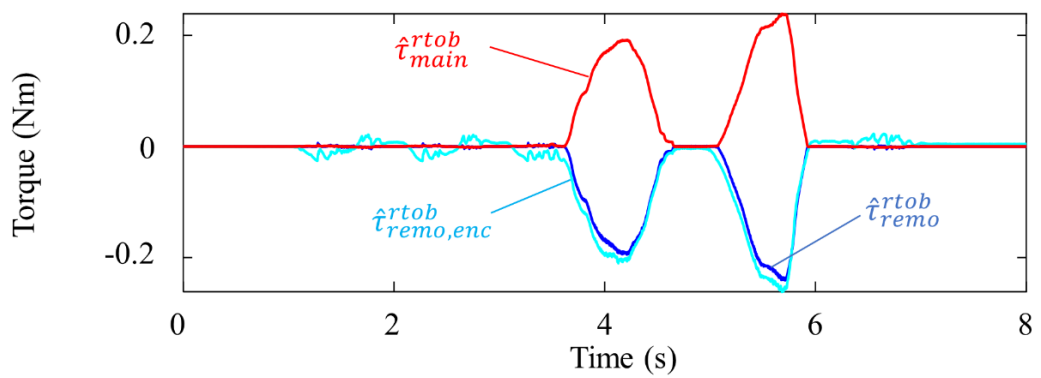
Fig. 7-10: Estimated torque in experiments for the proposed PFSL bilateral control.
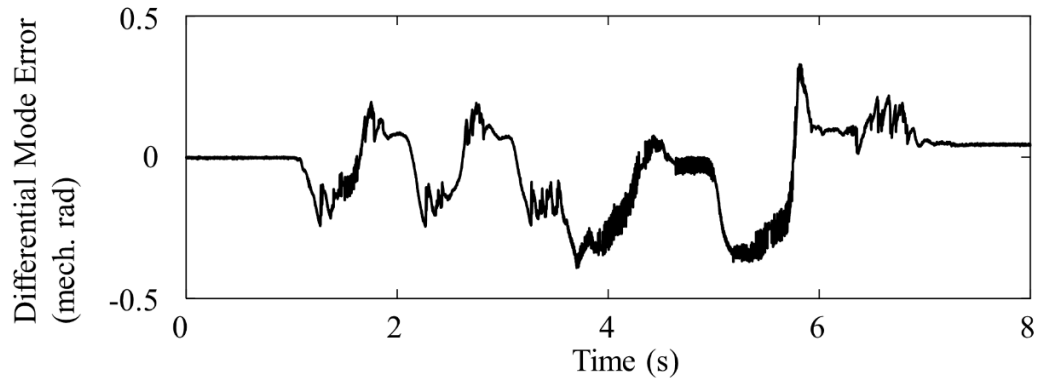
Fig. 7-11: Differential mode errors in experiments for the proposed PFSL bilateral control.
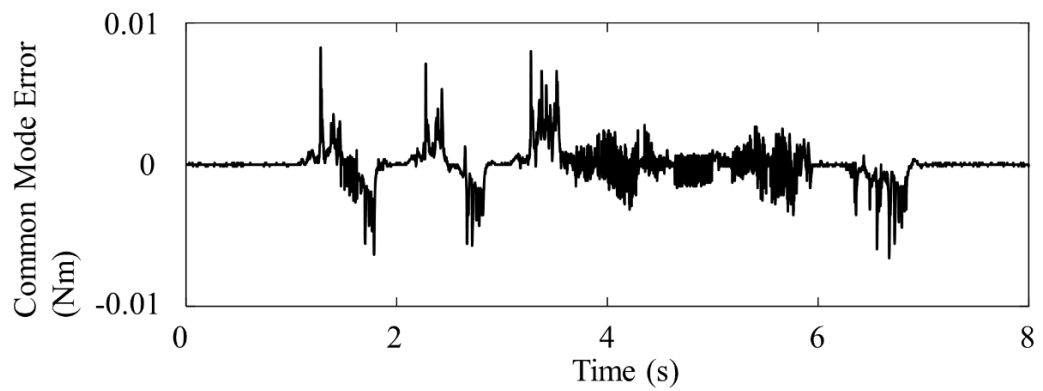
Fig. 7-12: Common mode errors in experiments for the proposed PFSL bilateral control.

7.6   Proposed PFSL Hybrid Position/Force Control

This section explains the proposed PFSL hybrid position/force control system for rubbing motion.

As described in Chapter 4 and experimental results in Section 5.7, the PFSL control systems' positioning performance is insufficient. When the estimated position has vibrations, the controller, WOB, and RFOB output values also have vibrations. In MDOF control systems, the vibrations in each control axis affect each other as a disturbance. By decoupling position control axes and force control axes, the circulation of the effects from the position estimation errors and vibrations can be reduced. The same design method of equivalent mass matrices in the controller, WOB, and RTOBwCT is utilized in the proposed PFSL hybrid control system. The block diagram of the proposed PFSL hybrid control system for rubbing motion is expressed in Fig. 7-13. Since the resolution of the estimated position depends on current detection systems, whose resolution is generally smaller than the resolution of position sensors, LPFs are utilized to derive the mechanical joint angles. These LPFs can reduce the noise and increase the resolution in integer arithmetic.
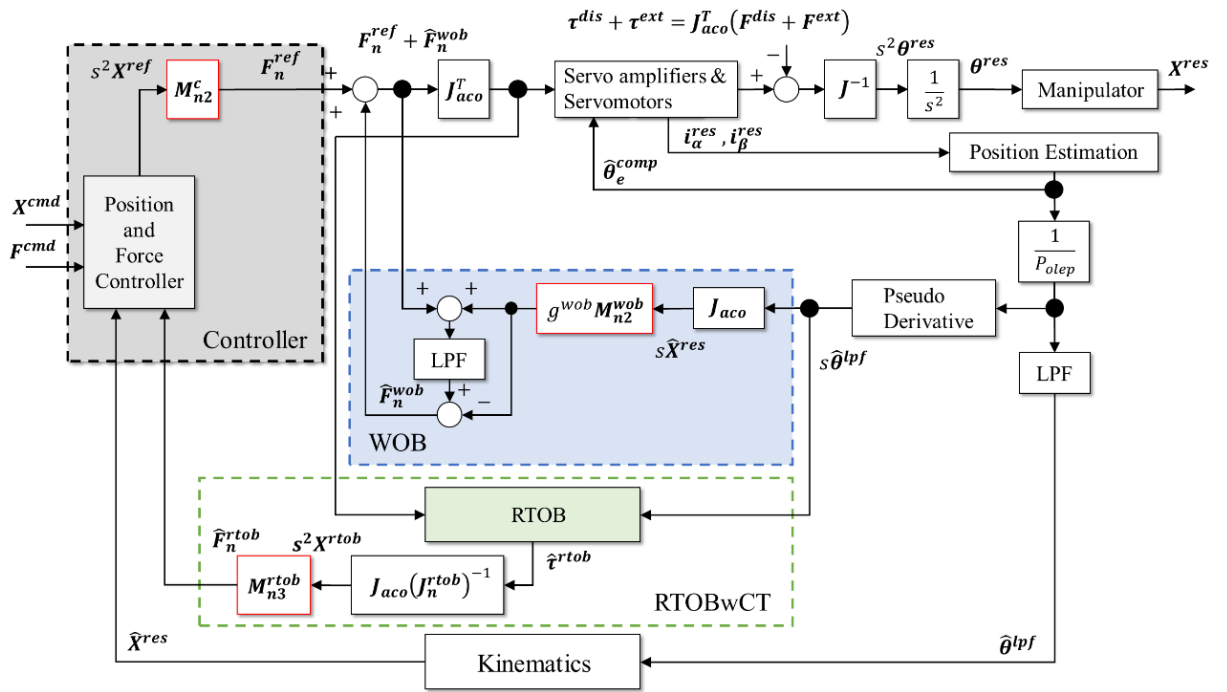
Fig. 7-13: Block diagram of the PFSL hybrid control system for rubbing motion.

7.7 Experiments with the Proposed PFSL Hybrid Control

This section shows the experimental setup and results of the proposed PFSL hybrid control system using a 4DOF manipulator.

7.7.1 Setup and Parameters for Experiments of PFSL Hybrid Control Systems

The experimental system shown in Fig. 7-14 was utilized. The link length and the kinematic model are the same as the manipulator shown in Fig. 6-6. The differences are the utilized motors and the material of the links. As a result, the frictional force of the manipulator was larger than the manipulator in Fig. 6-6. A similar type of motor used in Section 5.7 was used. The material was changed from ABS to aluminum to increase the stiffness of the links.

The rubbing and pushing motions were performed against the force gauge. The frequency characteristics of the pushing motion to the force gauge are also shown in Fig. 7-14. The gain values of frequency characteristics had larger around 30 Hz. The frequency response was obtained by using position sensors attached to the utilized motors and the force gauge, which is the contact target. However, other experiments did not use the detected position and force for the feedback information.

The nominal parameters of the test motor are shown in Table 7.3.

The force responses by two configurations of equivalent mass matrices were compared. One used equivalent mass matrices M_n^c, M_n^{wob}, and M_n^{rtob} shown in eq. (6.3) and eq. (6.4). The index is $\bigcirc_N$. The other used the matrices M with design values in the controller and RFOB. The index is $\bigcirc_M$. The parameters involved in position estimation were the same for each experiment. The control parameters are described in Table 7.4 The validity of the proposed controller was confirmed by two kinds of experimental commands shown in Table 7.5.

"Step" showed the force control performance during contact with the force gauge. "Chirp" showed the cross-coupling effects and the vibration suppression by the proposed method in rubbing motion by sinusoidal command. Force commands were decided according to experimental trial and error. The force command value was allowed to change within a range of about 0.5 N. However, when the value was too small, the manipulator did not move. In addition, when the value was too large, the control diverged.
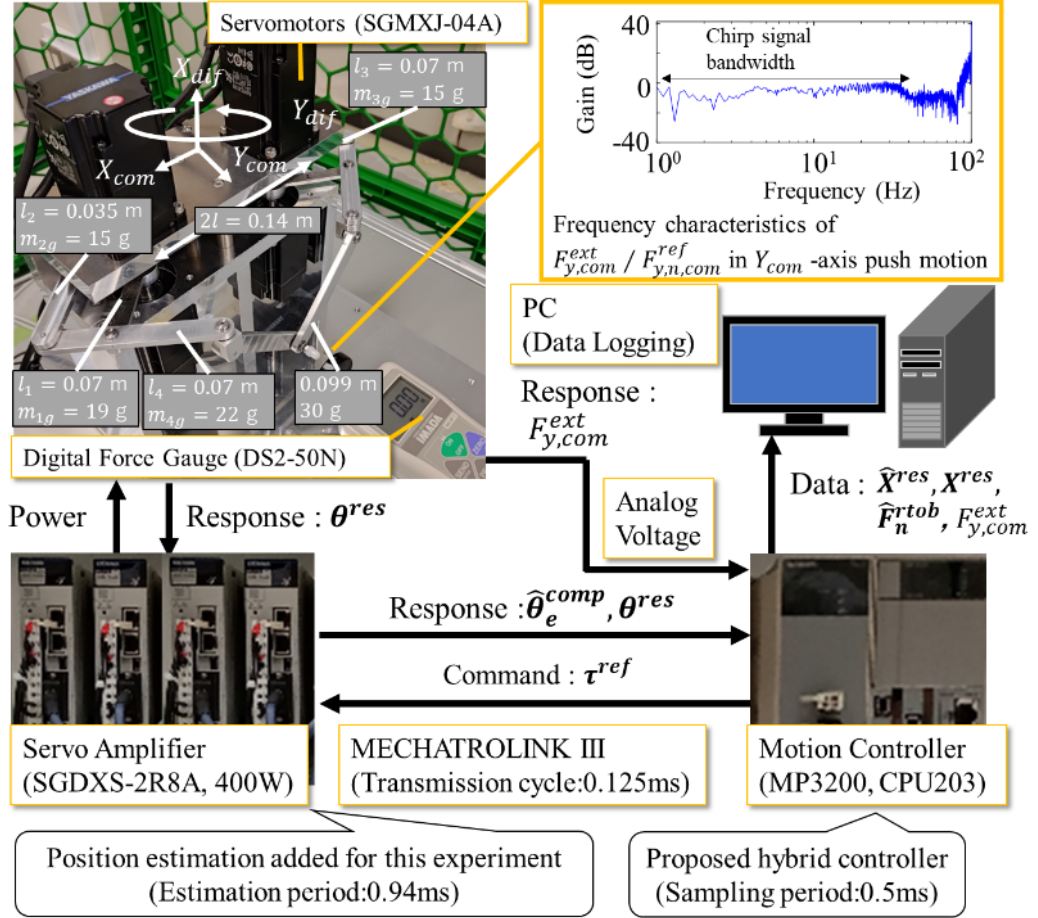
Fig. 7-14: System configuration for experiments to confirm the validity of the proposed hybrid PFSL control.

The acceleration reference values were derived by eq. (7.3).

$$
s^2 \boldsymbol{X^{ref}} = \begin{bmatrix} (G_p + G_{vel}s)\left(X_{dif}^{cmd} - \hat{X}_{dif}^{res}\right) \\ (G_p + G_{vel}s)\left(X_{com}^{cmd} - \hat{X}_{com}^{res}\right) \\ (G_p + G_{vel}s)\left(Y_{dif}^{cmd} - \hat{Y}_{dif}^{res}\right) \\ G_f\left(F_{y,com}^{cmd} - \hat{F}_{y,com}^{rtob}\right) \end{bmatrix} \tag{7.3}
$$

Table 7.3: Nominal parameters of motors in the 4DOF manipulator shown in Fig. 7-14.

Parameter	Value
R (Ohm)	1.4
L_d (mH)	2.6
L_q (mH)	3.1
Torque constant (Nm/A)	0.544
Ψ (V/(elec. rad/s))	0.109
Rotor inertia (kgm^2)	0.486×10^{-4}
Rated Power (W)	400
Rated velocity (mech. rad/s)	314.2
Rated torque (Nm)	1.27
Pole pairs	5

Table 7.4: Control parameters for experiments to confirm the validity of the proposed hybrid PFSL control.

Parameter	Values	Remarks
Sampling Period (Motion) (μs)	500	
Position Estimation Period (μs)	94	
Position Gain G_p (1/s^2)	158	2 Hz
Velocity Gain G_{vel} (rad/s)	25.1	
Force Gain G_f (1/kg)	1	
Cut-off frequency of Torque Filter (rad/s)	250	
Cut-off frequency of Pseudo Differentiation g^{pse} (rad/s)	126	
Cut-off frequency of Position Response (rad/s)	502	
Cut-off frequency of RTOB (rad/s) g^{rtob}	12.6	
Cut-off frequency of DOB (rad/s)	12.6	
Cut-off frequency of Compensation (rad/s) g^{sen}	10667	
Cut-off frequency of Compensation (rad/s) g^{low}	760	
g_h in Position Estimation (-)	0.5	
g^{low} in Position Estimation (rad/s)	251	
g^{comp} in Position Estimation (-)	0.02	
SMC Gains $\boldsymbol{p}^{\mathbf{T}}$ for the hyperplane	$\begin{bmatrix} 91 & 0.07 & 1 & 1.6 \times 10^{-5} \\ 1 & 1.6 \times 10^{-5} & 91 & 0.07 \end{bmatrix}$	
SMC Non-linear Gain	50	
Cut-off frequency of VDOB (rad/s)	1280	

Table 7.5: Relationship between indexes and experimental command.

Index of Experimental Command	$F_{y,com}^{cmd}$ (N)	X_{dif}^{cmd}, X_{com}^{cmd}, Y_{dif}^{cmd} (m)
Step	Step signal: $F_{y,com}^{cmd} = 1.2$ and 1.5	$X_{dif}^{cmd} = 0.066$, $X_{com}^{cmd} = 0.0$, $Y_{dif}^{cmd} = 0.0$
Chirp	Constant value: $F_{y,com}^{cmd} = 1.5$	$X_{dif}^{cmd} = 0.068 - 0.002\cos 0.04 \cdot 2\pi t^2$ $X_{com}^{cmd} = 0.004\sin 0.04 \cdot 2\pi t^2$, $Y_{dif}^{cmd} = 0.0$

7.7.2   Results of "Step"

Experimental results of the detected force and estimated force in "Step" are shown in Fig. 7-15. The detected and estimated force was similar to each condition and followed the external force, although the force vibrated. The detected force had a steady state error of about 0.2 N. The reasons for the error were the output torque error by position estimation error and the friction in the manipulator. According to the rising time, the responsiveness can be considered 2 Hz, a similar value to the cut-off frequency of RTOB. These results show that the proposed PFSL control system can achieve pushing motion by force control without other axes' motion.
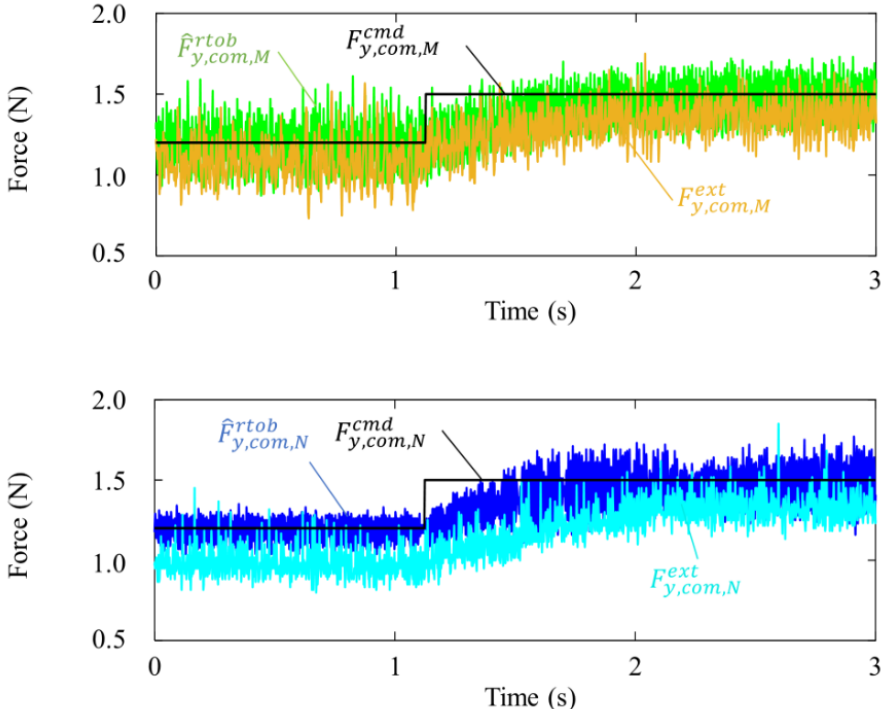
Fig. 7-15: Force step responses for experiments to confirm the validity of the proposed hybrid PFSL control.

7.7.3 Results of "Chirp"

The command and response in each axis are shown in Fig. 7-16. The position tracking performance needed to be improved in both configurations of equivalent mass matrices. The force response $F^{ext}_{y,com,M}$ by the equivalent mass matrix with design values had 0 values and vibrations around 8 s. Since the force gauge could detect only pushing force, the response indicates that the end-effector bounced back from the contact surface of the force gauge. On the other hand, the force response $F^{ext}_{y,com,N}$ with the proposed design method did not have 0. The end-effector could keep in contact. According to the result in Fig. 7-16 and Chapter 4, the proposed PFSL control system can achieve the rubbing motion. The FFT results of the detected force show the reasons for the unsatisfactory performance of the PFSL control system. The FFT results are shown in Fig. 7-17. The peaks by the proposed PFSL control system were lower than those by the PFSL control system using an equivalent mass matrix with design values. The experimental results show that the proposed position-sensorless control system and the equivalent mass matrix design method reduced the vibrations on the force control axis and realized the rubbing motion keeping contact.
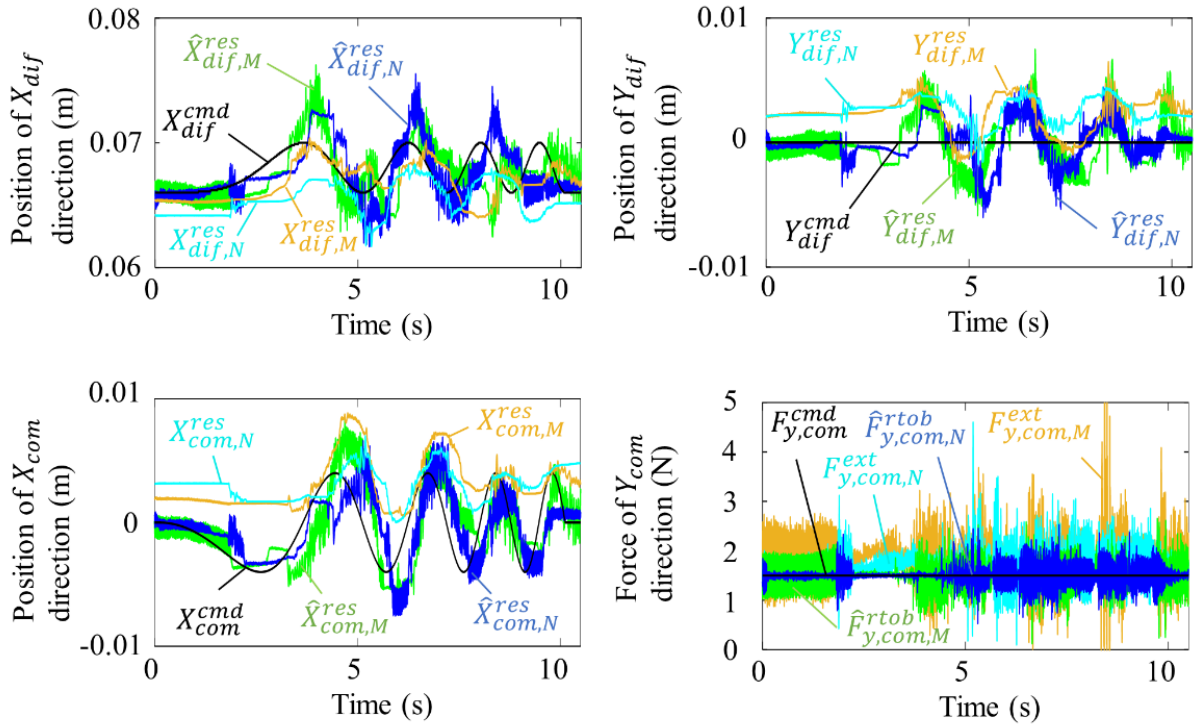
Fig. 7-16: Time series commands and responses of rubbing motion with hybrid PFSL control.
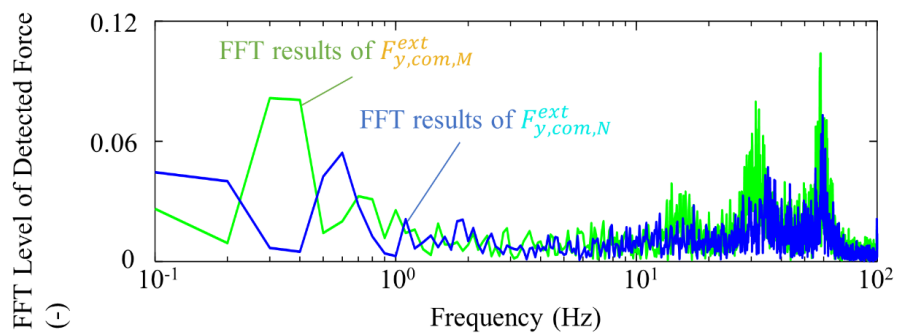
Fig. 7-17: FFT results of $F_{y,com}^{ext}$ in experiments to confirm the validity of the proposed hybrid PFSL control.

7.7.4 Discussion

According to Fig. 7-17, the responses had peaks around 15 Hz, 30 Hz, and 60 Hz. The frequency characteristics by pushing motion, shown in Fig. 7-14, indicated the mechanical system had gain peaks around 30 Hz. In addition, as a separate experiment, the vibration of the position estimation at the electric angle of the motor during the rubbing motion was confirmed. The data acquisition method was the same as in Section 5.7. The FFT result of the estimated position is shown in Fig. 7-18. The peak was around 67 Hz. Therefore, the vibrations on the force control axes were from the mechanical characteristics and the estimated position. The proposed PFSL hybrid control system reduced the mechanical and electrical cross-coupling effects on the force response during the rubbing motion. According to Chapter 4, a conventional position-sensorless control method could not achieve the rubbing motion. The validity of the proposed methods described in Chapter 5 and Chapter 6 was confirmed.

The reason for the unsatisfactory performance of the position control axes was the low gain from the errors and vibrations in the estimated position. The position estimation error means that some electrical angles cannot be achieved. The control systems vibrate if even one of the four axes fails to reach the electrical angle required for position synchronization for workspace motion. The solution is the improvement of the position estimation accuracy. Although the proposed methods realized rubbing motion by the PFSL control system, further position estimation accuracy is essential for practical use.
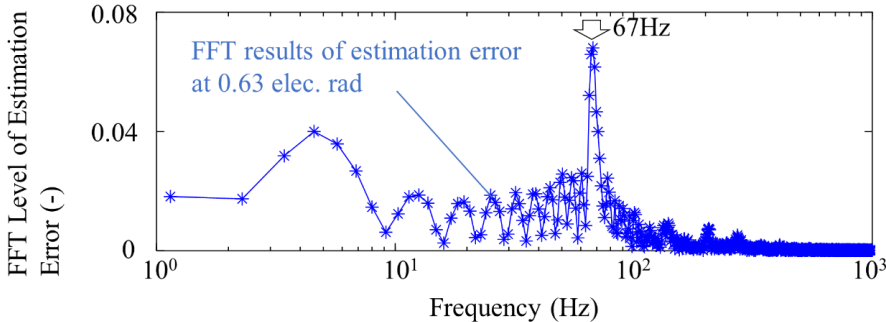
Fig. 7-18: FFT results of $\hat{\theta}_e^{comp}$ in experiments to confirm the validity of the proposed hybrid PFSL control.

7.8 Summary

This dissertation proposes the PFSL control systems. The PFSL control systems comprise the proposed methods described in Chapters 5 and 6. The results of the admittance control, the 4ch-bilateral control, and the hybrid position/force control were confirmed. The proposed methods improved the PFSL force control performance. The vibration of the reaction force was reduced. The feeling of contact can be transmitted from the "remote" system to the operator of the "main" system without position and force sensors in the "remote" system. In addition, the rubbing motion with the 4DOF manipulator could keep contact with the force gauge. The proposed methods in Chapters 5 and 6 realized pushing and rubbing motion with the PFSL control system. However, since the position estimation error is not zero, the positioning performance and the control gains are still insufficient. Even the performance of the proposed control method was unsatisfactory compared to the performance required in actual applications. Further improvement of position estimation accuracy is required.

Chapter 8

Conclusions

8.1 Conclusions of This Dissertation

Realization of position-and-force-sensorless (PFSL) robots is expected to extend applications of robots outside the factory. Those applications often require the force control function for flexible or contact operations. One of the examples of contact operation is rubbing motion. However, the control performance of PFSL systems with conventional methods needs to be improved for practical use. PFSL control systems consist of position-sensorless and force-sensorless control systems and utilize estimated position and force as feedback information. Since force estimation uses the estimated position, the performance improvement of position estimation is required as the fundamental technology. In addition, cross-coupling effects between position and force control axes decrease the force control performance of multi-degree-of-freedom (MDOF) systems. The cross-coupling effects can be expressed by the equivalent mass matrix. In PFSL control systems, the external force and the estimated position errors cause vibrations in position control axes. The cross-coupling effects from position control axes to force control axes cause vibrations in force control axes. A PFSL robot with a conventional position estimation method and an equivalent mass matrix with design values could not work. Therefore, position-sensorless control systems and an equivalent mass matrix design method for hybrid position/force control systems were proposed.

In Chapter 5, position-sensorless control methods considering the cross-coupling factors are described. Cross-coupling factors express the distortion of the magnetic flux vectors in motors and cause position estimation errors. The cause of the cross-coupling factors was explained by introducing the voltage

equation for IPMSMs, which takes into account the distortion of the magnetic flux vector. The position and cross-coupling factors estimation methods were proposed based on the introduced voltage equation. Unlike conventional methods, the method did not require reference tables from previous experiments or analyses. Since the current control model was based on the introduced voltage equation, the estimated cross-coupling factors were used in the controller and the conversion between the torque reference and the current command. The experimental results showed the position estimation error reduction, the vibration reduction, and the improvement of robustness to the disturbance. Although further improvement is essential concerning position estimation accuracy, it is clarified that position estimation and current control methods considering the cross-coupling factors can improve position-sensorless control systems.

In Chapter 6, the effect of the equivalent mass matrices in hybrid position/force control for MDOF systems was explained, and the suitable matrices for free motion and contact motion were discussed. Since an equivalent mass matrix can express the mass in the workspace motion, the non-diagonal elements show the cross-coupling effects between the workspace control axes. In free motion, an accurate model is important for stable operation. When the manipulators move fast, WOB with the equivalent mass matrix using design values can work accurately. On the other hand, in contact motion at low speed, the reaction force control is more important than stability. Since the non-diagonal elements of the equivalent mass matrix transport the disturbance effects from the position control axes to the force control axes in the force dimension, the decoupling between the position control axes' motion and the force control axes' motion is required. Therefore, the equivalent mass matrices with zero values in the non-diagonal elements for position and force control axes were introduced. The hybrid position/force control with switching of equivalent mass matrices was proposed. The switching depends on the expected velocity of the force control axes. The equivalent mass matrix decoupled the position control axes' motion and the force control axes' motion during contact. The disturbance, including vibrations, did not circulate between the position and force control axes. The experimental results showed the vibration reduction of the force control axes in the rubbing motion on hard objects.

In Chapter 7, the proposed PFSL control systems were described. In the PFSL control systems, DOB (WOB) and RFOB (RTOB) utilize the estimated position rather than position responses obtained from position sensors. With the improved position estimation accuracy and robustness of position-sensorless control systems by the proposed methods in Chapter 5, the vibration of the estimated force/torque in admittance control and 4ch-bilateral control with PFSL control systems is reduced. In MDOF PFSL hybrid position/force control systems, equivalent mass matrices described in Chapter 6 were used to

Table 8.1: Comparing the target bandwidth and achieved bandwidth.

Description	Force Control	Force Estimation	Position Control	Position Estimation
Goal	10 Hz	20 Hz	10 Hz	200 Hz
Current	-	-	2 Hz (1 axis)	20 Hz (1 axis)
Proposed(1DOF)	3 Hz	10 Hz	10 Hz	1.7 kHz
Proposed(MDOF)	0.1 Hz	2 Hz	2 Hz	1.7 kHz

decouple the position and force control axes' motion. The decoupling function suppressed the vibration from the position estimation. As a result, although the vibration and the control bandwidth were still insufficient for practical use, the rubbing motion keeping contact with the contact target was realized by combining the proposed methods.

This dissertation reveals the effectiveness of considering cross-coupling factors in the dq-axes inductance of IPMSMs in position-sensorless control systems and cross-coupling effects by the equivalent mass matrix in workspace control. The target bandwidth and the achieved bandwidth expressed by the controller gains are compared in Table 8.1. Although the achieved bandwidth of the gain setting in the force control and force estimation was lower than the goal, the bandwidth was expanded and improved. On the other hand, the bandwidth of the position control and position estimation gains for 1DOF achieved the goal. Since position estimation errors and vibrations disturb the synchronization of each joint in MDOF systems, the position control gain could not achieve the goal. Therefore, although the validity of the proposed methods can be confirmed, further position estimation error reduction is future work.

8.2 Future Work and Prospects

The fundamental problem of PFSL robots is position estimation errors and vibrations. The validity of the proposed equivalent mass matrices was confirmed by using detected values by position sensors. According to the simulation in Section 5.1, the desired maximum value of the position estimation error is 0.06 elec. rad. However, the proposed method could not achieve the desired goal. In position-sensorless control, the remained modeling error is from the axis of the utilized current. Modeling based on the actual dq-axes current has been used in this dissertation, assuming convergence of the estimated dq-axes to the actual dq-axes. Therefore, the next step is modeling based on the estimated dq-axes, and similar algorithms and findings could be used. Reducing the position estimation errors may increase the bandwidth of control and estimation. The proposed PFSL control system uses the estimated position and force derived from the common information of the detected current. The proposed configuration is considered more accessible to synchronize position and force data compared to the case where position and force data are obtained from a position sensor and a force sensor. Since hybrid control controls position and force simultaneously, the increased bandwidth may make the control systems more stable than sensor use. Furthermore, the confirmation of the robustness of the disturbance was on the load torque in the steady state. The load torque of each joint of robots dynamically varies with the posture and the motion of tasks. In addition, the temperatures of motors and environments around the robots also change during prolonged operation. As temperature varies, resistance and magnetic characteristics vary. Although position estimation methods by high-frequency voltage injection have the robustness of resistance variation, they are affected by the variation of the magnetic characteristics. The variation of the magnetic characteristics causes the variation of the cross-coupling factors in the dq-axes inductance. The proposed method corresponds to the dynamic variation of the cross-coupling factors. Therefore, some of the effects can be compensated by the proposed methods by using nominal inductance values of L_d and L_q in the application environments. However, the other adverse effects should also be confirmed and compensated for practical use. These issues in actual operation also need to be evaluated per applications in future work.

The proposed method improved the performance of the 1DOF position-sensorless system itself. Since cross-coupling factors relate to the magnetic saturation and resistance, the effects are significant in high-torque density IPMSMs. Therefore, the proposed method may contribute to the downsizing of IPMSMs for general position-sensorless control systems.

Since the position estimation accuracy is lower than that of position sensors, tasks requiring precise motion do not suit PFSL robots. However, the desired characteristics in applications requiring force control functions differ from those for precise positioning. The reaction force/torque can be more important than the instantaneous position-tracking error during contact motion, including rubbing motion. The advantages of PFSL robots with the proposed methods are mechanical robustness, cost, and size. For example, tasks in farms, construction, and welfare require force control functions and these characteristics. MDOF robots have not yet been widespread in these environments. PFSL robots are expected to develop these markets and contribute to a more productive society.

References

[1] Ministry of Education, Culture, Sports, Science and Technology: "White Paper on Science and Technology 2020," Nikkei Printing, 2020.

[2] Investigating R & D Committee on New Technologies for Industry Applications of PM motors: "Trend of New Applications of PM Motors and New Technologies toward their Spread," *IEEJ Technical Report,* vol. 1281, 2013.

[3] Investigating R & D Committee on latest trends of applications of AC motor drives in the users sight: "Trends of AC motor drive application from the users sights," *IEEJ Technical Report,* vol. 1385, 2016.

[4] YASKAWA Electric Corporation, YASKAWA Electric Corporation Centennial Business Office: "YASKAWA," YASKAWA Electric Corporation, 2015.

[5] C. Brosque, E. Galbally, O. Khatib, and M. Fisher: "Human-Robot Collaboration in Construction: Opportunities and Challenges," *2020 International Congress on Human-Computer Interaction, Optimization and Robotic Applications,* pp. 1–8, June 2020.

[6] G. Wonda, V. Amit, and S. V. Kumar: "Analyzing Human Robotic Interaction in the Food Industry," *Journal of physics: Conference Series,* vol. 1714, no. 1, pp.1–21, Jan. 2021.

[7] J. Jum, J. Kim, J. Seol, J. Kim, and H. I. Son: " Towards an Efficient Tomato Harvesting Robot: 3D Perception, Manipulation, and End-Effector," *IEEE Access,* vol. 9, pp. 17631–17640, 2021.

[8] Investigating R & D Committee on Small motors and their control technology to satisfy service robots requirements: "Small motors and their control technology to satisfy service robots requirements," *IEEJ Technical Report,* vol. 1518, 2021.

[9] The Japan Electrical Manufacturers' Association: "INVERTER 2019~2020," The Japan Electrical Manufacturers' Association, 2019.

[10] H. Matsugae, Y. Hatchisu, Y. Nagao and K. Fujita: "DSP-based all digital, vector control induction motor drives for spindle system," *21st Annual IEEE Conference on Power Electronics Specialists,* pp. 636–640, 1990.

[11] L. A. Jones and J. H. Lang: "A state observer for the permanent-magnet synchronous motor," *IEEE Transactions on Industrial Electronics,* vol. 36, no. 3, pp. 374–382, 1989.

[12] M. Schroedl: "Operation of the permanent magnet synchronous machine without a mechanical sensor," *1990 Fourth International Conference on Power Electronics and Variable-Speed Drives,* pp. 51–56, 1990.

[13] S. Ogasawara and H. Akagi: "Implementation and position control performance of a position-sensorless IPM motor drive system based on magnetic saliency," *IEEE Transactions on Industry Applications,* vol. 34, no. 4, pp. 806–812, 1998.

[14] M. J. Corley and R. D. Lorenz: "Rotor position and velocity estimation for a salient-pole permanent magnet synchronous machine at standstill and high speeds," *IEEE Transactions on Industry Applications,* vol. 34, no. 4, pp. 784–789, 1998.

[15] S. Ostlund and M. Brokemper: "Sensorless rotor-position detection from zero to rated speed for an integrated PM synchronous motor drive," *IEEE Transactions on Industry Applications,* vol. 32, no. 5, pp. 1158–1165, 1996.

[16] S. Sul, Y. Kwon and Y. Lee: "Sensorless control of IPMSM for last 10 years and next 5 years," *CES Transactions on Electrical Machines and Systems,* vol. 1, no. 2, pp. 91–99, 2017.

[17] Z. Zhang, C. Hu, Y. Zhang and W. Shen: "Research on High Frequency Voltage Injection Method for PMSM," *2019 14th IEEE Conference on Industrial Electronics and Applications,* pp. 266–269, 2019.

[18] H. -C. Yeh and S. -M. Yang: "Phase Inductance and Rotor Position Estimation for Sensorless Permanent Magnet Synchronous Machine Drives at Standstill," *IEEE Access,* vol. 9, pp. 32897–32907, 2021.

[19] Y. -C. Kwon, S. -K. Sul, N. A. Baloch, S. Murakami and S. Morimoto: "Design and Control of IPMSM Sensorless Drive for Mechanical Rotor Position Estimation Capability," *IEEE Journal of Emerging and Selected Topics in Power Electronics,* vol. 2, no. 2 pp. 152–158, 2014.

[20] Y. -C. Kwon, S. -K. Sul, N. A. Baloch, S. Morimoto and M. Ohto: "Design, Modeling, and Control of an IPMSM With an Asymmetric Rotor and Search Coils for Absolute Position Sensorless Drive," *IEEE Transactions on Industry Applications,* vol. 52, no. 5, pp. 3839–3850, 2016.

[21] R. Wang, H. Huisman and J. Persoon: "Sensorless Wide Speed Range Position Estimation Method for Permanent Magnet Synchronous Machines," *2021 23rd European Conference on Power Electronics and Applications (EPE'21 ECCE Europe),* pp. 1–8, 2021.

[22] X. Wu et al.: "Hybrid Position Estimation Strategy With a Smooth Transition for IPMSM Sensorless Drives in the Wide Speed Range," *IEEE Transactions on Power Electronics,* vol. 37, no. 7, pp. 7916–7927, 2022.

[23] K. Ide, M. Takaki, S. Morimoto, Y. Kawazoe, A. Maemura and M. Ohto: "Saliency-based Sensorless Drive of Adequate Designed 1PM Motor for Robot Vehicle Application," *2007 Power Conversion Conference,* pp. 1126–1133, 2007.

[24] A. Yamazaki and K. Ide: "Application trend of saliency-based sensorless drives," *2014 International Power Electronics Conference,* pp. 933–936, 2014.

[25] Z. Li et al.: "Sensorless Starting Control of Permanent Magnet Synchronous Motors with Step-up Transformer for Downhole Electric Drilling," *IECON 2018 - 44th Annual Conference of the IEEE Industrial Electronics Society,* pp. 689–694, 2018.

[26] The Japan Electrical Manufacturers' Association: "SERVO SYSTEM 2021˜2022," The Japan Electrical Manufacturers' Association, 2021.

[27] E. Nakano: "Mechanisms and Controls of Multi-jointed Manipulators," *Journal of The Society of Instrument and Control Engineers, vol. 15, no. 8, pp. 637–644, 1976.*

[28] T. Imamura: "Point of view from a robot manufacturer," *Journal of the Robotics Society of Japan, vol. 8, no. 1, pp. 66–69, 1990.*

[29] M. Jinno, F. Ozaki, T. Yoshimi, K. Tatsuo, M. Takahashi, M. Kanda, Y. Tamada, and S. Nagataki: "Development of a force controlled robot for grinding, chamfering, and polishing," *Proceedings of 1995 IEEE International Conference on Robotics and Automation,* pp. 1455–1460, 1995.

[30] G. Ferretti, G. Magnani and P. Rocco: "Toward the implementation of hybrid position/force control in industrial robots," *IEEE Transactions on Robotics and Automation,* vol. 13, no. 6, pp. 838–845, 1997.

[31] K. Saeki, N. Nishioki, N. Suzuki, and K.Okada: "Development, Design, and Production of Capacitive 6-Axis Force Sensor," *Journal of the Japan Society for Precision Engineering,* vol. 84, no. 4, pp. 307–310, 2018.

[32] S. Suzuki, Y. Kawai, Y. Yokokura, K. Ohishi, T. Miyazaki, T. Shinozaki: "Single-Inertialization Based on High-Backdrivability Control Using Equivalent Disturbance Compensator for Human Interaction Robot," *IEEJ Journal of Industry Applications,* vol.10, no. 3, pp. 282–291, 2021.

[33] F. Sherwani, M. M. Asad and B. S. K. K. Ibrahim: "Collaborative Robots and Industrial Revolution 4.0 (IR 4.0)," *2020 International Conference on Emerging Trends in Smart Technologies (ICETST),* pp. 1-5, 2020.

[34] F. Zeng, J. Xiao and H. Liu: "Force/Torque Sensorless Compliant Control Strategy for Assembly Tasks Using a 6-DOF Collaborative Robot," *IEEE Access,* vol. 7, pp. 108795-108805, 2019.

[35] G. Singh, V. K. Banga and T. Yingthawornsuk: "Artificial Intelligence and Industrial Robot," *2022 16th International Conference on Signal-Image Technology & Internet-Based Systems (SITIS),* pp. 622–625, 2022.

[36] G. Singh, V. K. Banga and T. Yingthawornsuk: "Imitation Learning for High Precision Peg-in-Hole Tasks," *2020 6th International Conference on Control, Automation and Robotics,* pp. 368–372, 2020.

[37] B. Li, G. Li, W. Lin and P. Xu: "Design and constant force control of a parallel polishing machine," *2014 4th IEEE International Conference on Information Science and Technology,* pp. 324–328, 2014.

[38] Z. Fang, J. Li, Q. Zhang, H. Lian, C. Zhang and G. Yang: "Modeling and Force Control of Robotic Polishing System for the Wheel Hubs," *2019 IEEE International Conference on Robotics and Biomimetics (ROBIO),* pp. 2660–2664, 2019.

[39] W. Iida and K. Ohnishi: "Reproducibility and Operationality in Bilateral Teleoperation," *The 8th IEEE International Workshop on Advanced Motion Control,* pp. 217–222, 2004.

[40] Guchuan Zhu, A. Kaddouri, L. A. Dessaint and O. Akhrif: "A nonlinear state observer for the sensorless control of a permanent-magnet AC machine," *IEEE Transactions on Industrial Electronics,* vol. 48, no. 6, pp. 1098–1108, 2001.

[41] S. Morimoto, K. Kawamoto, M. Sanada and Y. Takeda: "Sensorless control strategy for salient-pole PMSM based on extended EMF in rotating reference frame," *IEEE Transactions on Industry Applications,* vol. 38, no. 4, pp. 1054-1061, 2002.

[42] J. M. Liu and Z. Q. Zhu: "Improved Sensorless Control of Permanent-Magnet Synchronous Machine Based on Third-Harmonic Back EMF," *IEEE Transactions on Industry Applications,* vol. 50, no. 3, pp. 1861-1870, 2014.

[43] J. Kim, I. Jeong, K. Nam, J. Yang and T. Hwang: "Sensorless Control of PMSM in a High-Speed Region Considering Iron Loss," *IEEE Transactions on Industrial Electronics,* vol. 62, no. 10, pp. 6151-6159, 2015.

[44] R. Antonello, L. Ortombina, F. Tinazzi and M. Zigliotto: "Enhanced Low-Speed Operations for Sensorless Anisotropic PM Synchronous Motor Drives by a Modified Back-EMF Observer," *IEEE Transactions on Industrial Electronics,* vol. 65, no. 4, pp. 3069–3076, 2018.

[45] X. Song, B. Han, S. Zheng and S. Chen: "A Novel Sensorless Rotor Position Detection Method for High-Speed Surface PM Motors in a Wide Speed Range," *IEEE Transactions on Power Electronics,* vol. 33, no. 8, pp. 7083–7093, 2018.

[46] B. Nahid-Mobarakeh, F. Meibody-Tabar and F. -M. Sargos: "Back EMF Estimation-Based Sensorless Control of PMSM: Robustness With Respect to Measurement Errors and Inverter Irregularities," *IEEE Transactions on Industry Applications,* vol. 43, no. 2, pp. 485-494, 2007.

[47] F. Genduso, R. Miceli, C. Rando and G. R. Galluzzo: "Back EMF Sensorless-Control Algorithm for High-Dynamic Performance PMSM," *IEEE Transactions on Industrial Electronics,* vol. 57, no. 6, pp. 2092-2100, 2009.

[48] T. Y. Liu, Z. Q. Zhu, B. Shuang, Z. Y. Wu, D. A. Stone and M. P. Foster: "An Online Position Error Correction Method for Sensorless Control of Permanent Magnet Synchronous Machine With Parameter Mismatch," *IEEE Access,* vol. 9, pp. 135708-135722, 2021.

[49] M. Schroedl: "Sensorless control of AC machines at low speed and standstill based on the "INFORM" method," *IAS '96. Conference Record of the 1996 IEEE Industry Applications Conference Thirty-First IAS Annual Meeting,* pp. 270–277, 1996.

[50] E. Robeischl and M. Schroedl: "Optimized INFORM measurement sequence for sensorless PM synchronous motor drives with respect to minimum current distortion," *IEEE Transactions on Industry Applications,* vol. 40, no. 2, pp. 591-598, 2004.

[51] Ronggang Ni, Kaiyuan Lu, F. Blaabjerg and Dianguo Xu: "A comparative study on pulse sinusoidal high frequency voltage injection and INFORM methods for PMSM position sensorless control," *IECON 2016 - 42nd Annual Conference of the IEEE Industrial Electronics Society,* pp. 2600–2605, 2016.

[52] Mengesha Mamo, K. Ide, M. Sawamura and J. Oyama: "Novel rotor position extraction based on carrier frequency component method (CFCM) using two reference frames for IPM drives," *IEEE Transactions on Industrial Electronics,* vol. 52, no. 2, pp. 508–514, 2005.

[53] R. Leidhold: "Position Sensorless Control of PM Synchronous Motors Based on Zero-Sequence Carrier Injection," *IEEE Transactions on Industrial Electronics,* vol. 58, no. 12, pp. 5371–5379, 2011.

[54] K. Shimamoto, S. Morimoto and S. Fukumaru: "Sensorless control based on position estimation by switching operation of modified PWM," *IECON 2016 - 42nd Annual Conference of the IEEE Industrial Electronics Society,* pp. 2898–2903, 2016.

[55] M. X. Bui, D. Guan, D. Xiao and M. F. Rahman: "A Modified Sensorless Control Scheme for Interior Permanent Magnet Synchronous Motor Over Zero to Rated Speed Range Using Current Derivative Measurements," *IEEE Transactions on Industrial Electronics,* vol. 66 no. 1, pp. 102–113, 2019.

[56] J. -Y. Chen and S. -C. Yang: "Saliency-Based Permanent Magnet Machine Position Sensorless Drive Using Proposed PWM Injection and Shunt-Based Current Sensing for Position Estimation," *IEEE Transactions on Industrial Electronics,* vol. 68, no. 7, pp. 5693–5703, 2020.

[57] J. -Y. Chen, K. -Y. Hung, G. -R. Chen and S. -C. Yang: "Integration of Measurement Vector Insertion With Discontinuous PWM to Improve Saliency-Based Sensorless Drive Position Estimation," *IEEE Transactions on Power Electronics,* vol. 37, no. 12, pp. 15283–15296, 2022.

[58] G. Wang, H. Zhou, N. Zhao, C. Li and D. Xu: "Sensorless Control of IPMSM Drives Using a Pseudo-Random Phase-Switching Fixed-Frequency Signal Injection Scheme," *IEEE Transactions on Industrial Electronics,* vol. 65, no. 10, pp. 7660–7671, 2018.

[59] Ji-Hoon Jang, S. -K. Sul, Jung-Ik Ha, K. Ide and M. Sawamura: "Sensorless Drive of Surface-Mounted Permanent-Magnet Motor by High-Frequency Signal Injection Based on Magnetic Saliency," *IEEE Transactions on Industry Applications,* vol. 39, no. 4, pp. 1031–1039, 2003.

[60] S. Kim, Y. -C. Kwon, S. -K. Sul, J. Park and S. -M. Kim: "Position sensorless operation of IPMSM with near PWM switching frequency signal injection," *8th International Conference on Power Electronics - ECCE Asia,* pp. 1660–1665, 2011.

[61] S. Kim, J. -I. Ha and S. -K. Sul: "PWM Switching Frequency Signal Injection Sensorless Method in IPMSM," *IEEE Transactions on Industry Applications,* vol. 48, no. 5, pp. 1576–1587, 2012.

[62] B. Du, T. Zhao, S. Han, L. Song and S. Cui: "Sensorless Control Strategy for IPMSM to Reduce Audible Noise by Variable Frequency Current Injection," *IEEE Transactions on Industrial Electronics,* vol. 67, no. 2, pp. 1149–1159, 2020.

[63] Z. Wu and R. Li: "Sensorless Control of PMSM Based on Sliding Mode Variable Structure Control and Adaptive Sliding Mode Observer," *2021 24th International Conference on Electrical Machines and Systems,* pp. 2015–2019, 2021.

[64] F. Jiang, K. Yang, S. Sun, Y. Xu and A. Liu: "Back-EMF based Sensorless Control of PMSM with an Improved PLL for Eliminating the Position Estimation Fluctuation," *2019 22nd International Conference on Electrical Machines and Systems,* pp. 1–4, 2019.

[65] G. Wang, Z. Li, G. Zhang, Y. Yu, and D. Xu: "Quadrature PLL-Based High-Order Sliding-Mode Observer for IPMSM Sensorless Control With Online MTPA Control Strategy," *IEEE Transactions on Energy Conversion,* vol. 28, no. 1, pp. 214–224, 2013.

[66] G. Wang, T. Li, G. Zhang, X. Gui and D. Xu: "Position Estimation Error Reduction Using Recursive-Least-Square Adaptive Filter for Model-Based Sensorless Interior Permanent-Magnet Synchronous Motor Drives," *IEEE Transactions on Industrial Electronics,* vol. 61, no. 9, pp. 5115–5125, 2014.

[67] N. Haje Obeid and A. Battiston: "Model based angle compensation method for sensorless control of a wide range high speed PMSM," *IECON 2019 - 45th Annual Conference of the IEEE Industrial Electronics Society,* pp. 2701–2706, 2019.

[68] M. X. Bui, M. F. Rahman and D. Xiao: "A Hybrid Sensorless Controller of an Interior Permanent Magnet Synchronous Machine Using Current Derivative Measurements and a Sliding Mode Observer," *IEEE Transactions on Industry Applications,* vol. 56, no. 1, pp. 314–324, 2020.

[69] T. Wang, B. Shi, J. Xu and C. Gerada: "Accuracy improvement of carrier signal injection sensorless control for IPMSM in consideration of inverter nonlinearity," *IECON 2015 - 41st Annual Conference of the IEEE Industrial Electronics Society,* pp. 273–278, 2015.

[70] G. Wang, T. Li, G. Zhang, X. Gui and D. Xu: "Position Estimation Error Reduction Using Recursive-Least-Square Adaptive Filter for Model-Based Sensorless Interior Permanent-Magnet Synchronous Motor Drives," *IEEE Transactions on Industrial Electronics,* vol. 61, no. 9, pp. 5115-5125, 2014.

[71] A. Ravikumar Setty, S. Wekhande and K. Chatterjee: "Compensation of rotor position estimation error due to stator winding resistance in signal injection based sensor less PMSM drives," *2013 IEEE International Symposium on Sensorless Control for Electrical Drives and Predictive Control of Electrical Drives and Power Electronics,* pp. 1–5, 2013.

[72] T. Y. Liu, Z. Q. Zhu, Z. Y. Wu, D. A. Stone and M. P. Foster: "Improved Sensorless Control Method and Asymmetric Phase Resistances Determination for Permanent Magnet Synchronous Machines," *IEEE Transactions on Industry Applications,* vol. 58, no. 3, pp. 3624–3636, 2022.

[73] J. Hilverkus, M. Märkl, R. Hagl and R. Kennel: "Influence of Frequency Dependent Motor Resistance and Inductance on the Current Control Loop Design of Servo Drives," *2021 IEEE 30th International Symposium on Industrial Electronics (ISIE),* pp. 1–7, 2021.

[74] V. Petro, K. Kyslan, P. Bober and M. Lacko: "Optimization of Injected Voltage Amplitude for Low-Speed Sensorless Control of PMSM with High-Frequency Pulse Signal Injection," *2022 IEEE 20th International Power Electronics and Motion Control Conference,* pp. 721–727, 2022.

[75] Y. Li, Z. Q. Zhu, D. Howe and C. M. Bingham: "Modeling of Cross-Coupling Magnetic Saturation in Signal-Injection-Based Sensorless Control of Permanent-Magnet Brushless AC Motors," *IEEE Transactions on Magnetics,* vol. 43, no. 6, pp. 2552–2554, 2007.

[76] Y. Li, Z. Q. Zhu, D. Howe, C. M. Bingham and D. A. Stone: "Improved Rotor-Position Estimation by Signal Injection in Brushless AC Motors, Accounting for Cross-Coupling Magnetic Saturation," *IEEE Transactions on Industry Applications,* vol. 45, no. 5, pp. 1843–1850, 2009.

[77] H. Kaimori and K. Akatsu: "Behavior Modeling of Permanent Magnet Synchronous Motors Using Flux Linkages for Coupling with Circuit Simulation," *IEEJ Journal of Industry Applications* vol. 1, no. 7, pp.56–63, 2018.

[78] C. -E. Hwang, Y. Lee and S. -K. Sul: "Analysis on Position Estimation Error in Position-Sensorless Operation of IPMSM Using Pulsating Square Wave Signal Injection," *IEEE Transactions on Industry Applications,* vol. 55, no. 1, pp. 458–470, 2019.

[79] S. Morimoto, K. Shimamoto and T. Hanamoto: "Realization of High Torque Density Encoderless Servo Drive System," *IECON 2019 - 45th Annual Conference of the IEEE Industrial Electronics Society,* pp. 1284–1289, 2019.

[80] G. Wang, R. Yang and D. Xu: "DSP-Based Control of Sensorless IPMSM Drives for Wide-Speed-Range Operation," *IEEE Transactions on Industrial Electronics,* vol. 60, no. 2, pp. 720-727, 2013.

[81] Z. Chen, M. Tomita, S. Doki and S. Okuma: "An extended electromotive force model for sensorless control of interior permanent-magnet synchronous motors," *IEEE Transactions on Industrial Electronics,* vol. 50, no. 2, pp. 288-295, 2003.

[82] Y. Iwaji, R. Takahata, T. Suzuki and S. Aoyagi: "Position Sensorless Control Method at Zero-Speed Region for Permanent Magnet Synchronous Motors Using the Neutral Point Voltage of Stator Windings," *IEEE Transactions on Industry Applications,* vol. 52, no. 5, pp. 4020-4028, 2016.

[83] M. H. Raibert and J. J. Craig: "Hybrid Position/Force Control of Manipulators," *Transactions of the ASME,* vol. 102, pp. 126–133, 1981.

[84] O. Khatib: "A unified approach for motion and force control of robot manipulators: The operational space formulation," *IEEE Journal on Robotics and Automation,* vol. 3, no. 1, pp. 43–53, 1987.

[85] S. Sakaino, T, Sato, K. Ohnishi: "Position Constrained Bilateral Control by Oblique Coordinate Control Consideration Priority of Tasks," *IEEJ Journal of Industry Applications,* vol. 2, no. 6, pp. 298–305, 2013.

[86] H. Tai and T. Murakami: "Equivalent mass matrix based bilateral control for multi-degrees-of-freedom systems," *2010 11th IEEE International Workshop on Advanced Motion Control,* pp. 343–348, 2010.

[87] W. Lyu and T. Murakami: "Bilateral Control between Manipulators with Different Structure Considering Fluctuation of Equivalent Mass Matrix," *2019 IEEE International Conference on Mechatronics (ICM),* pp. 370–375, 2019.

[88] N. Togashi, T. Shimono, N. Motoi, and N. Oda: "Experimental Comparison of Design Methods for Equivalent Mass Matrix in Motion Control System based on Workspace Observer," *2014 IEEE 13th International Workshop on Advanced Motion Control,* pp. 669–674, 2014.

[89] N. Motoi, and R. Kubo: "An Implementation method of workspace observer considering fluctuation of equivalent mass matrix," *41st Annual Conference of the IEEE Industrial Electronics Society,* pp. 4568–4573, 2015.

[90] T. Murakami, F. Yu, and K. Ohnishi: "Torque Sensorless Control in Multidegree-of-Freedom Manipulator," *IEEE Transactions on Industrial Electronics,* vol. 40, No. 2, pp. 259–265, 1993.

[91] K. Ohnishi, M. Shibata, and T. Murakami: "Motion Control for Advanced Mechatronics," *Transactions on Mechatronics,* vol.1, issue 1, pp.56–67, 1996.

[92] L. Han, J. Mao, P. Cao, Y. Gan and S. Li: "Toward Sensorless Interaction Force Estimation for Industrial Robots Using High-Order Finite-Time Observers," *IEEE Transactions on Industrial Electronics,* vol. 69, No. 7, pp. 7275-7284, 2022.

[93] L. Roveda, A. A. Shahid, N. Iannacci and D. Piga: "Sensorless Optimal Interaction Control Exploiting Environment Stiffness Estimation," *IEEE Transactions on Control Systems Technology,* vol. 30, No. 1, pp. 218-233, 2022.

[94] T. Murakami, N. Oda, Y. Miyasaka, K. Ohnishi: "A Motion Control Strategy Based on Equivalent Mass Matrix in Multidegree-of-Freedom Manipulator," *IEEE Transactions on Industrial Electronics,* vol.42, no. 2, pp.123–130, 1995.

[95] H. Nakamura, K. Ohishi, Y. Yokokura, N. Kamiya, T. Miyazaki, A. Tsukamoto: "Force Sensorless Fine Force Control Based on Notch-Type Friction-Free Disturbance Observers," *IEEJ Journal of Industry Applications,* vol. 7, No. 2, pp. 117–126, 2018.

[96] T. Uzunovic, A. Sabanovic, M. Yokoyama, T. Shimono: "Novel Algorithm for Effective Position/Force Control," *IEEJ Journal of Industry Applications,* vol. 8, No. 6, pp. 960–966, 2019.

[97] S. Katsura, Y. Matsumoto and K. Ohnishi: "Analysis and experimental validation of force bandwidth for force control," *IEEE Transactions on Industrial Electronics,* vol. 53, No. 3, pp. 922–928, 2006.

[98] S. -H. Chien, J. -H. Wang and M. -Y. Cheng: "Performance Comparisons of Different Observer-Based Force-Sensorless Approaches for Impedance Control of Collaborative Robot Manipulators," *2020 IEEE Conference on Industrial Cyberphysical Systems (ICPS),* pp. 326–331, 2020.

[99] E. Sariyildiz, H. Sekiguchi, T. Nozaki, B. Ugurlu and K. Ohnishi: "A Stability Analysis for the Acceleration-Based Robust Position Control of Robot Manipulators via Disturbance Observer," *IEEE/ASME Transactions on Mechatronics,* vol. 23, no. 5, pp. 2369–2378, 2018.

[100] E. Sariyildiz, S. Hangai, T. Uzunovic and T. Nozaki: "Discrete-Time Analysis and Synthesis of Disturbance Observer-Based Robust Force Control Systems," *IEEE Access,* vol. 9, pp. 148911–148924, 2021.

[101] H. Kurumatani and S. Katsura: "Design of Nominal Parameters for Robust Sensorless Force Control Based on Disturbance Observer," *IEEJ Journal of Industry Applications,* vol. 8, No. 2, pp. 342–351, 2019.

[102] D. Janiszewski: "Load torque estimation in sensorless PMSM drive using Unscented Kalmana Filter," *2011 IEEE International Symposium on Industrial Electronics, Gdansk,* pp. 643–648, 2011.

[103] S. Akutsu, H. Sekiguchi, T. Nozaki and T. Murakami: "Position and torque sensorless motion transmission for haptic teleoperation using two types of voltage compensation," *2017 24th International Conference on Mechatronics and Machine Vision in Practice,* pp. 1–6, 2017.

[104] S. Akutsu, T. Nozaki and T. Murakami: "Position and Torque Sensorless Motion Transmission Using Parameter Identification Based on Least Mean Squares Method," *IECON 2018 - 44th Annual Conference of the IEEE Industrial Electronics Society,* pp. 5098–5103, 2018.

List of Achievements

Journals (First Author)

[1] <u>Keita Shimamoto</u> and Toshiyuki Murakami, "Force Sensorless Hybrid Position/Force Control with Equivalent Mass Matrices Switching for Decoupled Rubbing Motion," *IEEJ Journal of Industry Applications*, vol. 12, no. 2, pp. 107–116, 2023.

[2] <u>Keita Shimamoto</u> and Toshiyuki Murakami, "Position and Cross-Coupling Factors Estimation for Sliding Mode Current Control Based Position-Sensorless Control of IPMSM," *IEEE Access*, vol. 10, pp. 74873–74882, 2022.

[3] <u>Keita Shimamoto</u>, Kazuki Tanida, Takahiro Nozaki, and Kouhei Ohnishi, "Transmission of Force Sensation Achieved by Tendon-Driven Spherical Joint Mechanism," *IEEJ Transactions on Industry Applications*, vol. 133-D, no. 3, pp. 306–313, 2013. (in Japanese)

Journals (Co-author)

[1] Shinya Morimoto, <u>Keita Shimamoto</u>, Masanobu Kakihara, and Tsuyoshi Hanamoto, "Improving Position Estimation Accuracy of Magnetic Saliency Based Sensorless Control by Considering Cross-Coupling Factor," *IEEJ Journal of Industry Applications*, vol. 10, no 1, pp. 18–26, 2021.

[2] Yoshiki Ohno, <u>Keita Shimamoto</u>, Takahiro Mizoguchi, and Kouhei Ohnishi, "Method of Time-Delay Compensation in Multi-Degree-of-Freedom Bilateral Control Systems with Different Configurations," *IEEJ Transactions on Industrial Informatics*, vol. 134-D, no 3, pp. 317–324, 2014.

International Conferences (First Author)

[1] <u>Keita Shimamoto</u> and Toshiyuki Murakami, "Equivalent Mass Matrices Design Methods Considering Interference to Force Control in Force Sensorless Hybrid Control for Rubbing Motion," in *The IEEJ International Workshop on Sensing, Actuation, Motion Control, and Optimization, SAMCON 2022, Saitama, Japan*, March 8–10, 2022.

[2] Keita Shimamoto and Toshiyuki Murakami, "Performance Evaluation of Force Control and Reaction Force Estimation in Force Sensorless Hybrid Control for Workspace Based Controller," in *Proceedings of the IEEE 17th International Conference on Advanced Motion Control, AMC 2022, Padova, Italy*, February 18–20, 2022.

[3] Keita Shimamoto, "Estimation of dq-axis Mutual Inductances for Vibration Reduction of Encoderless Control," in *Proceedings of the IEEE 30th International Symposium on Industrial Electronics, ISIE 2021, Kyoto, Japan*, June 20–23, 2021.

[4] Keita Shimamoto, and Shinya Morimoto, "Position Estimation Accuracy Improvement for Magnetic Saliency Based Sensorless Control Including Cross-Coupling Factor," in *Proceedings of the International Power Electronics Conference, IPEC-Niigata 2018 -ECCE Asia, Niigata, Japan*, May 20–24, 2018.

[5] Keita Shimamoto, Shinya Morimoto, and Shingo Fukumaru, "Sensorless control based on position estimation by switching operation of modified PWM," in *Proceedings of the 42nd Annual Conference of the IEEE Industrial Electronics Society, IECON 2016, Florence, Italy*, October 23–26, 2016.

[6] Keita Shimamoto, Daiki Suzuki, and Kouhei Ohnishi, "Bilateral control for 4-DOF manipulator with a tendon-driven spherical joint mechanism," in *Proceedings of the 2014 IEEE 13th International Workshop on Advanced Motion Control, AMC 2014, Yokohama, Japan*, March 14–16, 2014.

[7] Keita Shimamoto, Yoshiki Ohno, Takahiro Nozaki, and Kouhei Ohnishi, "Time delay compensation for tendon-driven bilateral control using modal decomposition and communication disturbance observer," in *Proceedings of the 2014 IEEE International Conference on Industrial Technology, ICIT 2014, Busan, Korea (South)*, February 26–March 1, 2014.

[8] Keita Shimamoto, Kento Watanabe, and Kouhei Ohnishi, "Improvement in force control with force projection for 2-DOF tendon-driven spherical joint mechanisms," in *Proceedings of the 2013 IEEE International Conference on Mechatronics, ICM 2013, Vicenza, Italy*, February 27–March 1, 2013.

[9] Keita Shimamoto and Kouhei Ohnishi, "Motion control for 2-DOF tendon-driven spherical joint mechanisms," in *Proceedings of the 38th Annual Conference on IEEE Industrial Electronics Society, IECON 2012, Montreal, Canada*, October 25–28, 2012.

International Conferences (Co-author)

[1] Shinya Morimoto, <u>Keita Shimamoto</u> and Tsuyoshi Hanamoto, "Realization of High Torque Density Encoderless Servo Drive System," in *Proceedings of the 45th Annual Conference of the IEEE Industrial Electronics Society, IECON 2019, Lisbon, Portugal*, October 14–17, 2019.

[2] Sho Iwata, Kazuki Tanida, <u>Keita Shimamoto</u>, Kouhei Ohnishi, and Yasuyuki Yamada, "Bilateral control using compression type mechanical gravity canceller," in *Proceedings of the IEEE 13th International Workshop on Advanced Motion Control, AMC 2014, Yokohama, Japan*, March 14–16, 2014.

[3] Yoshiki Ohno, Ryohei Kozuki, <u>Keita Shimamoto</u> and Kouhei Ohnishi, "A novel time-delay compensation method for multi degree-of-freedom bilateral control system with different configuration," in *Proceedings of the 39th Annual Conference of the IEEE Industrial Electronics Society, IECON 2013, Vienna, Austria*, November 10–13, 2013.

[4] Kento Watanabe, <u>Keita Shimamoto</u>, and Kouhei Ohnishi, "Bilateral control with 2-DOF haptic spherical interface," in *Proceedings of the 38th Annual Conference on IEEE Industrial Electronics Society, IECON 2012, Montreal, Canada*, October 25–28, 2012.

[5] Tomoko Kawase, <u>Keita Shimamoto</u>, Kazuki Tanida, and Kouhei Ohnishi, "Application of tension control into linear motor-actuated cable differential-driven joint," in *Proceedings of the 12th IEEE International Workshop on Advanced Motion Control, AMC 2012, Sarajevo, Bosnia and Herzegovina*, March 25–27, 2012.

Domestic Conferences (First-author)

[1] <u>Keita Shimamoto</u> and Toshiyuki Murakami, "Position Estimation Compensation Considering dq-axis Mutual Inductance for Position-and-Torque-Sensorless 4ch-Bilateral Control," in *Proceedings of the IEEJ Technical Meeting on Mechatronics Control, MEC 2022*, December 3, 2022.

[2] <u>Keita Shimamoto</u>, Daiki Suzuki, and Kouhei Ohnishi, "Position Control Method for 4-DOF Manipulator with Tendon-driven Spherical Joints," in *Proceedings of the IEEJ Technical Meeting on Industrial Instrumentation and Control, IIC 2013*, March 7–8, 2013.

[3] <u>Keita Shimaoto</u>, Takahiro Mizoguchi, and Kouhei Ohnishi, "Performance Evaluation of 4-DOF Parallel Manipulator with A Tendon-driven Spherical Joint Mechanism," in *Proceedings of 2013 IEEJ Industry Applications Society Conference*, August 28–30, 2013.

Domestic Conferences (Co-author)

[1] Yoshitomo Matsumi, Yu Nakajima, Shinnosuke Yamaoka, Keita Shimamoto, and Kouhei Ohnishi, "Characteristic Analysis of Oblique Coordinate Based Bilateral Control System using Piezoelectric Actuator," in *Proceedings of the IEEJ Technical Meeting on Industrial Instrumentation and Control, IIC 2013*, March 7–8, 2013.

[2] Yoshiki Ohno, Keita Shimamoto, Takahiro Mizoguchi, and Kouhei Ohnishi, "Time-Delay Compensation Method for Multi Degree-of-Freedom Bilateral Control System with Different Configuration," in *Proceedings of the IEEJ Technical Meeting on Industrial Instrumentation and Control, IIC 2013*, March 7–8, 2013.

[3] Seiji Uozumi, Koyo yu, Keita Shimamoto, Takahiro Nozaki, and Kouhei Ohnishi, "Design Method of Function Mode Considering Shape of Grasping Object," in *Proceedings of the IEEJ Technical Meeting on Industrial Instrumentation and Control, IIC 2013*, March 7–8, 2013.

Awards

[1] Excellent Paper Presentation Award, Technical Committee on Mechatronics Control (MEC) IEEJ Industry Applications Society,

"Position Estimation Compensation Considering dq-axis Mutual Inductance for Position-and-Torque-Sensorless 4ch-Bilateral Control,"

January 10, 2023.

[2] IEEJ Best Paper Award, Industry Applications Society (IAS),

"Transmission of Force Sensation Achieved by Tendon-Driven Spherical Joint Mechanism,"

August 27, 2014.

[3] The 2013 IEEE, IES Best Conference Paper Award,

"Motion Control for 2-DOF Tendon-Driven Spherical Joint Mechanisms,"

November 11, 2013.